THE UNIVERSITY OF HULL

OFFSHORE OIL SPILL DETECTION USING SYNTHETIC APERTURE RADAR

being a thesis submitted for the degree of

Doctor of Philosophy

in the University of Hull

by

Suman Singha, M.Sc, M.Tech

May 2014

DECLERATION

I confirm that this is my own work and the use of all material from other sources has been properly and fully acknowledged. Some of the work in this thesis has been published in academic journals and some diagrams, tables and other material presented in the thesis have also been included in those publications. A list of published material based on work undertaken for this doctoral study is given on page *VI*.

This work was supported in part by the European Maritime Safety Agency–European Commission-Joint Research Centre collaboration for the "development and support of satellite monitoring techniques for oil spill detection" and University of Hull. The views, opinions, and findings contained in this thesis are those of the author and should not be construed as an official EMSA, JRC or European Commission position, policy, or decision.

Kingston upon Hull, United Kingdom (SUMAN SINGHA)

ABSTRACT

Among the different types of marine pollution, oil spill has been considered as a major threat to the sea ecosystems. The source of the oil pollution can be located on the mainland or directly at sea. The sources of oil pollution at sea are discharges coming from ships, offshore platforms or natural seepage from sea bed. Oil pollution from sea-based sources can be accidental or deliberate. Different sensors to detect and monitor oil spills could be onboard vessels, aircraft, or satellites. Vessels equipped with specialised radars, can detect oil at sea but they can cover a very limited area. One of the established ways to monitor sea-based oil pollution is the use of satellites equipped with Synthetic Aperture Radar (SAR).

The aim of the work presented in this thesis is to identify optimum set of feature extracted parameters and implement methods at various stages for oil spill detection from Synthetic Aperture Radar (SAR) imagery. More than 200 images of ERS-2, ENVSAT and RADARSAT 2 SAR sensor have been used to assess proposed feature vector for oil spill detection methodology, which involves three stages: segmentation for dark spot detection, feature extraction and classification of feature vector. Unfortunately oil spill is not only the phenomenon that can create a dark spot in SAR imagery. There are several others meteorological and oceanographic and wind induced phenomena which may lead to a dark spot in SAR imagery. Therefore, these dark objects also appear similar to the dark spot due to oil spill and are called as look-alikes. These look-alikes thus cause difficulty in detecting oil spill spots as their primary characteristic similar to oil spill spots. To get over this difficulty, feature extraction becomes important; a stage which may involve selection of appropriate feature extraction parameters. The main objective of this dissertation is to identify the optimum feature vector in order to segregate oil spill and 'look-alike' spots. A total of 44 Feature extracted parameters have been studied. For segmentation, four methods; based on edge detection, adaptive theresholding, artificial neural network (ANN) segmentation and the other on contrast split segmentation have been implemented. Spot features are extracted from both the dark spots themselves and their surroundings. Classification stage was performed using two different classification techniques, first one is based on ANN and the other based on a two-stage processing that combines classification tree analysis and fuzzy logic. A modified feature vector, including both new and improved features, is suggested for better description of different types of dark spots. An ANN classifier using full spectrum of feature parameters has also been developed and evaluated. The implemented methodology appears promising in detecting dark spots and discriminating oil spills from look-alikes and processing time is well below any operational service requirements.

ACKNOWLEDGEMENT

First of all, without His will; this would not have been possible. I wish to thank the ***ALMIGHTY GOD*** for giving me the *strength*, *health* and *determination* to carry out this research work through His divine grace.

The completion of my dissertation would not have been possible without the assistance, support and encouragement of many people. First, I would like to show my gratitude to my supervisor ***Dr. Tim Bellerby*** and ***University of Hull*** for giving this wonderful opportunity to carry out my doctoral study. I owe my profound gratitude and sincere thanks to my supervisor for giving me the guidance, support and most importantly for giving me the opportunity to work at NERC Earth Observation Science Laboratory which helped me to broaden my knowledge and experience. I consider myself fortunate to have had the opportunity to work under his supervision. His clarity of thoughts, creativity and his vast knowledge of different scientific fields has been a great source of inspirations.

I take this as an opportunity to thank ***'CleanSeaNet'*** team at ***European Maritime Safety Agency (EMSA),*** Portugal, especially ***Dr. Olaf Trieschmann***, for his able guidance which helped me to complete this thesis. I would also like to thank ***Dr. Michele Vespe***, at ***European Commissions' Joint Research Centre (JRC),*** Ispra, Italy for valuable input towards my thesis and ***Dr. Kostas N. Topouzelis*** at ***Department of Marine Science, University of Aegean***, Greece for helping me throughout my doctoral study in many aspects.

I acknowledge the ***European Space Agency (ESA)***, ***MacDonald, Dettwiler and Associates Ltd. (MDA)*** **and** ***European Maritime Safety Agency (EMSA)*** for the provision of Synthetic Aperture Radar imagery and ancillary data. I am thankful to ***Dr. Susanne Lehner*** and my current colleges at ***Maritime Security Lab, Earth Observation Centre, German Aerospace Centre (DLR)*** for supporting me during my thesis write up, in spite of their busy schedule and providing set of TerraSAR-X imagery.

At the end, I am short of words to express my feelings for my ***Maa and Baba***; to them I will always remain grateful throughout my life. Last but not the least I would like to thank ***Almut*** for being the love of my life and her support throughout my studies. They always stood beside me throughout all the challenges that I have faced.

Kingston upon Hull, United Kingdom (SUMAN SINGHA)

PUBLICATIONS RELATED TO THIS THESIS

I. Journal article : **S. Singha,** T. Bellerby and O. Trieschmann, "Satellite oil spill detection using artificial neural networks", *IEEE Journal of Selected Topics in Applied Earth Observations and Remote Sensing, ", Volume 6, Issue 6, Pages 2355 - 2363,* December 2013.

II. Journal article : **S. Singha,** M. Vespe and O. Trieschmann, "Automatic SAR based Oil Spill Detection and Performance Estimation via Semi-Automatic Operational Service Benchmark", *Marine Pollution Bulletin, Volume 73, Issue 1, Pages 199 - 209,* 15 August 2013.

III. Journal article: **S Singha,** D Velotto and S Lehner, "Near Real Time Monitoring of Platform Sourced Pollution using TerrraSAR-X over the North Sea" *Marine Pollution Bulletin, Volume 86, Issue 1-2, Pages 379 - 390,* 15 July 2014.

IV. Journal article (under review): K. Topouzelis, and **S. Singha** and D. Kitsiou, "Incidence Angle Normalization of Wide Swath SAR Data for Oceanographic Applications", *ISPRS Journal of Photogrammetry and Remote Sensing,* 2014.

V. Conference Paper: **S. Singha** and T. J Bellerby, "ANN-based image segmentation and feature extraction to distinguish oil spills from 'look-alike' spots in SAR imagery", *Geophysical Research Abstracts*, Vol. 13, EGU-2011-2209, Vienna, Austria.

VI. Conference Paper: **S. Singha,** T. J Bellerby and O. Trieschmann, "Detection and classification of oil spill and look-alike spots from SAR imagery using an artificial neural network", In Proc. *IEEE International Geoscience and Remote Sensing Symposium 2012,* Munich, Germany, pp.4403-4406.

VII. Conference Paper: **S. Singha**, K. Topouzelis, M. Vespe and O. Trieschmann, "Radiometric Normalization on SAR Images for Oil Spill Detection", In Proc. *ESA Living Planet Symposium 2013,* Edinburgh, United Kingdom (ESA SP-722, December 2013).

VIII. Conference Paper: S. Lehner, D. Velotto, **S. Singha**, A. Soloviev, "Oil Spill in SAR Satellite Imagery", *Gulf of Mexico Oil Spill & Ecosystem Science Conference*, January 2014, Mobile, Alabama, USA.

IX. Conference Paper: **S. Singha**, D. Velotto and S. Lehner, "Near Real Time Operational Oil Spill Detection Service Using Classification Tree", In Proc. *IEEE GOLD Remote Sensing Conference,* June 2014, Berlin, Germany.

CONTENTS

LIST OF FIGURES

LIST OF TABLES

CHAPTER 1
INTRODUCTION

1.1 GENERAL

An oil spill occurs due to intentional or unintentional release of oil into the natural environment as a result of human activity. This term often refers to the marine oil spills where oil is released into the ocean or coastal waters. Among different types of marine pollution, oil is a major threat to the sea ecosystems. About half of the total oil spills in the marine environment come from operative discharges by ships and in most of the cases these are illegal discharges. During last few decades, maritime transportation has grown steadily. More the number of ships more will be the probability of illegal oil discharges. Both oil tankers and other kinds of ships are among the suspected offenders of illegal discharges. Oil spill affect the marine ecosystem and cause enormous political, environmental and scientific concern. Writing in Nature Geoscience, a team of scientists (Li *et al.*, 2010) found that large quantities of oil spilled during the 1989 Exxon Valdez disaster can still be found beneath gravel beaches in Alaska which has been a serious threat to costal environment for last two decades. At the time of writing this dissertation a catastrophic event of oil spill has been occurred in the Gulf of Mexico. Oil has started spewing into the Gulf since British Petroleum's Deepwater Horizon rig exploded on 20 April 2010 killing 11 workers onboard. Scientists along with US government official have estimated that staggering five million barrels of crude oil relished into the fragile ecosystem (Source: BBC, 2010). On the other hand, in Europe, which is the world's largest market in crude oil imports, representing about one third of the world's total, 90% of oil and refined products are transported to and from the continent by sea; unfortunately, some of this oil makes its final way into the sea (Karantzalos *et al.,* 2008). Towards the compliance with marine legislation and the efficient surveillance and protection of coastal environments, automatic detection and tracking of oil spills and illegal oil discharges is of fundamental importance. The construction of a cost-effective remote sensing processing system has been the subject of research and development for approximately two decades (Hühnerfuss *et al.,*1986, 1987; Bern *et al.,* 1992; Skøelv and Wahl 1993; Wahl *et al.,* 1994b; ESA 1998; Espedal and Wahl, 1999; Solberg *et al.,*2007, Ivanov *et al.,* 2008; Ferraro *et al.,* 2010; Singha *et al.,* 2013a; 2013b), looking forwards, nowadays, to the construction of a fully automatic system that will identify objects with a high probability of being oil spills and will activate an alarm for further manual inspection and possible verification of the incident by a surveillance aircraft (Indregard *et al.,* 2004; Brekke and Solberg 2005a).

1.2 TYPES AND CAUSES OF OIL SPILL

Spills usually happen due to bad weather (hurricanes, storms, and earthquakes), intentional acts of violence (like war, vandals, or dumping) and human errors. The main reasons for oil spill are,

1. Spill due to tankers (boats that carry oil from one location to another) crashing, breaking, or running up on land
2. Spill due to breaking or leaking of pipelines (like the Alaska pipeline which pumps oil continuously)
3. Oil spill due to barges crashing
4. Spill due to oil wells blowing up
5. Spill from above and below ground oil storage tanks
6. Accidents of trucks carrying oil

7. Spill occurred in production facility (a company that takes pure (crude) oil, and changes it into other products (tar, asphalt, etc.))

8. Unknown locations and mystery spills (some people dump oil and other chemicals on purpose)

9. Spill due to miss operation in oil platforms (factories located in the ocean which pump oil from deep in the ocean floor)

10.Spill due to natural seepage (this is when natural oil found in the ground leaks up into the water)

Most incidents of oil spill are the result of a combination of actions and circumstances listed and hence contribute to varying degrees of oil spills. Table 1.1 enumerates incidence of spills of different sizes in terms of the primary event or operation in progress at the time of the spill occurring 1974 to 2008. These "causes" have been grouped into Operations and Accidents. Spills for which the relevant information is not available or where the cause is not one of those listed have been put under Other/unknown category.

Table: 1.1 Incidence of spills by cause during 1974-2008 (Adapted from ITOPF online database)

	Less than7 Tones	**Between 7 and 700 Tones**	**Greater than 700 Tones**	**Total**
OPERATIONS				
Loading /Discharging	2825	334	30	3189
Bunkering	549	26	0	575
Other Operations	1178	56	1	1235
ACCIDENTS				
Collisions	175	303	99	577
Groundings	238	226	119	583
Hull Failures	576	90	43	709
Fire & Explosions	88	16	30	134
Other/Unknown	2188	152	26	2366
TOTAL	7817	1203	348	9368

It is apparent from Table 1.1 that,

(1) Most spills from tankers result from routine operations such as loading, discharging and bunkering which normally occur in ports or at oil terminals
(2) The majority of these operational spills are small, with some 91% involving quantities of less than 7 tons
(3) Accidental causes such as collisions and groundings generally give rise to much larger spills, with at least 84% of incidents involving quantities in excess of 700 tons being accredited to such factors.

1.3 MAJOR OIL SPILLS IN THE PAST

On April 20, 2010 an explosion and subsequent fire onboard the *Deepwater Horizon* semi-submersible Mobile Offshore Drilling Unit (MODU), situated about 40 miles (64 km) southeast of the Louisiana coast in the Macondo Prospect oil field, triggered a catastrophic event of oil spill. This environmental disaster is now considered the largest in U.S. history. The federal government’s estimate of the total spill volume amounts to 5 million barrels, of which 800,000 barrels were recovered (Source: BBC, 2010). If counting oil spills on land, then the largest amount of oil ever lost was during the Persian Gulf War. Some of the major international oil spills have been enlisted in Table 1.2.

Table: 1.2 Oil spills of over 100,000 tones or 30 million US gallons, ordered by tones (Updated and adapted from IFOPT, 2010 online database)

Spill / Tanker	Location	Date	Tones of crude
Gulf of Mexico(Deepwater Horizon)	**Gulf of Maxico**	**20th April**	**700,000 (Approx)** **5 Million barrel**
Gulf War oil spill	Persian Gulf	January 23, 1991	136,000 - 1,500,000
Ixtoc I oil well	Gulf of Mexico	June 3, 1979	454,000 - 480,000
Atlantic Empress / Aegean Captain	Trinidad and Tobago	July 19, 1979	287,000
Fergana Valley	Uzbekistan	March 2, 1992	285,000
Nowruz oil field	Persian Gulf	February 1983	260,000
ABT Summer	Angola	1991	260,000
Castillo de Bellver	Saldanha Bay, South Africa	August 6, 1983	252,000
Amoco Cadiz	Brittany, France	March 16, 1978	223,000
Amoco Haven tanker disaster	Mediterranean Sea near Genoa, Italy	1991	144,000
Odyssey	700 nautical miles (1,300 km) off niva	1988	132,000
Sea Star	Gulf of Oman	December 19,	115,000
Torrey Canyon	Scilly Isles, UK	March 18, 1967	80,000 - 119,000
Irenes Serenade	Navarino Bay,	1980	100,000
Urquiola	A Coruña, Spain	May 12, 1976	100,000

1.4 OIL SPILL AND ITS ENVIRONMENTAL IMPACT

Oil spill can pose serious threats to the marine environment. The severity of impact of an oil spill depends on a number of factors, including the oil characteristics. Even large spills of refined petroleum products, such as gasoline, evaporate quickly and cause only short-term environmental effects. On the other hand, crude oils, heavy fuel oil, and water-in-oil mixtures may cause widespread and long-lasting physical contamination of shorelines. Chronic offshore oil producing platform sourced pollution poses significant threat to costal environment. Some examples of platform sourced pollution are presented in Fig 1.1, 1.2 and 1.3. Natural conditions, such as water temperature and weather, also influence the behaviour of oil in the marine environment.

The term oil describes a broad range of both natural hydrocarbon based substances as well as refined petroleum products. Most refined petroleum products are mixtures of many types of hydrocarbon-based substances. Commonly used products refined from crude oil include fuel oil, gasoline, kerosene, and jet fuel. Each type of crude oil and refined product has characteristic physical and chemical properties. These properties together affect the oil spread and its break down, hazard to marine and human life and threat to natural and man-made resources.

Many impacts due to oil spill have been documented in the scientific and technical literature. However, all the effects of oil pollution are yet to be completely understood, an indication of the likely scale and duration of damage can usually be deduced from the information available. However, it can be difficult to present a balanced view of the realities of spill effects, given the often highly charged and emotional nature of a spill and its aftermath (Kingston, 2002). The scientific community can become polarised into opposing camps with one side intent on quantifying every aspect of damage, and the other emphasising the capacity of the environment to recover naturally. However simple reality is that sometimes significant damage occurs, sometimes not and the aim of this section is to draw together general information is known about spill effects and their longevity.

The importance of plankton in primary productivity of the oceans and as a temporary home for the eggs and larvae of fish, shellfish, and shoreline organisms is well known. Laboratory studies have demonstrated toxic and sub-lethal effects on the plankton caused by oil, and there is little doubt that there is potential for widespread impact. Unfortunately, plankton is extremely difficult to study reliably because they are amongst the most variable of marine communities in space and in time. The presence of oil on open water is also patchy and discontinious, making it difficult to establish where and when the plankton might have been exposed to the oil. In addition to that, the possibility of long-term effects cannot be excluded, there is no indication that oil-induced losses of eggs and larval stages cause a significant decline in adult populations (Kingston, 2002).

Seabirds are amongst the most vulnerable inhabitants of open waters since they are easily harmed by floating oil. Species that dive for their food or which congregate on the sea surface is particularly at risk. Although oil ingested by birds during attempts to clean themselves by preening may also be lethal, the most common cause of death is from drowning, starvation and loss of body heat following fouling of plumage by oil.

Cleaning and rehabilitation after oiling is often attempted, but for many species it is rare for more than a fraction of oiled birds to survive cleaning and rarer still for those that survive to breed successfully after release. Penguins are an exception and are much more resilient than most other birds. When handled properly, the majority are likely to survive the cleaning process and rejoin breeding populations (Burger, 1993; ITOPF).

Edwards *et al.,* (1996) pointed out that wildlife other than fish and sea creatures, including mammals, reptiles, amphibians, and birds that live in or near the ocean, also might be poisoned by oil waste. The hazards for wildlife include toxic effects of exposure or ingestion, injuries such as smothering and deterioration of thermal insulation, and damage to their reproductive systems and behaviours. Long-term ecological effects that contaminate or destroy the marine organic substrate and thereby interrupting the food chain are also harmful to the wildlife, so species populations may change or disappear.

Coastal areas are usually thickly populated and attract many recreational activities and related facilities that have been developed for fishing, boating, snorkelling and scuba diving, swimming, nature parks and preserves, beaches, and other resident and tourist attractions. Oil waste that invades and pollutes these areas and negatively affects human activities can have devastating and long-term effects on the local economy and society. Property values for housing tend to decrease, regional business activity declines, and future investment is risky (Edwards *et al.,* 1996).

1.5 NEED FOR OIL SPILL DETECTION

Over the past decade there has been considerable increase in maritime transportation, which has increased the risk of oil spill in the marine environment. More number of off shore oil platforms also increases the potential illegal oil discharges (Brekke, 2005; Fingas and Brown, 1997). The possible environmental impacts by oil spill have already been discussed in the previous section.

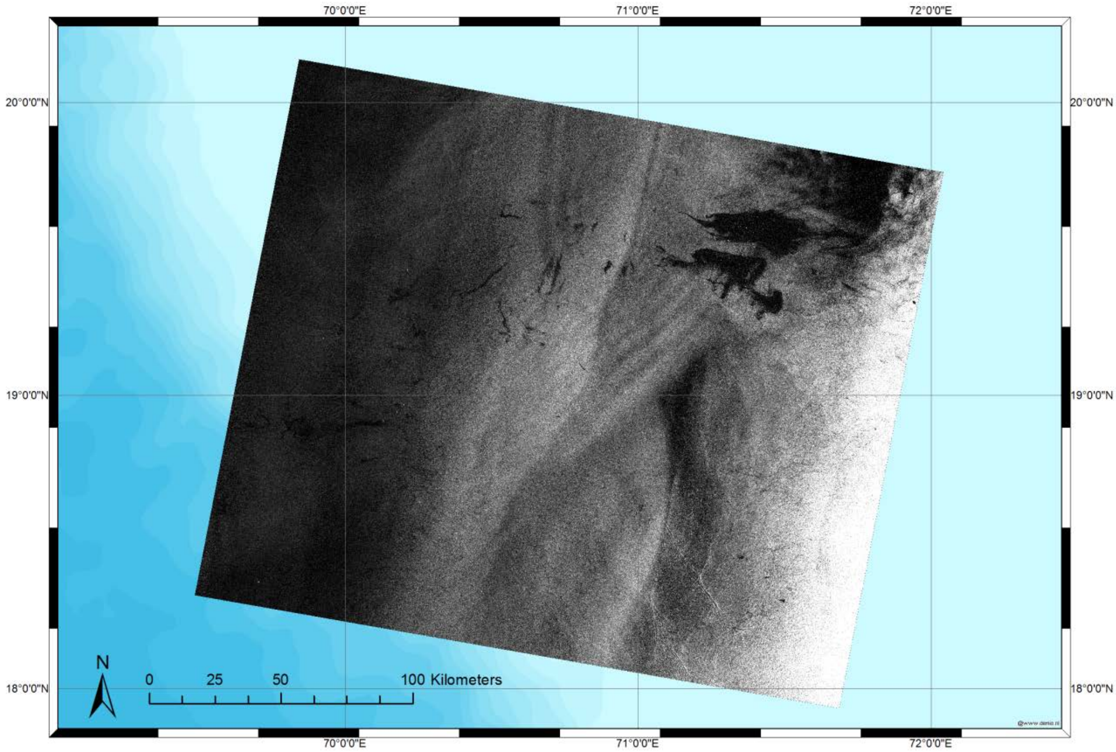

Figure 1.1: TerraSAR-X images acquired in Wide ScanSAR mode (270 × 200 km range × azimuth, Beam: Wide_002, VV-pol) all acquired over cluster of offshore oil platforms (near Mumbai coast, India) on 06th November 2013 at 13:17:21 UTC, shows spill from the monitored offshore platforms UTC (©DLR, Image acquired under project id: OCE2015, Principal Investigator: Suman Singha).

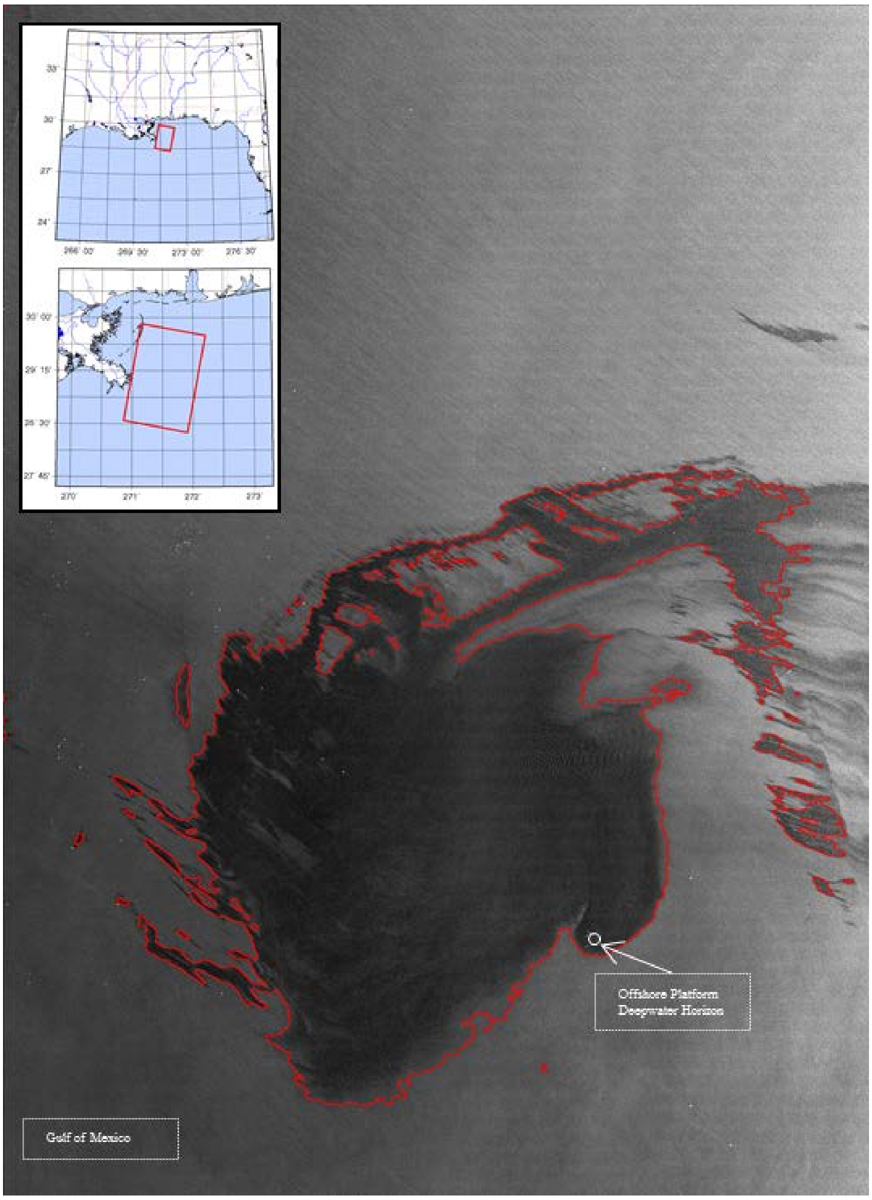

Figure 1.2: TerraSAR-X images acquired in ScanSAR mode (Polarization:VV) all acquired during Gulf of Mexico incident on 30th April 2010 at 11:59 UTC. The results show detected spill from the monitored offshore platform Deepwater Horizon UTC (©DLR, Image acquired under project id: OCE1045, Principal Investigator: Domenico Velotto).

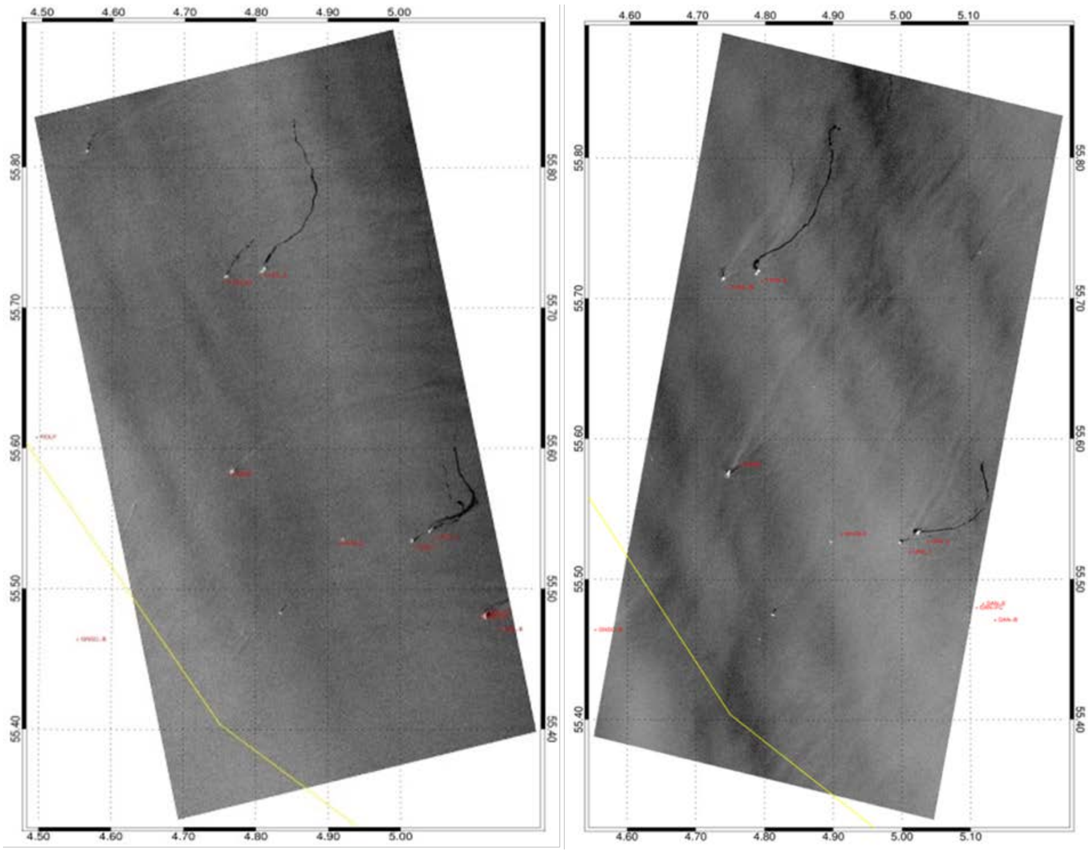

Fig 1.3: Two consecutive acquisitions by TerraSAR-X in StripMap mode (a) 8th of June 2011 at 17:10:53 UTC ascending pass. (c) 9th of June 2011 at 06:07:37 UTC descending pass UTC (©DLR, Image acquired under project id: OCE1045).

It is very important that the location, extent and amount of the spilled oil should be known exactly to the oil spill cleanup response teams (skimmers and boomers) for proper planning of operations. In European context, after Erika and Prestige disaster European Commission established European Maritime Safety Agency in the marine environment in the framework of Directive 2005/35/EC (amended by Directive 2009/123/EC; EMSA, 2011; 2014) “on ship-source pollution and on the introduction of penalties, including criminal penalties, for pollution offences”. In particular Commission tasked EMSA to ‘work with the Member States in developing technical solutions and providing technical assistance in relation to the implementation of this Directive, in actions such as tracing discharges by satellite monitoring and surveillance and identifying potential polluter.

1.6 ROLE OF REMOTE SENSING FOR OIL SPILL DETECTION

Remote sensing offers the advantage of being able to observe events in remote and often inaccessible areas. It happens to be an attractive source of information for detecting locations of oil spills. Again, information on the rate and direction of oil movement can be obtained through multi-temporal imaging and thereby assisting in drift prediction modeling for facilitating in cleaning up.

For ocean spills, remote sensing data can be obtained from airborne platforms, thermal infrared imaging, airborne laser fluouro sensors, airborne and space borne optical sensors, as well as airborne and space borne Synthetic Aperture Radar (SAR) (Indregard *et al.*, 2004; Brekke and Solberg, 2005; Jha *et al.*, 2008)

In early use of remote sensing included data from only visible and infrared (i.e., optical) sensors photography but it was not possible to both detect and monitor the extent of the oil spills simultaneously (Fingas *et al.,* 1999), due to coarse temporal resolution of the data, absence of any clear discriminating feature between oil spill and surrounding sea surface, unavailability of data in night (in case of visible sensor) or during bad weather conditions (e.g. cloud cover).

Synthetic Aperture Radar (SAR) sensors have an advantage over optical sensors in that these are capable of providing data even under adverse weather conditions or during night. Users of remotely sensed data for oil spill applications include the Coast Guard, national environmental protection agencies and departments, oil companies, shipping industry, insurance industry, fishing industry, national departments of fisheries and oceans, and departments of defense.

The Public and media are usually keen to know about the progress of a spill, which demands the exact location and extent of the oil spill. Day and night imaging and capability to discriminate the oil spills by SAR enables remote sensing an extremely viable and useful tool for detecting oil spill particularly in a marine environment.

However, oil spill detection using remote sensing is still in its early phase of research, though it has been proved that the remote sensing data, specifically the SAR (Synthetic Aperture Radar) images are most advanced and reliable tool for this purpose (Fingas *et al.,* 1999; Mercier *et al.,* 2006; Marghany, 2004).

The oil spills in SAR images appear as dark features due to the fact that the oil film decreases the backscattering of the sea surface, where as the surrounding spill-free sea is bright, which helps in detecting an oil spill in a SAR image (Alpers and Huhnerfuss. 1988). The analysis of this basic fact needs to start from a description of different mechanisms responsible for the sea surface radar backscattering. The radar sensors on board the various satellites usually carry SAR sensor operating in C band which is an advantage for detecting oil spills. In this frequency range, a minimum wind field of 2–3 m/s creates sufficient brightness in the image and makes the oil film visible (Litovchenko *et al.,* 1999). On the other hand, when the wind speed is too high, it causes the spill to disappear, because the short waves receive enough energy to counterbalance the dumping effect of the oil film.

1.7 RESEARCH OBJECTIVE

A detailed literature review of oil spill detection techniques has been carried out to define the objectives and is provided in Chapter 2. Detection of the dark spots is the first and basic step of identifying an oil spill in a SAR image. Though, the oil spills are characterised by dark spots, it may also be the result of meteorological or oceanographic effects. These look-alike features pose a fundamental problem to the identification of oil spills from remote sensing data. Therefore an element of discrimination must be included in the methodology for oil spill detection. The specific objectives of this study are described below.

1. Detection and segmentation of all dark signatures, through different state of the art segmentation techniques and assessment of results.
2. Extraction of extended set of feature parameters for each dark spots, which usually are related to its shape, gradient and radar backscattering parameters.
3. Assessment of those feature extraction parameters in terms of their effectiveness to distinguish oil spill and other 'look-alike' phenomenon and rank them according to its importance.
4. Development and evaluation of two classification technique based on Artificial Neural Network (ANN) and rule-based algorithm in 'Near Real Time' (NRT) context.
5. Development of automated processing chain based on proposed algorithms which will be used as an in-house service quality assessment tool for 'CleanSeaNet' Service of European Maritime Safety Agency.

1.7.1 The European Oil Spill Surveillance and Vessel Detection Service: ‘CleanSeaNet’ (Adapted from EMSA, 2011; 2014)

Monitoring of European waters for discharges of oil from ships and other sources is particularly challenging as the European Union is an inundated peninsula with an extensive coastline and several semi-enclosed seas. The European Marine Safety Agency (EMSA) provides the operational satellite monitoring service, CleanSeaNet, to support spill response activities of European coastal states. The CleanSeaNet service is based on analysing satellite borne Synthetic Aperture Radar images, enriched oil spill identification and vessel detection information, and provides alerts to the national users in 26 coastal states in nominally less than 30 min. This makes ‘CleanSeaNet’ first, state of the art Near Real Time (NRT) operational service at pan European level.

CleanSeaNet was launched in 2007 and the service was set up to support Member States’ actions to combat deliberate or accidental pollution in the marine environment in the framework of Directive 2005/35/EC (amended by Directive 2009/123/EC) “on ship-source pollution and on the introduction of penalties, including criminal penalties, for pollution offences” and in particular Article 10. Article 10 tasked EMSA to ‘work with the Member States in developing technical solutions and providing technical assistance in relation to the implementation of this Directive, in actions such as tracing discharges by satellite monitoring and surveillance.

The service is available to 26 coastal States, including all European Union coastal States, Croatia, Turkey, Iceland, and Norway. Users have access to the CleanSeaNet service via a web portal hosted at EMSA. Nations which are party to MARPOL 73/78 (Regulation 34 of Annex I MARPOL 73/78 have the obligation to follow up any possible violation against the regulation and therefore to verify potential spills. The verification procedure differs from coastal state to coastal state according to available means. Most common in Europe is the use of aerial surveillance aircrafts equipped with specialized sensor systems. These aircrafts are on stand-by or have scheduled missions often harmonised with the satellite overpass. Besides the verification of possible spills their task is identifying possible polluters.

The yearly analyses of over 2,000 CleanSeaNet images support the national response activities in terms of greater consistency, efficiency and effectiveness. The CleanSeaNet service and the coastal state verification provide information for decision making processes and a traceable first element of the different chains of evidence needed for prosecution within the Coastal States. This part of the thesis will provide an overview of the European activities in the field of oil spill monitoring, polluter identification and the follow up by coastal states in order to obtain the first elements of evidence for prosecution of the potential polluter.

Table 1.3 : Sensors mode currently used for EMSA's 'CleanSeaNet' operational service

Satellite	Image Mode	Description	Coverage Range×Azimuth (KM)	Spacing Pixel × Line (meters)
ENVISAT (Discontinued)	ASA_WSM_1P	Wide Swath Mode medium-resolution	405 × 405	75 × 75
RADARSAT-1 (Discontinued)	RS1_SNA	ScanSAR Narrow	300 × 300	25 × 25
RADARSAT-2	RS2_SNA	ScanSAR Narrow	300 × 300	25 × 25

RADARSAT-2	RS2_SCW	ScanSAR Wide	500 × 500	50 × 50
COSMO-SKYMED	CSK_WR	ScanSAR WideRegion	100 × 100	15 ×15
COSMO-SKYMED	CSK_HR	ScanSAR HugeRegion	200 × 200	50 × 50
TerraSAR-X (Emergency)	TSX_SC	ScanSAR	100 × 150	8.25 × 8.25
TerraSAR-X (Emergency)	TSX_SC_W	ScanSARWide	200 × 200	35 × 35

About 457,000 tonnes of oil are released by shipping into the ocean every year, impacting water quality and, marine and coastal ecologies (GESAMP, 2007). The largest single cause of pollution from maritime transport is deliberate dumping of oil at sea. Marine oil spills, both illicit and accidental, pose a severe risk in terms of ecological damage and socio-economic losses for European coastal areas. Europe has a coastline of 70,000 km along two oceans and four seas: the Atlantic and the Arctic Oceans, and the Baltic, North, Mediterranean and Black Seas. The disasters involving the vessels ERIKA off the French coast in 1999 (spilling 20,000 tonnes of oil) and PRESTIGE in 2002 off the Spanish coast (spilling 63,000 tonnes of oil), severely impacted the environment in the affected coastal areas and led to a substantial political discussion, which contributed to the decision to establish the European Maritime Safety Agency (EMSA).

The EU Parliament has requested that "*Member States shall take the necessary measures to achieve or maintain good environmental status in the marine environment by the year 2020 at the latest*" (EP, 2007) in the framework of the Marine Strategy Framework Directive, and the strategy of the OSPAR commission is to "*move towards the target of the cessation of discharges, emissions and losses of* *hazardous substances by the year 2020*" (OSPAR, 2003). International law (e.g. MARPOL, 73/79) forbids deliberate pollution, but laws require enforcement. With the entry into force of Directive 2005/35/EC on ship-source pollution and on the introduction of penalties, including criminal penalties for pollution offences (as amended by Directive 2009/123/EC) EMSA is tasked to "*work with the Member States in developing technical solutions and providing technical assistance in actions such as tracing discharges by satellite monitoring and surveillance*". In line with this, the Agency has set up and provides a European operational system for oil spill and vessel detection called CleanSeaNet, which is based on the analysis of synthetic aperture radar (SAR) images from satellites.

The CleanSeaNet service offered to authorities in European coastal states supplements existing surveillance systems at national and regional level and supports the response of Coastal States for locating polluters and mitigating the impact of accidental spills. The follow up to CleanSeaNet detections is then the responsibility of each Coastal State, but the responses vary considerably from one country to the other. In some countries, each time a satellite acquisition is planned an aircraft is either in flight or on standby, thus increasing the chances of catching a polluter in the act. Some European Member States are now imposing fines of many hundreds of thousands of Euros for deliberate pollution in violation of MARPOL regulations.

Coastal States can also utilize CleanSeaNet detections to trigger inspections in port when vessel traffic monitoring systems and AIS information allow the identification of the possible source. A number of polluters have been fined on the basis of evidence collected during such inspections. Directive 2005/35/EC as amended does not establish any legal reporting obligation on administrative or judicial follow-up, and it is therefore hard to establish how often this occurs. (Adapted from EMSA, 2011; 2014).

1.7.2 The CleanSeaNet service

CleanSeaNet uses Synthetic Aperture Radar (SAR) satellite sensors which "illuminate" the ocean surface and process the back scattered signal. This signal contains information on the level of roughness of the sea surface. The damping effect of floating oil films reduces the back scattered signal and appears as black patches in the images, which enables SAR sensors to detect oil slicks. Satellite SAR imagery has proven to be an effective tool to detect oil spills at sea as it has the capacity to cover large areas day and night and is almost unaffected by cloud cover.

The SAR satellites primarily used are ENVISAT ASAR from the European Space Agency, RADARSAT-1/RADARSAT-2 from the Canadian Space Agency and MDA, and COSMO- SKYMED from the Italian Space Agency. Unfortunately, communication with CleanSeaNet's primary satellite, ENVISAT was lost in April 2012. Looking to the future the planned GMES Sentinel-1 mission series will be important for routine monitoring, while other X-band radar data from TerraSAR-X (German Aerospace Centre, DLR) could potentially be used for specific campaigns and in case of an oil spill emergency along with routine operational use.

After acquisition by the satellite, SAR data are transmitted to a network of contracted ground receiving stations (CLS, France; Edisoft, Portugal; E-Geos, Italy and KSAT, Norway, As of September, 2013), where the data is processed and the image interpreted by image analysts.

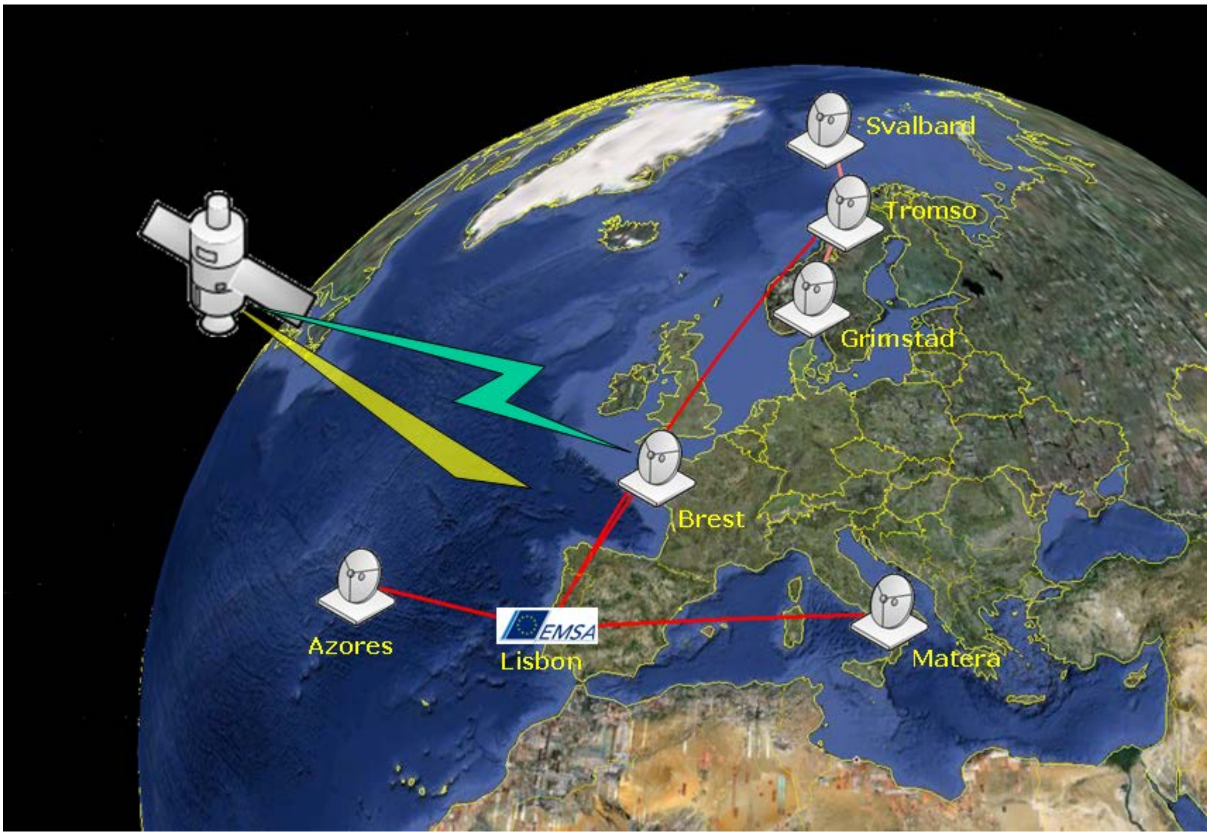

Fig 1.4: Ground station location for 'CleanSeaNet' operational service (as of 2013 ©EMSA).

The shortest possible delay between detection and alert is essential for a rapid response by the Coastal State and to increase the likelihood of catching a polluter in the act. It is a CleanSeaNet contractual obligation that SAR images, results of oil spill analysis and ancillary information are delivered and made available to Coastal States shortly after the time of the satellite acquisition. For satellite images covering 400 km by 400 km, the analysis is provided in maximum of 30 minutes. For images of different dimensions the time varies slightly. In case of a detected oil slick, an alert message to the end user is transmitted by phone call as well as e-mail.

Table 1.4: Number of images ordered and delivered by 'CleanSeaNet' in year 2012(©EMSA).

Satellite	Status	No of Images	Delivery rate
ENVISAT	Ordered	530	72%
	Delivered	383	
RADARSAT-1	Ordered	683	86%
	Delivered	584	
RADARSAT-2	Ordered	1380	91%
	Delivered	1258	
COSMO-SKYMED	Ordered	14	89%
	Delivered	9	
TOTAL	Ordered	2607	86%
	Delivered	2234	

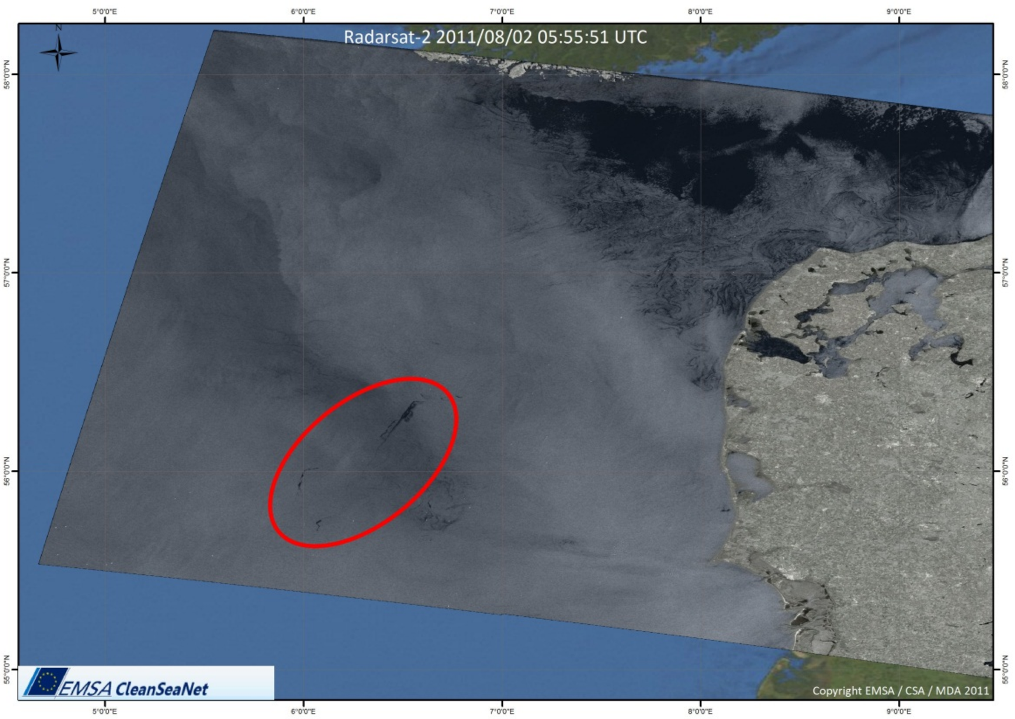

Figure 1.5: CleanSeaNet RADARSAT 2 image acquired on 2nd August 2011 covering Danish and Norwegian coastal area – showing clearly released oil patches (RADARSAT-2 image © CSA/MDA/EMSA)

CleanSeaNet began operating in April 2007 and the oil pollution response authorities of 26 European Coastal States have now access to the service. Between the beginning of the service and January 2011, over 1,000 million km^2 of European seas (approx. 2,800 times the area of Germany) were monitored, equivalent to more than 50,000 flight hours with aerial surveillance aircraft. More than 8,800 possible oil slicks were detected, but not all of these detections were oil. On average, the trend is a global reduction in the number of potential spills detected in the images: from 10.77 possible spills identified per million km^2 in 2008 to 5.68 per million km^2 in 2010 (EMSA, 2011; Singha et al., 2013). A study showed that the percentage of detections checked on-site by aircraft within 3 hours and confirmed as oil varies from one region to another and reach values up to 80%.

Fig 1.6: 'CleanSeaNet' operational coverage area shown in blue. Yellow patches show the image acquisition capability (as of 2013 ©EMSA).

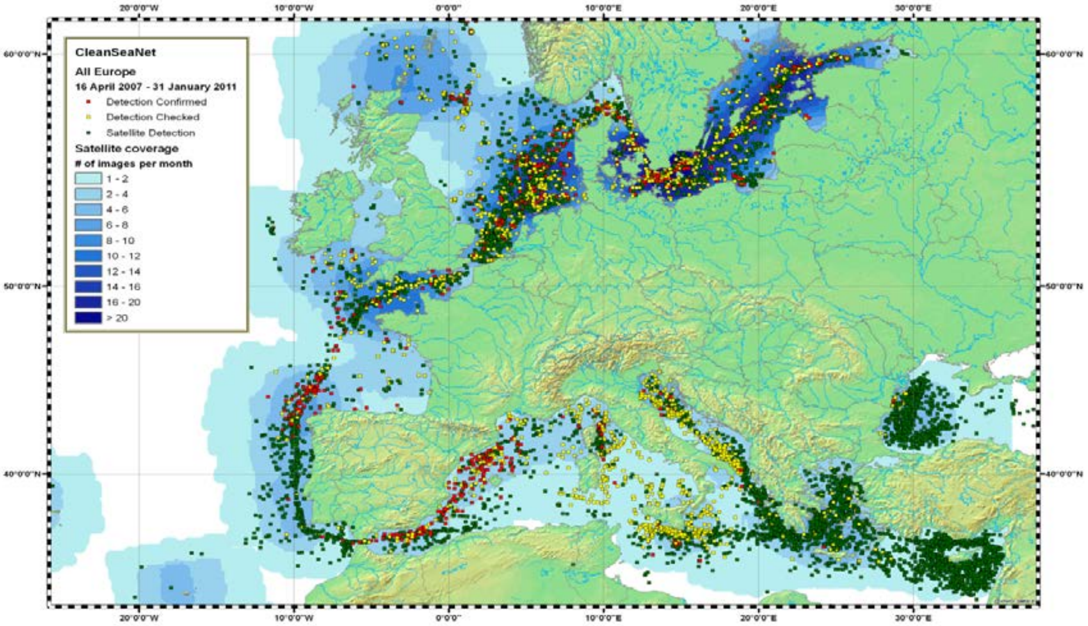

Fig 1.7. 'CleanSeaNet' oil spill location map in EU waters occurred from Jan 2009 to Jan 2011. Different shades of blue patches showing operational coverage area (Source: ´CleanSeaNet´ first generation report © EMSA 2013, Presented in Singha et al., 2013a).

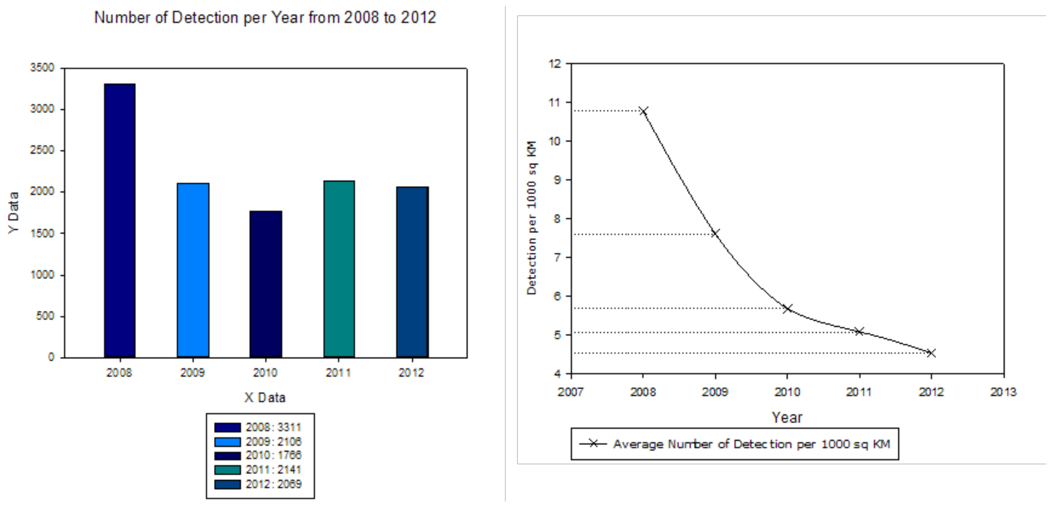

Fig 1.8: Number of SAR images delivered per year for 'CleanSeaNet' service (left hand) and number of oil spills reported per year on European waters (right hand).

SAR image data is able to detect ships and quite often their wakes. Therefore CleanSeaNet has been further developed to also provide a vessel detection service.

In order to identify vessels suspected of causing pollution, traffic monitoring information from AIS (Automatic Identification Systems) data is necessary.

CleanSeaNet provides vessel track information via the EMSA 'SafeSeaNet' service as an additional layer on top of the SAR image in order to identify potential polluter. 'SafeSeaNet' is a pan-European electronic information system which harmonises the way maritime data on ship movements and cargoes is exchanged and which provides vessel tracking information throughout Europe. Therefore possible to link a recent spill to a vessel if either the vessel is attached to the spill or the vessel track matches the pattern and shape of the spill, and if there is no ambiguity between the different potential polluters observed in the vicinity of this spill.

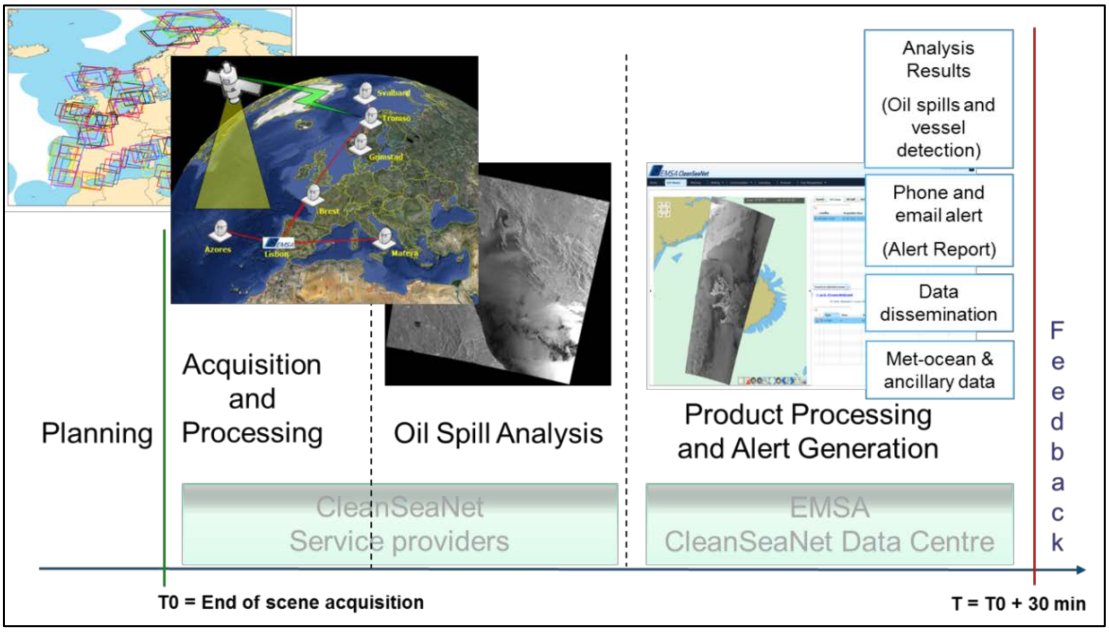

Fig 1.9: CleanSeaNet – the steps of a 30 min. near real time service performed at different locations: image planning (EMSA), satellite acquisition and image processing, oil spill analyses (service providers), harmonised product dissemination to coastal states and alert generation (©EMSA).

Oil spill modelling tools further assist in the identification of vessels responsible for illegal discharges (spill backtracking) and for prediction of spill drift and fate (spill forecasting) to support decision making for pollution response activities. Backtracking of spills and the intersection of the spill trajectory with vessel tracking data can limit the number of potential polluters and allows authorities to carry out more in-depth checking of suspicious vessels. Complementing the information provided to the Coastal States users CleanSeaNet includes additional sets of information, such as wind and swell information derived directly from the SAR data, sea surface temperature maps, surface chlorophyll maps, and reference data sets including nautical charts. All information is provided via a tailored web user interface and as “web services” following the standards and recommendations of INSPIRE (Infrastructure for SPatail InfoRmation in Europe) and OGC (Open Geospatial Consortium) with regard to architecture, catalogues/metadata, sensor planning, ordering, web mapping services, data access and dissemination amongst others.

During an accidental oil spill EMSA can place emergency orders for fast delivery of satellite radar imagery for the affected area and provide emergency pollution reports to the relevant authorities at Member States. In case of major accidental spills the International Charter for Space and Major Disasters provides a unified system of space data acquisition and delivery to those affected by disasters including marine pollutions. The Charter can be activated by civil protection, rescue, defence or security bodies from the country of a Charter member. The Monitoring and Information Centre (MIC) operated by the European Commission in Brussels is one of the authorised users and may request the activation of the Charter in support of a major marine pollution incident. In that case, EMSA is the foreseen Project Manager and coordinates the delivery and analysis of radar and optical satellite images made available through the Charter to monitor the evolution of the spill.

1.7.3 Coastal state activities

The EMSA CleanSeaNet service triggers national surveillance activities which can take different forms, e.g. surveillance aircraft, helicopter, or patrol vessel. In addition to the verification of potential spills, their task is to identify possible polluters and if necessary to optimize response operations to minimise the environmental impact. By complementing national aerial and vessel surveillance with satellite images, a more cost effective use of these expensive resources is achieved.

Within Europe, use of aerial surveillance aircraft equipped with specialized sensor systems is common. Within the BONN Agreement and HELCOM regions a common equipment standard has been agreed. This includes Side-looking Airborne Radar (SLAR) as wide-range sensor system and InfraRed/UltraViolet (IR/UV) line scanner as narrow-range sensor system. Photo and video cameras for documentation purposes complement the arrangement (BONN Agreement Aerial Operations Handbook, 2009). These aircraft are on stand-by or have scheduled missions, often harmonised with the satellite overpass. Some member states plan flight missions with their aircraft to be in the area covered by the satellite imagery at the same time or shortly after to verify possible detections made by the radar sensors of the satellite. By planning the reception of satellite images at least one month or more in advance it is easily possible to align the national surveillance activities with the satellite overpass in order to have the national means available on scene as soon as possible if needed.

Oil pollution from ships which is observable by satellite can constitute a MARPOL violation, which therefore needs to be verified by the relevant coastal state. The verification of CleanSeaNet detections is vital as a radar sensor only identifies the effect on damping of the wave system. Reasons for this damping might be e.g. glassy sea due to low wind areas, an algae boom, ice on water or, of course, oil on the water. By using visual observation methods or specialized sensor systems like IR/UV line scanner, Forward Looking Infrared Camera (FLIR) or Laser Fluoro Sensors (LFS), oil spills can be differentiated from natural phenomena (Fig 1.10).

Having identified an oil spill, the next challenge is the identification of the (possible) polluter by combining the information provided by CleanSeaNet with the information retrieved by national means, and any jurisdictional follow-up activities. Once a possible polluter has been identified, the amount and type of necessary evidence needed to be collected by the authorities in order to effect a prosecution differs a lot within Europe.

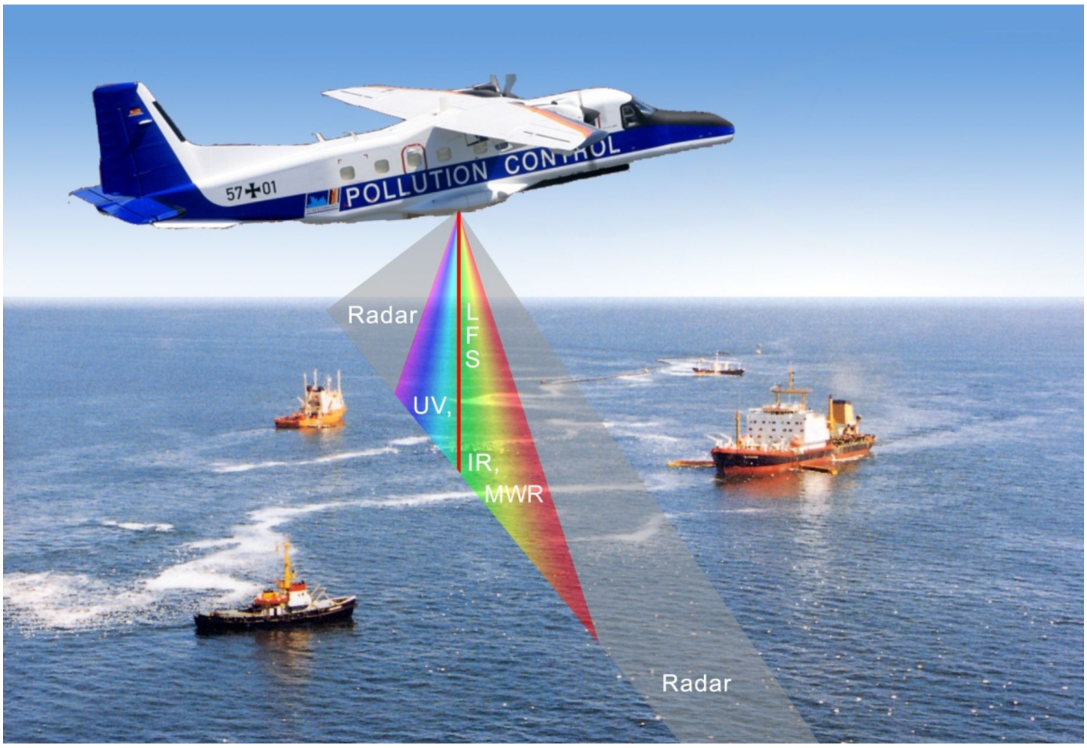

Fig 1.10: Schematic demonstration of the different line sensors on board of an aerial surveillance aircraft (example from Germany, (©EMSA, Source: Trieschmann and Reichenbach, 2012)

Having identified the polluter and brought the offence to court, the judgment and penalties also differ as well. In some countries the judgment and penalties are focused on the ship crew (e.g. in Germany) while in other countries also the shipping company might be judged. In Norway for example the shipping company might be judged due to the reason that an effective safety management system on board of the vessel established by the company would have prevented the violation (Adapted from EMSA Workshop on Enhancing the effectiveness of the law enforcement chain in combating illegal discharges 15-16 February 2011). This has also an effect on determining the fines or penalties, which would be higher for a shipping company then for a single crew member.

The intention of the European Member States and the European Union to set up an end-to-end surveillance chain in order to detect oil pollutions occurring in European seas, to identify the potential polluters and to collect the necessary evidence for judicial follow up are supported by CleanSeatNet and its integration into national activities. Besides routine surveillance activities satellite imagery provides a near real time trans-boundary overview of the actual situation at sea focused on possible oil pollution. It has been demonstrated that satellite services allow co-ordination of surveillance resources operated at a regional level and thus an improvement in cost efficiency for aerial and vessel assets. Certainly the purchase of a large volume of imagery and services creates a cost reduction due to economies of scale.

However, discrepancies between legal systems (e.g.: evidence admitted in court, level of penalties) might encourage ships routinely engaged in illegal discharges to pollute in areas with a reduced risk of being observed. Therefore successful enforcement relies on the mutual understanding, exchange of information, coordination and cooperation of maritime surveillance, port inspection, and enforcement authorities within and between coastal States. This will definitely lead to an increased deterrence effect. The statistics shows already a reduction in the amount and size of the spills which might be caused by the higher frequency of surveillance of the European seas by combined national means and satellite surveillance, but also in the cooperation activities by Member States in enforcing pollution free seas (This section is adapted from Trieschmann et al., 2003; Trieschmann and Reichenbach, 2012 and EMSA annual reports).

1.8 ORGANIZATION OF THE THESIS

The work presented in this dissertation has been organized into six chapters. Chapter 1 introduced the problem and its scope so as to define the objective of the present study. The chapter also outlines European Maritime Safety Agency's 'CleanSeaNet' activity as this research was developed in conjunction with the service.

In chapter 2, a review on different types of remote sensing sensors used for oil spill detection has been provided. This chapter also covers a detailed literature review of oil spill detection techniques using remote sensing data including detection of oil spill on single- polarimetric and multi-polarimetric SAR data.

Chapter 3 puts an emphasis on the mathematical backgrounds of the approaches used in this study for oil spill detection from SAR imagery. This chapter includes the basics artificial neural network for segmentation and classification and the rule based technique. It also highlights the importance of feature extraction measures in distinguishing oil spill spots from other look-alike features in remote sensing image.

In chapter 5, the results from this work and their analyses have been presented, which also includes the statistical evaluation of various feature extraction parameters used to distinguish between look-alikes and oil spill.

Finally, Chapter 6 provides summary, conclusions, future scope from the present work and a short discussion towards completely automated oil spill detection chain for NRT services like 'CleanSeaNet'.

CHAPTER 2

A REVIEW OF REMOTE SENSING FOR OIL SPILL DETECTION

2.1 INTRODUCTION

Large spills of oil and related petroleum products have serious biological and economic impacts in the marine environment. Remote sensing plays an increasingly important role in oil spill response efforts even for small discharges from offshore oil producing platforms. Through the use of modern sensors, oil can be monitored on the open ocean round the clock. Sensors can be placed on different platforms such as vessels, aircraft, and satellites. Vessels, especially if equipped with specialized radars, can detect oil at sea but they can cover a very limited area. However, the vessels are necessary in case of oil sampling, if required. The main systems to monitor the sea-based oil pollution are therefore aircraft and satellite based sensors. At present, very few airborne sensors dedicated to oil spill monitoring are available. Further, the operating cost of aircraft based sensors is also much higher as compared to the satellite based sensors.

Even though sensor design and electronics are becoming increasingly sophisticated and less expensive, the operational use of satellite remote sensing data lags behind the technology. Attempts to use the remote sensing satellites for oil spill detection started since 1995. Several general reviews on oil spill detection from remote sensing have been published (e.g., Fingas *et al.*, 1996; Fingas and Brown, 1997a, 1997b, 2005). These reviews demonstrate that there is still no well-established method for the detection of oil spill from remote sensing data.

Remote sensing sensors operating in ultraviolet to microwave region in the electromagnetic spectrum have been used for detecting offshore oil spills and have been listed in Table 2.1.

Table 2.1 Remote sensing bands and related instruments used for oil spill detection (Source: Goodman, 1994)

BAND	WAVELENGTH
Ultraviolet	250-350 nm
Visual	350-750 nm
Near Infrared	1-3µm
Mid-band Infrared(MIR)	3-5µm
Thermal Infrared(TIR)	8-14 µm
Passive Microwave	2-8mm
Rader	1-30cm

In this chapter, an overview of various remote sensing sensors for oil spill detection, their merits, demerits and usage through a set of existing studies has been provided followed by an overview of oil spill detection methodology.

2.2 PASSIVE REMOTE SENSING SENSORS

There are two kinds of remote sensing, passive remote sensing and active remote sensing. Passive sensors detect natural radiation that is emitted or reflected by the object or surrounding area being observed. Reflected sunlight is the most common source of radiation measured by passive sensors. Examples of passive remote sensors include film photography, Infrared, charge-coupled devices, and radiometers.

2.2.1 UV sensors

The ultraviolet (UV) sensors can be used to map sheens of oil as oil slicks display high reflectivity this region even at thin layers (<0.01 μm). Fused ultraviolet and infrared images can often be used to produce a relative thickness map of oil spills. Ultraviolet cameras, although inexpensive, are generally not used in this process, as it is difficult to overlay the camera images (Goodman, 1988 in Fingas and Brown, 1997a). Rather, data from infrared scanners and push-broom scanners can be easily superimposed or fused to produce these IR/UV overlay maps. Ultraviolet data are also subjected to many interferences or false images such as wind slicks, sun glints, and biogenic material (Fingas and Brown, 1997a; 1997b). Since these interferences are often different than those for infrared sensing, combining IR and UV can provide a more positive indication of oil than using either sensor alone. However, UV images are based on the reflected sunlight and hence cannot operate at night.

2.2.2 Visible sensors

Optical sensors operating in visible wavelengths have been widely used in oil spill remote sensing despite of many shortcomings. In the visible region of the electromagnetic spectrum (approximately 400 to 700 nm), oil has a higher surface reflectance than water, but also shows limited nonspecific absorption tendencies. Sheen (micro layer of oil substance) shows up silvery and reflects light over a wide spectral region down to the blue. As there is no strong information which can distinguish oil from background in the 500 to 600 nm region, this region is often filtered out to improve contrast in the images (O'Neil *et al.*, 1983). However, oil has no specific characteristic that distinguishes it from the background (Brown and Fingas, 2005).

Taylor (1992) studied the oil spectra both in the laboratory as well as in the field and observed flat spectra with no usable features to distinguish it from the background. Therefore, techniques that separate specific spectral regions are not useful for the detection of oil spills. However, it has been found from the field experiments that high contrast in visible imagery can be achieved by setting the camera at Brewster angle (53 degrees from vertical) and using a horizontally aligned polarizing filter which passes only that light reflected from the water surface. This is the component that contains the information on surface oil (O'Neil *et al.*, 1983). It has been reported that this technique increases contrast by up to 100%. Filters with band-pass below 450 nm can also be used to improve contrast.

The reflectance of oil is higher than that of the water but oil also absorbs some radiation in the visible region. These sensors are therefore not appropriate for oil detection as it is difficult to distinguish oil from the background, as can be seen from an image

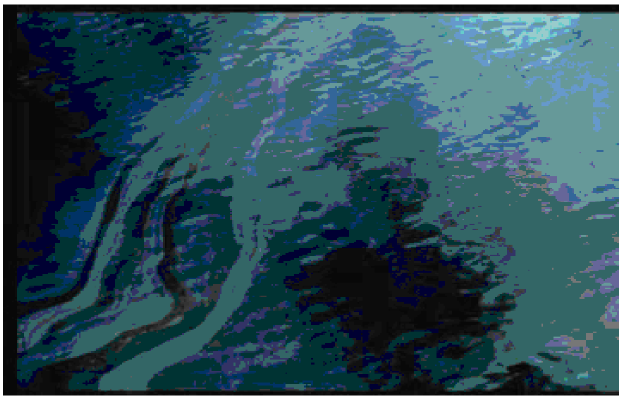

Fig 2.1 Image of Exxon Valdez oil spill captured by a sensor in the visible range (Source: NOAA, 2007, Jha *et al.*, 2008)

Improvements in sensor technologies have led to the development of hyperspectral sensors such as Airborne Visible/Infrared Imaging Spectrometer (AVIRIS) and Airborne Imaging Spectrometer for Applications (AISA). A hyperspectral image consists of tens to hundreds of spectral bands and can provide a spectral signature for oil spill. However, conventional techniques for multispectral data analysis may not be used to investigate hyperspectral images (Landgrebe, 2003 in Jha *et al.,* 2008).

Plaza *et al.,* (2001) and Salem and Kafatos (2001) have reported the use of hyperspectral data for oil spill detection. The extensive spectral information can be used to discriminate between crude oil (a mineral oil consisting of mixture of hydrocarbon of natural origin basically black and yellow in color) and light oil (refined crude oil). Minute concentrations of crude oil can also be detected using hyperspectral images (Jha. *et al.,* 2008).

2.2.3 IR sensors

There are three distinct bands in the infrared region (Table 2.1) in which the atmospheric transmission is sufficiently low to allow detection from an airborne and space borne platforms. Tests in these three bands were carried out in the 80's to investigate the region which is most suitable for oil spill detection from remote sensing (O'Neil *et al., 1983*).
Oil absorbs solar radiations and emits some part of it as the thermal energy, mainly in the thermal infrared (TIR) 8-14 μm region. Oil has a lower emissivity than the water in the TIR region and therefore has a distinctively different spectral signature in this region (TIR) as compared to the background water (Salisbury *et al.,* 1993). Tests for

near IR (1-3µm) and mid-IR systems (3.4 to 5.4 µm) over the TENYO MARU oil spill could not detect the oil spill in these ranges (Fingas and Brown, 1997).

The cost of the system operating in the infrared is the lowest for the near-IR, with an increasing factor of five for the mid-IR camera and a further increasing factor of three for cameras operating in the Thermal IR for offshore oil spill detection. Infrared devices cannot detect emulsions (water-in-oil emulsions) under most circumstances (Jha. *et al.,* 2008). This is probably due to the high thermal conductivity of emulsions as they typically contain 70% water and thus do not show a temperature difference.

2.2.4 Microwave radiometers

MWR (Microwave radiometer) is usually an airborne passive sensor (except MSMR sensor onboard OCEANSAT-1 satellite) and has been used for oil spill detection and oil thickness measurement. MWR works in the wavelength region of 2-8 mm in the EM spectrum. Oil emits stronger microwave radiation than water and appears brighter than the background water. Measuring oil thicknesses with MWR involves the interference of radiation from the upper and lower boundaries of the oil film. Microwave emission is the highest when oil film thickness is equal to an odd multiple of one quarter of the wavelength of the emitted energy. This may lead to an estimation of multiple values of thicknesses for a given signal (Bolus, 1996; Fingas and Brown, 1997a). MWR sensors can work in both day and night and requires a special antenna to receive the emitted microwave radiation and also a dedicated aircraft. However, MWR sensors are costly and it is complicated to put them into operation. Moreover, MWR sensors require information about many environmental characteristics and oil properties for accurate oil detection (Trieschmann *et al.,* 2003).

The Swedish Space agency carried out some work with different systems, including a dual band, 22.4- and 31-GHz device, and a single band 37-GHz device (Fast, 1986). Skou *et al.,* 1994 and Sorensen (1992) describe a 2-channel device operating at 37.5 and 10.7 GHz. Mussetto *et al.,* 1994 describe the tests of 44-94-GHz and 94-154-GHz, 2-channel devices over oil slicks. They show that the correlation with slick thickness is poor and suggest the use of factors other than thickness also change surface brightness. They also suggested that a single-channel device might be useful as an all-weather, relative-thickness instrument (Fingas *et al*., 2002).

Passive microwave radiometers may have potential as an all-weather oil sensor but their main disadvantage is the low spatial resolution.

2.3 ACTIVE REMOTE SENSING SENSORS

Active sensors, on the other hand, emit energy in order to scan objects and areas whereupon a sensor then detects and measures the radiation that is reflected or backscattered from the target. RADAR is an example of active remote sensing where the time delay between emission and return is measured, establishing the locations, height, speed and direction of an object.

2.3.1 Laser fluorosensor

Laser fluorosensors are airborne active sensors that take advantage of the fact that certain compounds in petroleum oils absorb ultraviolet light and become electronically excited. This excitation is rapidly removed through the process of fluorescence emission, primarily in the visible region of the spectrum. Since very few other compounds show this tendency, fluorescence is a strong indication of the presence of oil. Natural fluorescing substances, such as chlorophyll, fluoresce at sufficiently different wavelengths than oil to avoid confusion. As different types of oil yield slightly different fluorescent intensities and spectral signatures, it is possible to differentiate between classes of oil under ideal conditions (Brown *et al.*, 1996).

Most laser fluorosensors used for oil spill detection employ a laser operating in the ultraviolet region of 300 to 355 nm. With this wavelength of activation, there exists a broad range of fluorescent response for organic matter, centered at 420 nm. This is referred to as Gelbstoff or yellow matter, which can be easily annulled. Chlorophyll yields a sharp peak at 685 nm. The fluorescent response of crude oil ranges from 400 to 650 nm with peak centers in the 480 nm region (Brown *et al.*, 1996, 2004).

2.3.2 SAR sensors

As discussed in previous chapters, active microwave sensors have been commonly used for operational ocean pollution monitoring. These are often preferred to optical sensors due to the all-weather and day and night capabilities. Although, analysing active microwave images is much more complex compared to optical images but often preferred due to its exceptional capability.

The two basic types of radar that can be used to detect oil spills and for environmental remote sensing in general are Synthetic Aperture Radar (SAR) and Side-Looking Airborne Radar (SLAR). The latter is an older, but less expensive technology, which uses a long antenna to achieve spatial resolution. Synthetic aperture radar uses the forward motion of the aircraft to synthesize a very long antenna, thereby achieving very good spatial resolution, which is independent of range, at the expense of sophisticated electronic processing. While inherently more expensive, the SAR has greater range and resolution than the SLAR. In fact, comparative tests show that SAR is immensely superior (Mastin *et al.,* 1994; Wahl *et al.,* 1994a, 1996). Both airborne and space borne SAR have been used for oil spill monitoring. Spaceborne SAR data coupled with airborne SAR data is recognized as the most efficient way to monitor oil spill more synoptically (Brown and Fingas, 2005).

The NASA's SEASAT satellite, which was launched in 1978, was the first satellite designed to observe the sea surface with an L-band SAR system. Later, SAR systems were launched by the Russian Space Agency (RSA), the European Space Agency (ESA) and the Canadian Space Agency (CSA). The main satellites which were used or are in operational status for monitoring oil spills are presented in Table 2.2

Table 2.2 Satellites carrying SAR instruments focusing in oceanographic applications (as of April 2014).

Satellite (sensor)	Operative	Owner	Band
SEASAT	1978 – 1978	NASA	L
ALMAZ	1991 – 1992	RSA	S
ERS-1	1991 – 2000	ESA	C
ERS-2	1995 – 2011	ESA	C
RADARSAT-1	1995 – operating	CSA	C
ENVISAT (ASAR)	2002 – 2012	ESA	C
ALOS (PALSAR)	2006 – 2011	JAXA	L
RADARSAR-2	2007– operating	CSA	C
TerraSAR-X/TanDEM-X	2007 – operating	DLR	X
Cosmos Skymed	2007 – operating	ASI	X
RISAT-1	2012-operating	ISRO	C
KOMPSAT-5	2013-operating	KARI	X
Sentinel 1	2014- operating	ESA	C

ASI – Italian Space Agency, DLR – German Aerospace Centre, ESA – European Space agency, JAXA - Japan Aerospace Exploration Agency, NASA – National Aeronautics and Space Administration (USA), ISRO – Indian Space Research Organization, KARI – Korea Aerospace Research Institute.

Imaging with Synthetic Aperture Radar

Each SAR system has its own configuration in terms of frequency, polarization, resolution, swath width etc., however the underlying operating concept for each is the same. A detailed description of the theory for the SAR is beyond the scope of this thesis, but a short introduction to the main principles of SAR is given in the following (kept on a "need to know" with regard to oceanographic applications and this thesis).

SAR Principles

SAR is side-looking imaging radar operating from a moving platform. A typical SAR flown on a satellite has a quite large rectangular antenna of about 10 m × 1 m (according to Curlander and McDonough, 1991), SEASAT had an antenna size of 10.7 m × 2.2 m, ERS-1 10 m × 1.0 m and RADARSAT-1 15 m × 1.6 m). The longest side is aligned with the orbit track and the radar beam is sent out to the side of the satellite. SAR produces two-dimensional (2-D) images. One dimension is called the range or across-track, the other dimension is called the azimuth (or along-track) and is perpendicular to the range (see figure 2.2).

Imaging Geometry of the SAR

Figure 2.2 shows the viewing geometry of the side-looking SAR moving in azimuth direction. The nadir is directly beneath the platform. The microwave beam is transmitted obliquely with respect to the direction of flight and illuminates a swath which is offset from nadir. Radar backscatter values are collected from a footprint area and later processed to form the SAR image. At all ranges the radar antenna measures the radial line of sight distance (slant range) between the radar and each target on the surface. The ground range distance is the true horizontal distance on the ground corresponding to each point measured in slant range.

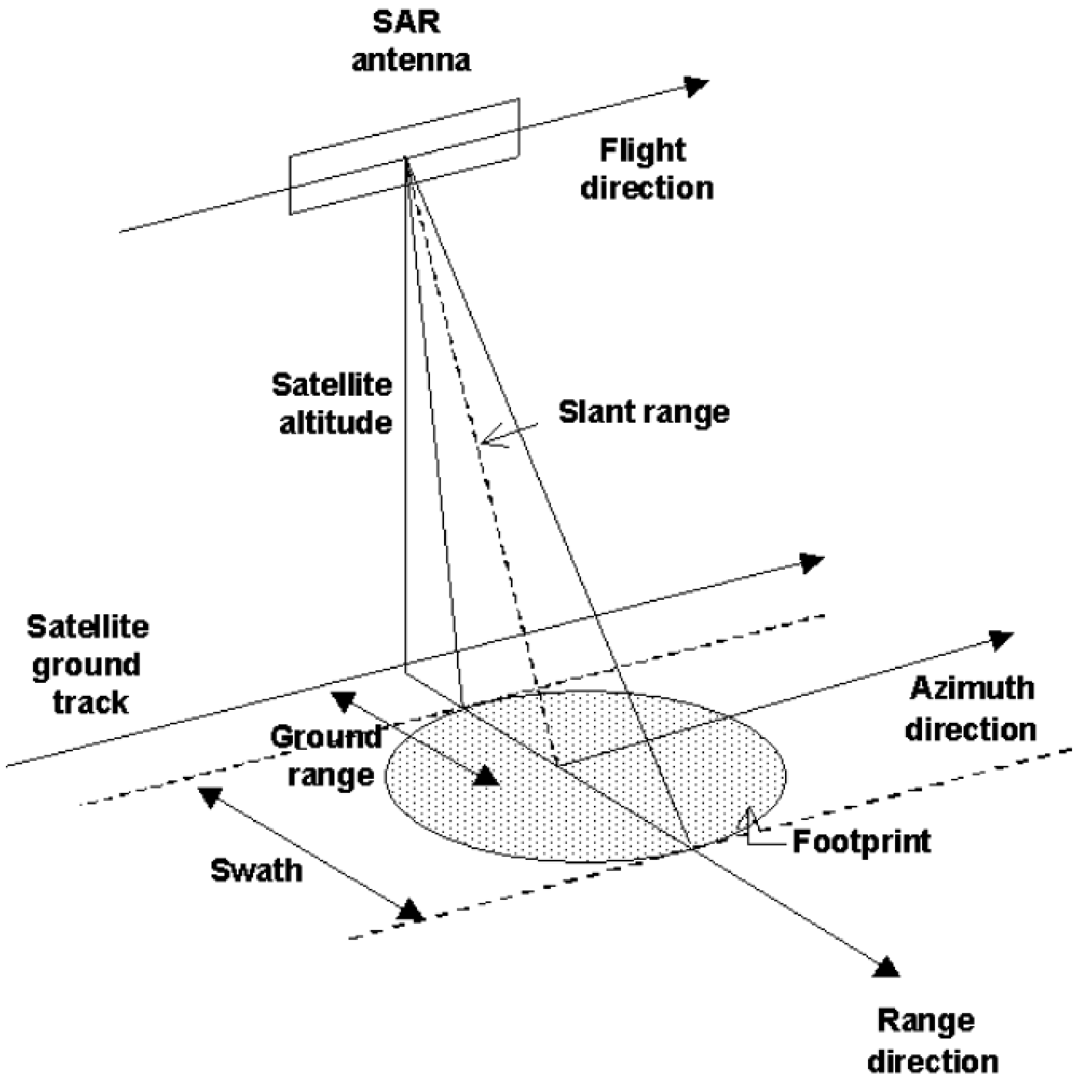

Figure 2.2: The side-looking SAR moving in azimuth direction. (Source: ESA Radar Course III)

Range Resolution

The resolution of the radar in range (ground) is defined as the minimum range separation between two objects that can be distinguished by the system. If the arrival time of the pulse echo from the more distant point is later than the arrival time of the echo from the nearer point, each point can be distinguished in the time history of the radar echo. Range is determined by precisely measuring the time from transmission of a pulse to receiving the echo from a target. Objects that are located at the same distance from the SAR sensor, before a given azimuth value, will therefore be located at the same position in the SAR image. Because of this, certain geometrical effects can appear in SAR images. This is of particular importance for land applications, but of less relevance for ocean feature applications. The ground range resolution is defined as

$$R_{ground\_range} = \frac{c}{2Bsin\theta} \tag{2.1}$$

where c is the speed of light, $B = \frac{1}{\tau}$ is the pulse bandwidth, τ is the pulse duration and θ is the incidence angle (see figure 3.3). Finer ground range resolution can be achieved by using a shorter pulse length. However, this can only be done within certain engineering design restrictions. Therefore, the radar system range resolution relies instead on the type of pulse coding and the way in which the return from each pulse is processed. All radar systems like e.g. SLAR or SAR resolve targets in the range dimension in the same way, but it is the ability of SAR to produce relatively fine azimuth resolution (in the dimension parallel to the line of flight) that differentiates it from other radars.

Azimuth Resolution

The beam width defines the azimuth resolution. As the beam fans out with increasing distance from the radar the spatial resolution decreases. In addition to the range, the beam width depends on the antenna length. To obtain fine azimuth resolution, a physically long antenna in the along-track dimension is needed to focus the transmitted and received energy into a sharp beam. Antenna lengths of several hundred meters are often required. However, the key principle satellite SAR is to utilize the forward motion of the platform to synthesize a long antenna. As the SAR moves forward, a series of pulses is transmitted and received such that any given target on the surface is illuminated many times. The space-borne SAR then collects the data while flying and processes the data as if it came from a physically long antenna. This means that as the sensor moves along the satellite track, echoes are recorded coherently (the radar signal is recorded as a function of time) and combined in a processor to synthesize a much longer antenna (or aperture) than the physical one present. The distance the spacecraft flies while it records the reflected radar pulses from the target is known as the synthetic aperture. This is illustrated in Fig 2.3. A target at far range will be illuminated for a longer period (due to the wider beam) of time than a target at near range. The expanding beamwidth, combined with the increased time the target is within the beam as ground range increases, balance each other. Therefore, the resolution remains constant across the entire swath.

A narrow synthetic beam width results from the relatively long synthetic aperture, which yields finer resolution than is possible from a smaller physical antenna. The resolution in the azimuth dimension is generally limited by:

$$L_a/2$$

This simply states that the best possible azimuth resolution for a SAR system that can

be achieved with a physical antenna of length L_a (azimuth dimension) is half the antenna length. This also states that improved resolution comes from smaller antennas (Adapted from Curlander and McDonough, 1991 in Brekke 2007; Moreira et al., 2013).

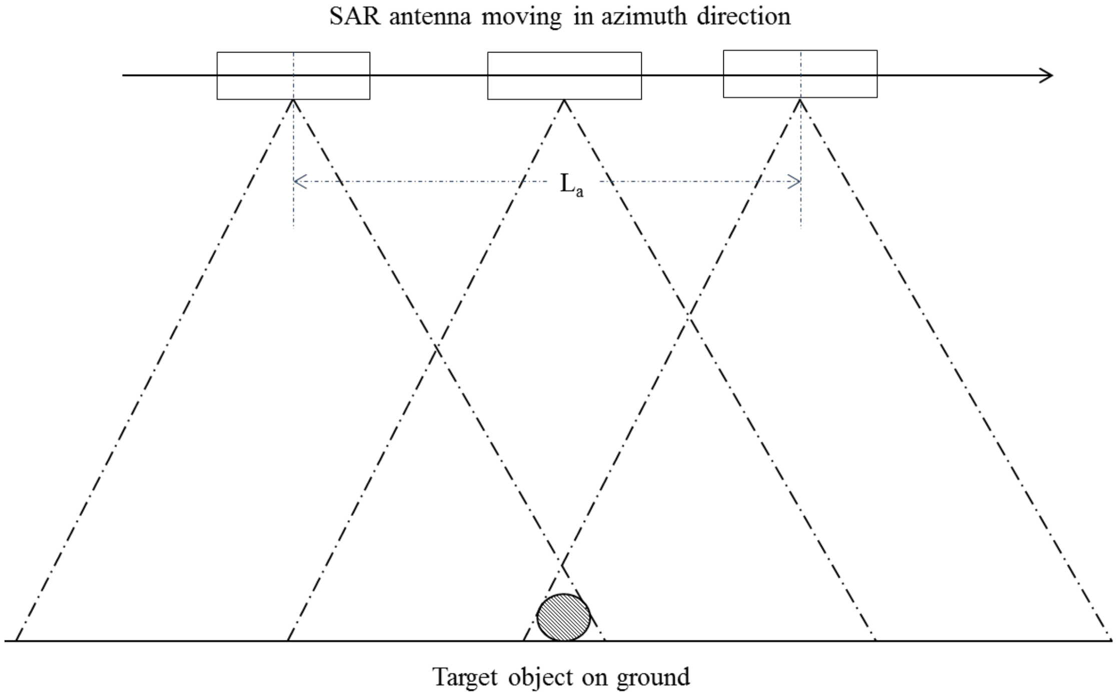

Fig 2.3: Forming of synthetic aperture.

Figure 2.3 shows as a target first enters the radar beam, the backscattered echoes from each transmitted pulse begin to be recorded. As the platform continues to move forward, all echoes from the target for each pulse are recorded during the entire time that the target is within the beam. The point at which the target leaves the view of the radar beam determines the length of the synthesized antenna.

Scattering Mechanisms

In SAR imaging, there are several important factors that decide how strong a signal is reflected back from the target area. These factors can be divided into satellite system factors:

- Radar beam incidence angle
- Radar wavelength
- Polarization of the radar signal

and ground surface factors:

- Roughness of the surface
- Geometrical structure of the surface
- Dielectric properties of the surface
- Wind speed
- Angle between the radar beam and the wind

The objective of this section is to provide a brief overview of target scattering mechanisms mainly surface scattering, in context to oil spill detection in the following section of this Chapter.

Surface Scattering

For flat terrain, the local reflection angle is the same as the incidence angle. Most of the incident energy will be reflected away from the sensor, resulting in a very low return signal. Rough surfaces will scatter incidence energy in all directions and return a significant portion of the incident energy back to the antenna. On the ocean surface it is the waves that make the surface rough. Whether the surface is perceived rough or not, depends on the wavelength of the SAR.

Bragg Resonance Model

The ocean surface wave is known to contain a wide spectrum of wavelengths from short ripples of a few millimetres to waves which picks lays hundreds of meter apart. Bragg models are most frequently used for describing scattering from the sea surface. Due to the large dielectric constant of water (ε= 80), the scattering mechanism is exclusively surface scattering. Scattering from natural terrain and vegetation is generally a combination of surface scattering and volume scattering. Volume scattering results from dielectric discontinuities within the media (Curlander and McDonough, 1991). Thus, volume scattering does not play any role in case of ocean surface backscatter modelling. The particular application of the Bragg resonance model to the ocean surface, which is a complex representation of a wide spectrum of different wavelengths, requires the assumption that the Bragg mechanism is able to select just those waves that are in resonance (Brekke 2007). The Bragg equation presented below, defines the ocean wavelengths for Bragg scattering as a function of radar wavelength and incidence angle:

$$\lambda_s = \frac{n\,\lambda_r}{2Sin\theta} \text{ (n=1, 2….)} \qquad (2.2)$$

Where defines λ_s the wavelength of the Bragg-selected waves, θ is the incidence angle and λ_r is the radar wavelength (Fig 2.4). It is therefore assumed that at first approximation of Bragg resonance equation is the primary mechanism for backscattering radar pulses (where n = 1, Curlander and McDonough, 1991).

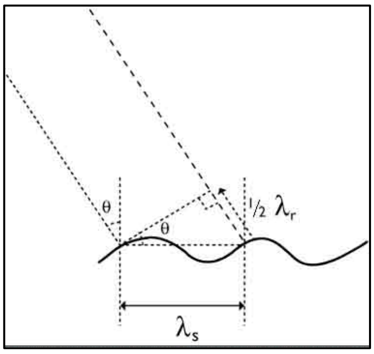

Fig 2.4: Bragg resonance model diagram (Source: ESA Radar Course III)

Note that to be selected by the resonance, the Bragg waves need to propagate toward or away from the looking direction of the radar antenna. Equation 2.2 indicates that the surface waves which influence the radar backscatter are those of comparable wavelength to the microwaves. It is the short gravity and capillary-gravity waves to which the radar responds directly. The Bragg condition also implies, for a given SAR, that the resonant surface waves will be shorter at more oblique incidence angles. This also relates to the general observation that the backscatter for a given sea state decreases with increasing incidence angle (the backscattered radar power is proportional to the spectral energy density of the Bragg waves and the spectral distribution decays at shorter wavelength), and will be discussed in details in Chapter III.

For RADARSAT-1 and ENVISAT ASAR with C-band frequency, a radar wavelength of 5.7 cm and incidence angles in the range of $20^{\circ} - 50^{\circ}$ will this model give Bragg resonant sea wavelengths λ_s in the range of 8.3-3.7cm. In Equation 3.1, the Bragg resonant wave has its peak at right angles to the range direction. For surface waves with peaks at an angle ϕ to the radar look direction we get:

$$\lambda_s' = \lambda_s Sin\,\phi \tag{2.3}$$

where λ_w' is the wavelength of the surface waves propagating at angle ϕ to the radar look direction. The illustration given in Fig 2.5 shows the resonant surface wavelengths will increase when ϕ increases.

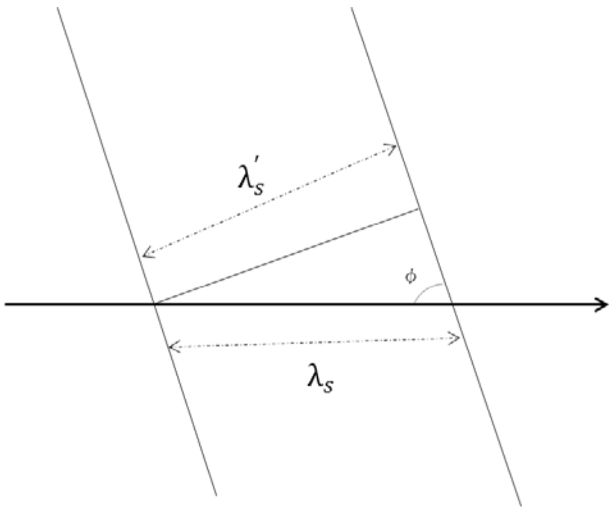

Fig 2.5: Peak at an angle φ to the look direction of the SAR

The two primary factors influencing the transmission characteristics of the signals from any given radar system are the wavelength and the polarization of the energy pulse used (Lillesand *et al.,* 2004). The SAR transmits pulses of electromagnetic (EM) energy in the microwave range (wavelength: 1mm to1m) of the EM spectrum. Table 2.2 enlists some of the SAR sensors used for oceanographic applications. RADARSAT-1, RADARSAT-2 and ENVISAT ASAR are examples of C-band SAR. According to Lillesand *et al.,* (2004) the wavelength of a radar signal determines the extent to which it is attenuated and/or dispersed by the atmosphere. Serious atmospheric effects on radar signals are restricted to the shorter wavelengths (less than about 4 cm). Even at these wavelengths, under most operating conditions the atmosphere only slightly attenuates the signal. Polarization refers to the orientation of the electric field. Most SARs are designed to transmit microwave radiation either horizontally polarized (H) or vertically polarized (V). Similarly, the antenna receives either the horizontally or vertically polarized backscattered energy, and some radars can receive both. Four polarization combinations are: HH - (like-polarized) for horizontal transmit and horizontal receive, VV - (like-polarized) for vertical transmit and vertical receive, HV - (cross-polarized) for horizontal transmit and vertical receive and VH - (cross-polarized) for vertical transmit and horizontal receive. Since various objects modify the polarization of the energy they reflect to varying degrees, the mode of signal polarization influences how the objects look in the resulting imagery (adapted from Brekke 2007 and Lillesand *et al.*, 2004).

2.4 SAR SENSOR FOR OIL SPILL DETECTION

The brightness of the captured image bears a definite relation to the backscatter property of the target surface. Brightness of the sea surface image depends upon several factors, such as local wind speed, proximity to the land surface etc. Sea has a large dielectric constant. The microwave signals cannot penetrate the surface of the sea beyond a few millimetres (Hühnerfuss *et al.,* 1986; Alpers and Huhnerfuss, 1988). As discussed before, the sea scattering process is dominated by surface scattering, where surface roughness significantly influences microwave energy backscattered from the sea surface (Espedal and Wahl, 1999). The sea surface roughness is dependent on the sea waves which are controlled by the wind. In general, the incidence microwave energy is scattered from short waves (less than 1m in wavelength) and reflected from long waves (100 m in wavelength) (Ulaby *et al.,* 1986). The possibility of detecting oil spill by a SAR image relies on the fact that layer of oil dampen the capillary wave which decreases the backscattering of the sea surface, which results in a dark spot that contrasts with the brightness of the surrounding spill free area. Backscatter energy from spill free area are mainly governed and affected by constructive and destructive interference. Fig 2.6 illustrates the mechanism for constructive and destructive interference.

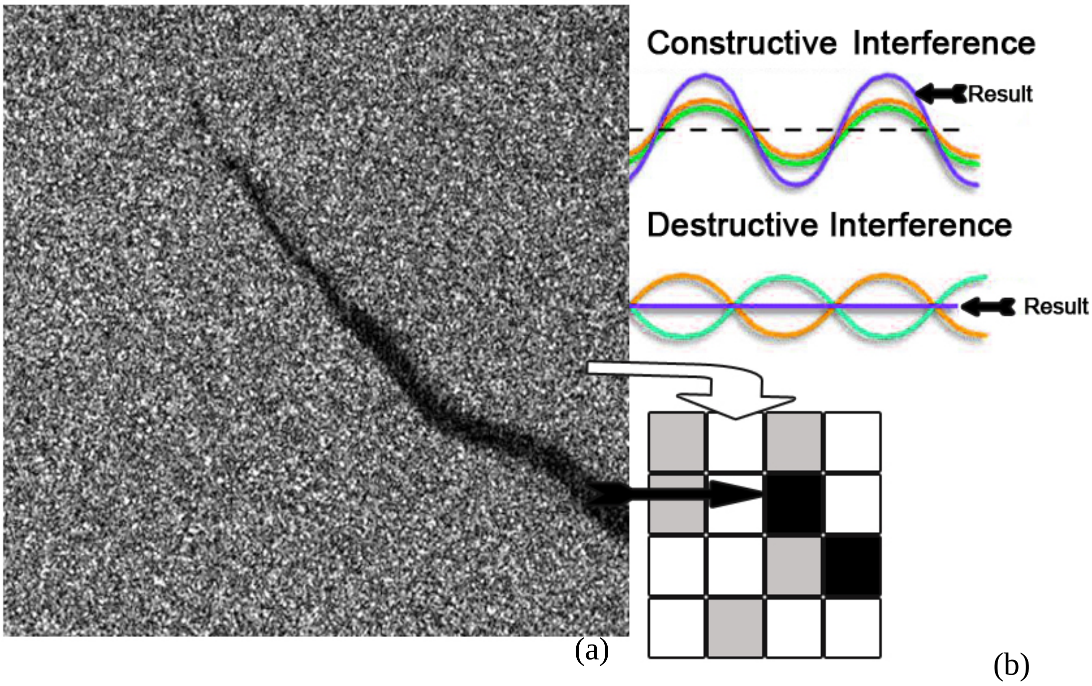

Figure 2.6. Illustration of speckle noises: (a) Speckle noises in a homogeneous region (Image Courtesy: Kostas N. Topouzelis) (b) Principle of speckle noises.

There are different mechanisms responsible for the sea surface radar backscattering, which strongly depend upon the incidence angle of the radar sensor. In a quite large range of angles, approximately from 20º to 55º, the main agent of radar backscattering are the wind-generated short gravity-capillary waves (Hühnerfuss *et al.*, 1987, 1994). The oil film has a dampening effect on these waves locally decreasing the backscattering. It is generally assumed that a light wind field exists in order to activate short gravity capillary waves so that the image with required characteristic can be obtained. The minimum wind speed in fact depends on the frequency of observation and the incidence angle. The most commonly used band in SAR sensor is the C and X band. In this frequency range, a minimum wind field of 3–4 m/s creates sufficient brightness in the image and makes the oil film visible (Espedal *et al.*, 1996, 1999). On the other hand, if the wind speed is too high (10–12 m/s) it causes the spill to disappear since the short waves receive enough energy to counterbalance the damping effect of the oil film on the ocean surface (Garcia-Pienda *et al.*, 2009; Singha *et al.*, 2013).

There may be two reasons behind this phenomenon; the short waves receive enough energy to counterbalance the dampening effect of the oil film or when the sea-state is fully developed, the turbulence of the upper sea layer may break and/or sink the spill or a part of it. Several manmade and natural ocean phenomena damp the wind generated short gravity – capillary waves. For this reason, some areas appear dark on SAR imagery in contrast to the surrounding sea. In summary, radar optimized for oil spills is useful in oil spill remote sensing, particularly for searches of large areas and for night-time or foul weather work. The technique is highly prone to false targets and limited to a narrow range of wind speeds. Figure 2.7 shows an example RADARSAT-2 SAR image containing a verified oil spill where the image is already brightness corrected for the incidence angle (adapted from Singha *et al.*, 2013a).

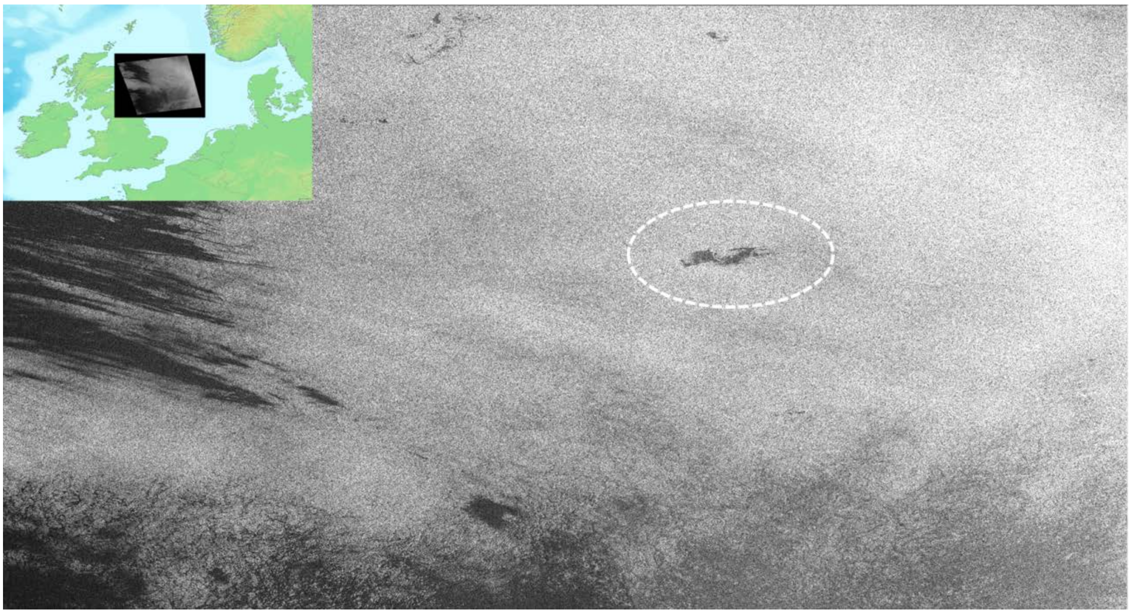

Fig 2.7: Example of dark spots on a RADARSAT-2 ScanSARNarrow Beam (SNB-1F) image acquired on 27th of March 2012 at 17:28:59 over North Sea near the coast north-east England and Scotland (Right hand side inset). The bright white circle showing the potential oil spill spots reported by EMSA along with other look-alike spots. (CleanSeaNet Image ID: 21283, Radarsat-2 image © CSA/MDA/EMSA 2012).

It has also been observed that the wind direction relative to the plane of the incident radar wave also affects the backscatter level in a scene (Alpers and Huhnerfuss, 1988).

A crosswind (wind blowing perpendicular to the range direction) produces lower backscattering than an upwind or downwind (wind blowing along the range direction). Wind speeds ranging between 3–7 m/s have been found to be optimal oil spill detection (Mera *et al.,* 2012; Singha *et al.,* 2013). Figure 2.8 shows an example of dark spot identified as oil spill on a TerraSAR-X VV polarised image. The oil spill visible on the TerraSAR-X image was accidentally released by a Gennet platform located on North Sea.

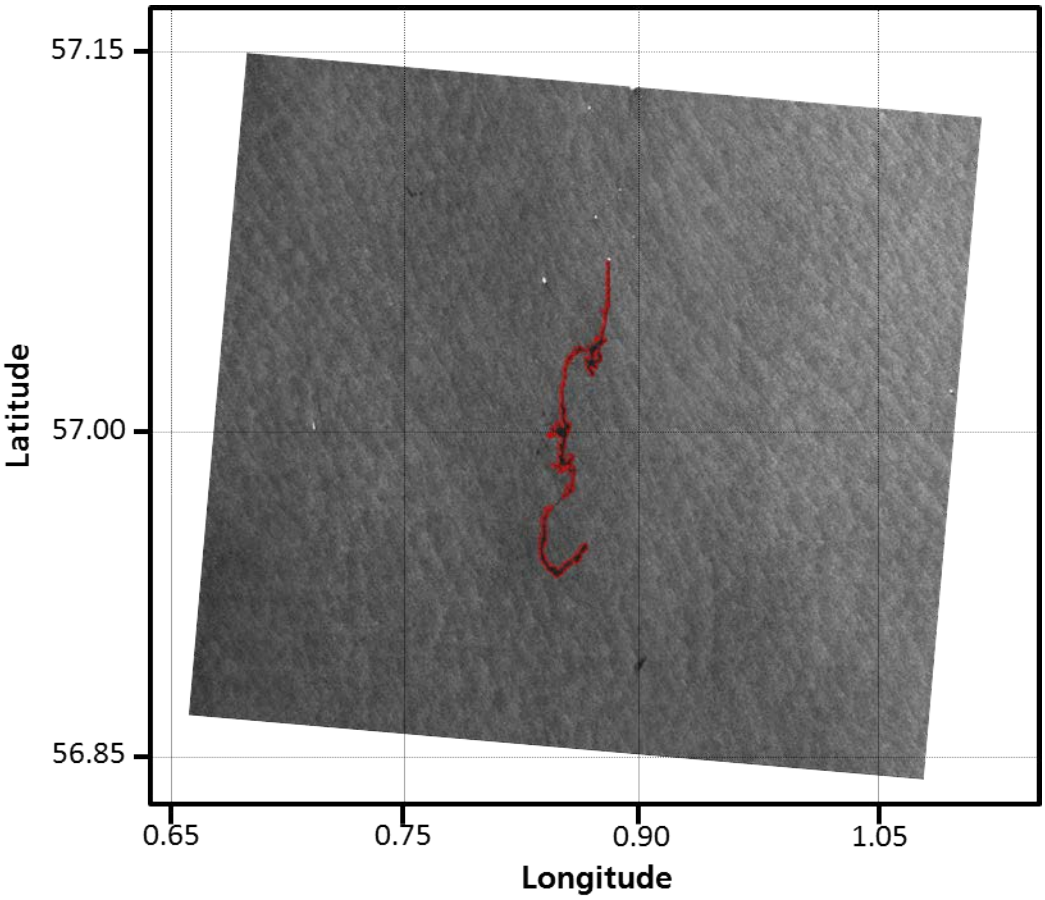

Fig 2.8: A sub-scene of the TerraSAR-X ScanSAR VV-pol acquired on 2011-08-19 on 06:15:43 showing conformed oil spill from Gannet Platform at North Sea 113 miles (180km) off Aberdeen (TerraSAR-X image © German Aerospace Centre, DLR 2013).

The main systems to monitor sea-based oil pollution are the use of satellites equipped with Synthetic Aperture Radar (SAR). Most studies used low resolution SAR data (quick-looks, single polarization), with nominal spatial resolution of 100m × 100 m, to detect oil spills (Espedal *et al.*, 1998, Kubat *et al.*, 1998; Espedal and Wahl 1999; Solberg *et al.*, 1999; Del Frate *et al*,. 2000; Espedal and Johannessen 2000; Fiscella *et al.*, 2000; Pavlakis *et al.*, 2001, Miranda *et al.*, 2004; Keramitsoglou *et al.*, 2003, 2005; Kontoes *et al.*, 2005; Nirchio *et al.*, 2005; Topouzelis *et al.*, 2007; Solberg *et al.*, 2007). Multipolarization detection is also exploited in recent years (Migliaccio 2009; Velotto et al 2011) and discussed in Section 2.7. Low resolution data are sufficient for large scale monitoring. Small and fresh spills however cannot be as efficiently detected (Karathanassi *et al.*, 2006). The possibility of detecting an oil spill in a SAR image relies on the fact that the oil film decreases the backscattering of the sea surface resulting in a dark spot that contrasts with the brightness of the surrounding spill-free sea. However, there are several reasons other than oil spills that may cause a dark spot in the SAR image. Therefore, the main challenging part of oil spill detection using SAR image is to discriminate between look-alike spots and oil spill spots.

Any area on an image which is sufficiently darker than the neighboring area can be characterized as a dark spot. It is particularly difficult to determine how much darker an area has to be for characterize the area as a dark spot. Even in a single image, the degree of darkness and contrast required for the dark areas characterization is not uniform (NOAA, 2010). Dark formations may be caused due to low wind areas, organic film, fronts, areas sheltered by land, rain cells, current shear zones, grease ice, internal waves, upwelling zones, down welling zones, small scale eddies etc (Trivero *et al.*, 1996; Gade and Alpers, 1999; Solberg *et al.*, 2007; Alpers *et al.*, 2013).

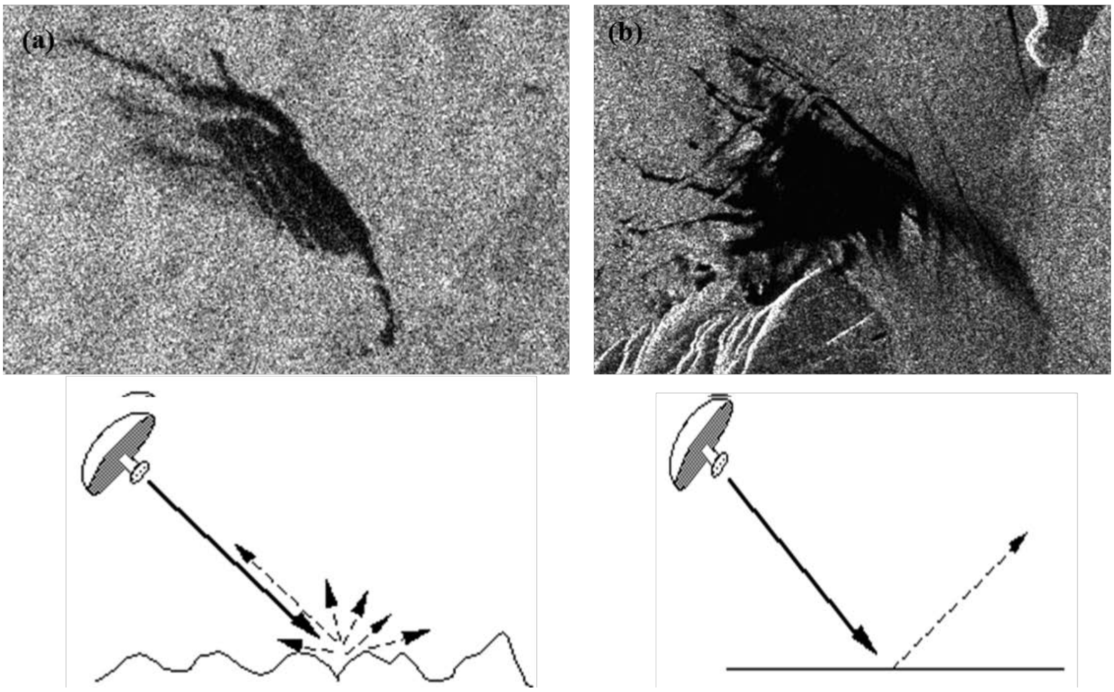

Figure 2.9: Two examples of dark formations: (a) Verified oil spill on a SAR image taken on 6 September 2005 close to Ancona, Italy. (b) Verified look-alike on a SAR image taken on 25 August 2005 close to Otranto, Italy (Adapted from Topozeiles *et al.*, 2007).

It can be observed from Fig 2.9 that the dark spot due to oil spill and due to other reasons are quite analogous. Therefore, many a time the spot due to other reasons is also known as look-alike. It is thus very clear that distinction between oil spill and look-alike spot is a complex task. Some of the natural phenomenon which creates 'look-alikes' on SAR images are discussed below (Bern *et al.,* 1992; Brekke and Solberg 2005; Brekke 2007).

Natural biogenic surfactants/natural film

Natural biogenic slicks are produced by plankton and fish substances normally released into the environment. Surfactants accumulate in convergent zones by internal waves and current/eddy fields, but are mixed into the upper ocean and rapidly disperse and disappear under windy conditions. Fresh-water run-off containing biogenic material can also cause natural slicks. Figure 2.10 shows an example of natural film near East Yorkshire coast and Humber Estuary.

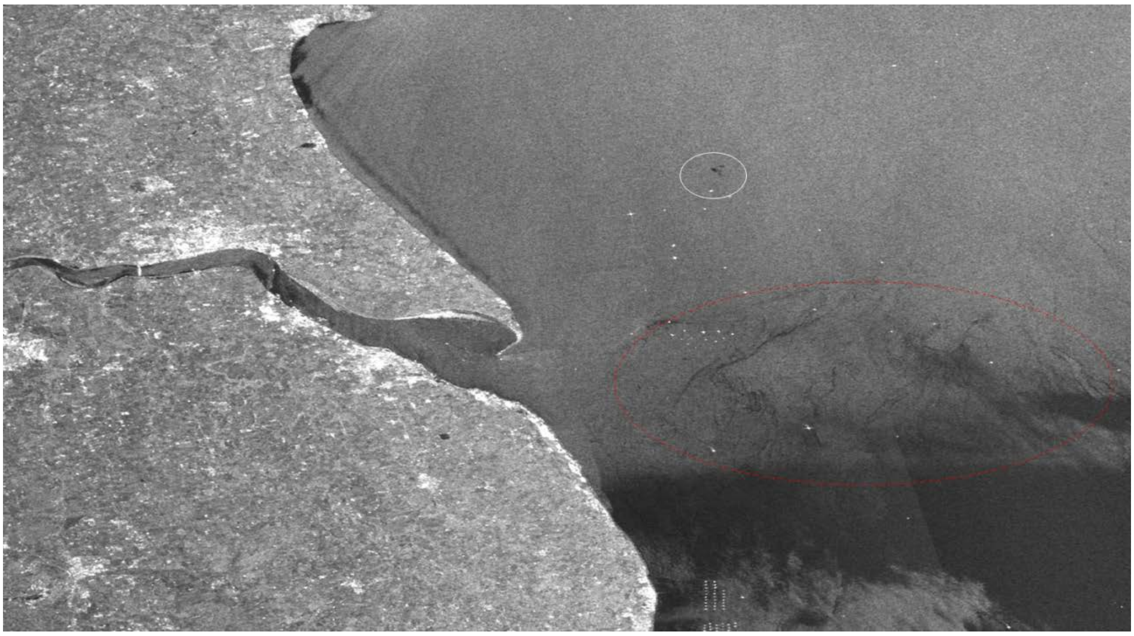

Fig 2.10: Image extract from a ENVISAT ASAR WideSwath Mode image over ease coast of United Kingdom showing a possible oil spill (white circle) and look-alike spots due to biogenic films indicated in red dotted circle (CleanSeaNet Image ID: 5620, ENVISAT ASAR image © ESA/EMSA 2012).

Natural mineral surfactants

Natural mineral slicks are the result of ocean-bottom oil seeps. (This phenomenon should not be considered as a look-alike if we are strictly looking for man-made oil pollution). However this kind of natural phenomenon is very rare in European waters.

Sea ice

Sea ice can also responsible for reducing the ocean surface backscatter. In particular, grease ice (composed of small ice crystals, form when seawater begins to freeze) dampens Bragg waves and produces areas of extremely low backscattering (Brekke, 2007). As it accumulates on the sea surface, grease ice forms slick patterns similar to those produced by mineral or biogenic surfactants (Singha *et al.,* 2013b). Figure 2.11 shows an example of grease ice, and effect of sea ice on oil spill detection capability.

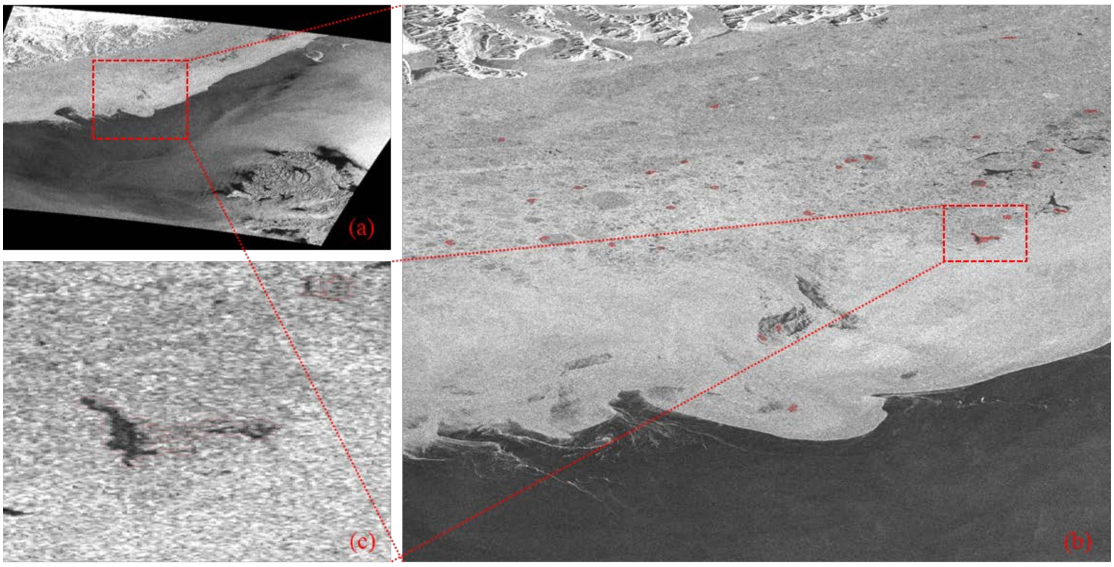

Figure 2.11: Example of sea ice on and its effects on oil spill detection capability. (a) RADARSAT-2 ScanSARWide HH polarized image acquired on 24th March 2012 at 08:20:51 acquired near coast of Greenland and Iceland over Atlantic sea. (b) Presence of dark spots due to sea ice (in red outlined polygon). (c) Example of 'look-alike' due to presence of ice. CleanSeaNet Image ID: 19899, RADARSAT-2 image © CSA/MDA/EMSA 2012).

Low surface winds

As the sea surface roughness is dependent on the wind conditions, an often seen feature imaged by SAR over the ocean is the wind speed variability itself. Dark areas appear with wind speeds below the threshold wind speed of about 3 m/s (which is the threshold for generation of Bragg waves). Areas of wind shadowing by coastal topography are also commonly observed in SAR imagery. The islands and high mountains shelter the water surface from the wind, and the Bragg wave growth is reduced on the lee side. An example wind shadow on SAR image shown in Figure 2.12.

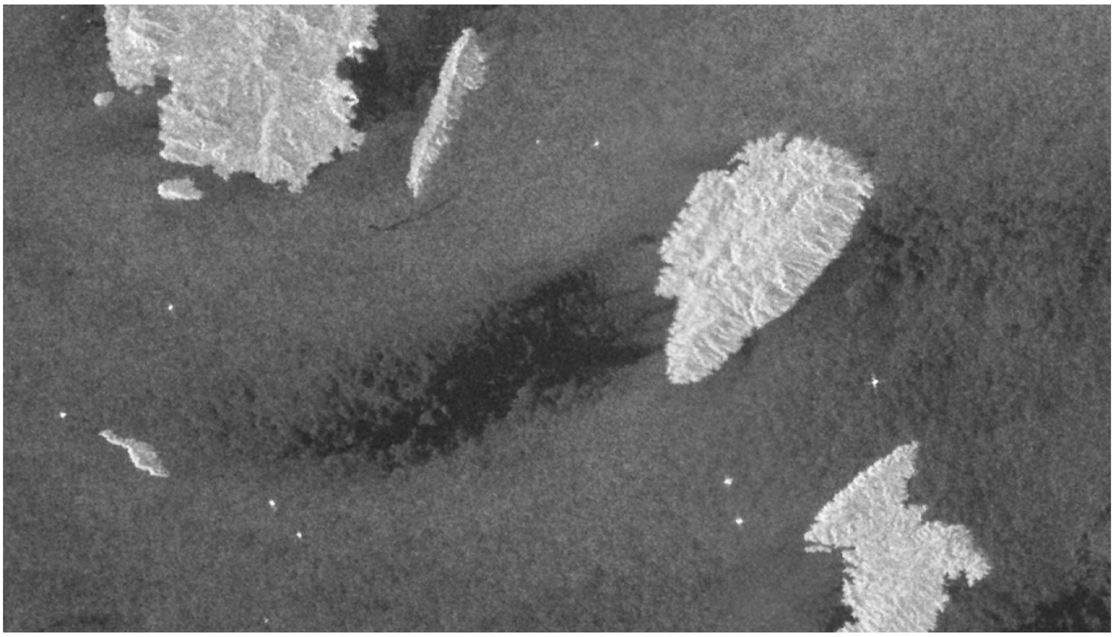

Fig 2.12: Example of wind shadow by the island shown on an image extract from an ENVISAT ASAR WideSwath Mode, HH polarized image acquired on 16th February 2011 at 20:23:12 over Mediterranean Sea near southern coast of Greece. (CleanSeaNet Image ID: 3726, ENVISAT image © ESA/EMSA 2012).

Rain cells

There are two processes involved when low-backscatter signatures are caused by rain in SAR imagery. First, atmospheric attenuation due to volume scattering will tend to decrease the backscattering toward the SAR over an area under a rain system. Second, depending on the wind speed and Bragg wave scale, the raindrop impact on the sea surface may tend to dampen the Bragg waves. C-band is affected more by rain volume scattering, while L-band is more sensitive to Bragg wave dampening. Figure 2.13 shows an example of the effect of rain cells on a C-band RADARSAT-2 SAR image acquired near south west coast of United Kingdom. The backscatter damping is quite similar for oil spill and rain event on a C-band SAR images (X-band SAR images also affected in a similar way but in higher degree).

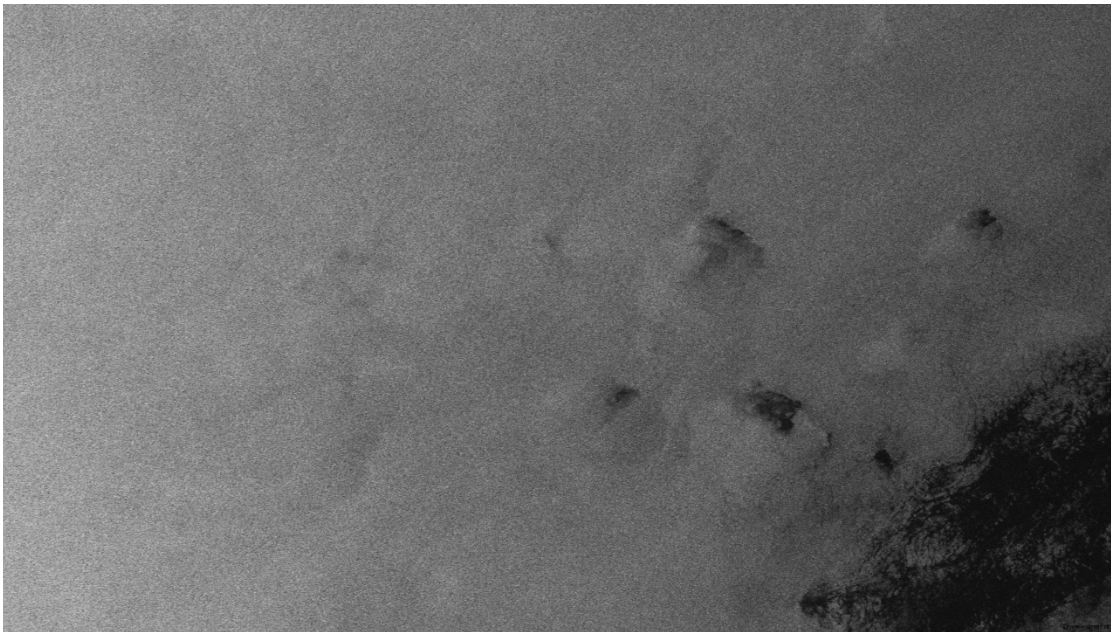

Fig 2.13: Example of rain cell presence on an excerpt from an RADARSAT-2 SAR ScanSARWide Beam, HH polarized image acquired on 28th of April 2011 at 20:23:12 over Celtic Sea near south-western coast of United Kingdom. (CleanSeaNet Image ID: 21149, RADARSAT-2 image © CSA/MDA/EMSA 2012).

Shear zones

Shear zones appear as narrow, bright or dark curving signatures in SAR images. Shear zones occur in areas of strong currents.

Internal waves

Internal gravity waves in the ocean can affect the local sea surface velocities and thus the Bragg wave spectrum. This modulation allows imaging internal waves by SAR. The radar image of internal waves consists of adjacent bright and dark bands. Internal waves can also accumulate surfactants, in which case the internal waves are imaged as parallel dark bands. Internal waves appear in shallow water, and the wavelength is typically several kilometres. Figure 2.14 shows an example of what could be internal waves.

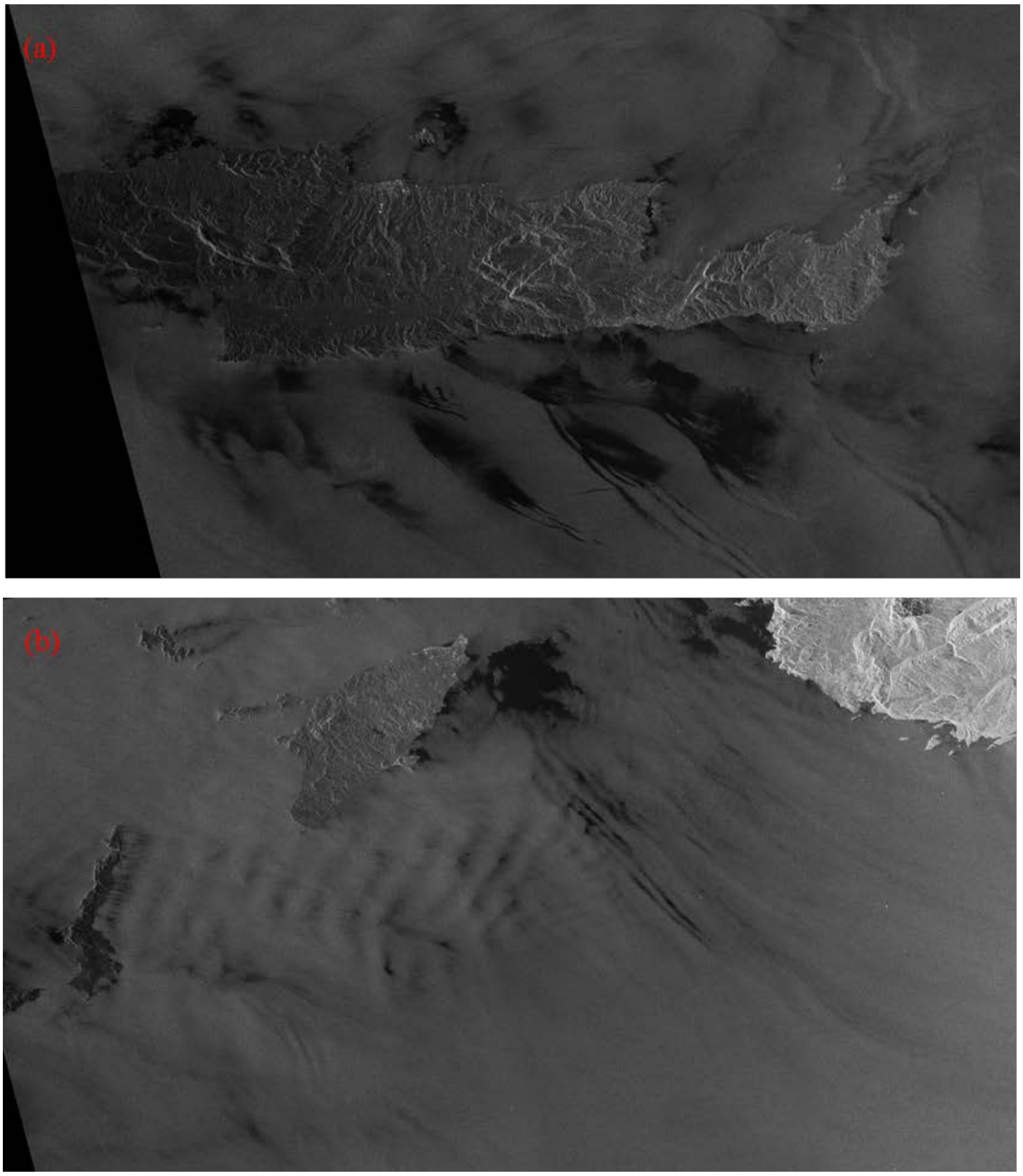

Fig 2.14: Example of internal waves shown on image excerpts from two ENVISAT ASAR WideSwath Mode, HH polarized image acquired over Mediterranean Sea. (CleanSeaNet Image ID: 6579 (Fig (a) acquired on 1st May 2011 at 20:10:52) and 6583 (Fig (b) acquired on 4th May 2011 at 20:00:36). ENVISAT image © ESA/EMSA 2012.

These ocean features reflect either meteorological or oceanographic conditions. There are also some low-backscattering phenomena caused by large oil installations or ships. An example is turbulent ship wakes that decrease the surface roughness when wind waves are present and they are often observed in SAR images. Table 2.3

shows weather limitations and damping characteristics of some of the low backscattering features described in this section.

Table 2.3: Weather limitations and damping of some low-backscattering features. (Source: Brekke 2007).

Phenomenon	Weather limitations	Damping [dB]
Oil spill	Wind speed <= 15 m/s	0.6 - 13.0
Natural film	Wind speed <= 7 m/s	0.8 - 11.3
Grease ice	Winter season and cold nights close to ice edge.	14.0 - 19.0
Threshold wind speed area	Wind speed <= 3 m/s 9.6 - 18.5	9.6 - 18.5
Shear zones	Wind speed <= 10-12 m/s	1.4 - 6.2
Internal waves	Wind speed <= 8 m/s	0.8 - 6.0

2.5 SAR IMAGE QUALITY ASPECT

Satellite-based SAR is gradually becoming a useful tool for operational maritime monitoring and surveillance applications. Services based on SAR images rely on level of image quality that, if not entirely fulfilled, may affect the performance and accuracy of the operational algorithms (processing chain) and degrade the reliability of operational services. However, it is not always clear how to quantitatively measure and access SAR image quality level from the delivered products. It is evident that, in European Union there is a widespread start-up of nearly operational oil spill and ship detection services using SAR imagery. In a recent study, Vespe and Greidanus (2012) discussed most relevant quality issues of satellite SAR images related to maritime applications which was a part of research activity carried out by European Maritime Safety Agency for its ‘CleanSeaNet’ service in conjunction with European Union Joint Research Centre. In that study, Vespe and Greidanus (2012) reported a set of quantitative measures that can be estimated from satellite images used in operational applications like ‘CleanSeaNet’. These quantitative measures are designed to verify the suitability of the delivered image with respect to product specification requirements but also to assess how well the image can be used in a particular maritime application.

As discussed in Chapter I, Primarily wide swath X-band (2.4–3.75 cm) and C-band (3.75–7.5 cm) images are used for operational purpose due to its large coverage and cost effectiveness (e.g. ENVISAT ASAR Wide Swath Mode, RADARSAT 2 SAR ScanSAR Wide and ScanSAR Narrow for 'CleanSeaNet' operation). Quality of SAR images is a key factor for this kind of operational services which deals with oil spill detection, ship surveillance and ocean surface wave modeling. In Europe, oil spill detection from satellite SAR has become operational with the CleanSeaNet service being provided at EU level by EMSA. The image analysis is still carried out mostly by visual inspection, but automatic processing support is expected to increase in near future. Although there are some image quality issues which need to be addressed before an operational service migrated to an automatic processing chain. Some of the issues are discussed below.

As discussed earlier, these wide swath images are generally affected by trends of reduced radar backscatter of the sea induced by the incidence angle increase at far range. Figure 2.15 demonstrates this issue on a RADARSAT-2 SAR imagery along with a line profile plot from. At the time of acquisition the incidence angle at the center of the image was 34.4708^{o} and platform was in descending mode. High backscatter at near range and progressively low backscatter at the far range are clearly visible from the image and corresponding profile plot. This particular phenomenon which is intrinsic to SAR images obstructs the process of feature detection on ocean surface such as oil spill and ship detection. Rest of this section will discuss different SAR image quality aspects and its quality aspects. Section 3.2.6 in Chapter III investigates different techniques for compensating this reduced backscatter trend.

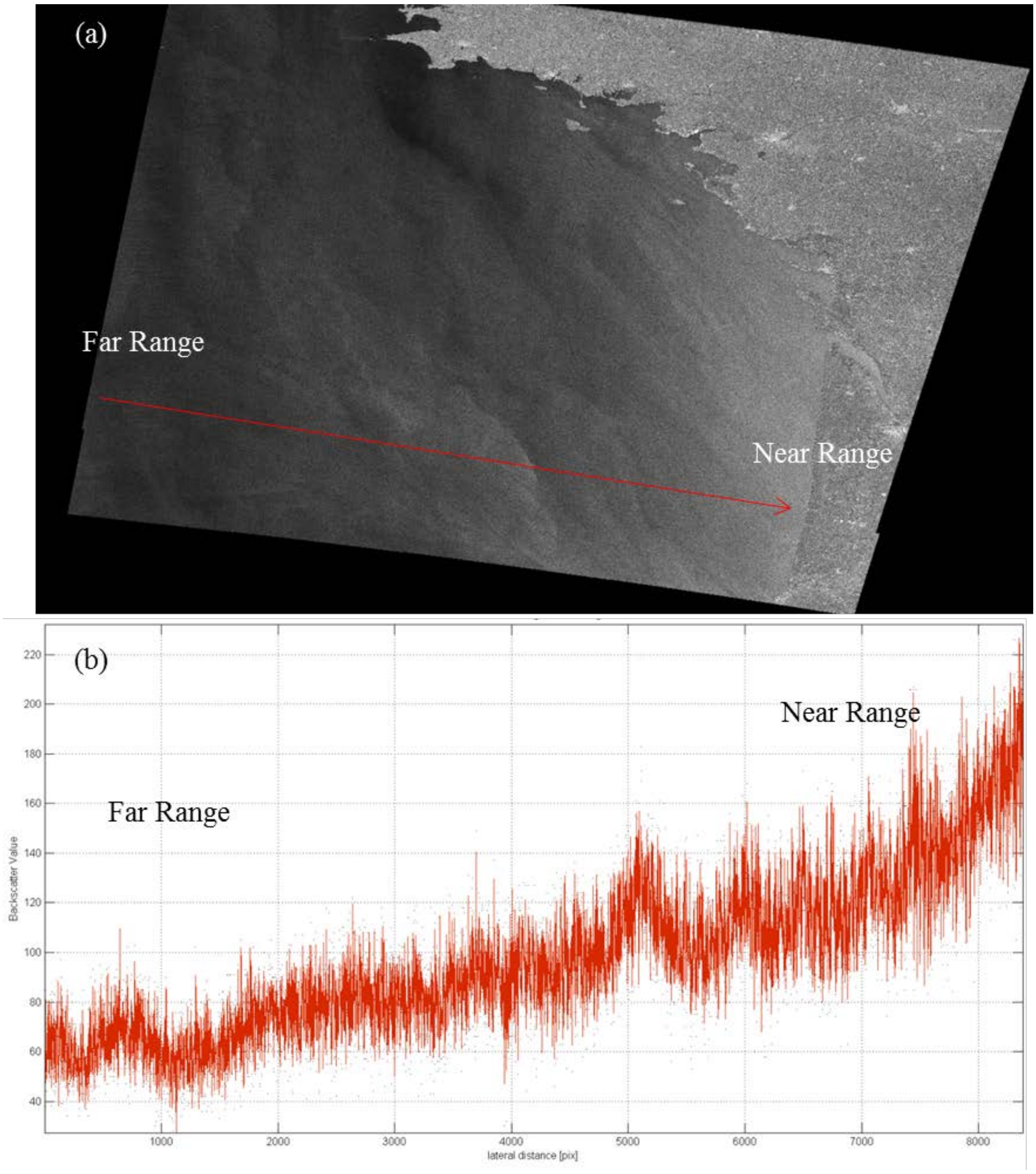

Fig 2.15: (a) RADARSAT-2 ScanSARWide Beam (SWB_1F Operational Mode, Descending orbit) image acquired on 22nd of May 2012 at 06:23:56 over Bay of Biscay near the west coast France. (b) Profile plot of backscatter value along the red line indicated in Fig (a) (CleanSeaNet Image ID: 22458, Radarsat-2 image © CSA/MDA/EMSA 2012).

Some SAR image ambiguity and sensor induced anomaly can seriously affect the quality of the end product, e.g., interference by manmade objects, azimuth and range ambiguities, etc. In such cases, the SAR image may be in accordance to specifications, but the impact of these artefacts can still jeopardize the service products. In other cases, operationally delivered images are not in accordance to specifications, e.g., due to processing errors or radiometric performance degradation and sensor intrinsic issues. However, depending on the extent of the errors, it may still be possible to analyse the image after some pre-processing. This might lead to satisfactory results of the operational service. The pre-processing tool mentioned above is developed as a part of this research activity, to address those image quality issues. This pre-processing tool is described in details in Chapter III Section 3.2.

There are some specific types of image ambiguities which might jeopardize the desirable output of the operational service, specifically services related to oil spill and ship detection. This discussion is not only based on theory but also on experience from analysing over 2000 maritime SAR images during a research activities in European Maritime Safety Agency, Portugal. Quality issues that are discussed have actually been encountered and found to create problems for maritime applications during that research activity. Some of those image ambiguity issues are discussed below.

Radiometric Sensitivity

The measure for the radiometric sensitivity is the Noise Equivalent Sigma Zero ($NE\sigma_0$), i.e., the value of backscattering coefficient that would give a signal level equal to receiver noise level. A good sensitivity is needed to detect oil spills at low wind, under high incidence angle and at HH polarization, as the sea surface has a low backscatter under those conditions. Also, cross polarization is favourable for ship detection, but today, it is often sensitivity limited (as opposed to clutter limited). For a few of the newer satellite SAR systems, e.g., Radarsat-2 and TerraSAR-X, reference $NE\sigma 0$ profiles are delivered with the product metadata. In other cases, the sensitivity would need to be estimated on the calibrated image. This can be done by measuring the apparent backscattering in those areas where the backscattering is known to be extremely low. Water regions at near-zero wind conditions are particularly suited for this purpose. However, as it is mostly uncertain if a low-backscatter area is really below the $NE\sigma 0$, this estimate is often only sure to give an upper bound. Moreover, the $NE\sigma 0$ is range dependent, and to estimate it for all range values, one needs to have near-zero backscatter areas present at several ranges. The sensitivity of a SAR instrument given below is a function of system parameters satellite velocity *V*, receiver temperature *T*, bandwidth *B*, noise *F*, overall losses *Ltot* and average transmission power *Pt*, along with geometric parameters slant range *R*, incident angle η and antenna gain *G*.

$$NE\sigma_0(\eta) = \frac{4K\ V\ T\ B\ F\ L_{tot}\ (4\pi R)^3 Sin\ (\eta)}{\lambda^3\ c\ P_t\ G(\eta)^2} \tag{2.4}$$

The constants are the wavelength λ, Boltzmann constant *K* and speed of light *c*. The most relevant parameters which are negatively affecting the instrument sensitivity are a reduced transmission power, a decreased antenna gain, or an increase of losses. As the sea surface has a low backscatter at low wind, low incidence angle or in cross-polarisation, maritime applications typically require a significant sensitivity (Adapted from Vespe and Greidanus, 2012).

Radiometric Resolution

The radiometric resolution is a parameter describing the capability of a sensor to resolve objects or homogeneous areas characterised by different backscattering coefficients. For a SAR system, the radiometric resolution is limited by the presence of speckle noise. It can be improved by multi-look processing or by using post-processing speckle filters. The Equivalent Number of Looks (ENL) is related to the averaging of possibly overlapping sub-apertures (looks) in the SAR image formation and can be estimated from a homogenous portion of the image through the computation of the mean μ and standard deviation σ of the intensity I as follows:

$$ENL = \left(\frac{\mu(I)}{\sigma(I)}\right)^2 \tag{2.5}$$

According to Brooks and Miller, 1979 (in Vespe and Greidanus, 2012), the ENL determines the radiometric resolution Γ as

$$\Gamma = 10log_{10}(\mu + \sigma) - 10log_{10} = 10log_{10}\left[1 + \frac{1}{\sqrt{ENL}}\right] \tag{2.6}$$

A good radiometric resolution is essential to detect small and low contrast oil spills. In the past, ENL values were not provided in the metadata, and they can depend not only on the specific mode but even for the same mode on the ground station where the image was received. This led to the need to estimate ENL from the image itself, or at least estimate it as a function of image mode and ground station using a set of images. The newer SAR systems provide the ENL, but it is still important to verify it. This can be done by dividing the image in windows (of e.g. 200 × 200 pixels) and applying (2.5), leading to an ENL estimate for each window. Very high pixel values (viz., from targets) should be discarded in the averaging. Perfectly homogeneous areas will yield a true ENL estimate, while any texture in the window will increase the apparent ENL value. The lowest values found can therefore be taken to be ENL estimates. Figure 2.16 shows an example of this process. A particular issue can occur in ScanSAR images, where the different sub-swaths may have different ENLs. Sometimes overlap areas occur where the ENL is much higher due to the averaging applied.

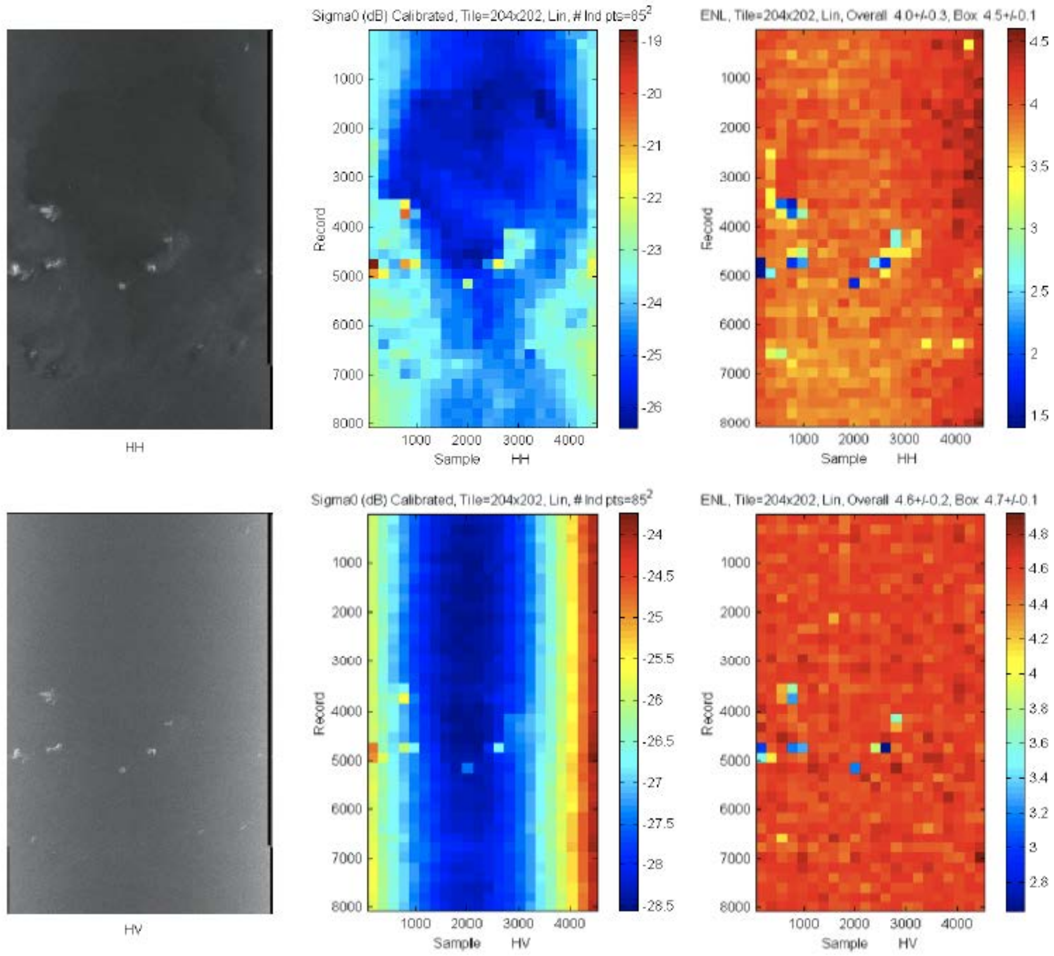

Fig 2.16: ENVISAT-ASAR Alternating Polarisation image over the sea (left column), processed to give mean σ^0 (centre column) and ENL estimate (right column) in windows of 200 x 200 pixels. Top HH; bottom HV (ASAR data © ESA 2006 Processing carried out by Vespe and Greidanus, 2012 © JRC/EMSA 2012).

In Fig 2.16 the σ_0 of HV image, one can recognise the antenna pattern correction in range direction (horizontal), while the ENL is at constant maximum value, indicating that the image shows NEσ_0 and not sea clutter, except in some locations where rain cells occur. In HH mostly actual sea clutter is imaged, leading to structure in the σ0 image and lower values in the ENL image. It was found that the estimated ENL is 4.7 for both channels (Source: Vespe and Greidanus, 2012).

Radiometric Error, Accuracy, and Stability

The radiometric error $\delta\Gamma$ is a measure of the relative radiometric calibration performance. It can be estimated from the image by measuring the radiometric variation in regions of expected homogeneous backscattering coefficient. In addition to the radiometric error, also, the radiometric accuracy (absolute calibration) and stability (over time) are relevant. All these parameters are difficult to estimate on marine images without a dedicated calibration setup. For ScanSAR images, there are two other important quality aspects.

Residual Scalloping (Azimuth): This is a periodic variation of pixel intensity along track (striping), resulting from imperfect compensation of the azimuth antenna pattern modulation (Jin 1996 in Vespe and Greidanus, 2012). Its strength δsc can be directly measured from the image. Scalloping leads to missed oil spill and ship detections, but in practice, it is found that the impact is very limited.

Radiometric Mismatch (Elevation): Beam radiometric mismatch is due to wrong antenna pattern correction in the elevation beam, resulting in pronounced pixel value discontinuity between two ScanSAR beams (Feng and Jun, 2007 in Vespe and Greidanus, 2012). This kind of artifact may result in unsatisfactory image segmentation process and CFAR algorithms because it disrupts local statistics, leading to both false alarms and missed targets close to the transition. Just as for the residual scalloping effect, its magnitude δ_{em} can be directly measured on the image. In the example in Fig. 2.17, after median filtering along the azimuth direction of the highlighted area straddling the two beams, the mismatch is measured as larger than 2 dB.

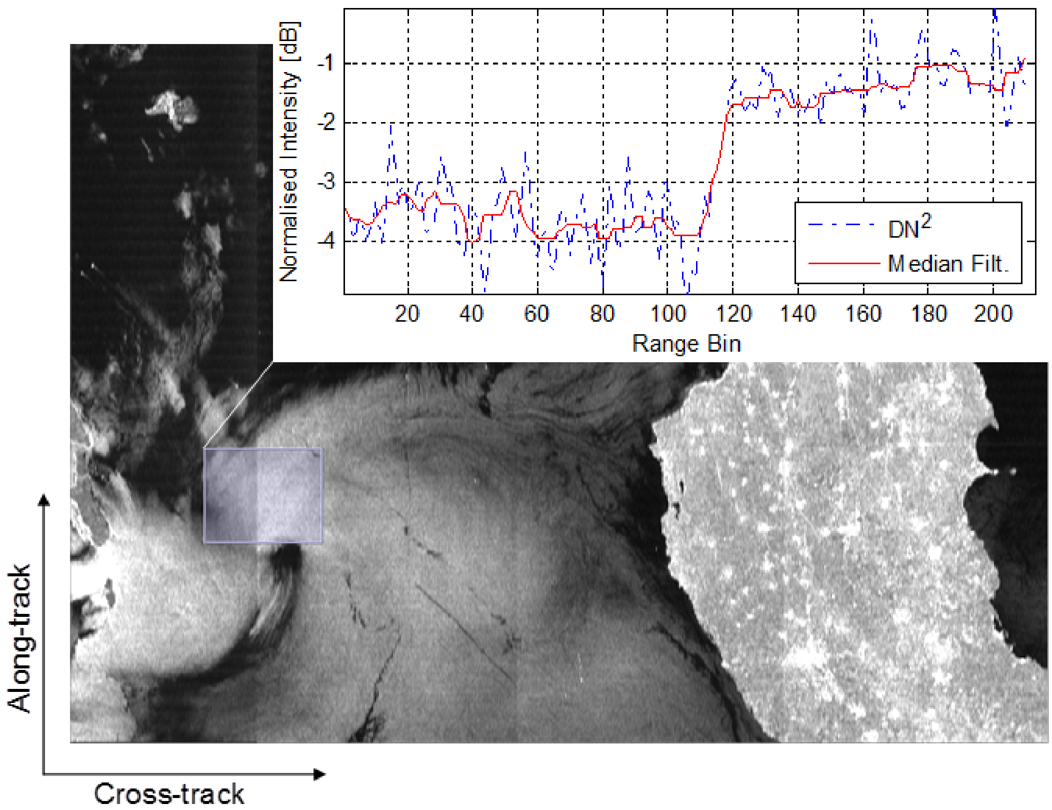

Fig 2.17: Inter-beam seams and measured radiometric mismatch after azimuth filtering (COSMO-SkyMed data © ASI 2010, Source: Vespe and Greidanus, 2012).

Ambiguities

Ambiguities are ghost images of strong targets, displaced by a determinate amount from the source target in range or azimuth direction. Ships and man-made objects (e.g., oil rigs) over the ocean surface, call for all the three physical scattering models: single-bounce returns, due to direct backscattering from surfaces perpendicular to the radar beam; double-bounce returns, due to the dihedral formed by the vertical ship's conducting plates and the sea surface; multiple-bounce returns, caused by ship's complex metallic structure (Lee *et al.,* 2006 in Velotto *et al.*, 2013). Hence, ships show a larger backscatter, (Measured normalized radar cross section in dB) by SAR is higher than the one measured from the surrounding sea surface, where the wind driven ocean waves (Bragg waves, discussed in previous section) are responsible for a smaller backscatter signal (Velotto *et al.*, 2013). In some cases strong backscatter from land can create bright patches on the sea area (Fig 2.18b).

Single and multi-polarization SAR images are affected by the presence of range and azimuth (or Doppler) ambiguities which arise due to the fact that the data are sampled with the pulse repetition frequency (PRF). The system is usually designed in order to avoid range ambiguities by selecting the correct swath. High PRF value responsible for smaller the swath. On the other hand, if the PRF is set too low, the Doppler history of returns at different azimuth positions is the same, causing aliasing. These "false" targets become visible particularly in low backscatter area, i.e., over the ocean surface in low wind speed area primarily on HH polarized images (Velotto *et al.*, 2013; Vespe and Greidanus, 2012).

As mentioned earlier, areas near the coast can be strongly affected by high backscatter from land based sources. Ambiguities can lead to false alarms in case of both oil spill and ship detection. The Azimuth Ambiguity to Signal Ratio (*AASR*) of a SAR image represents the ratio of the energy of the ghosts in azimuth produced by the antenna sidelobes and the main lobe, and can be formulated as follows:

$$AASR(PRF) = \sum_{\substack{m=-\infty \\ m\neq 0}}^{\infty} \int_{-B_D/2}^{B_D/2} G^2\,(f + m.PRF)df \Big/ \int_{-B_D/2}^{B_D/2} G^2\,(f)df \qquad (2.7)$$

where G is the azimuth antenna pattern, B_D the Doppler bandwidth and PRF the Pulse Repetition Frequency. Such ambiguities appear at a distance D_{AA} from the main peak:

$$D_{AA} = \frac{R_{sl}\lambda\, PRF}{2V[1-\cos\theta/T_{rev}]} \qquad (2.7)$$

where R_{sl} is the slant range to the point of interest, θ the orbit inclination of the satellite and T_{rev} the number of satellite revolutions per day. Higher orders of ambiguities may appear at multiples of D_{AA} from the main peak. Experience shows that azimuth ambiguities (Figure 2.18) are today a real problem for processing chains used for ship detection and oil spill detection in regard to identifying potential polluters.

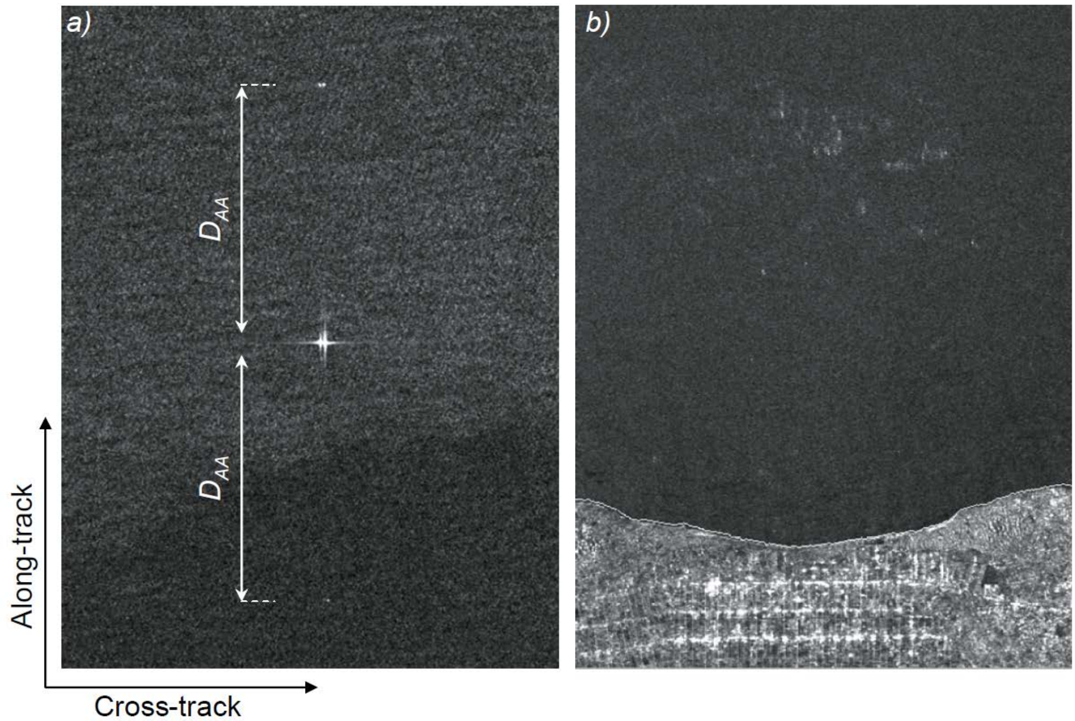

Fig 2.18: First order ambiguities from a ship (Image (a) ENVISAT ASAR data © ESA 2006) and from buildings on land (Image (b) ENVISAT ASAR data © ESA 2007) Source: Vespe and Greidanus, 2012.

In principle, it is possible to detect and suppress spurious spots induced by azimuth ambiguities by checking whether there is a stronger source target present at the known distance (D_{AA}). However, this does not work perfectly always, due to four causes. First, a source target will not be found if it is outside the image. Typical azimuth ambiguity distances are 5-10 km, so this will occur for a part of the cases. Second, due to composite targets (like ships or ambiguity sources on land), fading leads to strong and unpredictable variations in the measured ambiguity ratios, as the ambiguities are imaged under different path lengths between the constituent elementary scatterers of the composite target. Third, higher order ambiguities are easily overlooked, also because *e.g.* the 2nd ambiguity can be stronger than the first because of the mentioned fading. Finally, in ScanSAR images, the different constituent beams generally have different *PRFs*, so the ambiguities appear at different distances (Figure 2.19). To recognise ambiguities, it is in the first place needed to know the exact locations of the beam edges, and moreover, in beam overlap areas the ambiguities appear double (Adapted from Vespe and Greidanus, 2012).

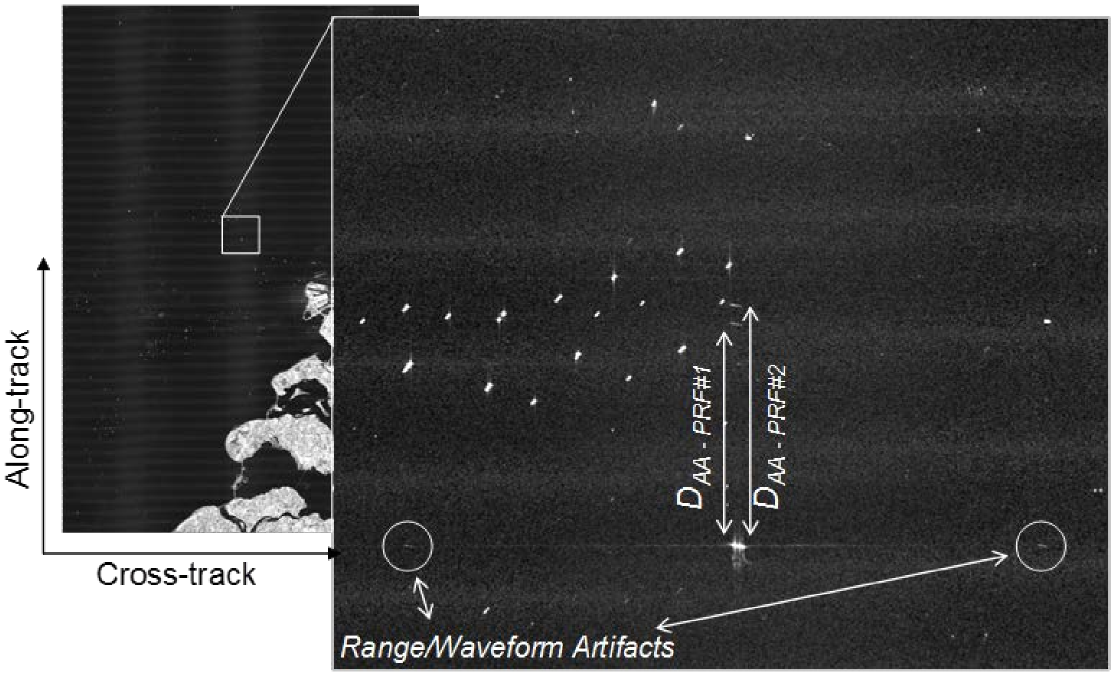

Fig 2.19: ScanSAR double azimuth ambiguities due to different PRF values in correspondence of overlapping beams (TerraSAR-X data; © German Aerospace Center (DLR) 2009; Source: Vespe and Greidanus, 2012).

In a recent study by Velloto *et al.,* 2013 shows the process of detection and discrimination of azimuth ambiguities using Generalized K distribution approach on dual pol TerraSAR-X SAR imagery. Proposed methodology is based on the intrinsic configuration of monostatic two-channel PolSAR systems and relies on the distinctive signature of azimuth ambiguities in cross-polarized channels. Automatic Identification System (AIS) messages were used as ground truth data to evaluate and validate their proposed methodology.

In ScanSAR and Wide Swath ScanSAR mode, the PRF is tuned according to coverage diagrams (chronograms) to reduce azimuth and range ambiguities, while the sub-swaths are designed to overlap in order to avoid data gaps. Range ambiguities typically occur much further away from the source than azimuth ones, in the order of 100 km. For that reason, they are more challenging to recognise (Vespe and Greidanus, 2012). They typically appear in seas some 100 km west or east from urban / industrial areas or steep topography. A special case of range ambiguity is nadir return, which shows up as a bright linear feature through the image at constant range (Figure 2.20). Backscatter signal from nadir are very strong due to near-specular reflection from targets within a very narrow slant range distance, hence the bright linear object appear in the middle of the range coverage.

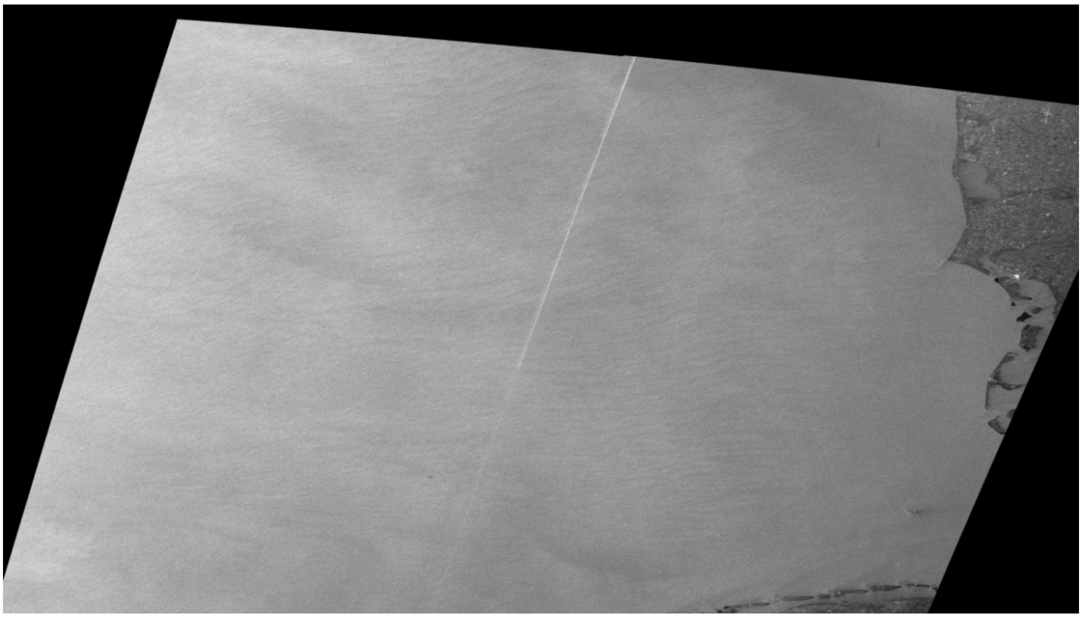

Fig 2.20: Example of artefact on an excerpt from an RADARSAT-1 ScanSARNarrow Beam, HH polarized image acquired on 7th of August 2011 at 05:57:35 over North Sea near northern coast of Germany. (CleanSeaNet Image ID: 12362, RADARSAT-1 image © CSA/MDA/EMSA 2012).

Interference Artifacts

Microwave frequency emissions from ground objects, near the band of the illuminating radar frequency can cause bright features in the SAR image. As these features affect the local statistics, it may again cause false alarms or mask objects (Vespe and Greidanus, 2012). The effect is variable and depends on the interference bandwidth and radiation pattern. Some types of microwave frequency interference are easy to recognize with some experience—e.g., narrow-band and pulse-like emissions show up in the image with an extension corresponding to the range and azimuth compression widths (responsible for creating 'barcode' like objects on SAR images). Figure 2.21 shows presence of 'barcode' like objects on ENVISAT ASAR and RADARSAT-2 SAR images. These figures also show the backscatter signal attenuation and gain caused by interference through an image profile indicated by the red arrow on the image.

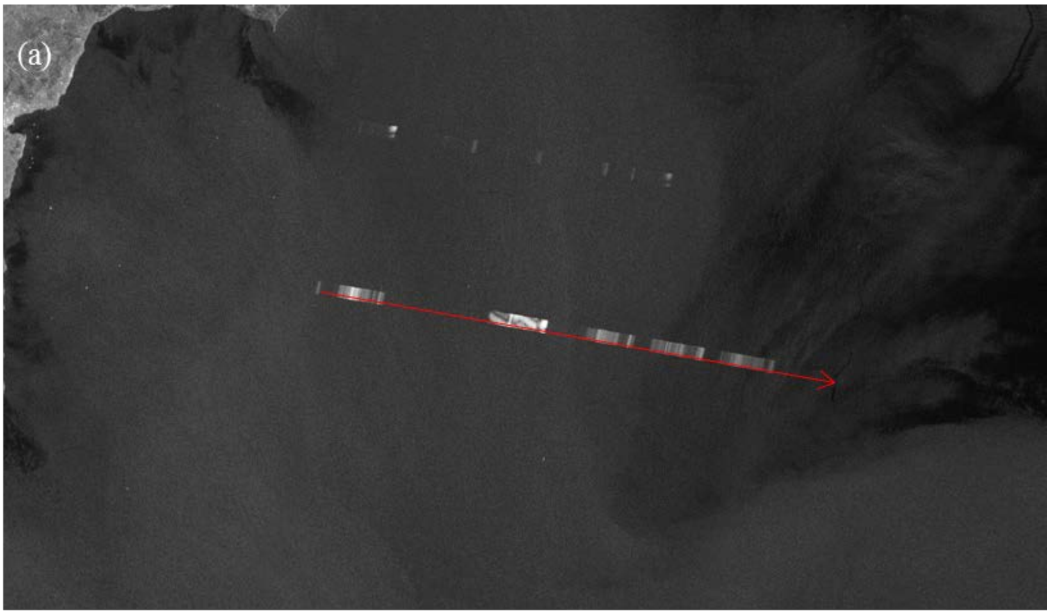

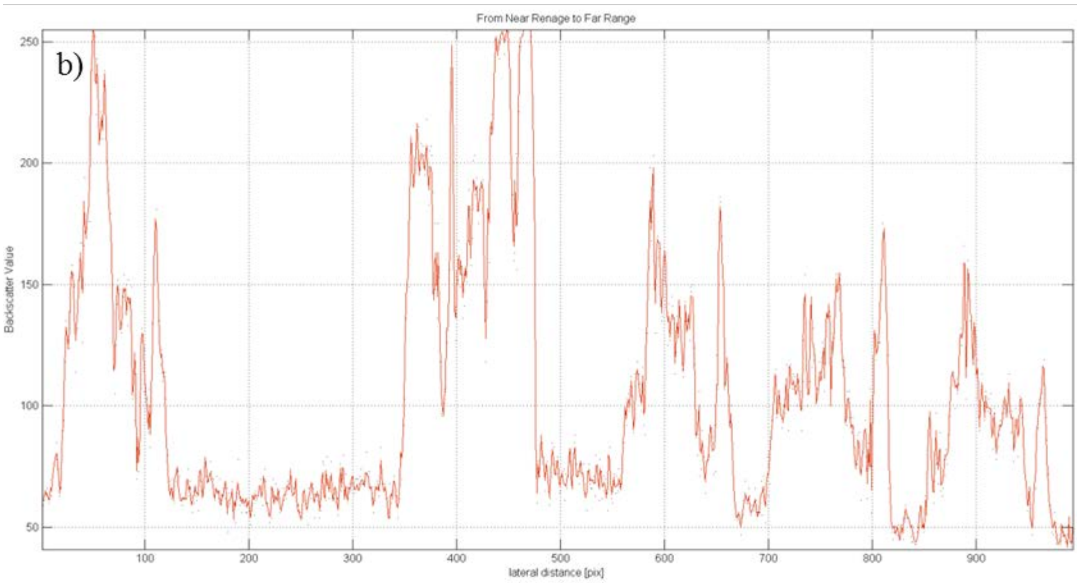

Fig 2.21: Example of artefact on an excerpt from an ENVISAT ASAR WideSwath Mode, HH polarized image acquired on 30th of August 2011 at 08:22:22 over Baltic Sea near east coast of Bulgaria. (CleanSeaNet Image ID: 11978, ENVISAT image © ESA/EMSA 2012).

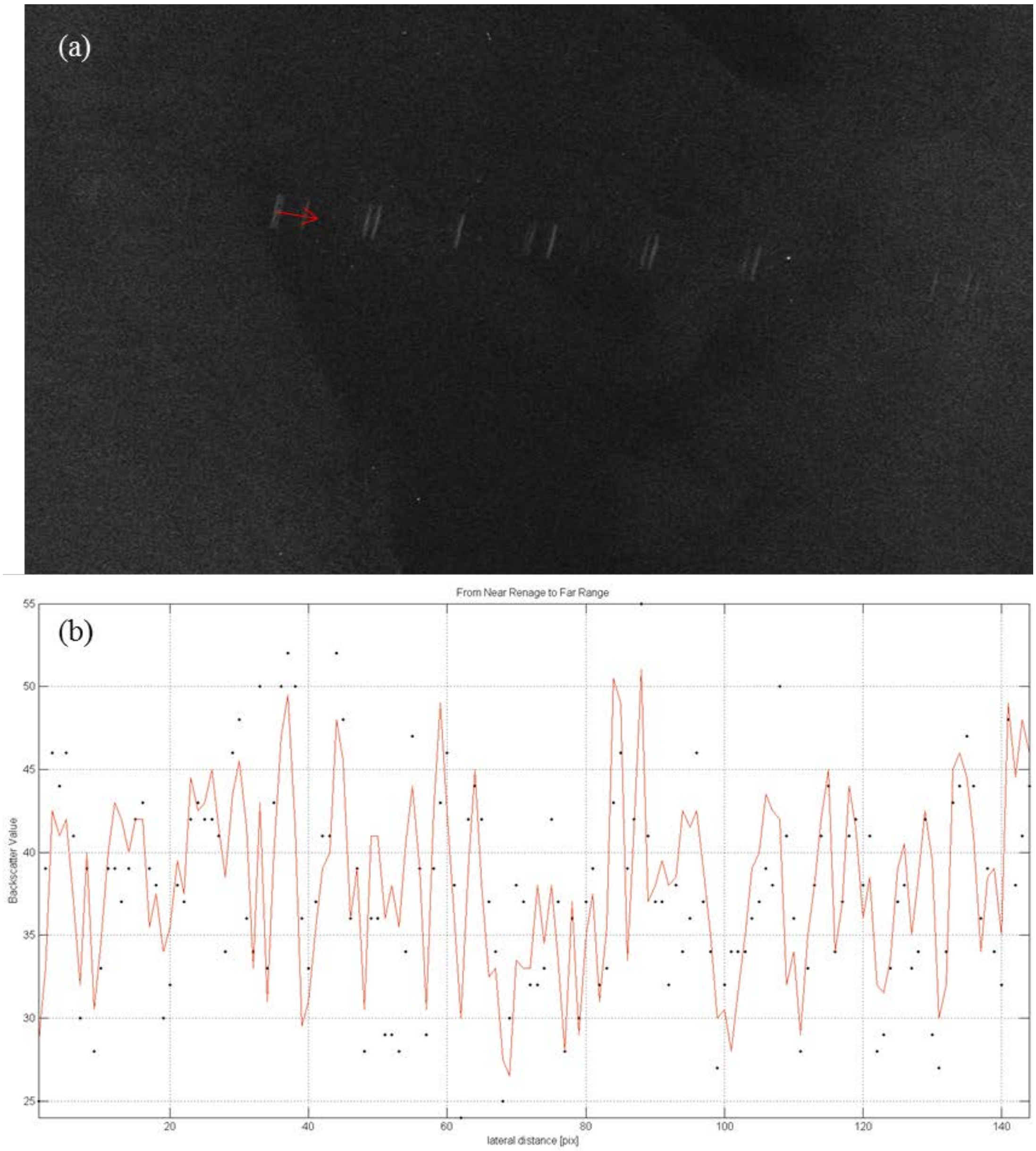

Fig 2.22: Example of artefacts on an excerpt from an RADARSAT-2 SAR ScanSARWide Beam image acquired on 22nd of May 2012 at 06:23:56 over Bay of Biscay near northern coast of Spain. (CleanSeaNet Image ID: 22458, RADARSAT-2 image © CSA/MDA/EMSA 2012).

Missing Data

Most of the current SAR instruments [e.g., ENVISAT-ASAR, Radarsat-2, and Cosmo-SkyMed] deliver the number of missing lines and data blocks in the *raw* data used for producing higher level products. TerraSAR-X products contain the value of gap and missing line percentage limits and whether the product percentages are beyond such significance limits. A limited amount of missing raw data may result in a reduced geometric resolution in the final processed products. A larger amount may result in missing data in the processed product. Fig 2.23 shows the effect of missing data and scalloping on an ENVISAT ASAR image. Since such missing data become normally a block of pixels with a value of zero, their occurrence is easy to spot also using automatic tools. When left unnoticed and unmasked, missing data may not only result in missed targets but could also significantly bias the local statistics in the image, leading to false alarm.

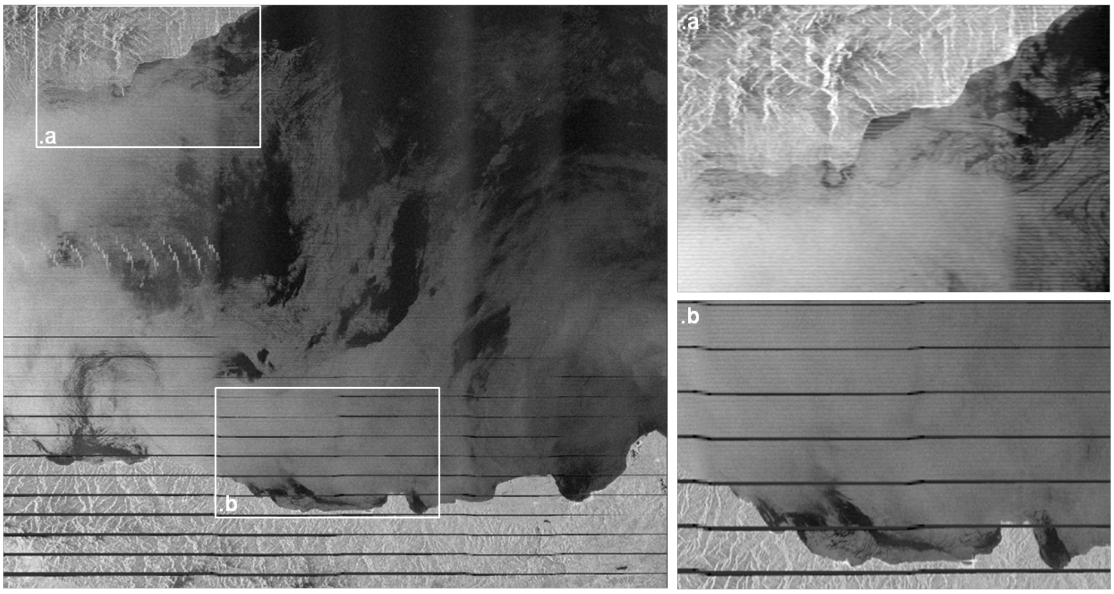

Fig 2.23: ENVISAT ASAR Wide-Swath-Mode (WSM) product acquired on 14th of May 2011 at 07:41:08 showing (a) pronounced scalloping, emissions, and (b) large stripes of missing data (CleanSeaNet Image Id: 6590; © ESA/EMSA 2011).

2.6 OIL SPILL DETECTION APPROACHES FOR SINGEL POLARIZED SAR IMAGE

There are two approaches for oil spill detection from SAR images,

i) Visual image interpretation

ii) Digital image processing

2.6.1 Visual image interpretation

Visual image interpretation is the most popular approach for oil spill detection as it is not complex and under certain circumstances can be easily reproduced, albeit, it mostly depends on the experience of the interpreter. In this approach, interpreters are supposed to be trained and well conversant with the use of image interpretation elements to detect oil spills through image interpretation. At first stage, all the possible candidates of being oil spills are detected on a SAR image. Then a discrimination process is performed to distinguish oil spills from look-alikes. Some look-alikes are quite easy to classify as these have characteristic shapes and configurations completely different from the oil spill spots (Berkke and Solberg, 2005a). However, a first sight analysis is not sufficient in complicated cases. The discrimination becomes particularly difficult in the presence of natural oil slicks or areas with low wind speeds. In this situation, a more detailed analysis is necessary, where several factors have to be taken into account. The most important are: the wind conditions, the period of the year, the shape analysis, the slick size and the general morphology/bathymetry of the observed area.

The knowledge of wind conditions is crucial, as low wind speeds of 2-3 m/sec result in many dark formations while with wind speeds above 8-10 m/sec, the oil cannot be detected (Elachi, 1987; Espedal and Wahl, 1999; Gade *et al.*, 2000; Singha *et al.*, 2013b). The period of the year is useful to discriminate natural slicks (i.e. algae bloom) and grease ice on summer, while the slick size is considered to exclude low wind areas or even large natural slicks. The general morphology of the observed area is crucial to distinguish dark formations caused by suddenly change of the wind conditions (i.e. the passage form a region in which the wind is not present to another in which wind is blowing). In many cases, the dark formations are the result of the sheltering action due to area topography (e.g, areas close to the land, high submarine mountains, and oil platforms). More complicated cases are the areas containing fronts, which are boundaries between water masses with dissimilar properties, like two water masses of different densities (due to different temperatures or/and salinities). In these cases, dark formations can have extremely high combinations of shapes and sizes (Topouzelis *et al.,* 2008a).

Shape analysis is very useful for discriminating oil spills from look-alikes spots, mainly natural phenomena, since the two categories have specific characteristics. Shape analysis takes into consideration the characteristics of the border, the tails and the roundness or elongedness of the dark formations (Berkke and Solberg 2005a, 2005b). The borders of man-made spills are usually very well defined, with a sharp step in the backscattering values between the spilled region and the surrounding region. On the contrary, natural phenomena usually have more structured borders. However, old oil spills are having a more complex border structure than a fresh one. The tails can be thin, straight or slightly curved for oil spills, while look-alikes present a “natural” behavior in the image with smoother turnings. Look-alikes can be some kilometers in length probably due to wind sheltering action and are usually connected with natural structures like eddies (Espedal *et al.,* 1998; Del Frate *et al.,* 2000).

Roundness of dark formations is essential for identifying fresh spills, elongated with or without curves. Usually man made spills are elongated, while many natural phenomena have round shaped. Roundness cannot really be measured, therefore is generally based on the experience of the photo-interpreter. In general, it can thus be assumed that dark formations can be usually detected by image interpreters as potential oil spills according to the following criteria (Berkke and Solberg, 2005a, 2005b),

• Dark homogeneous spots in a uniform windy area

• Linear dark areas, not extremely large, with abrupt turns i.e. most likely abrupt turns due to wind directions change or surface current. Natural slicks in these conditions tend to disappear.

Dark formations are usually classified by image interpreters as look-alikes according to the following criteria,

• Low wind areas

• Coastal zones due to wind sheltering

• Elongated dark areas with smooth turnings in spiral shape.

Thus, in visual image interpretation, the experience of the interpreter and especially his/her ability to apprehend the nature of the image manifestations becomes a critical factor (Indregard *et al.,* 2004). Therefore, efforts are being made to develop digital image processing methods which may detect and identify dark formations as oil spills in an automatic or in a semi-automatic way (Topouzelis 2008b).

2.6.2 Digital image processing

As discussed in the previous section at operational level, it is almost impossible to detect oil spill by visual image interpretation approach due to large amount of data. Therefore, digital processing of SAR images has been introduced. Several published papers on development of oil spill detection algorithms for SAR images (e.g. Espedal *et al*, 1999; Solberg *et al*, 1997, 1999; Del Frate *et al.*, 2000; Fiscella *et al.*, 2000; Marghany *et al.*, 2001; Topouzelis *et al.*, 2002, 2009; Keramitsoglou *et al.*, 2005; Singha *et al.*, 2013a; 2013b) describe a structure comparable with the one in Fig 2.24

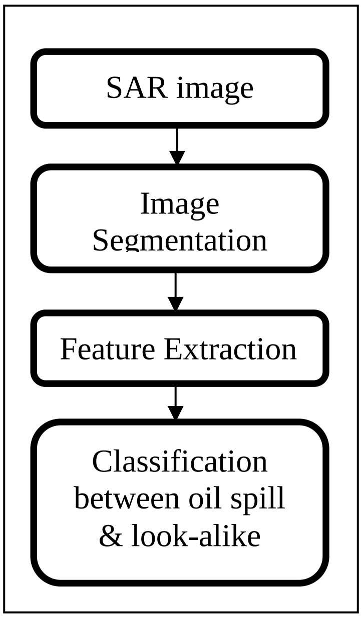

Fig 2.24: Flowchart for sequence of steps for oil spill detection using digital image processing technique.

As oil spills are characterized by low backscattering levels, these suggest the use of thresholding or other complex dark spot segmentation techniques as a first step of oil spill detection techniques using digital image processing (Shu *et al.*, 2010a; Shu, 2010b). From the segmented dark spot image, feature extraction is used to compute features for each dark spot whether the spot belongs to oil spill or any other oceanographic and metrological phenomenon. This feature extracted data are then fed to classifier for classification between oil spill and look-alike spots.

2.6.2.1 Image segmentation

Oil spills are characterized by low backscattering level suggesting the use of thresholding for dark spot segmentation. It is the most significant step in digital image processing approach. If any potential dark spot is missed in this step then it may not be classified in further stages (Huang *et al.*, 2005; Brekke, 2007).

Many basic and advanced image segmentation algorithms have been used by the researchers. An early attempt of segmentation of ERS-1 SAR images has been described in Skoelv *et al*. (1993). The algorithm simply looks for bimodal histograms in a window size of N×N pixels. N was set to 25 pixels.

In Solberg *et al*. (1999), the detection of dark spots was based on adaptive thresholding. This thresholding is based on an estimate of the typical backscatter level in a large window. The adaptive threshold is set to *k* dB below the estimated local mean backscatter level. The window (100 ×100 of size pixels) is moved across the image in small steps to threshold all pixels in the scene. Wind data (the wind level) is used to determine *k*. The relationship between wind level and *k* value is indirectly proportionate. The wind level is set manually as one of four categories: low, low/medium, medium, or high wind. This dark spot detection procedure may not always define the correct border between the oil slick and the surrounding sea when the surroundings are heterogeneous (particularly in low-wind conditions a number of look-alikes are present). Parts of the surroundings are sometimes included in the detected spot. A clustering step is therefore used to avoid this. After spot detection, each spot is clustered into two clusters. The idea is that if the spot includes part of its surroundings, the oil slick will consist of the darkest cluster. If the two clusters are sufficiently separated and the darkest cluster is sufficiently large compared to the brightest, the darkest cluster used as the dark spot; otherwise, the original spot is kept.

A comparison of regular statistical classifier and Support Vector Machine (SVM) was reported by Brekke and Solberg (2008) using 103 ENVISAT ASAR WSM images. They have also developed an automated confidence estimator to tune the tread off between true and false positive alarms as occurrence of oil spill events are very rare compered to 'look alikes'.

Fiscella *et al.* (2000) used an automatic approach for dark spot detection. This automatic procedure, first masks the land areas, then selects the dark regions with a NRCS (Normalized Radar Cross Section) lower than one half of the average NRCS for the sea area in the image. It then rejects the selected areas that are too small or too large. Very small regions are rejected because these slicks are not significant from the coast guard point of view, and the very large ones are rejected because these are probably areas with no wind. Remaining selected as potential dark spot.

Del Frate *et al.* (2000) applied a dedicated oil spill processing and analysis tool based on edge detection. Once defined, the region of interest by the user, the tool analyses the overall backscattering of the region and produces a histogram. Typically, histograms in the presence of a dark region contain two peaks; the lower peak is located around the mean backscattering value of the dark object, while the taller peak is located around the mean value of the background. The local minimum value between the two peaks is used for the segmentation of the image. For this purpose, the darkest pixel in the region is selected as the starting point for the region growing segmentation algorithm. The region grows until the neighbouring pixels have a value greater than the threshold value (i.e., the local minimum previously calculated). This method allows defining the border around the dark region.

To allow dealing with mixed surface-cover classes and unsharp boundaries among regions, Barni *et al.* (1995) proposed an algorithm based on fuzzy clustering. A membership function μA(x) is assigned to each pixel x, which measures how much the pixel belongs to a set A. The fuzzy c-means (FCM) algorithm is applied, and a pyramid structure is used in finding the membership values. Uncertain pixels are tested in the lower pyramid level. Neighboring regions are identified, and a Sobel operator is used to enhance the main edges of the original filtered image. Regions, whose common border does not have a high enough percentage of large gradient points, are merged together. One difficulty with fuzzy clustering is to find out the optimum number of clusters.

Derrode *et al.* (2007) implemented a vector Hidden Markov Chain (HMC) in order to segment the dark spot on ERS-2 SAR and ENVSAT ASAR images. By considering that a film has a specific impact on the ocean wave spectrum and by taking into account the specificity of SAR images, authors developed and adapted the model to a multiscale description of the original image. It yields an unsupervised segmentation method that takes into account the different states of the sea surface through its wave spectrum. Results were satisfactory in terms of segmentation accuracy; however, the stationarity assumption of the Markov chain model was a limitation for the analysis of full size radar images in an operational and real time context.

Recent work has demonstrated that Neural Networks (NNs) represent an efficient tool for modeling a variety of nonlinear discriminant problems. Neural networks may be viewed as a mathematical model composed of several nonlinear computational elements called neurons, operating in parallel and massively connected by links characterized by different weights (Bishop 1995; Ziemke 1996; Kanellopoulos and Wilkinson, 1997; Del Frate *et al.,* 2000; Kavzoglu and Mather, 2003). Neural networks have been successfully used for remote sensing applications (Bishop 1995, Arora and Foody, 1997; Del Frate *et al*., 2000; Kavzoglu and Mather, 2003). Also, several studies in remote sensing data analysis using neural networks have been presented by Kanellopoulos *et al*., (1997) and Atkinson and Tatnall, 1997.

Topouzelis *et al.* (2002) used neural network for dark spot detection. A fully connected feed forward neural network with 1 (input): 3 (hidden):1 (output) architecture, which produced the highest accuracy in dark spot detection was selected. The neural network was trained with the backpropagation algorithm. For each test data, a binary image containing the dark area and the surrounding sea was produced. I this case the dark spot either belong to oil spill or look-alike. The binary image was subsequently vectorised to extract a number of features.

Topouzelis *et al.* (2007) concluded that a simple fully connected feed-forward neural network with 1: 3: 1 topology with learning rate 0.5, momentum factor 0.9 and backpropagation training algorithm had given 94 % overall accuracy for dark spot detection in a SAR image. In this study, two neural networks were used for image segmentation purpose and as well as classification purpose.

Topouzelis *et al.* (2008a) have also suggested that in high special resolution imagery dark spot detection using thresholding may fail due to nonlinear behavior of the pixel value contained in the dark spot and the area around it. Therefore, they applied and compared two feed forward neural networks, i.e. Multilayer Perceptron (MLP) and Radial Basis Function (RBF) networks, to detect dark spot in high resolution satellite SAR images. MLP topology performs significantly better than the RBF topology for segmenting the dark spot in a SAR image.

Karantzalos and Argialas (2008) also applied level set segmentation method to dark spot detection. In their method, a combination of anisotropic diffusion filtering and morphological levelling filtering is first used to reduce speckle noises to some degree. The Chan-Vese level set segmentation model is then applied to segment an image into dark spots and background.

Li and Li (2010) developed a new method for automated detection of dark spots from SAR intensity imagery, which combines a marked point process, the Bayesian inference and the Markov chain Monte Carlo (MCMC) technique. In this method, a marked point process defined by density function with respect to Poisson measure is used to characterize the locations of oil spills and statistical distribution of intensities for the corresponding pixels in the SAR data. The reversible jump Markov chain Monte Carlo (RJMCMC) algorithm is used to simulate the process from the density function. The optimal locations of oil spills are found by maximizing the density function. The proposed method is robust in order to deal with speckle noises and achieved promising results in their experiment. However, the nature of the method is still a two-phase classification method. It has the common problem that any two-phase classification method will have on dark spot detection (see Section 3.1). Also, the RJMCMC simulation is time-consuming. As reported in Li and Li's experiment, detection in a single SAR image with a dimension of 512×512 pixels spend 20 minutes under the MATLAB platform.

Shu *et al.* (2010) have proposed a dark spot detection technique with spatial density thresholding. Spatial density feature was used to discriminate between dark spot and the background particularly to enhance the separability between two classes. Pixels with intensity values below the threshold are regarded as potential dark-spot pixels while the others are potential background pixels. Second, the density of potential background pixels is estimated using kernel density estimation within each window. Pixels with densities below a certain threshold are the real dark-spot pixels. Third, an area threshold and a contrast threshold are used to eliminate any remaining false targets. In the last step, the individual detection results are mosaicked to produce the final result.

Even though a variety of methods have been applied for dark spot detection, the common goal is to detect all suspicious slicks and to preserve the slick shapes in a SAR image. The latter is of most importance for the success of discriminating oil spills from look-alikes, which requires the use of feature extraction. As seen from the review, most of previous methods detect dark spots by utilizing the intensity feature. However, the effect of speckle noises and various contrasts between dark spots and the background bring great difficulties to the detection in the intensity domain. To overcome the problem, multi-scale approaches decompose image into multi-resolution layers and implement the detections at different scales. However, how to identify the proper detection scales and how to combine the detections on different scales are unsolved issues. Up to now, none of existing methods is able to detect dark spots effectively and efficiently. In most cases, speed is sacrificed for robustness or vice versa in a few other cases.

2.6.2.2 Feature extraction

There are a certain number of characteristics that are considered an oil spill signature. This section introduces some feature extraction parameters which are useful in discriminating between an oil spill and other phenomena that cause backscattering attenuation.

From the segmented image, a number of features need to be extracted for each slick. Depending only upon the intensity based statistical parameters it almost impossible to differentiate between oil spill and look-alike spot (Solberg and Volden, 1997; Brekke and Solberg, 2005b). This is the reason why so many studies applied this kind of features. Table 2.4 provides a list of features adopted in various studies on oil spill detection using SAR image.

The individual features can typically be categorised into following classes (Brekke and Solberg, 2005):

Geometry and shape of segmented region

Geometry and shape features (Feature # 1, 2, 3, 4 in Table 4) have been applied in most of the studies. If the oil slick is a fresh oil spill released from a moving ship (a tanker cleaning its tank), *elongatedness* appears to be appropriate. It is expressed as a ratio between the width and length of the slick. Among the shape features, the perimeter and the area of the object may also be considered. These types of features were common for various types of algorithms mentioned in Table 2.3.

Backscatter level of the spot and its surrounding

Several researchers have shown that some statistical parameters such as mean and standard deviation related the intensity values of pixels are useful feature. In Del Frate *et al.,* (2000), it was shown that the features related to the gradient of the backscattering value from background to slick provided the most valuable information lead to classification purpose. Due to the heavy effect of wind speed, the *background standard deviation* (Feature # 9 in Table 2.4) was also shown to be an important discriminate parameter.

Spot contextual features

Spot contextual features depend on weather conditions at the time of image acquisition, as the speed of the wind, and also on the distance of oil spill location from possible oil spill source such as ships or oil rigs on offshore. In Espedal *et al.* (1999), the distance to bright spot (ships on SAR images) and to pollution source (i.e. oil platforms) was used. In Solberg *et al.* (1999) also, improved results were obtained by classifying dark spots in the context of their surrounding and weather information.

Texture

In contradiction to pixel intensity itself, texture provides information about spatial correlation among the neighbouring pixels. Power-to-mean ratio (Feature # 20 in Table 2.4) of the slick and surroundings was used in Solberg *et al.* (1999) as a measure of homogeneity.

Table 2.4 Set of feature parameters used in various studies (Del Frate *et al.*, 2000; Fiscella *et al.*, 2000; Topouzelis *et al.*, 2002; Marghany *et al.*, 2001; Espedal *et al.*, 1999; Solberg *et al.*, 1999)

#Features	Del Frate *et al.*, 2000	Fiscella *et al.*, 2000	Topouzelis *et al.*, 2002	Marghany *et al.*, 2001	Espedal *et al.*, 1999	Solberg *et al.*, 1999
1.Area	✓	✓	✓		✓	✓
2.Perimeter	✓	✓				
3.Perimeter to Area Ratio(P/A)		✓				
4.Slick Width						✓
5.Slick complexity	✓	✓ (Form Factor)	✓ (Asymmetry)			✓ (First Invariant Planar Moment)
6.Length to Width Ratio			✓			
7.Spreading	✓					
8.Object/dark area standard deviation	✓	✓	✓			
9.Background Standard Deviation	✓	✓	✓			
10.Max contrast (between object and background)	✓			✓	✓	✓
11.Mean contrast (between object and background	✓					
12.Mean Gradient	✓	✓	✓		✓	✓
13.Gradient Standard Deviation	✓					
14.Slick Radar Backscattering		✓	✓		✓	
15.Outside Slick Radar Backscattering		✓				
16.Standard Deviation Ratio Inside		✓				
17.Intensity Standard Deviation Ratio Outside		✓				

18.ISRI to ISRO Ratio		✓				
19.Power to Mean Ratio			✓			✓
20.Local area contrast ratio		✓				
21.Homogeneity of surroundings				✓		✓
22.Entropy				✓		
23.Energy				✓		
24.Correlation				✓		
25.Distance to a Point Source						✓
26.Number of Detected Spot in the Scene						✓
27.Correlation				✓		
28.Close to Big Areas				✓		
29.Close to Land				✓		
30.Close to Fractal Object				✓		
31.Average NRCS inside dark area		✓				
32.Average NRCS in limited area outside dark area		✓				
33.Gradient of the NRCS across the dark area perimeter		✓				

The data extracted via feature extraction are input to a classification algorithm for detection of oil spill and look-alike, and their discrimination.

If the features have high discriminatory power, the classification problem will become easy and any classifier may produce accurate results. However, there appears to be no systematic study conducted to identify a set of feature extraction measures that may become standards for input to a classification algorithm,

2.6.2.3 Dark-spot classification

Since, a number of look-alike phenomena can create dark spots in a SAR image; the purpose of the classifier is to distinguish oil spills from the other ‘look-alike’ dark spots.

An approach based on multilayer perception (MLP) neural network with two hidden layers (using 11:8:8:1 topology), was proposed and implemented on SAR images (Del Frate *et al.*, 2000). The input to the neural network was a set of features extracted and considered as a feature vector. The input data was scaled between 0.01 and 0.99, and the network was trained using the back propagation algorithm. The results showed that 18% of real oil spills were misclassified as look-alike, and 10% of look-alikes were misclassified as oil spill, with an overall rate of misclassified pixels as 14%. Real oil spill spots misclassified as look-alike spots can be considered as more serious than look-alike spots misclassified as oil spill spot.

Fiscella *et al.* (2000) adopted two classification procedures; one based on Mahalanobis classifier and another based on compound probability classifier. Methodology (compound probability classifier) assumes **x** as the feature vector for the unknown input, and let $\mathbf{m}_1$, $\mathbf{m}_2$ be the two classes: oil spill and look-alike. Then the error in matching $\mathbf{x}$ against $\mathbf{m}_j$ is given as $\| \mathbf{x} - \mathbf{m}_j \|$ (i.e., the Euclidean distance). A minimum-error classifier computes $\| \mathbf{x} - \mathbf{m}_j \|$ for j= 1 to 2 and chooses the class for which this error is minimum.

The accuracy of the classifier depends on how accurately the input patterns resemble the templates and how strong the features are to distinguish various classes, or in other words the within group variability is smaller than the between groups variability. Some of the limitations of simple minimum-Euclidean distance classifiers can be overcome by using the Mahalanobis distance r_j^2 as,

$$r_j^2 = (\mathrm{x} - \mathrm{m_j})^T \, C^{-1} \, (\mathrm{x} - \mathrm{m_j}) \tag{2.8}$$

where **C** is the variance covariance matrix for **x**

The probability p an individual belongs to an oil spill class is estimated knowing the Mahalanobis distances of a pixel l from the two classes (Kendal *et al*. 1983). The percentage of the total data correctly classified, with p>2/3, was found as 78% and, with p>1/2, as 83%.

Another method was based on compound probability classifier. In this case, n features x_i are considered (i = 1, 2, ..., n), to estimate the probability distribution functions p_i (x_i) for oil spill and q_i (x_i) for look-alike classes. Then, the probability p that a dark area belongs to oil spill class can be found as,

$$\mathrm{p} = \frac{1}{1 + \pi qi(xi) / pi(xi)} \tag{2.9}$$

This method yielded approximately same result as was obtained from Mahalanobish classifier.

Solberg *et al.* (1999) proposed a statistical modeling with a rule based approach. The probabilities assigned using Gaussian density function and derived from a signature database of 7,051 dark formations containing 71 oil spills and 6,980 look-alikes. These dark formations were extracted from 84 ERS SAR images, from which 36 did not contain any oil spills. The method correctly classified 94% (67 out of 71) of oil spills and 99% (6,905 out of 6,980) of look-alikes with statistical modeling coupled with a rule based classifier.

In a recent study by Solberg *et al,.* (2007), an updated version (previous study uses less number of feature extraction parameters) of the method was presented for Radarsat and Envisat images. The training dataset consisted from 56 ENVSAT WSM ASAR images and 71 Radarsat SAR images while the reported test data set consisted of 27 Envisat images containing 37 oil spills and 12110 look-alikes. The method had an accuracy of 78% in oil spill classification (29 out of 37) and of 99% in look-alike classification (12,033 out of 12,110).

Keramitsoglou *et al.* (2006) estimated the probability of a dark formation to be oil spill using an artificial intelligence fuzzy modeling system. The method was developed on 9 ERS-1/2 SAR images and tested on 26 images. Five features were used as inputs, in general different from those used before. The method responded perfectly on 23 of 26 images, resulting in an overall performance of 88%.

Combination of two neural networks was successfully used for dark formation detection, and oil spill and look-alike discrimination using high resolution SAR images by Topouzelis *et al.* (2002). The second neural network was designed on the basis of 10 features (Table 2.3). The neural network was trained with the backpropagation training algorithm, using the training set of 45 look-alikes and 35 oil spills. The test set was then classified using the set of weights previously discovered (at the time of training). The results showed that from the 34 oil spills contained in the test set, only three were misclassified to look-alikes, the accuracy of 91%, and from the 45 look-alikes, 6 were misclassified as oil spills, i.e. 87% accuracy.

A recent study by Topouzelis *et al.* (2009), investigates the potential of genetic algorithm for oil spill detection. As genetic algorithms are successful in discovering an optimal or near-optimal solution amongst a number of possible solutions, it was used for finding appropriate set of feature extraction parameters. The proposed method eas unique, as it searches though a large number of combinations derived from the 25 features (Stathakis *et al.,* 2006; Topouzelis *et al.,* 2009;). The results show that a combination of 10 features yields the most accurate results. Based on a dataset consisting of 69 oil spills and 90 lookalikes, classification accuracies of 85.3% for oil spills and in 84.4% for look-alikes are achieved.

Comparison between different classifiers in terms of their classification accuracies is very complicated. Mainly because oil spill detection approaches use different data sets, have different dark spot detection techniques; extract arbitrary number of features and in the end use of different classification methodology (Topouzelis, 2008b). Therefore, the reported classification accuracies cannot be directly compared. Although a legitimate comparison between algorithms derived and human derived result can be carried out on a same dataset. In this thesis comparision and benchmarking were carried out for proposed algorithms and human operator.

Another issue with high importance for the detection methodologies is the computational time. Unfortunately, there are no sufficient data in the literature to compare the methodologies in terms of necessary time from image acquisition to final classification between oil spill and look-alike spots. This comparison should be made under the same data in order to check not only the time frame, but also the accuracy and efficiency of different methodology. Nevertheless, it could be point out that as long as the methodologies have been developed, the most time consuming step for analyzing a new image is the dark formation detection step (Mercier *et al.*, 2006; Topouzelis, 2008b). Once the dark formations have been detected, the feature calculation step and the classification step need some seconds to complete their actions.

2.7 OIL SPILL DETECTION APPROACHES USING MULTI-POLARIZED SAR IMAGE

Conventionally, oil spill detection methodologies based on single polarization SAR images. As discussed in the previous sections, dark spots related to oil spills can be discriminated from 'look-alikes' based on a set of features describing the contrast, shape, homogeneity and surroundings of the slick. Satisfactory overall classification accuracy is reported for single-polarization oil spill detection, but in certain cases the oil slicks cannot be discriminated from look-alikes due to algae and sea ice. In the recent years, a number of studies have shown that polarimetric SAR can improve the detection capability and discrimination between oil slicks and 'look-alikes' caused by biogenic films. New polarimetric approaches, based on dual-pol and quad-pol SAR data, have been developed for different environmental remote sensing applications. In the context of oil spill detection discrimination, polarimetric models and analysis tools have recently been proposed, showing that polarimetric SAR data can be successfully employed to both observe oil slicks and distinguishing them from weak-damping look-alikes (Migliaccio et al., 2007, 2009a,b; Nunziata et al., 2008, 2011, 2013; Velotto et al., 2011; Zhang et al., 2011). All these proposed approaches based on a common theoretical background which is, under low-to-moderate wind conditions (3-12 m/s) and at intermediate incidence angles (20^o to 35^o), both the spill free ocean surface and the surface effected by algae (biogenic look-alikes) produce bragg scattering while, on the other hand oil-covered sea surface, a completely different, i.e. non-Bragg, scattering mechanism is in place (Nunziata et al., 2013). Oil spill detection using polarimetric data developed using theoretical and physical based approach and capable to measure the departure from Bragg scattering (Migliaccio et al., 2007, 2009a,b, 2011a,b, 2012; Nunziata et al., 2008, 2011, 2013; Skrunes et al 2012; Velotto et al., 2011). It has been shown that this departure can be effectively measured through some polarimetric features, discussed below.

Several features computed from dual-pol or quad-pol data have been proposed. These include both quad-pol polarimetric features like entropy and anisotropy, mean scattering angle, polarimetric span, conformity coefficient, as well as the dual-pol features standard deviation of the copolarized phase difference (CPD) and the copolarized correlation coefficient. As dual-pol SAR imagery is now available on a regular basis from Cosmo Skymed and TerraSAR-X, and quad-pol data from RADARSAT-2, oil spill detection using polarimetric SAR can now be implemented for operational services. Although, there are some recent studies claiming that multi-polarization (dual and quad pol) data can give better discrimination between oil spills and their surroundings (Migliaccio *et al.,* 2007; 2009; Nunziata et al., 2008, 2011, 2013; Velotto *et al.*, 2012) the difference in classification accuracy between single polarimetric and multi-polarimetric data has not yet been studied on a large dataset.

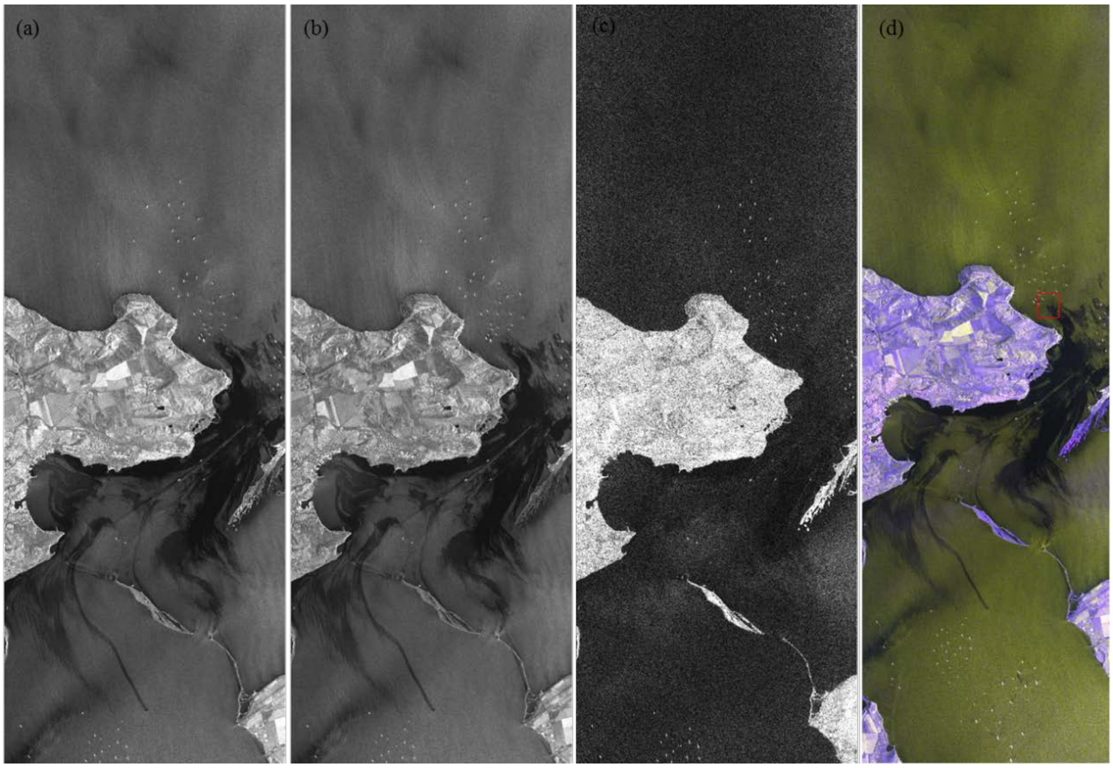

Fig 2.25: TerraSAR-X HH polarised (a), VV polarised (b) and HH-VVimage(c), and (d) shows an color coded image obtained by Red=abs(HH); Green=abs(VV); Blue = abs (HH-VV). (TerraSAR-X image © German Aerospace Centre, DLR 2012, Source: Velotto *et. al.*, 2011).

A fully polarimetric SAR sensor captures four combinations of copolarized (VV and HH) or cross-polarized (VH and HV) signals in a 2 × 2 scattering matrix of complex elements with amplitude $|S_{XY}|$ and phase ψ_{XY}.

$$S = \begin{bmatrix} S_{VV} & S_{VH} \\ S_{HV} & S_{HH} \end{bmatrix} \tag{2.10}$$

At large incidence angles ($\theta = 20^0\ to\ 60^0$) the scattering mechanism at the sea surface is often simulated as Bragg scattering (Solberg 2012). The received backscatter is mainly caused by the spectral component of the surface which is in resonance with the radar wavelength and the angle of incidence. If we assume a Bragg-scattering model, the scattering matrix of the ocean surface may be written as (Hanjsek et al., 2003 in Solberg 2012)

$$S = \begin{bmatrix} S_{VV} & S_{VH} \\ S_{HV} & S_{HH} \end{bmatrix} = m_s \begin{bmatrix} B_{VV}(\epsilon, \theta) & 0 \\ 0 & B_{HH}(\epsilon, \theta) \end{bmatrix} \tag{2.11}$$

where the coefficient m_s is the backscatter amplitude and ϵ is the complex permittivity. This is related to the roughness condition of the sea surface. B_{HH} and B_{VV} denote the Bragg scattering coefficients.

$$B_{HH} = \frac{Cos\ \theta - \sqrt{\epsilon - Sin^2\theta}}{Cos\ \theta + \sqrt{\epsilon - Sin^2\theta}} \tag{2.12}$$

$$B_{VV} = \frac{(\varepsilon - 1)(Sin^2\theta - \epsilon(1 + Sin^2\theta))}{(\epsilon Cos\theta + \sqrt{\epsilon - Sin^2\theta})^2} \tag{2.13}$$

One of the main limitations of the Bragg model is the small surface roughness validity range and its saturation of sensitivity to volumetric moisture content (Hanjsek et al., 2003 in Solberg 2012). Another restriction of the Bragg model is its inability to describe depolarization effects, which further reduces its usefulness for interpretation and inversion of data from natural surfaces. Some of the polarimetric features presented below are indicators of the presence and degree of Bragg scattering. While the absolute phases of the received copolarized backscatter are regarded as uniform, the phase difference between the received backscatter E_{HH} and E_{VV} is often similar to the phase difference between S_{HH} and S_{VV}. The phase difference is claimed to be zero for a Bragg scattering model (Guissard 1994). The copolarized phase difference is denoted CPD and is given by

$$CPD = \psi_{HH} - \psi_{VV} \tag{2.14}$$

CPD has a probability distribution (pdf) that depends on the number of looks l and the complex correlation coefficient between HH and VVρ_{CO} (Joughin et al., 1994; Lee et al., 1994). ρ_{CO} is described in Jha *et al.*, 2008. When HH and VV are uncorrelated, the probability distribution of CPD becomes uniformly distributed between (-180, 180), and it will be like a Dirac delta function if HH and VV are highly correlated ($\rho_{CO} = 1$). For 0 <ρ_{CO}<1, the probability distribution of CPD will be Gaussian distributed with mean ψ and standard deviation σ inversely related to ρ_{CO} (Migliaccio *et al.*, 2009).

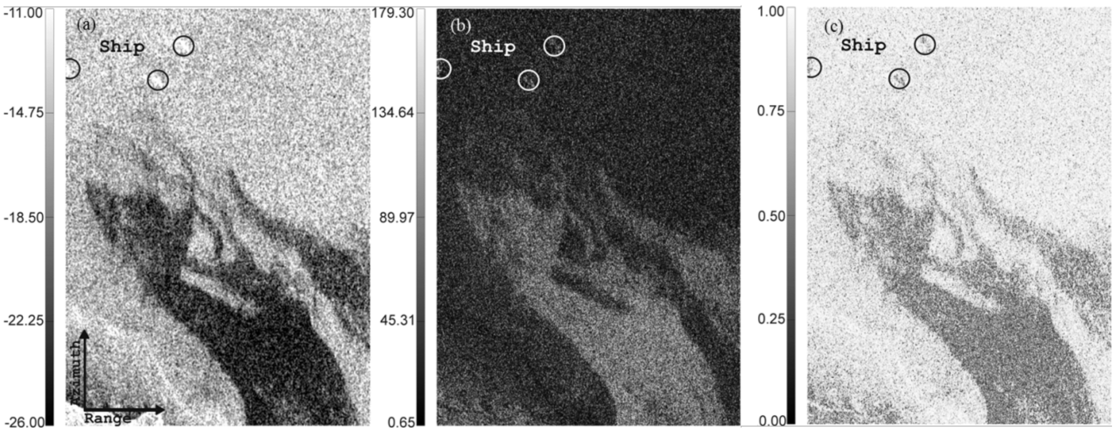

Fig 2.26: Excerpt of the SAR data relevant to the ROI shown in Fig. 2.25d labeled as Oil Spill: (a) VV squared modulus image and (b and c) measured $\hat{\sigma}$ and $\hat{\rho}$ maps obtained by using a 3 × 3 moving window. (a) VV squared modulus image (in decibels). (b) 3 × 3 $\hat{\sigma}$ map (in degrees). (c) 3 × 3 $\hat{\rho}$ map. (TerraSAR-X image © German Aerospace Centre, DLR 2012, Processing : Velotto et al., 2011).

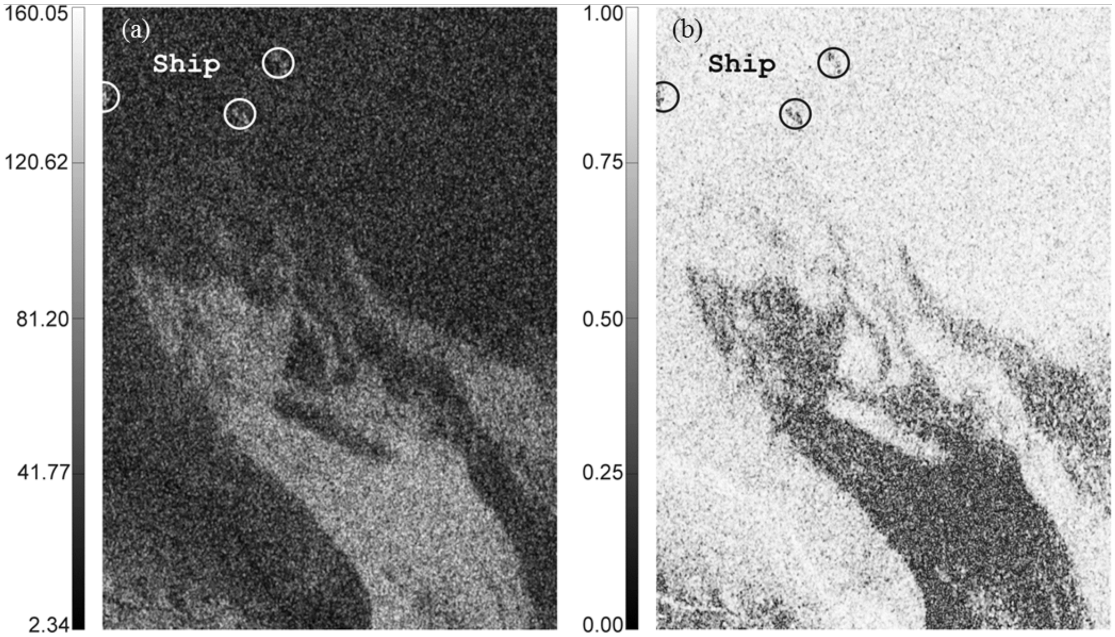

Fig 2.27: Filter output for the ROI labeled as Oil 1 using a 5 × 5 window size: (a) and (b) Measured $\hat{\sigma}$ and $\hat{\rho}$ maps. (a) 5×5 $\hat{\sigma}$ map (in degrees). (b) 5×5 $\hat{\rho}$ map (TerraSAR-X image © German Aerospace Centre, DLR 2012, Processing : Velotto et al., 2011).

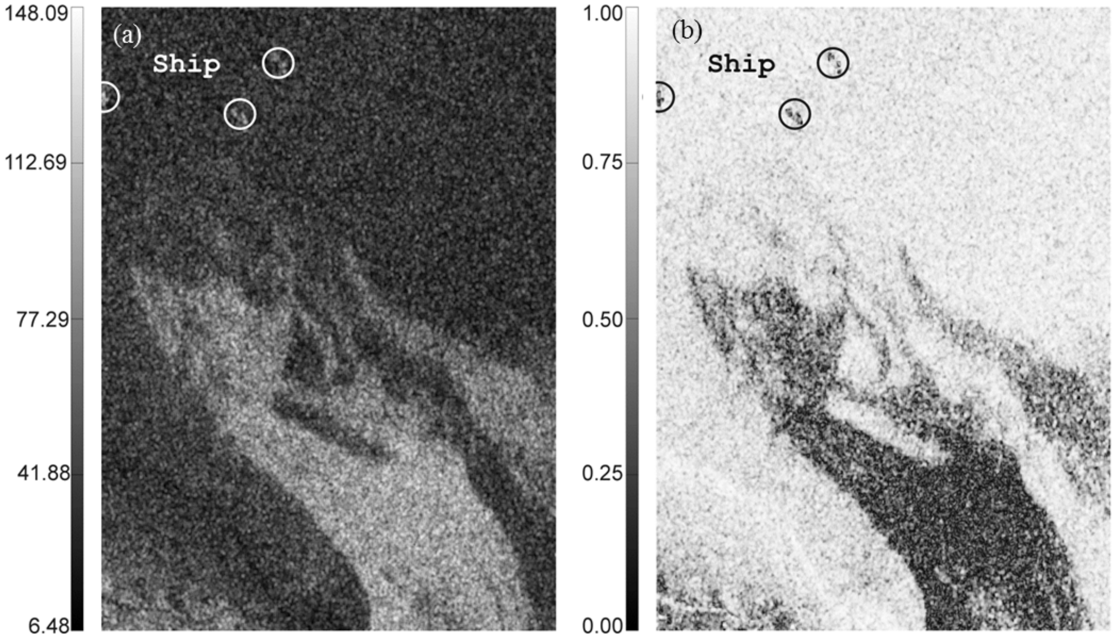

Fig 2.28: Filter output for the ROI labeled as Oil 1 using a 7 × 7 window size: (a) and (b) Measured $\hat{\sigma}$ and $\hat{\rho}$ maps. (a) 7 × 7 $\hat{\sigma}$ map (in degrees). (b) 7 × 7 $\hat{\rho}$ map (TerraSAR-X image © German Aerospace Centre, DLR 2012, Processing : Velotto et al., 2011).

For an oil-free surface, ρ_{CO} will be high and σ will be very small resulting in a narrow distribution. This will also be the case for a biogenic slick if Bragg scattering still is dominant. Oil-covered sea surface, on the other hand, will have low correlation, and σ will be higher resulting a wider distribution (Velotto *et al.*, 2011). Migliaccio *et al.*, 2007 used the standard deviation (σ) of the CDP computed in local windows as an indicator of the presence of an oil slick.

Nunziata *et al.,* (2013) suggests a simple threshold of degree of polarization to distinguish oil-covered from slick-free sea surface. The study shows, if DoP is less than 0.45, the region is characterized by a high level of depolarization and can be clearly associated with oil-covered areas and if DoP is greater than 0.45. This region is subject to negligible depolarization and can be clearly associated with spill free ocean surface.

Table 2.5 enlisted some of the dual pol and quad pol features recently proposed by Migliaccio *et al.*, 2007; 2009; Velotto *et al.*, 2011; Skrunes *et al* 2012; Nunziata *et al.*, 2008, 2011, 2013.

Table 2.5: Polarimetric features used for discriminating oil spill and look-alike.

Polarimetric Mode	Feature	Studied by
Quad Pol	Entropy (H)	Migliaccio *et al.*, 2007 Skrunes *et al.*, 2012
Quad Pol	Anisotropy (A)	Migliaccio *et al.*, 2007 Skrunes *et al.*, 2012
Quad Pol	Polarimetric Span	
Quad Pol	Mean scattering angle	Skrunes *et al.*, 2012
Dual Pol/ Quad Pol	Standard deviation of CPD	Migliaccio *et al.*, 2007 Velotto *et al.,* 2011 Skrunes *et al.*, 2012 Brekke et al., 2014
Dual Pol/ Quad Pol	Amplitude coherence	Velotto *et al.*, 2011
Dual Pol/ Quad Pol	Co-pol ratio	Brekke et al., 2014
Dual Pol/ Quad Pol	Co-pol correlation coefficient (ρ_{CO})	Migliaccio *et al.*, 2009 Skrunes et al 2012
Dual Pol/ Quad Pol	Co-pol power ratio	Skrunes *et al.*, 2012
Quad Pol	Pedestal height	Nunziata *et al.*, 2011
Dual Pol/ Quad Pol	Degree of polarization	Nunziata *et al.*, 2013

The literature review suggests that oil spill detection from remote sensing is mainly based on the use of SAR images (Single and Multi polarized). The methodologies based on polarimetric SAR data have sparingly been used for operational environment and still in there development stage. Proposed methodologies (dual or quad pol) are still need to be tested and calibrated in operational environment and its cost effectiveness is still an issue as dual-pol or quad-pol data are relatively expensive compared to single pol data. Currently, single polarized SAR images extensively used for operational oil spill detection purpose. Detecting oil spill from single polarized SAR images involve three basic steps, segmentation, feature extraction and classification. A number of algorithms and measures have been implemented by several authors, which have produced varied results. One of the main objectives of this study is to standardizing and benchmarking proposed methodologies in order to implement them into operational services like 'CleanSeaNet'. Oil spill detection from multi-polarized SAR images also shows great potential for integrating into operational activity.

Operational oil spill monitoring is currently done using a combination of satellite monitoring and aircraft surveillance (Mainly conducted by EU member states of in case of 'CleanSeaNet' notification). The combined use of satellite-based synthetic aperture radar (SAR) images and aircraft surveillance flights is a cost-effective way to monitor oil spills in large ocean areas and catch the polluters. The flagship operational oil spill monitoring and vessel detection service, 'CleanSeaNet' hosted by European Maritime Safety Agency adapted the similar way to monitor European waters. Next Chapter describes proposed methodologies which are proposed to be used as an in- house assessment tool in order to monitor the operation service quality.

CHAPTER 3

EXPERIMENTAL DATA SET AND METHODOLOIES

3.1 INTRODUCTION

In previous chapters, the concepts for oil spill detection techniques implemented by different researchers were discussed in details. This chapter describes the mathematical background of the two approaches implanted and investigated for operational oil spill detection from SAR imagery along with a detailed description of image preprocessing step which is common to both methodologies. A brief description about the experimental data set (training and testing) has also been described in this chapter. ENVISAT ASAR, RASARSAT-1 and RASARSAT-2 SAR images were provided by European Maritime Safety Agency in framework of 'CleanSeaNet' operation specifically for this research study along with a number of ENVISAT ASAR images provided by ESA under its Category 1 project. Various algorithms under image segmentation, different feature extracted parameters along with its importance and two classification techniques have been discussed. This chapter is organized in four main sections, first two sections describe the per-processing tool developed for various oceanographic applications and detailed description about the experimental datasets. Third section describes different image segmentation techniques followed by description of full spectrum of feature extracted parameters, different feature extracted parameters were also evaluated in order to determine individuals' ability to discriminate between oil spill and look-alike. Last section describes the two classification technique based on ANN and rule based algorithm along with comparison between these two classification techniques. Fig 3.1 shows a consolidated flow chart for the methodology used in this thesis.

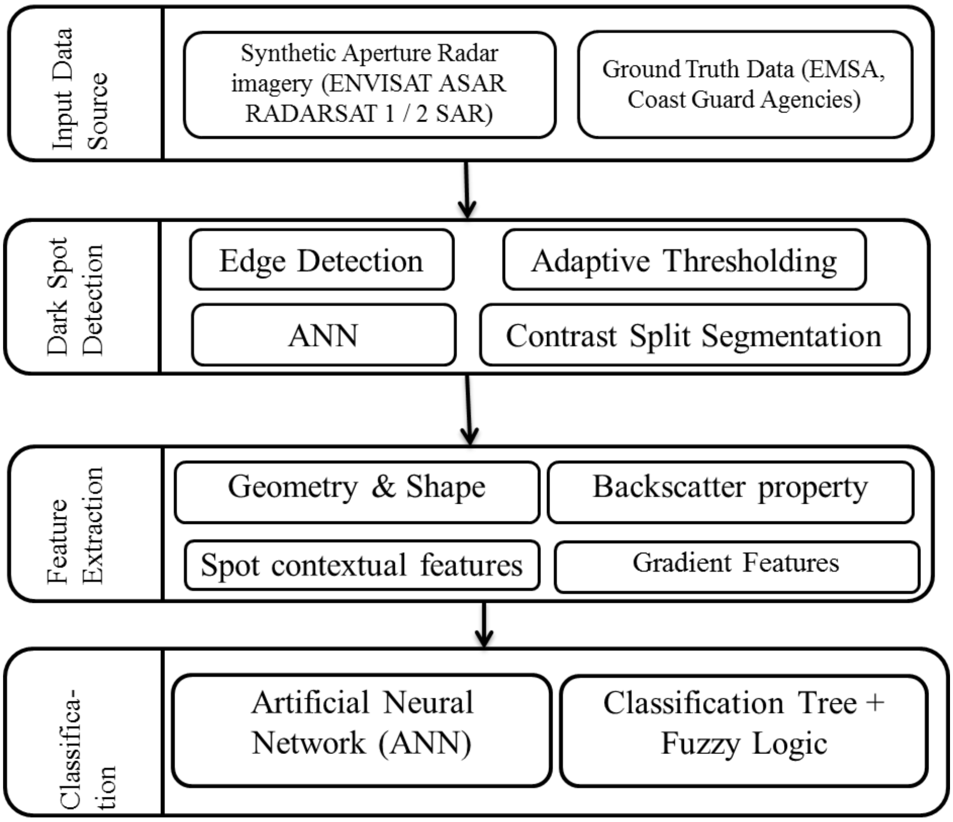

Fig 3.1: A flowchart of the methodology for oil spill detection using ENVISAT ASAR and RADARSAT SAR imagery.

3.2 PRE-PROCESSING TOOL FOR SAR OCEANOGRAPHIC APPLICAITIONS

The "Image Pre-processing Tool" is a MATLAB based application for land-masking and radiometric normalisation of SAR images. The tool is designed in order to overcome the backscattering instability of the sea surface due to the incidence angle increase at far range, typically yielding brightness progressive reduction over the image (Fig 3.2; 3.3). This phenomenon is particularly significant for wide swath modes of operation (Singha *et al.,* 2013a, 2013b, 2013c). This creates the need for time consuming multi resolution processing, i.e. image subdivision into a set of almost homogenous levels. By exploiting the backscattering characteristics of the sea surface, it is possible to produce a flat and homogeneous image background while preserving the spatially confined backscattering transitions due to vessels or oil spills. The radiometric normalisation also enables the transformation of the original image pixel values into an enhanced dynamic range that shall be fully exploited by the following segmentation procedure.

The image preparation procedure also implements land-masking in order to further reduce the computational burden of the subsequent image processing phase, which consists of dark areas segmentation and oil-spill/"look-alike" discrimination. Oil spills on the European waters are observed relatively often. Pollution due accidental and deliberate oil spill from ships and offshore platforms represents a serious threat to the marine and costal environment. Operational oil spill monitoring such as ‘CleanSeaNet’ hosted by European Maritime Safety Agency (EMSA) is currently using SAR based maritime surveillance for oil spill and ship detection. Primarily, conventional wide swath X-band (2.4–3.75 cm) and C-band (3.75–7.5 cm) images are used for operational purpose due to its large coverage and cost effectiveness (e.g. ENVISAT ASAR Wide Swath Mode, RADARSAT 2 SAR ScanSAR Wide). Newly introduced TerraSAR-X WideScanSAR and traditional ScanSAR mode has also been investigated for its inclusion into the service. Quality of SAR images is a key factor for this kind of operational services. Unfortunately, these wide swath images are generally affected by trends of reduced radar backscatter of the sea induced by the incidence angle increase at far range (Fig 3.2). This particular phenomenon which is intrinsic to SAR images obstructs the process of feature detection on ocean surface, hence the classification of features. This section of this thesis investigates different techniques for compensating this reduced backscatter trend.

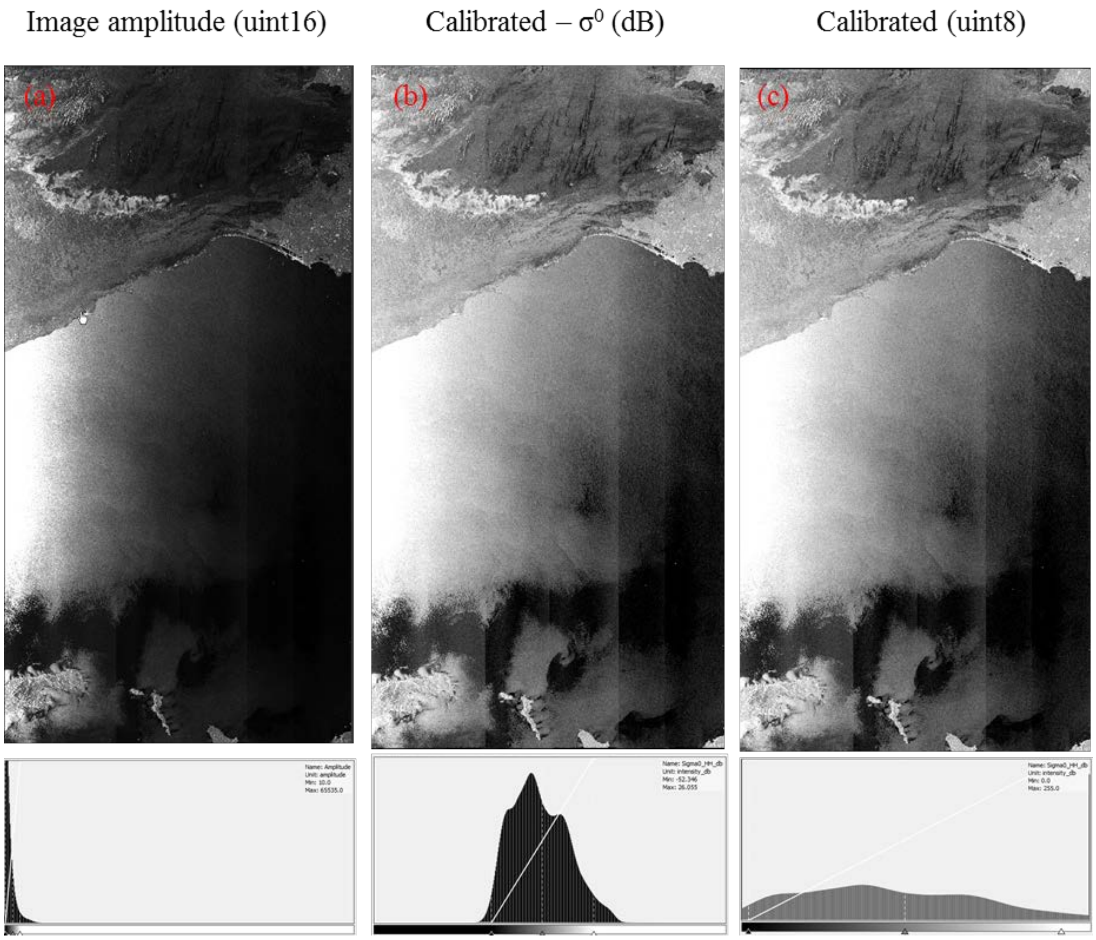

Fig 3.2: (a) ENVISAT ASAR Wide Swath Mode HH polarized image acquired on 13-MAR-2011 20:05:06, showing progressive backscatter reduction from near range to far range. (b) Calibrated σ^0 and (c) Calibrated 8-bit image and there corresponding histogram (Image Id: ENVISATASA_WSM_1PNIPA20110313_200506_000001353100_00244_47241_8433.N1, Image provided by Kostas Topouzelis).

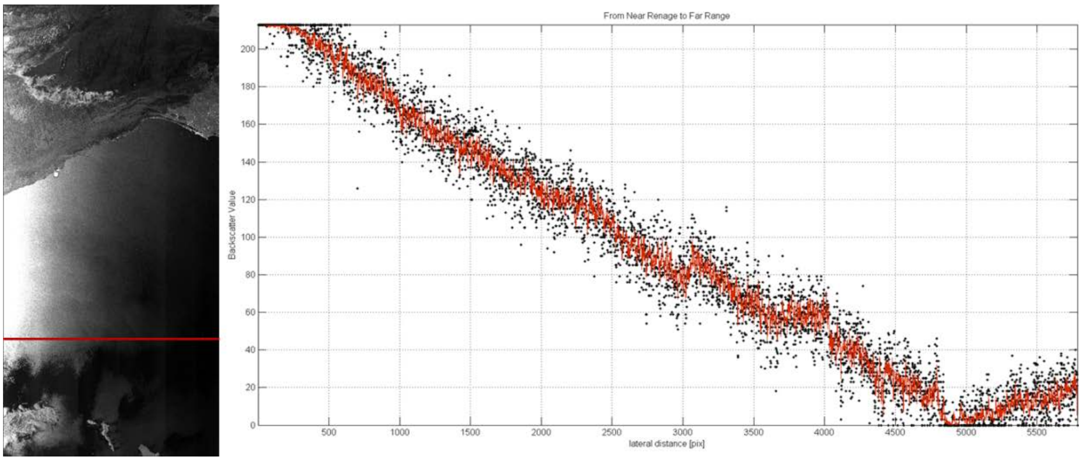

Fig 3.3: Slant-range dependent dynamic range (red) and speckle (black dots) of an ENVISAT ASAR Wide Swath Mode Image profile (indicated by red line on the image).

Figure 3.3 shows an average profile plotting of backscatter value from near range to far range. Ten consecutive lines (across-track) from an ASAR wide swath image was used to show the decreasing backscatter trend. It is evident from the plot that the image under inspection is effected by inter beam seam and the back dots scatter around the red line shows the magnitude of the speckle present in the image. In order to overcome these intrinsic drawbacks for SAR oceanographic applications, a robust and automated image pre-processing tool has been developed, which in later stage will be used by different oil spill detection methodology (Singha *et al.,* 2013b, 2013c). The proposed tool has been extensively tested and calibrated using C-band (ENVISAT and RADARSAT-2) and few X-band (TerraSAR-X) SAR data. Following section describe the pre-processing tool step by step along with intermediate results. The proposed pre-processing tool is still in development phase and its being implemented in MATLAB environment which might also be useful for other oceanographic applications (e.g sea ice classification).

3.2.1 Procedures and Mathematical model

This section describes the main operations performed by the Image Pre-processing toolbox, together with the mathematical model (See Fig 3.4 for the block diagram for the toolbox). All the images are initially calibrated and transformed into 8-bit Geotiff format for further processing. Calibration phase was carried out by standard methodology using standard calibration constant.

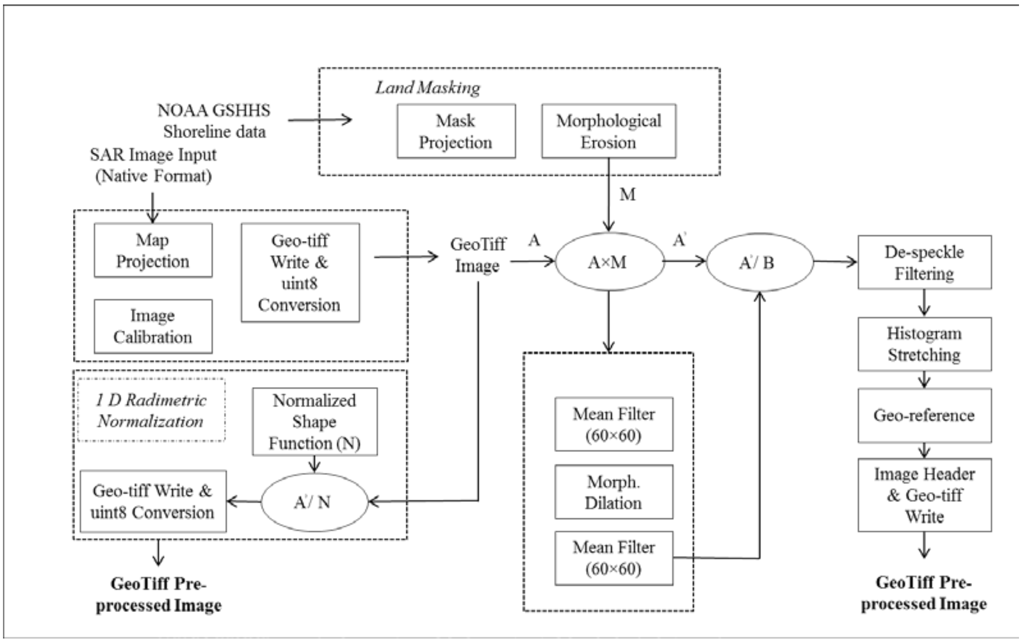

Fig 3.4: Block diagram of the SAR image pre-processing tool for oceanographic applications (adapted from Singha *et. al.*, 2013b, Technical Report EMSA, page vii).

3.2.2 'GSHHS' File Information Retrieval

The high resolution world shoreline distribution vector data imported by the Image Pre-processing tool are derived from the public domain Global Self-consistent, Hierarchical, High-resolution Shoreline Database (GSHHS) made available by the NOAA National Geophysical Data Center (GSHHS 2013a; 2013b; Currently GSHHG - Global Self-consistent, Hierarchical, High-resolution Geography Database).

The Image Pre-processing Tool reads GSHHS vector data from the intermediate resolution data gshhs_i.b (GSHHS b, 2013). The data related to the area of interest are extracted for land masking operation. Such area is delimited using the bounding box information retrieved from the header file of "-geoN.tif" input image (Fig: 3.5). Extracted shoreline information is then used to create a binary mask for the land masking operation. The subset of the vector data extracted from the GSHHS file is returned into a polygon data structure array (Fig: 3.6). Such array is subsequently converted into a raster base map through the definition of the appropriate number of matrix elements per latitude and longitude degrees (using grid interpolation technique, see Fig: 3.7). These values are equal to the dimensions of SAR image and therefore derived from the RADARSAT or ASAR input files (Fig: 3.5). The mask matrix representing the shoreline distribution within the area of interest is eventually obtained by filling the sea and land areas respectively with zeroes and ones.

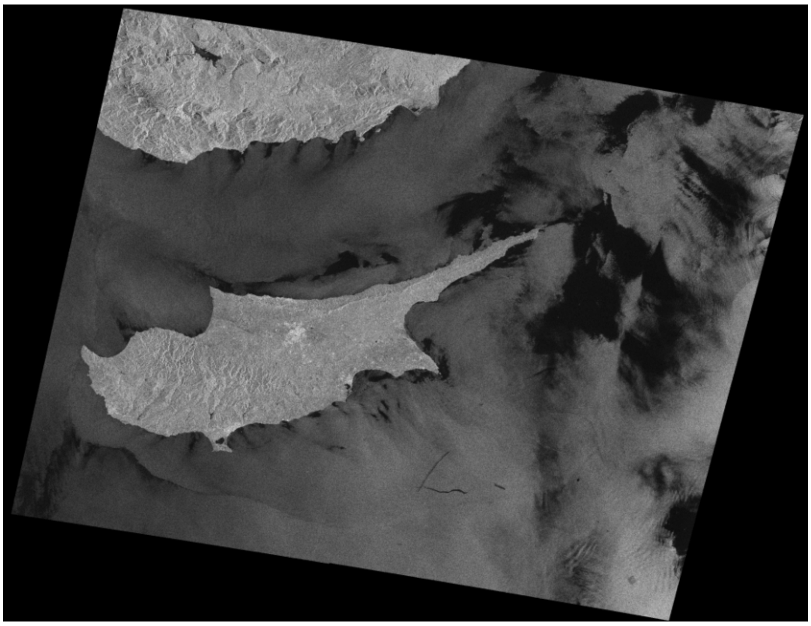

Fig 3.5: SAR pre-processing: Original SAR image (RADARSAT-2 ScanSARWide image acquired on 12th June 2012 at 17:31:51 over Mediterranean Sea. ©MDA/EMSA, adapted from Singha *et. al.*, 2013b, Technical Report EMSA, page vii.

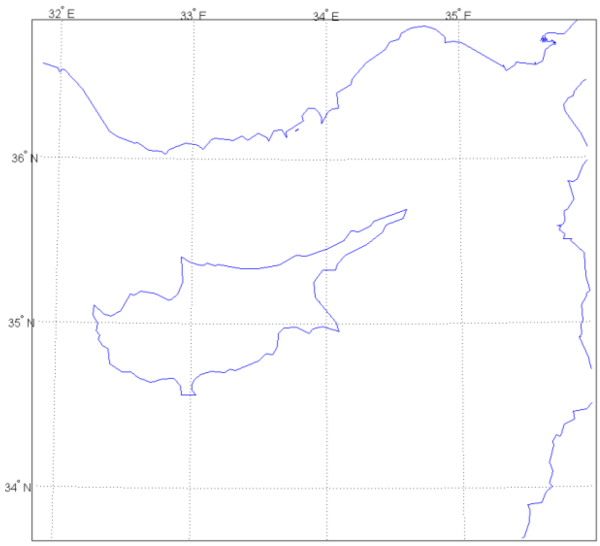

Fig 3.6: SAR pre-processing: Extracted coastline layer from 'GSHHS' layer for land masking process. Coastline information was extracted using image header file information (corner coordinates).

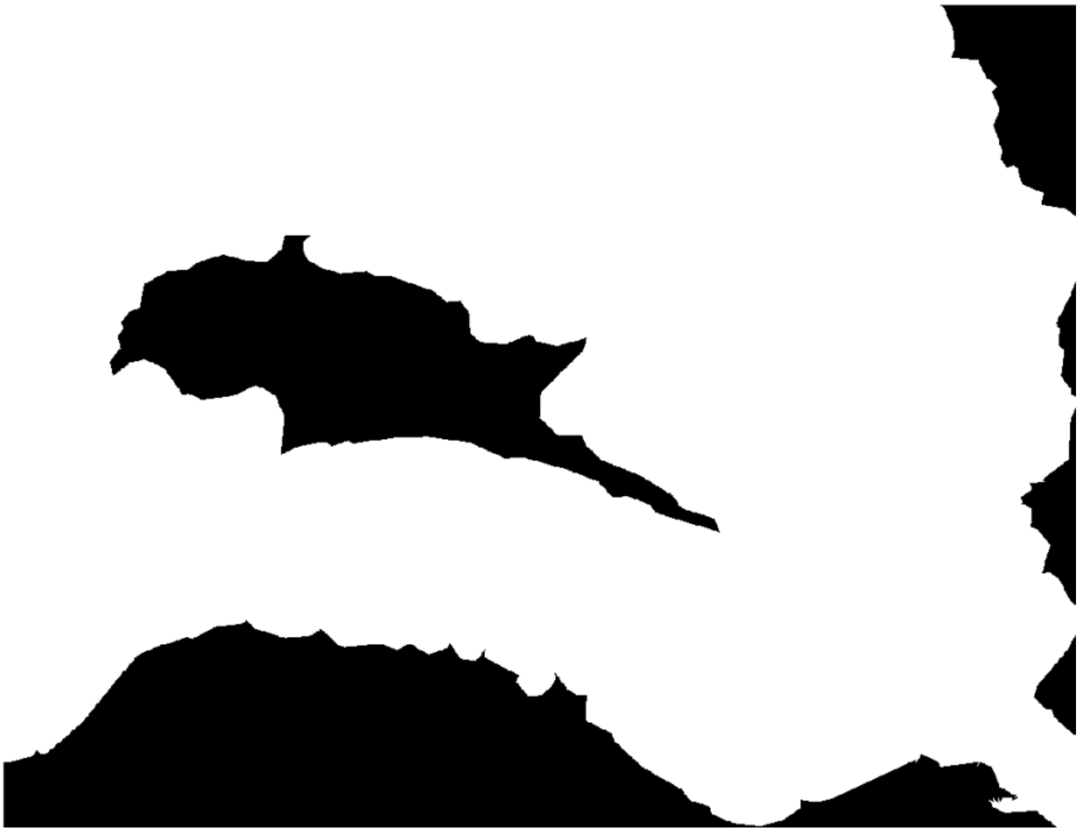

Fig 3.7: SAR pre-processing: Extracted binary raster layer from 'GSHHS' coastline information. (Aadapted from Singha *et. al.*, 2013b, Technical Report EMSA, page vii).

3.2.3 Mask Back-projection

The geo-referenced raster map representing the land/sea spatial distribution within the SAR image bounding box is subsequently back-projected to match the "-geo1.tif" image. This operation is performed using the referencing matrix extracted from the header of the "-geoN.itf" image, representing the transformation from pixel to spatial coordinates.

The resolution of the back-projected land mask is commensurate to the "Mask interpolation factor (lat/lon)". This parameter can be set from the 'MATLAB configaration' file and is used to linearly interpolate the mesh grid built from the "-geo1.tif" input image tile points (Fig: 3.8). The higher the interpolation factor, the larger computational burden is implied. This functionality is performed in order to correct for inaccuracies intrinsic to the land-mask and geo-coding process already performed on the input file. The back-projected mask buffering is performed on the basis of morphological erosion (Serra, 1982; Heijmans H.).

Fig 3.8: SAR pre-processing: Back projected binary raster layer from 'GSHHS' coastline information.

3.2.4 Morphological Erosion

The back-projected mask representing with ones the sea spatial distribution is eroded in order to expand the land area identified by zero values. Main intention of this operation was to eliminate any land feature from the land-masked image which might be present due to the low resolution of GSHHS data compared to SAR image. The size of the disk shaped structuring element can be adjusted in order to achieve the optimal trade-off between erosion and sea backscattering masking. The effects of the buffering operation are illustrated in Figure 3.9: the first image was masked without buffering (i.e. math morphology disabled using the configuration file). It can be seen that some land areas are not masked with the result of upsetting the background estimation close to the shoreline (Fig: 3.10 and 3.11).

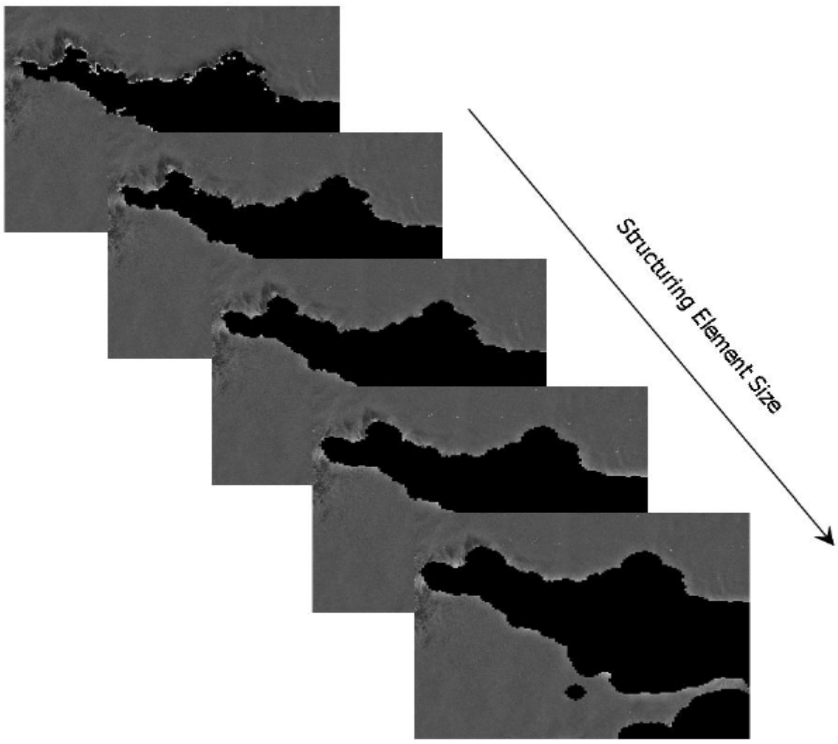

Fig 3.9: Morphology structuring element size effect on the land-mask erosion (the first image has no math morphology applied).

Fig 3.10: SAR pre-processing: Back projected and morphologically eroded binary raster layer.

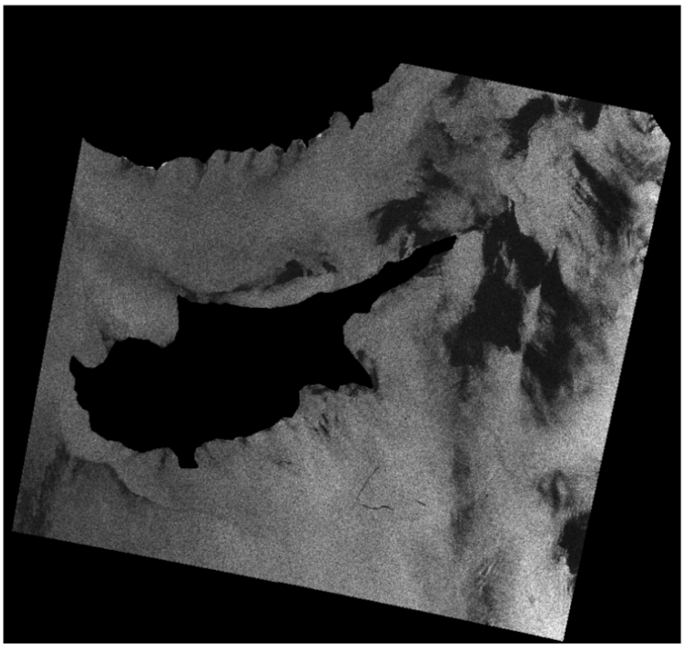

Fig 3.11: SAR pre-processing: Projected land-masked image.

With the increase of the structuring element size, the land influence on the background is progressively removed, while the buffering area increased. This has the effect of masking the sea surface in proximity of the coast.

3.2.5 Speckle Noise Reduction

The filtering operation is crucial in order to reduce the speckle in the image and therefore the number of false positive detections. The trade-off between the edge preservation and the speckle noise reduction has to be taken into account for oil-spill detection applications. The size of the kernel and the type of approach are to be appropriately chosen also to minimise the execution time when required. In the following figures, the results of the implemented filters are illustrated on an oil-spill feature extracted from a RADARSAT-2 image. The oil spill highlighted in Fig 3.12 reported by EMSA's 'CleanSeaNet' service (Image Id: 22208 Oil Spill ID: 9023).

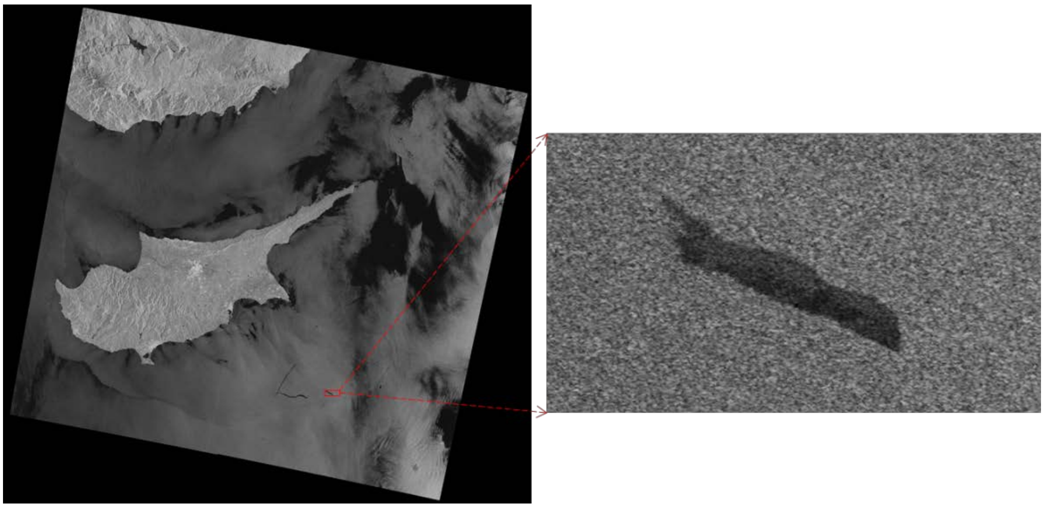

Fig 3.12: SAR pre-processing: Original SAR image (RADARSAT-2 ScanSARWide image acquired on 12th June 2012 at 17:31:51 over Mediterranean Sea) and a reported oil spill (CleanSeaNet oil spill Id: 9023) spot present in the image (Red rectangle) ©MDA/EMSA.

Image filtering techniques are implemented in order to reduce the problem of radar speckle while preserving high frequency object features like edges and backscattering transitions. This high frequency noise can be thought of as multiplicative noise and can be reduced using a number of de-speckling filters (Sheng and Xia, 1996). The Image Pre-processing Tool implements four speckle removing filter (Mean, Median, Lee and Local Region) described below:

Mean Filter: the central pixel of the sliding window is replaced with the mean value of the entire window. Although computationally efficient, this filter is not ideal for edge and transition preserving image preparation (Fig 3.13).

Median Filter: the central pixel value is estimated as the median of the pixels covering the sliding window. This filter is recognised as an effective edge preserving smoothing technique, although it is less effective for very high frequency features (point-like backscattering transitions) (Fig 3.14).

Lee Filter: This filter computes the sliding window statistics (mean and standard deviation) in order to estimate the central pixel value. In particular, this filter assumes that the statistics of the sliding neighbourhood is equal to the central pixel statistics (Fig 3.15).

Local Region Filter: the region around the pixel of interest is subdivided into eight sub-regions (N, NE, E, SE, S, SW, W and NW). The central pixel of the sliding neighbourhood is replaced by the mean of all values within the sub-region presenting the lowest variance, i.e. the most uniform region (Fig 3.16).

The window filter size can be specified through the previously mentioned MATLAB configuration file. The size of the sliding neighborhood of the pixel of interest significantly influences the output image quality: a small window size leads to lower speckle mitigation, whereas a large window size implies a lower resolution, loosing subtle details within the image while mitigating the speckle noise completely.

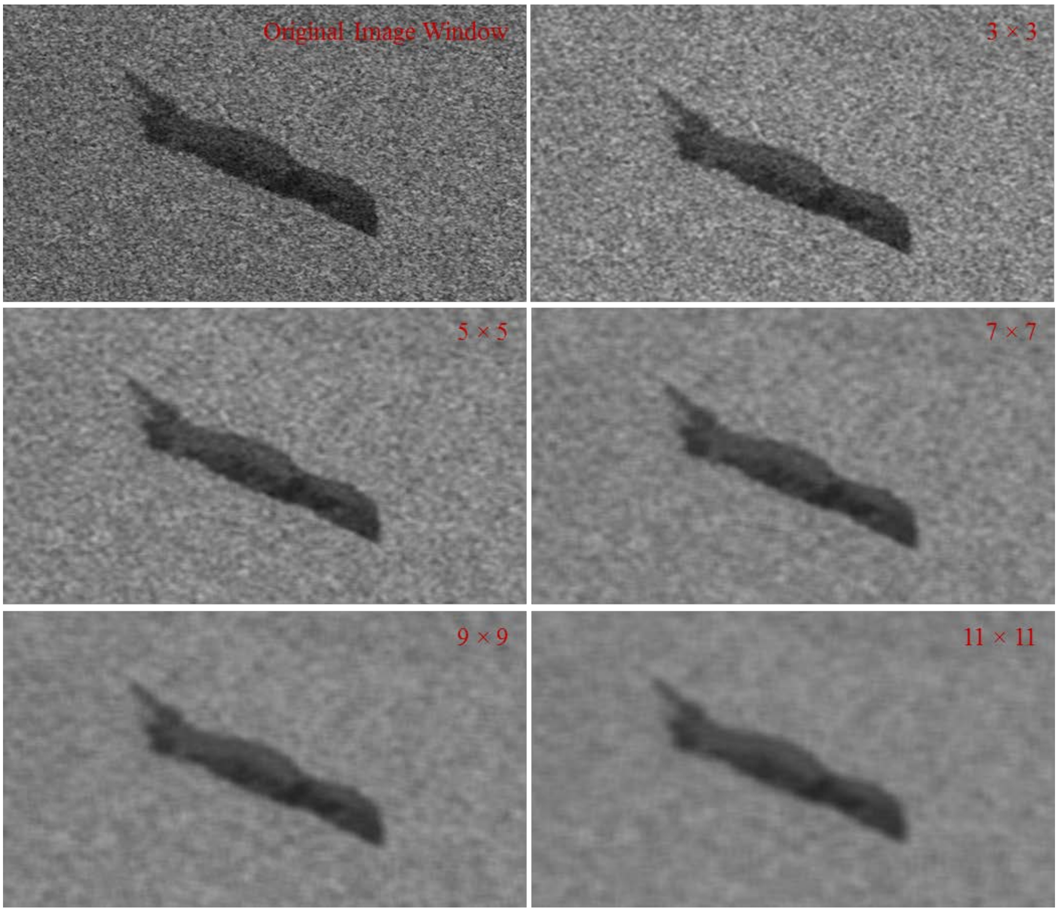

Fig 3.13: Mean filtering on an image window extracted from RADARSAT-2 SAR image with different kernel size (3×3 to 11×11).

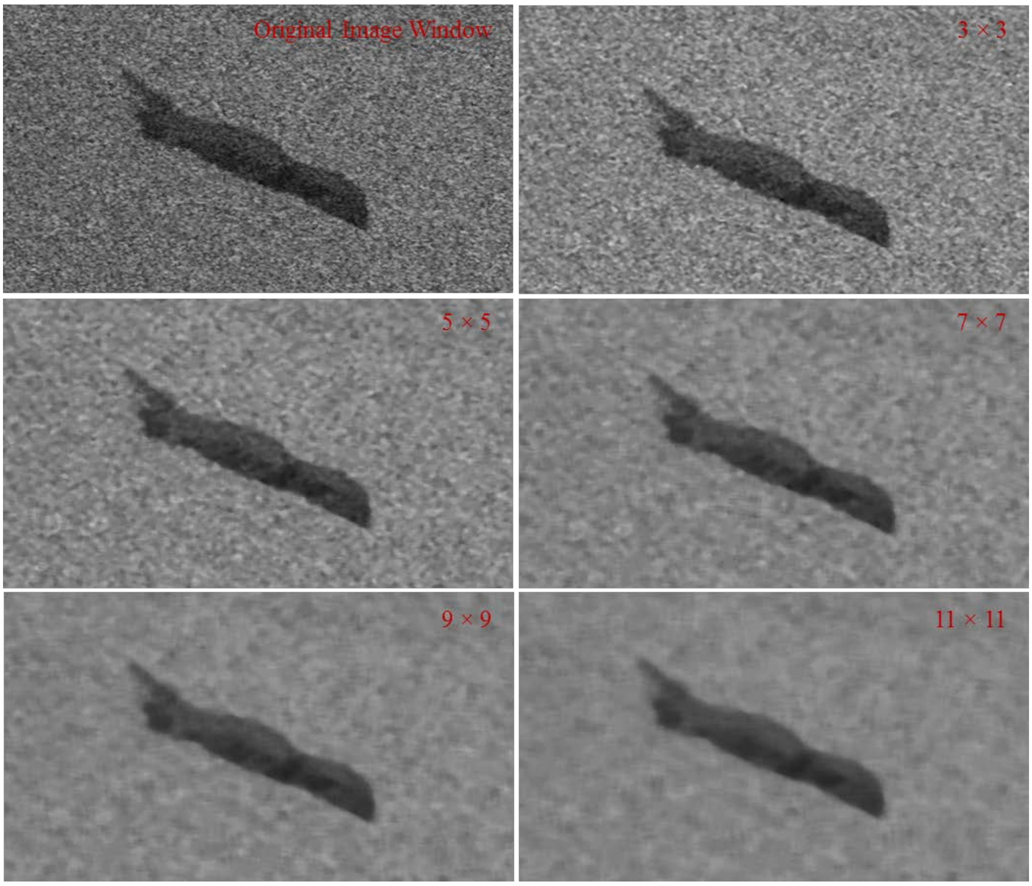

Fig 3.14: Median filtering on an image window extracted from RADARSAT-2 SAR image with different kernel size (3×3 to 11×11).

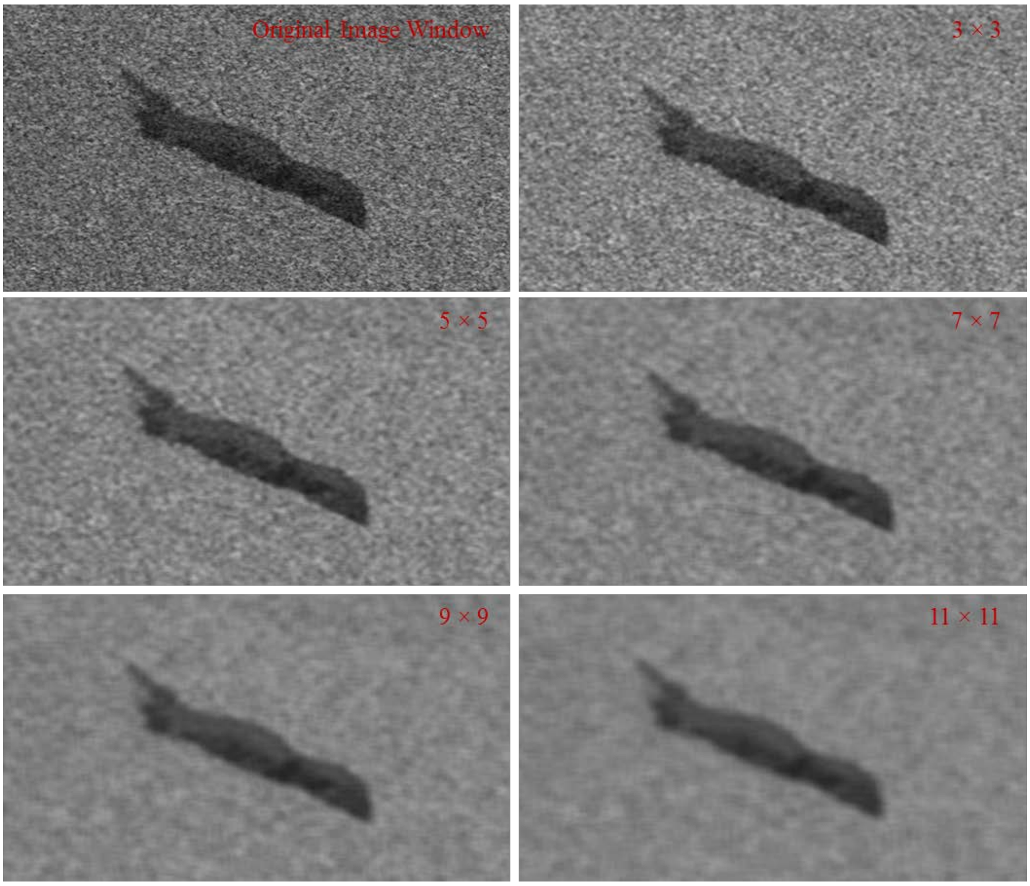

Fig 3.15: Lee filtering on an image window extracted from RADARSAT-2 SAR image with different kernel size (3×3 to 11×11).

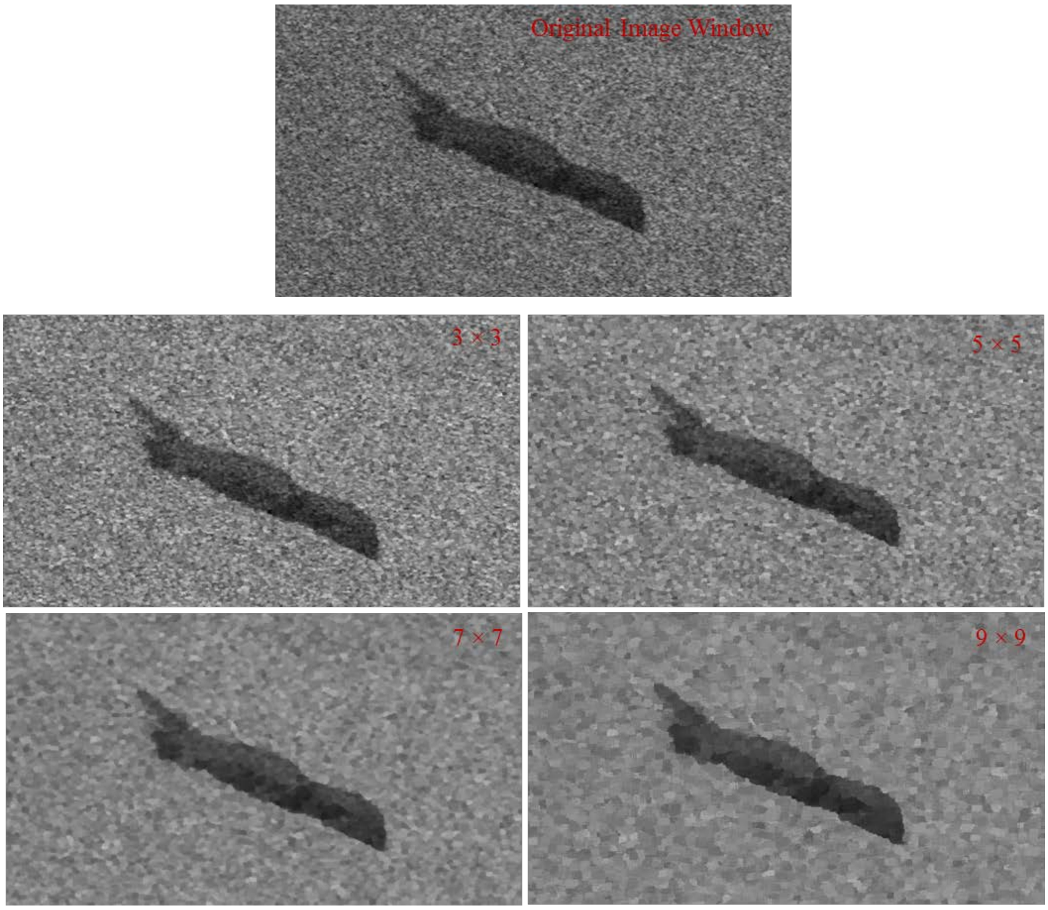

Fig 3.16: Local Region filtering on an image window extracted from RADARSAT-2 SAR image with different kernel size (3×3 to 11×11).

As evident from Figure 3.13-3.16, the local region filtering technique performs better than others in terms of preserving the shape of dark objects even at larger window size.

3.2.6 Radiometric Normalization Techniques

It is well known that different scattering mechanism characterize the observed SAR scene. The back-scattering coefficient σ^0 is dependent on the shape and the dielectric properties of the target, polarization, illuminating frequency, and incidence angle.

Furthermore, the link between σ^0 and the geometric and radiometric parameters is regulated by two major scattering mechanisms:

• Volume Scattering: it is characterized by reduced dependency on the incidence angle (e.g. vegetation);

• Surface Scattering: it shows strong dependency on the incidence angle (e.g. calm sea). Details were discussed in Chapter II Section X (*Scattering Mechanisms*)

In order to make full use of the dynamic range, the image is first calibrated (σ^0 calibration for ASAR range detected products - ASA_WSM_1P, ASA_IMM_1P) and then radiometrically normalized in order to remove the incidence angle dependency. Two separate techniques were investigated in this study, 1-D Backscattering shape function derivation and 2-D background estimation and removal. Some other techniques to remove the incidence angle dependency are proposed in Topouzelis *et al.*, 2014 (in review, page vii).

1-D Backscattering shape function derivation:

A theoretical backscattering profile in elevation direction, scaled with the calibration factor, is applied to the This methodology leads to a short execution time but is not effective when local differences in sea state are present in the area of interest (particularly likely for wide swath SAR images).

Step by step processing:

1) 8-bit Geotiff image and ingestion and corresponding header file information retrieval.

2) GSHHS High resolution land masking operation including morphological erosion to avoid masking inaccuracy

3) 1-D radiometric normalisation is computed through intensity multiplication using a tangent shape function applied to the incidence angle. Since the incidence angles φ_{Inc} are not available from the Geotif input image, depending on the satellite platform, the range-variable $\varphi_{Inc}(r)$ values are retrieved according to the following steps (Incedence angle information in range can also be derived from image metadata provided by service provider). First wide swath images divided in 400 column strip and incidence angle are calculated using the following formula for each strip.

$$\eta_{OffNadir} = sin^{-1}[(ER/(ER+H))\, sin(\varphi_{Inc}\text{-}nr)] \tag{3.1}$$

$$\psi = (\pi - \eta_{OffNadir})-(\pi - \varphi_{Inc}) = \varphi_{Inc} - \eta_{OffNadir} \tag{3.2}$$

$$d\psi = SW(i)/ER \tag{3.3}$$

$$r^{2} = ER^{2} + (ER+H)^{2} - 2\, ER\, (ER+H)\, cos(\psi+d\psi) \tag{3.4}$$

$$sin\, (\eta_{OffNadir} + \alpha ElAp) = ER\, sin\, (\psi+d\psi)/\, r \tag{3.5}$$

$$\varphi_{Inc}(r) = sin^{-1}[((ER+H)/ER)\, sin(\eta_{OffNadir} + \alpha ElAp)] \tag{3.6}$$

where φ_{Inc}-nr is the incidence angle at near range, ER the Earth radius, H the altitude of the satellite and SW(i) the swath spanning from zero to the full swath covered by the radar mode (see Fig: 3.17). Finally the pixel value assigned using the following equation

$$\text{Normalized Value} = \tan\, (\varphi_{Inc}(r) * \pi /180))^{\text{ShapeFactor}} \tag{3.7}$$

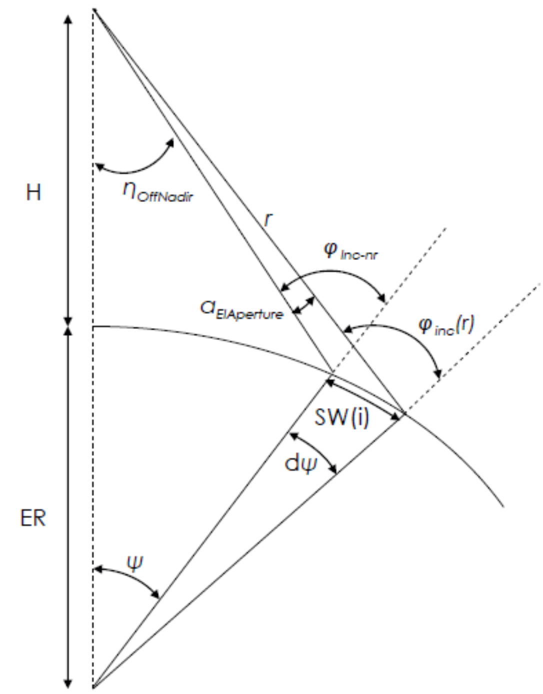

Fig 3.17: Calculation of incidence angle

Shape Factor is determined manually based on image quality and contains. Shape factor usually ranges between 1.0 to 4.0. Figures below shows the normalization results with different shape factor on a ENVISAT ASAR Wide Swath Mode HH polarized image acquired on 13-MAR-2011 at 20:05:06 (Fig: 3.17 to Fig: 3.24). The red line on image represents the location of the profile which is 10 consecutive row (range).

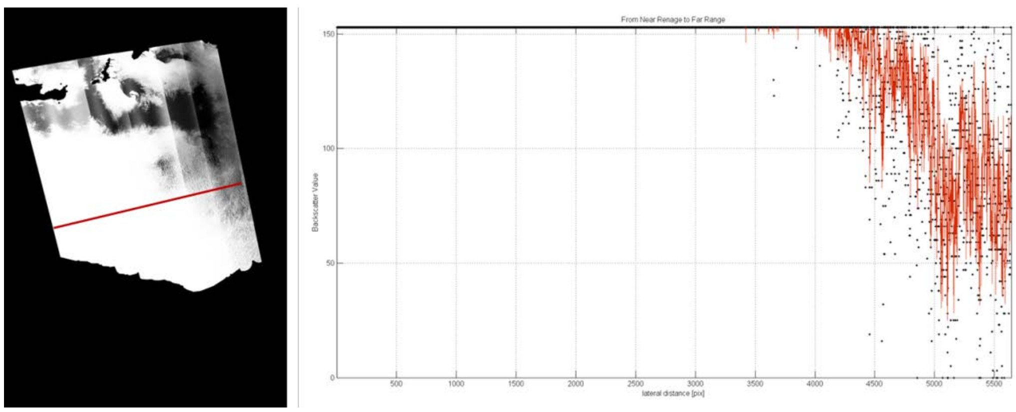

Fig 3.18: One D radiometric normalization using shape factor 0.5 and corresponding profile dynamics.

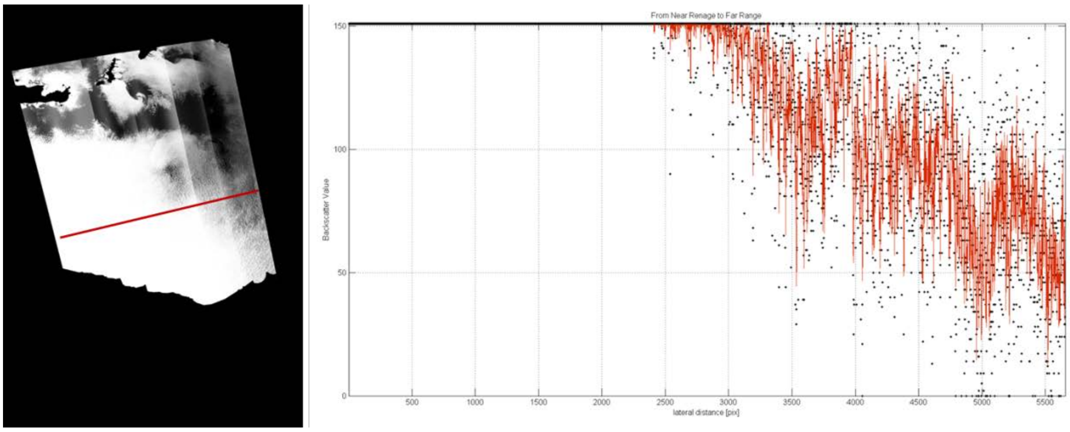

Fig 3.19: One D radiometric normalization using shape factor 1.0 and corresponding profile dynamics.

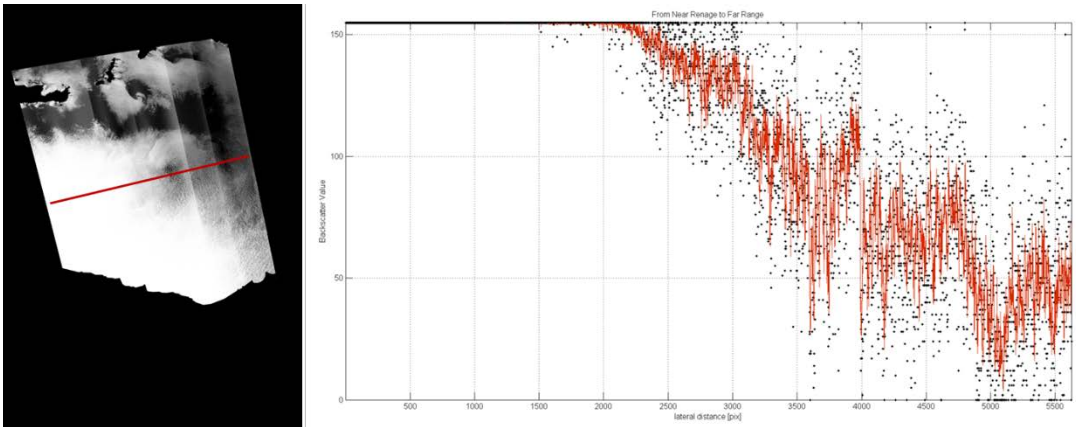

Fig 3.20: One D radiometric normalization using shape factor 1.5 and corresponding profile dynamics.

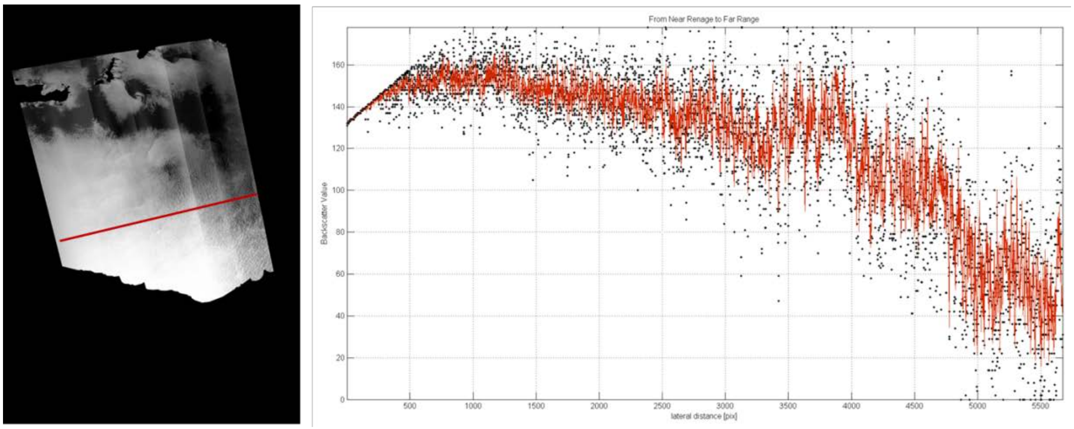

Fig 3.21: One D radiometric normalization using shape factor 2.0 and corresponding profile dynamics.

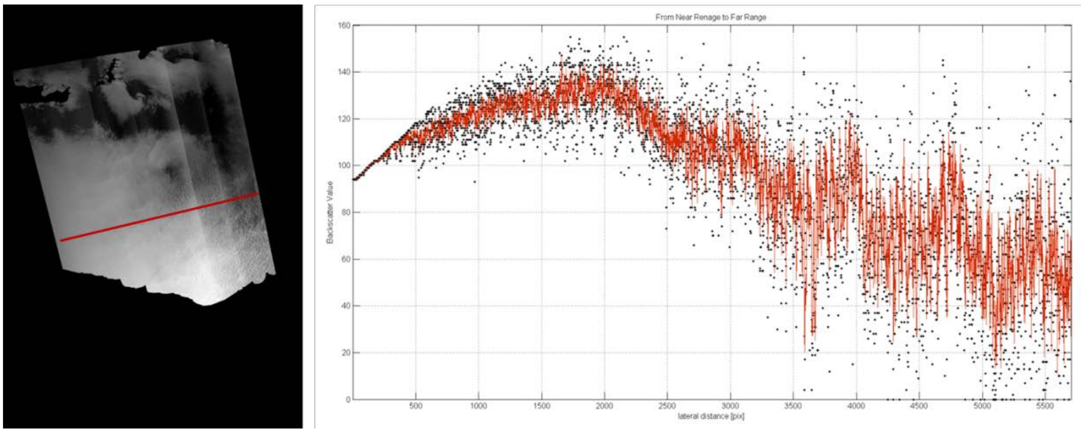

Fig 3.22: One D radiometric normalization using shape factor 2.5 and corresponding profile dynamics.

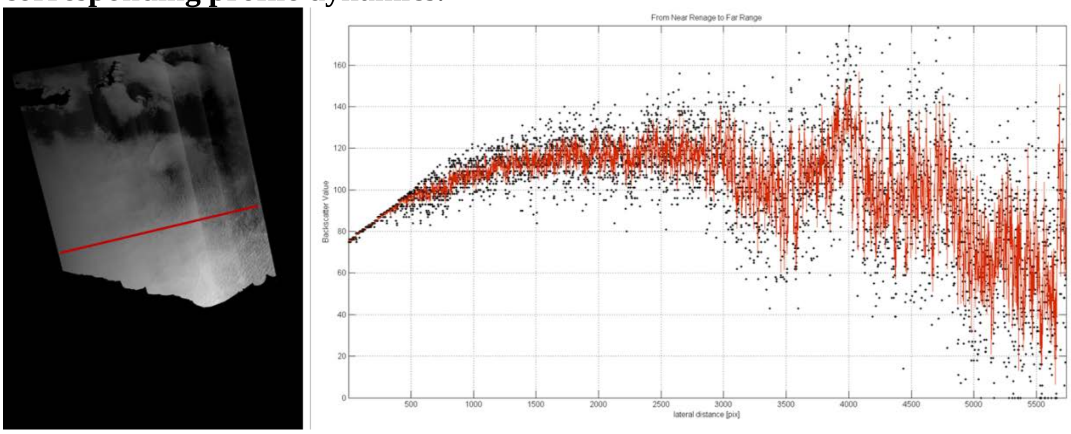

Fig 3.23: One D radiometric normalization using shape factor 3.0 and corresponding profile dynamics.

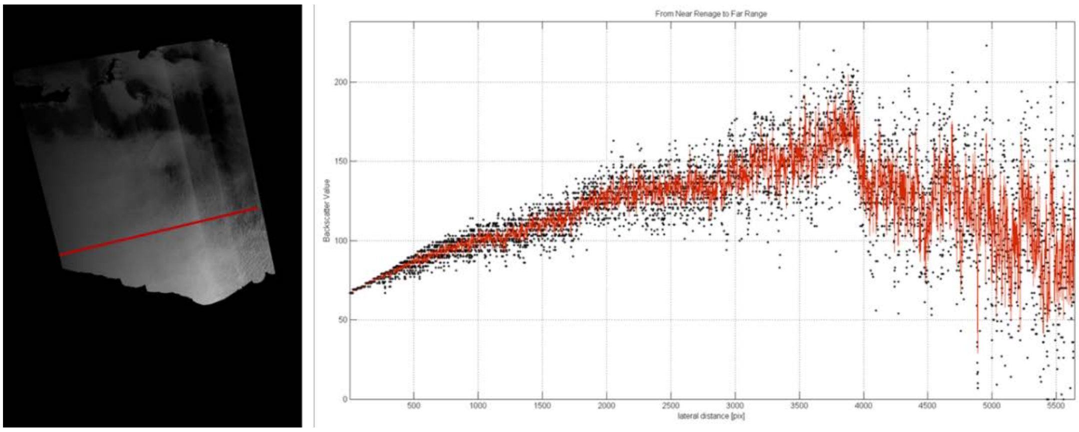

Fig 3.24: One D radiometric normalization using shape factor 3.5 and corresponding profile dynamics.

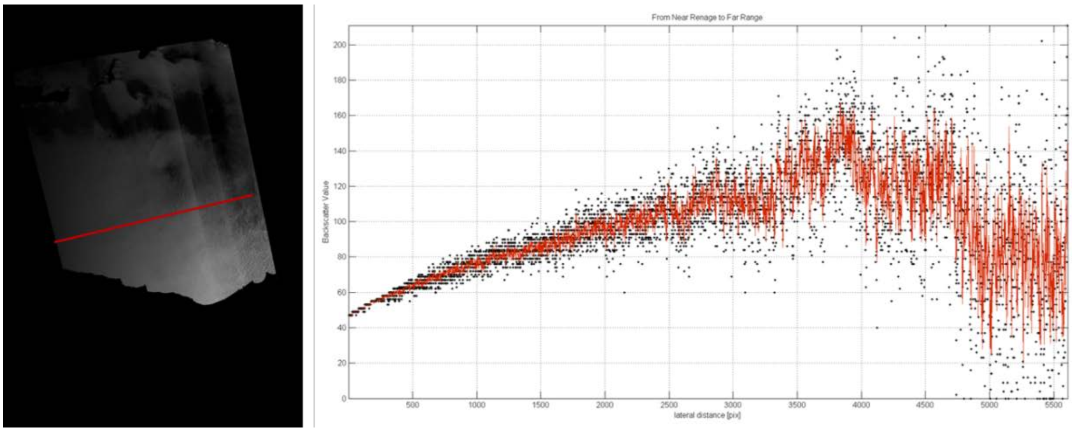

Fig 3.25: One D radiometric normalization using shape factor 4.0 and corresponding profile dynamics.

For the above example, after investigating different profile dynamics it's evident that a reasonable normalization was achieved with shape factor 3.0. Shape factor value above or below 3.0 will jeopardize the normalization process for this particular image.

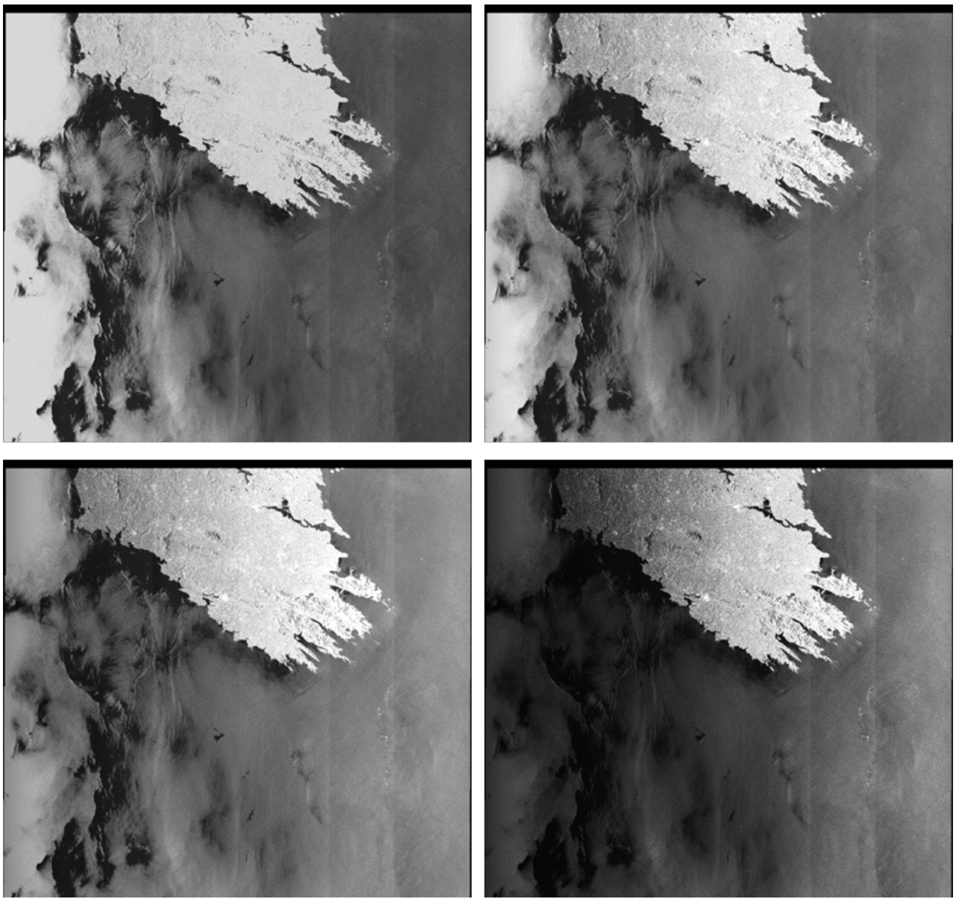

Fig 3.26: 1-D radiometric normalization performed on ENVISAT ASAR WSM image with different Shape Factor (Singha et al. 2013c).

Another One D Radiometrically normalized image presented above (Fig 3.26) with different shapefactor (1.0, 1.5, 2.0 and 2.5) shown in figure below. In the following example a desirable normalization was achieved with shape factor value of 2.0.

2-D background estimation and removal:

The backscattering background is calculated by averaging and smoothing the image after land-masking operation. This image background removal process depends on the backscatter data and is therefore only indirectly linked to the incidence angle. Land-masked and filtered images are divided into 100×100 sub-images and subsequent sub-images were normalized using local backscatter statistics.

This approach is more accurate than the previous ones in terms of radiometric normalization performance since it locally estimates the backscattering floor, removing more of the background variations due to the sea state conditions. A step by step processing approach is given below.

Step by step processing:

1) 8-bit Geotiff image and ingestion and corresponding header file information retrieval (see figure 3.28 a).

2) GSHHS High resolution land masking operation including morphological erosion to avoid masking inaccuracy (See Figure 3.28 b).

3) Image resize and divide the resized image into square sub-images (number of square depends on the imaging mode, usually 100×100)

4) Mean Filtering using 50×50 image window on resized image (See figure 3.27 c).

5) Divide the original image into stripes of 100 rows

6) Normalization on each strip performed using the following equation on pixel by pixel basis (See figure 3.27)

$$Final\ Filtered\ Image = \frac{Land\ Masked\ Original\ Image}{Land\ Masked\ Mean\ Filterd\ Image} \times 255$$

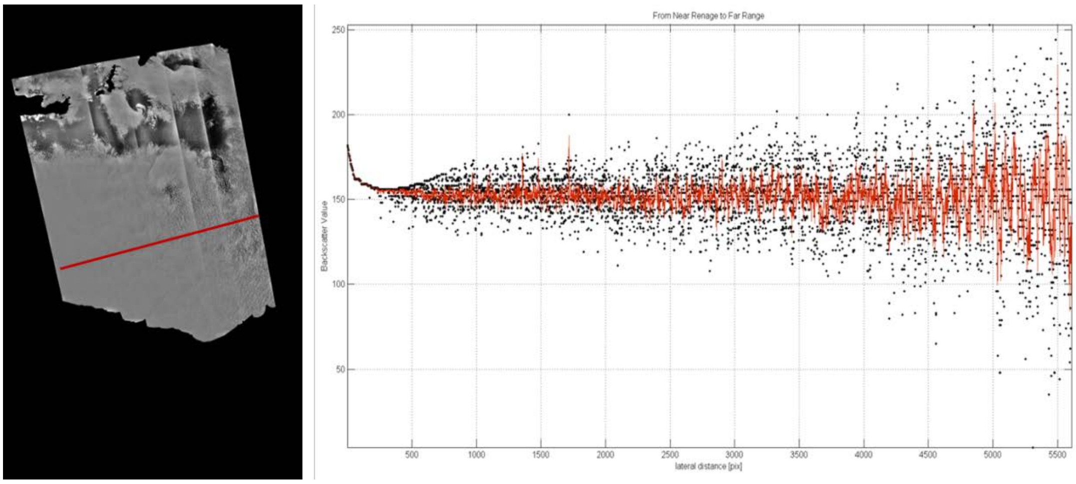

Fig 3.27: Two D radiometric normalization and corresponding profile dynamics

Figure 3.28 describes the image pre-processing step by step which are image ingestion (Fig 3.28a), land masking (Fig 3.28b and 3.28c), filtering and Two D normalization process (Fig 3.28d).

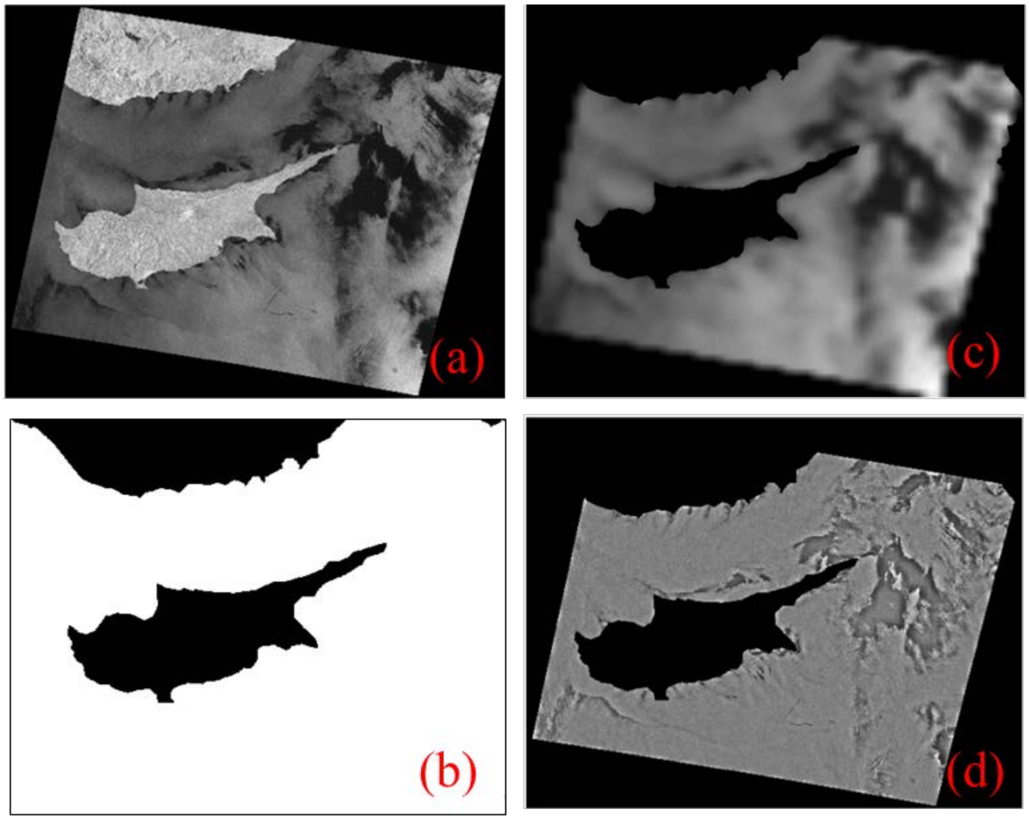

Fig 3.28: SAR pre-processing:– a) Original SAR image (RADARSAT-2 ScanSARWide image acquired on 12th June 2012 at 17:31:51 over Mediterranean Sea b) Back-projected eroded land-mask, c) Land-masked estimated background d) Final processed output.

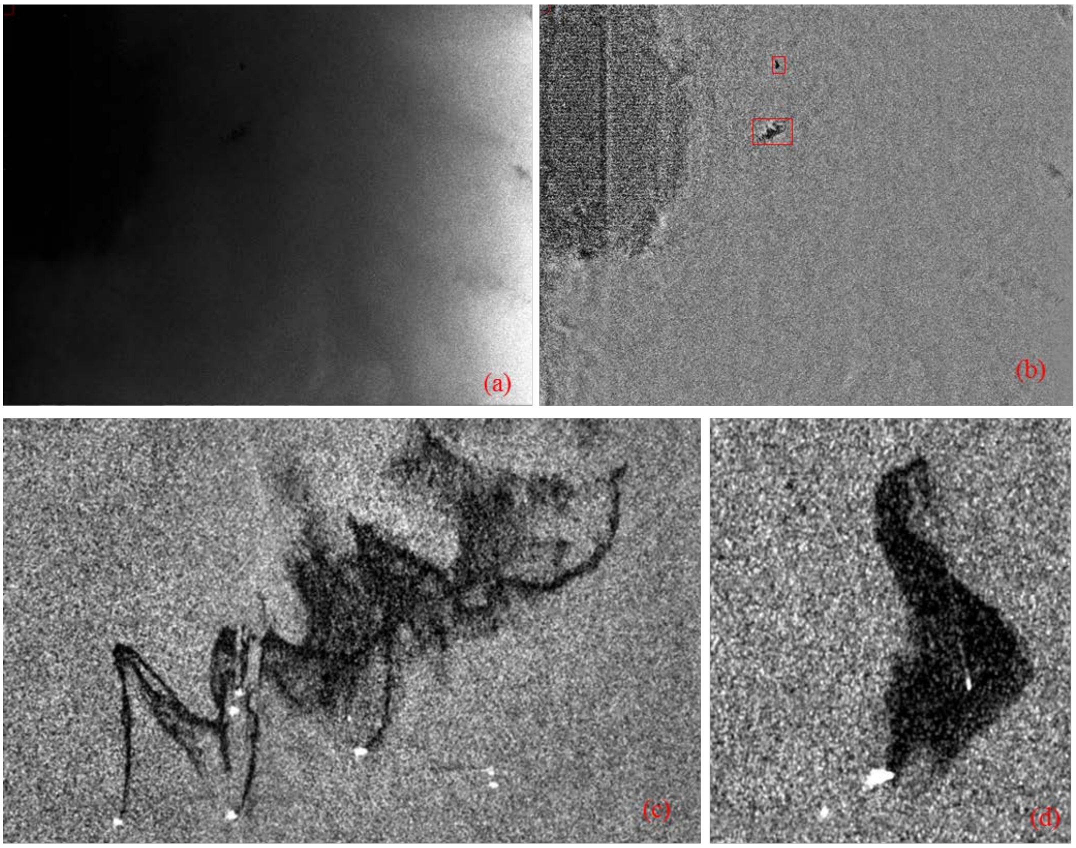

Fig 3.29: (a) TerraSAR-X image acquired in Wide ScanSAR mode (270km x200 km, range x azimuth Beam. Wide_001, VV-pol) all acquired over known North Sea platform sites (near Scotland coast) on 30th August 2013 at 06:24:28 UTC (©DLR, Image acquired under project id: OCE2015, Principal Investigator: Suman Singha). (b) Final pre-processed image using Two D normalization technique.

The pre-processing tool with proposed Two D normalization process was finalized as a tool to process bulk number of SAR images. The proposed pre-processing tool has also been evaluated for X-Band SAR images (e.g TerraSAR-X) as X-band SAR images are now been used for operational services. One example of Two D normalized TerraSAR X WideScanSAR data shown in Fig 3.27. The proposed pre-processing technique can be tailored for other related oceanographic applications such as ship detection, Iceberg monitoring and ocean surface dynamics monitoring. Pre-processed ENVISAT ASAR and RADARSAT-2 SAR images then used for two different oil spill detection methodology. The first methodology is based on 'Artificial Neural

Network' and the second one is based on 'Classification Tree' coupled with 'Fuzzy Logic'.

3.3 EXPERIMENTAL DATA SET

This section presents the description and the characteristics of the SAR data used in this study. The characteristics of the data sets which have been used for this study, are known a priori, therefore it will be expedient to evaluate the implementation and validation of various models for oil spill detection.

Data Set 1: A number of C-band VV polarized ERS-2 Synthetic Aperture Radar (SAR) image ENVISAT ASAR and RADARSAT-2 images containing an oil spill and a look alike have been gathered from different sources. First methodology based on ANN algorithm was trained and calibrated using 97 ERS-2 SAR and ENVSAT ASAR images of individual verified oil spills or/and look-alikes obtained from the European Space Agency (ESA) and European Maritime Safety Agency (EMSA). This training and calibration dataset consisted of 183 reported oil spill spots and 720 'look-alike' features. The methodology was validated using a separate and mutually exclusive dataset incorporating 82 ENVISAT ASAR and RADARSAT-2 SAR images obtained from European Maritime Safety Agency (EMSA). This validation dataset consisted of 226 reported oil spill spots and 4670 'look-alike' features. Figure 3.28 shows an example RADARSAT-2 SAR image containing a verified oil spill which was a part of validation dataset.

Data Set 2: A total of 38 images were used to train the automatic oil spill detection system based on Classification tree, and include ENVISAT ASAR

Wide Swath mode and RADARSAT-1 and 2 HH polarised, ScanSAR Narrow mode (Table 3.1). For each image, EMSA information on oil spill detections formed the training set, providing a total of 237 dark patches labeled as oil spills. Each spill reported by EMSA was classified as oil spill by experienced operator. Some of these patches are fragments of the same spilled area, and therefore belong to the same event and treated as a single spill. As discussed earlier, in order to further reduce small detections due to speckle and large patches due to met-oceanic look-alikes, only the dark areas with a size between 0.15 km^2 and 35 km^2 are considered. The dataset is significantly heterogeneous, providing fresh and old spills, characterized either by straight, distorted or amorphous shapes, and identified by large or reduced contrast with the surrounding sea backscatter. Moreover, the dataset contains a comprehensive set of look-alikes, including phenomena such as Lee waves, natural slicks, ship wakes, low wind and wind shadow areas and algae bloom affected areas. The recorded number of look-alike feature is significantly higher for this dataset. Table 3.1 shows the CleanSeaNet image id used for training and calibration purpose (used in Singha *et. al.*, 2013b).

Table 3.1 : Images obtained for training from 'CleanSeaNet' archive (Data Set 2).

1	3726_ASA_WSM_1PNACS20110216_202311_000000592097_00229_46882_0001
2	3773_ASA_WSM_1PXCLS20110225_101715_00000073X000_00000_47005_1008
3	5604_ASA_WSM_1PXCLS20110314_211506_00000122X000_00000_47256_1156
4	5620_ASA_WSM_1PXCLS20110327_213807_00000165X000_00000_47443_1253
5	5621_ASA_WSM_1PXCLS20110328_210221_00000104X000_00000_47457_1268
6	5700_ASA_WSM_1PNTSS20110312_204856_000000673100_00230_47227_0330
7	3816_ASA_WSM_1PNACS20110226_205847_000000592097_00

	372_47026_0001
8	5848_ASA_WSM_1PNACS20110309_094008_000000972098_00022_47177_0001
9	5874_ASA_WSM_1PNACS20110319_083426_000001032098_00164_47320_0001
10	5877_ASA_WSM_1PNACS20110326_203030_000000822098_00272_47428_0001
11	5889_ASA_WSM_1PNACS20110314_081626_000000612098_00093_47248_0001
12	6442_ASA_WSM_1PXCLS20110505_210946_00000092X000_00000_48003_1650
13	6455_ASA_WSM_1PXCLS20110521_100030_00000171X000_00000_48226_1894
14	6549_ASA_WSM_1PNTSS20110519_093412_000000723102_00338_48197_0058
15	6570_ASA_WSM_1PNACS20110508_094112_000000972099_00380_48039_0001
16	6579_ASA_WSM_1PNACS20110501_201051_000001162099_00286_47945_0001
17	6582_ASA_WSM_1PNACS20110504_084856_000000742099_00322_47981_0001
18	6583_ASA_WSM_1PNACS20110504_200035_000000612099_00329_47988_0001
19	6587_ASA_WSM_1PNACS20110510_194033_000000612099_00415_48074_0001
20	6588_ASA_WSM_1PNACS20110511_075303_000000612099_00422_48081
21	6595_ASA_WSM_1PNACS20110519_075953_000000612100_00035_48196
22	6749_RS1_20110601051413.047.SCN8.NEAR.1.00000
23	3895_RS1_20110224054015.048.SCN.NEAR.1.36130
24	6613_RS2_20110504_062650_0046_SCNA_HH_SCN_131549_0000_0000000
25	6616_RS2_20110506_052538_0046_SCNA_HH_SCN_131838_0000_0000000
26	6617_RS2_20110507_045716_0046_SCNA_HH_SCN_131998_0000_0000000
27	6620_RS2_20110510_050917_0046_SCNA_HH_SCN_132481_0000_0000000
28	6622_RS2_20110512_055133_0046_SCNA_HH_SCN_132811_0000_0000000
29	6624_RS2_20110514_175050_0046_SCNA_HH_SCN_133199_0000_0000000
30	6632_RS2_20110524_050116_0044_SCNA_HH_SCN_134796_0000_0000000
31	6633_RS2_20110529_055544_0045_SCNA_HH_SCN_135605_0000_0000000
32	6634_RS2_20110530_052540_0043_SCNA_HH_SCN_135742_0000_0000000

33	3868_RS2_20110219_053920_0043_SCNA_HH_SGF_120541_2439_4687837
34	3885_RS2_20110206_164414_0045_SCNA_HH_SGF_118773_2062_4687797
35	5661_RS2_20110316_050953_0046_SCNA_HH_SGF_124056_3095_4984113
36	5667_RS2_20110330_162728_0045_SCNA_HH_SGF_126262_3562_4984131
37	5898_RS2_20110402_164004_0041_SCNA_HH_SGF_126674_3659_4984374
38	5914_RS2_20110422_053057_0045_SCNA_HH_SGF_129564_4267_4984341

Data Set 2 also consist of same validation dataset mentioned in Data Set 1 which are 82 ENVISAT ASAR and RADARSAT-2 SAR images consisted of 226 reported oil spill spots and 4670 'look-alike' features along with some additional RADARSAT-2 dataset as it generally used for operational activity. These 118 images (35 ENVISAT ASAR images with pixel spacing of 75m and 83 RADARSAT-2 SAR images with pixel spacing of 25m), containing 361 identified oil spills by service provider and 5728 potential look-alike spot identified by visual interpretation technique forms the reference dataset. Figure 3.28 shows an example RADARSAT-2 SAR image containing a verified oil spill reported by EMSA.

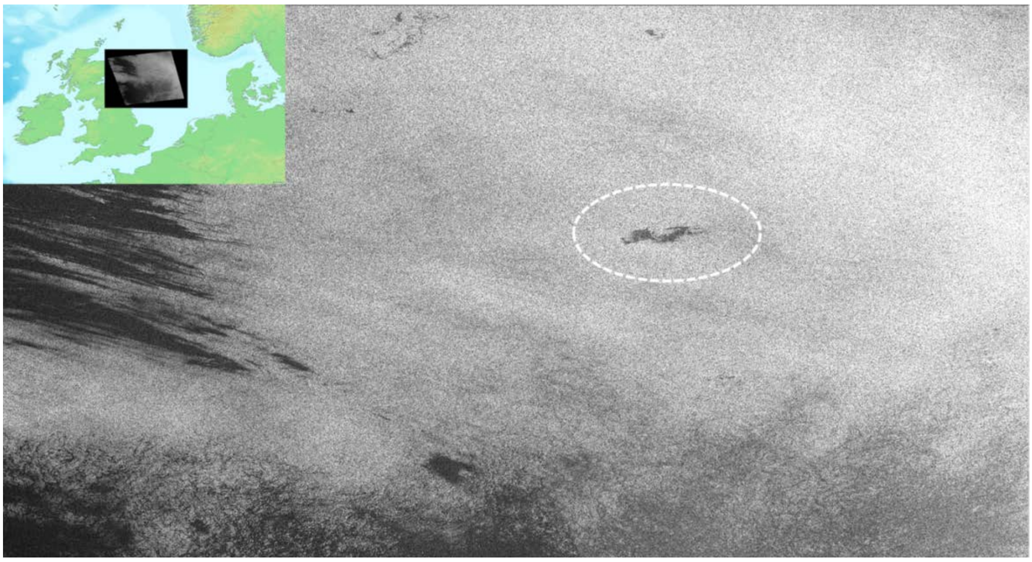

Fig 3.30: Example of dark spots on a RADARSAT-2 ScanSARNarrow Beam (SNB-1F) image acquired on 27th of March 2012 at 17:28:59 over North Sea near the coast north-east England and Scotland (Right hand side inset). The bright white circle showing the potential oil spill spots reported by EMSA. (CleanSeaNet Image ID: 21283, Radarsat-2 image © CSA/MDA/EMSA 2012, Singha *et. al.*, 2013b).

The image Pre-Processing is designed to compensate the trend of radar backscatter of the sea induced by the incidence angle increase at far range, typically yielding progressive brightness reduction over the image. This effect is particularly significant for wide swath radar modes of operation (Singha *et. al.*, 2013a, 2013c). The necessary radiometric normalization can be achieved by dividing the image cross-track profiles by the tangent function of the relevant incident angle. An alternative process to radiometric normalization is represented by image background removal. This de-trending approach, if designed for areas bigger than the size of the event of interest, compensates backscatter fluctuations due to large metoceanic phenomena, while preserving the smaller scale backscattering transitions due to vessels or oil spills. Image background removal also enables, through histogram stretching, transformation of the original image pixel values into an enhanced dynamic range that can be fully exploited by the subsequent segmentation procedure. Radar speckle reduction is also applied using 2-D edge preserving filters with variable kernel sizes depending on the image resolution. The image preparation procedure also implements land-masking in order to further reduce the computational burden of the subsequent image processing phase, which consists of dark areas segmentation and oil-spill/"look-alike" discrimination.

The backscatter statistical distribution remains almost unchanged by the whole pre-processing stage. Figure 3.31 shows the histogram of the native (blue) and pre-processed (green) data over the same area. The lower standard deviation is due to the normalization process, which reduces the brighter and increases the values of darker pixel. The image is an ASAR wide swath mode, with Equivalent Number of Looks ~14, which is a measure of the averaging process applied, therefore the backscatter converges to a normal distribution for the central limit theorem.

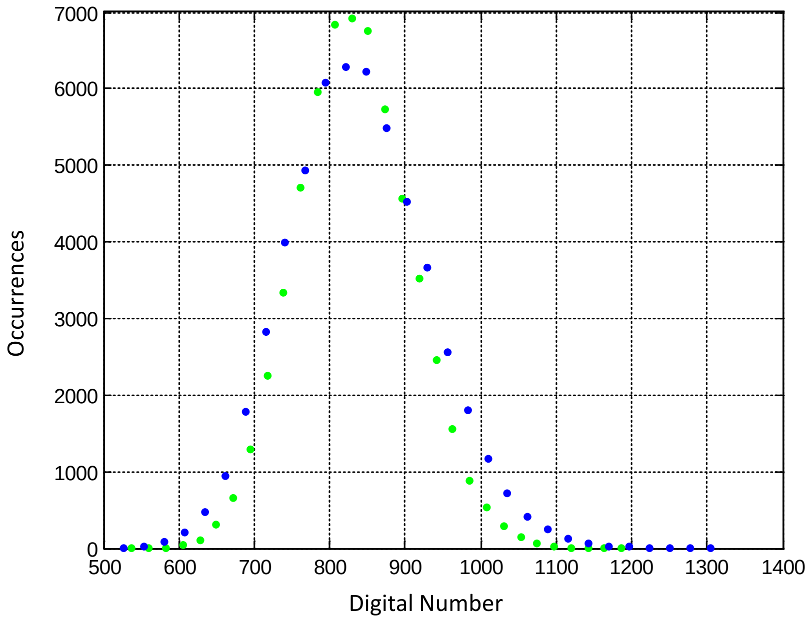

Fig 3.31: Statistical analysis of sea backscatter (land-free) distributions extracted by the native (blue) and pre-processed (green) data.

Image Pre-Processing highlights large bright areas presenting significant positive backscatter contrast (see Figure 1.c). The size of such bright objects is comparable to the size of the filter used to extract the image background, and can be linked to wind fronts and other instability areas. Bright objects are also of interest and are used in the classification process: as an example, if dark patches present high density of bright objects in their neighborhood, they can be discarded as being oil spills since potentially wind instability areas.

3.4 SEGMENTATION TECHNIQUES

Four diverse image segmentation techniques were performed and evaluated, Artificial Neural Network (ANN), Edge detection segmentation, Adaptive thresholding and Contrast split segmentation. Segmentation techniques have been chosen in a way that the whole processing chain achieve the near real time requirements.

Image segmentation in the new methodology is performed using a new Artificial Neural Network (ANN). This was compared against two established methodologies: i) Edge detection segmentation and ii) Adaptive Thresholding.

3.4.1 Segmentation using ANN

Figure 3 shows the architecture of the feed-forward back propagation neural network used for segmentation (Singha et al., 2012, 2013). The input layer consists of three neurons, corresponding to the intensity value of a given SAR image pixel, the 3 × 3 pixel-centered mean intensity and the 3 × 3 pixel-centered standard deviation. The output layer consists of two neurons corresponding to the two classes (i.e., dark spot and background). The numbers of neurons in the hidden layer was determined by trial and error (Atkinson and Tatnall 1997; Calabressi et al., 1999). For each SAR image, training areas pertaining to the dark formation and background were selected. The neural network architecture was then varied by adding hidden neurons and assessing the resulting effect on the accuracy of image segmentation. Fig 4(a) suggests that no significant changes in accuracy were observed after increasing the number of hidden neuron from six to seven and higher. Using the test data set described above, a hidden layer of six neurons was selected as optimal (Fig 3.28(b)).

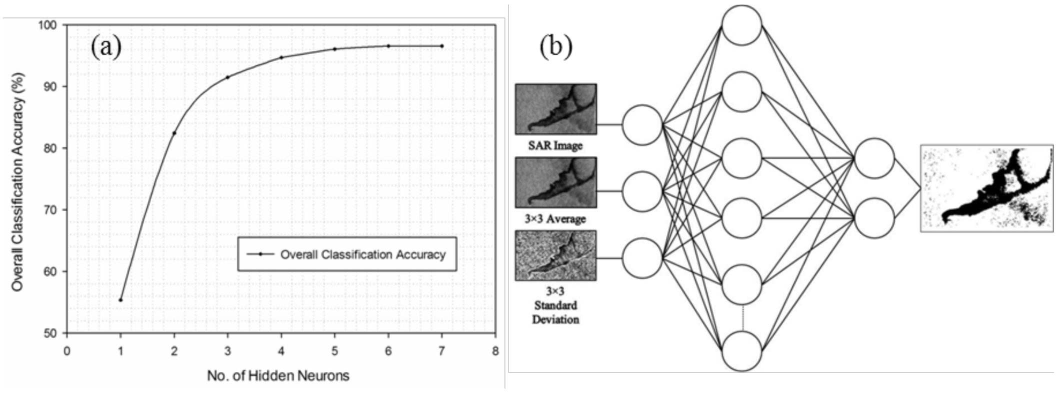

Fig 3.32: Accuracy assessment and ANN architecture for segmentation

3.4.2 Edge Detection Segmentation

Two alternative algorithms were implemented to assess the relative performance of the ANN approach with respect to established techniques. The first of these was Edge Detection (Pathegama and Göl 2005). In this type of segmentation, two types of parameters must be specified: edge detection parameters and segmentation parameters. The three edge detection parameters are: *pre-smoothing* factor, *threshold* and *minimal length*. The pre-smoothing factor specifies the number of times the image is smoothed before edge detection. A differencing threshold is then employed to detect edge pixels: if the difference between intensity value of a pixel and the intensity of one of its neighboring pixels is higher than the threshold, then the pixel is considered as a candidate for edge pixel. The appropriate threshold value is selected arbitrarily and varies from image to image. Specifying a higher threshold will result in smaller number of edges, which in turn may reduce the number of segments. As the pre-processed images were not affected by the reduced backscatter trend caused by increased incidence angles, a static threshold could be applied on each image, based on global statistics of individual image. In this study, threshold values varied from 45 to 70 DN for different SAR images in training and calibration dataset with an 8bit dynamic range.

The minimal length parameter refines the number of edges to be used for further analysis. Any edge lengths less than a minimum value, measured in pixel units, are eliminated. The segmentation parameter used for segmenting the image after edge detection is minimum value difference. *Minimal Value Difference:* Specifies the minimum value difference between neighboring segments. Specifying the higher minimum value difference results smaller number of segments. If the value difference between neighboring pixels is less than minimum value, then these are considered as a part of the same segment. Both of these parameters were manually optimized on an image by image basis.

3.4.3 Adaptive Thresholding

The second established segmentation technique employed was Adaptive Thresholding (Solberg et al., 1999). Here the detection threshold for a given pixel is set to a fixed dB below the mean value of an encompassing 5×5-pixel moving window. This technique has proven to be both robust and simple to implement. The optimal threshold separation is dependent on wind speed. In this present study, as wind speed data was unavailable, the threshold was set to 50 (manually optimized for 8-bit dynamic range) to give an optimal result. Fig 6 shows an image segmentation using the edge detection and adaptive thresholding approaches.

3.4.4 Contrast Split Segmentation

The Contrast Split Segmentation algorithm segments an image into high and low backscatter regions. It is based on a threshold that maximizes the contrast between the resulting bright objects (consisting of pixels with pixel values above the threshold) and dark objects (consisting of pixels with backscatter values below the threshold). The algorithm first executes chessboard segmentation, which splits the image into square objects 50×50 window, then performs the split on each square. It achieves the optimization by considering different pixel values as potential thresholds.

The test thresholds range from the minimum threshold to the maximum threshold, with intermediate values chosen according to the step size and stepping type parameter. If a test threshold satisfies the minimum dark area and minimum bright area criteria, the contrast between bright and dark objects is evaluated. The test threshold causing the largest contrast is chosen as the best threshold and used for splitting a predefined 50×50 window. This is followed by a preliminary discrimination stage based on size of the dark patch detection and its distance to the shoreline as shown in Fig 3.33. Specifically, in order to further reduce small detections due to speckle and large patches due to met-oceanic look-alikes, only the dark areas with a size between 0.15 km^2 and 35 km^2 are considered. It is worth noting that operational spills larger than this threshold are seldom observed and that, when observed, are however likely to be fragmented into smaller areas. Moreover, the patches very close to land areas are filtered out as most often its lookalike induced by wind shadow areas (in some cases river outflows). The segmentation algorithm was applied to the 38 images, leading to 40358 identified patches which can be oil spills or look-alikes from ENVISAT ASAR and 24539 from RADARSAT products.

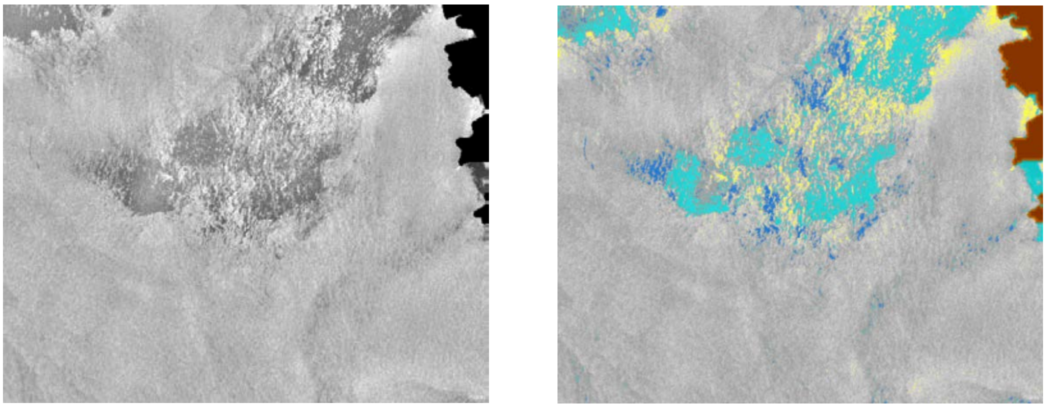

Fig 3.33: Radiometric normalized input image (left) and contrast based segmentation (right). Bright objects are highlighted in yellow, while darker objects (dark blue) are selected between the low backscattering patches (blue) on the basis of their area and distance from land (brown).

Evaluation of each technique and segmentation results are discussed the next chapter along with comparison between different techniques.

3.5 Feature Extraction

Two different feature extraction parameter set have been used for this study, first feature extraction parameters set was designed as feed for the Artificial Neural Network and the second one is designed for the rule-based algorithm. The output of the segmentation stage is a binary image depicting dark objects and the background. The next stage of the algorithm involves the generation of a vector of features that quantitatively describe relevant characteristics of the object, including: backscattering attenuation, shape, size, texture, and boundary characteristics. The resulting vector depicts the characteristics of each object and forms the basis for computing feature descriptors.

Feature Set 1:

A range of features have been suggested in the literature (Solberg et al., 1999, 2007; Fiscella et al., 2000; Del Frate et al., 2000; Topouzelis et al., 2003, 2007, 2008; Brekke and Solberg 2005). Based on a review of previous studies, 14 feature parameters were selected. These are listed in Table 1.

Table 3.2 Set of feature parameters used for ANN base methodology

Feature Category	Features	Descriptions
Shape Features	**1.Area (A)**	The area of the dark spot measured in pixel units from a vectorized image
	2.Perimeter (P)	The total boundary length of the dark spot measured in pixel units from a vectorized image.
	3.Shape complexity: Perimeter to Area Ratio (C)	The perimeter of the image object divided by two times the square root of its area multiplied by π. $C = \frac{P}{2\sqrt{\pi A}}$
Backscatter	**4. Dark spot mean**	Mean value of the pixels

Features	**(μ_d)**	belonging to dark spot.
	5. Dark spot standard deviation (σ_d)	Standard deviation value of the pixels belonging to dark spot.
	6. Backgrounds mean (μ_b)	Mean value of the pixels belonging to local background area around the dark spots.
	7. Backgrounds standard deviation (σ_b):	Standard Deviation value of the pixels belonging to local background area around the dark spots.
	8. Dark spot power to mean ratio $\left(\frac{\sigma_d}{\mu_d}\right)$	Ratio between standard deviation and mean value of the pixels belonging to the dark spot.
	9. Background power to mean ratio $\left(\frac{\sigma_b}{\mu_b}\right)$	Ratio between standard deviation and mean value of the pixels belonging to the background.
Gradient Features (gradient calculation see text)	**10. Gradient mean (μ_g)**	Mean value of the gradient.
	11. Gradient standard deviation (σ_g)	Standard deviation value of the gradient.
	12. Gradient max (G_{max})	Maximum value of the gradient.
	13.Gradient min (G_{min})	Minimum value of the gradient.
	14. Gradient power to mean ratio $\left(\frac{\sigma_g}{\mu_g}\right)$	Ratio between gradient standard deviation and gradient mean value.

Three categories of feature were taken into account: shape, backscatter and gradient. Gradient values were calculated using a SOBEL operator (Richards and Jia 1999). This is a discrete differentiation operator, computing an approximation of the gradient of the image intensity function. At each point in the image, the result of the SOBEL operator is either the corresponding gradient vector or the norm of this vector. The SOBEL operator is based on convolving the image with a small, separable, and integer valued filter in the horizontal and vertical directions and is therefore relatively inexpensive to compute. However, this gradient approximation is relatively crude, in particular for high frequency variations in the image. The operator uses two 3×3 kernels which are convolved with the original image - one for horizontal changes G_x, and another for vertical G_y (Keramitsoglou et al., 2006). If **A** is the source image, and $\mathbf{G}_x$ and $\mathbf{G}_y$ are the horizontal and vertical derivative approximations, then:

$$G_Y = \begin{bmatrix} +1 & +2 & +1 \\ 0 & 0 & 0 \\ -1 & -2 & -1 \end{bmatrix} \otimes A \qquad \text{and} \qquad G_X = \begin{bmatrix} +1 & 0 & -1 \\ +2 & 0 & -2 \\ +1 & 0 & -1 \end{bmatrix} \otimes A \tag{3.8}$$

Where $\otimes$ denotes the 2-dimensional convolution operation.

At each point in the image, the resulting gradient approximations can be combined to give the gradient magnitude, using:

$$G = \sqrt{G_x^2 + G_y^2} \tag{3.9}$$

This information can also be used to calculate the gradient's direction:

$$\Theta = \arctan 2\left(G_y, G_x\right) \quad with\ \Theta\ in\left[-\pi, \pi\right] \tag{3.10}$$

For example, Θ is 0 for a vertical edge which is darker on the left hand side. The gradient power to mean ration is used to represent the contrast in the gradient image in quantitative terms (Richards and Jia 1999).

Feature Set 2:

The second set of feature extraction parameters involves the generation of a vector of features that quantitatively describe relevant characteristics of the object such as backscatter, shape, size and textures (e.g. Grey Level Co-occurrence Matrix GLCM, Haralick et al., 1973). Number of elements in this set is higher than the previous as this set is designed for rule based classifier and consider contextual features (e.g. distance to shore line, association with possible source). Although features shape and backscatter have been commonly used in literature, gradient features are relatively untested with only gradient magnitude having been previously studied (Solberg et al., 1999). From each segmented image, based on the indications (treated as ground truth) given by 'CleanSeaNet', the set of samples from both look-alikes C_{LL} and oil spill C_{OS} classes are formed. The sets have been additionally divided into ENVISAT ASAR and RADARSAT sensors given the different resolution, polarisation and radiometric properties of the two instruments. Each sample is characterised by a series of features that are then analysed in order to select the most suitable samples for classification purposes. These features are grouped into categories as shown in Table 3.3

Table 3.3: Set of feature used for classification based methodology

Shape Features	Backscatter Features
- Area	- Normalised Amplitude
- Border Length	- Standard Deviation
- Length	- Contrast to Neighbour Pixels
- Width	- Standard Deviation to Neighbour Pixels
- Length/Width	- Mean Difference to Neighbour Objects
- Compactness (Polygon)	
- Asymmetry	***Texture Features***
- Density	- GLCM Homogeneity
- Shape Index	- GLCM Contrast
- Length of Longest Edge (Polygon)	- GLCM Dissimilarity
- Number of Edges (Polygon)	- GLCM Entropy
- Number of Inner Objects	- GLCM Ang. 2nd moment
- Perimeter (Polygon)	- GLCM Mean
- Average Branch Length	- GLCM standard deviation
- Average Area Represented by Segments	- GLCM Correlation
- Curvature over Length	
- Degree of Skeleton Branching	***Spatial Features***
- Length of Main Line (no Cycles)	- Number of Bright Patches - Number of Low Backscattering Patches
- Length/Width (only Main Line)	- Rel. area of Bright Patches
- Number of Segments	- Distance to Shore Line
- Curvature Standard Deviation	- Rel. area of Low Backscattering Patches
- Standard Deviation of Area represented by Segments	
- Width (only Main Line)	

In order to evaluate the spatial relationships between objects, basic geometric properties were calculated including distance and relative areas (in number of pixels) with respect to either the entire scene or a certain region. Detailed descriptions of the 41 listed features can be found in Table 1.

From a basic analysis of the feature histograms their distributions are often multimodal *non-parametric*. The density function estimation $p(f_i \;|C)$ of the i-th feature f_i is implemented through a window that adapts depending on the volume of data, such Parzen Window (Duda et al., 2001). Once the probability densities are evaluated for each class, the degree of class separation can be measured by using the Patrick-Fisher distance, defined as follows:

$$d(f_i)_{PF} = \left(\int_D \left[p(f_i(x) \mid C_{OS}) P_{OS} - p(f_i(x) \mid C_{LL}) P_{LL} \right]^2 dx \right) \tag{3.11}$$

where the probabilities can be thought of as risk of pollution (P_{OS}) and probability of observing a look-alike (P_{LL}) over the area of interest. If a dark patch is detected in the proximity of a shipping lane, for example, this can be modelled by increasing P_{OS}. Nevertheless, in this study we concentrate on evaluating a score of class separation for the single features f_i. The events “oil spill” and “look-alike” are assumed equally probable, therefore the prior probabilities are P_{OS} = P_{LL} = 0.5. Equation 1 allows a ranking of the single features based on their density functions. In the following figures, the densities of the feature parameters are shown for ENVISAT ASAR and RADARSAT SAR images together with the relevant histogram, non-parametric distribution and distribution with lowest residue. Majority of the distribution were tested for the lowest residue. ‘Generalised Extreme Value’ (GEV) distribution achieved lowest residue for each feature. A detailed statistical analysis for those extracted feature given in the next chapter.

3.6 Classification

Two separate classifiers have been developed, first one is based on Artificial Neural Network and second one is a non-parametric classification approach represented by Classification (or decision) Trees.

3.6.1 Artificial Neural Network

In the final processing stage, a neural-network based classifier is trained and used to distinguish oil spills from look-alikes based on the fourteen-element feature vector describing each dark object. A range of feed-forward network architectures were investigated, with a final topology of 14-14-5-1 (two hidden layers; Figure 3.30) found to be the most accurate as well as efficient (see the Results section below).

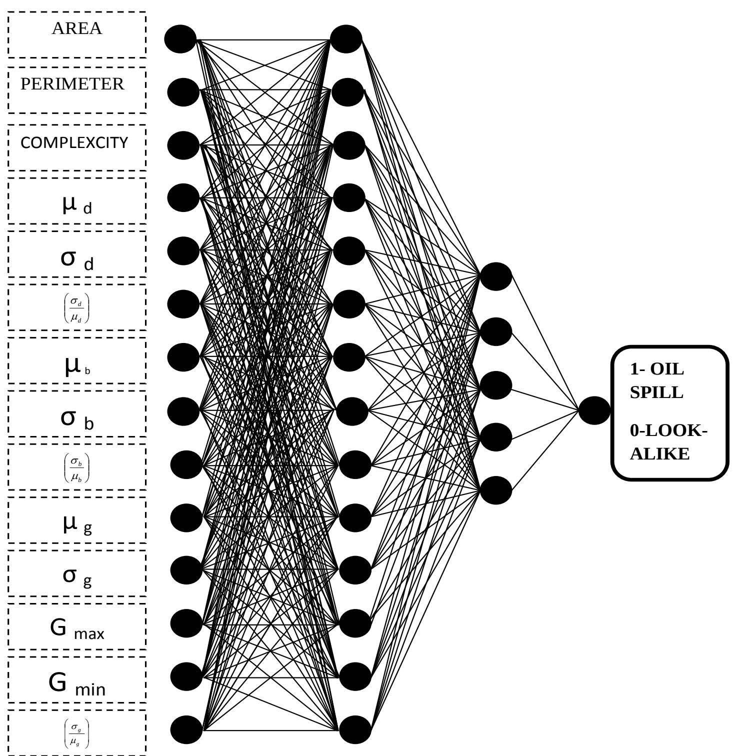

Fig 3.34: Schematic diagram of the Neural Network implemented for classification between oil spills and look-alikes.

Several different combinations of training set, testing set and neural network training parameters (including momentum factor, learning rate and the number of iterations) were tested in order to optimize classification accuracy.

Calibration on this proposed methodology based on ANN was carried out using a large dataset obtained from European Maritime Safety Agency. Calibration process and results obtained using this algorithm is presented in the Results and Discussion chapter.

3.6.2 Rule Based classification

Classification is implemented using a preliminary classification-tree classifier followed by a fuzzy logic algorithm. The subdivision in two stages is motivated by the highly unbalanced dataset, where look-alikes outnumber oil spill area samples. For this reason, a relatively small false alarm rate will still remain in a high number of look-alikes classified as oil spills, calling for an additional discrimination stage. In other words, through the implementation of a cost function, the first classification stage has the objective of balancing the dataset by introducing two different weights to misclassification error: the cost associated to look-alikes classification as oil spills is lower than the one related to missed oil spill detection (i.e. oil spill classified as look-alikes).

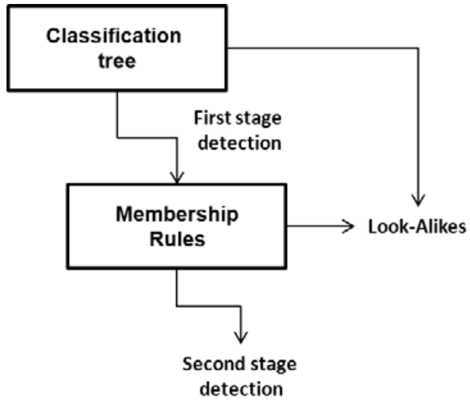

Fig 3.35: Two-stage classification process.

Classification Tree Definition

A non-parametric classification approach is represented by Classification (Decision) Trees. Such methodology is based on binary recursive splitting of data into branches, identifying the higher separation between the classes. In our case, the partition is based on the probability density functions described in the previous Section. At each node, the best rule that splits the data into the two classes is chosen in terms of higher separation between the data. After the tree is formed using the set of available "training" data, its performance is evaluated on additional mutually exclusive data. This stage is also known as "validation". The size of the obtained tree is a measure of its complexity. It's been observed that higher the complexity of the tree, the lower the generalisation capabilities of the classifier. If the tree size increases, classification performance over spills not used in the training phase is reduced. This is a consequence of the fact that the tree performs well only on the specific data set used to define it ("overfitting"). The selection of a tree that minimises both classification error and complexity is therefore envisaged. The validation phase therefore allows to "prune" the tree, and to reduce the complexity while increasing the generalisation performance.

One of the validation techniques widely used on predefined set of data is the *N*-fold cross validation. This is performed on the dataset by randomly partitioning the samples into *N* subsets of approximately equal size and class proportion. *N*-1 sets are used to build the training set, while the remaining set is used for validation. The cross-validation is then repeated *N* times and each one of the *N* subset of data is used only once as validation data. The 10-fold cross-validation is implemented in this work to estimate the misclassification error (number of misclassified samples over the total number of samples) related to a specific tree configuration. This means that different tree configurations are built using 9 oil spill and look-alike subsets and tested over the remaining one. In the following, the tree configuration analysis is reported separately for the ASAR and RADARSAT instruments (Singha et al., 2013b).

ASAR

After cross-validation, the resulting tree is chosen on the basis of the minimum misclassification error (see Fig 3.36) and complexity. This is represented by a 15 leaf node tree (see Fig 3.37).

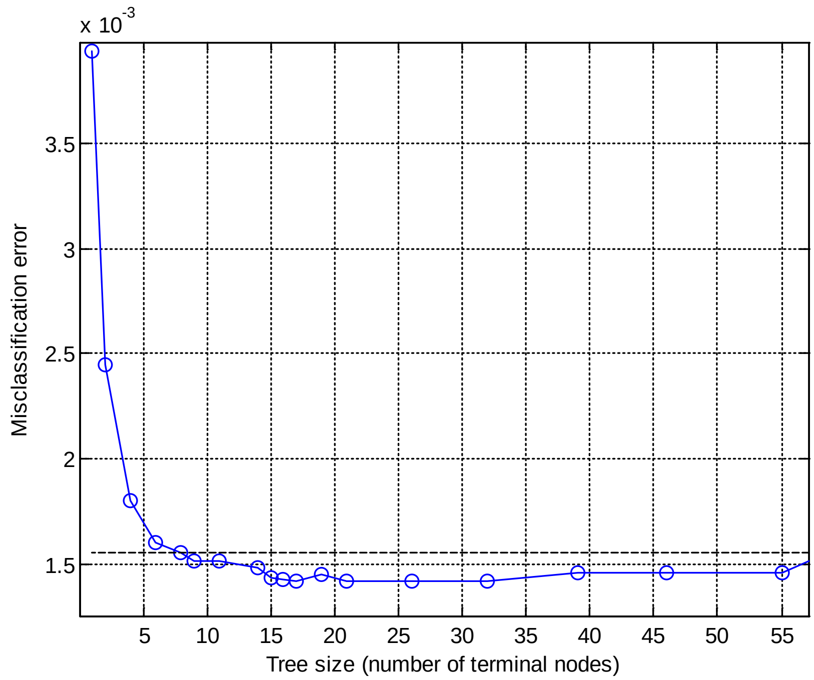

Fig 3.36: ASAR misclassification error associated to tree size and one standard error above the minimum misclassification error tree (dashed).

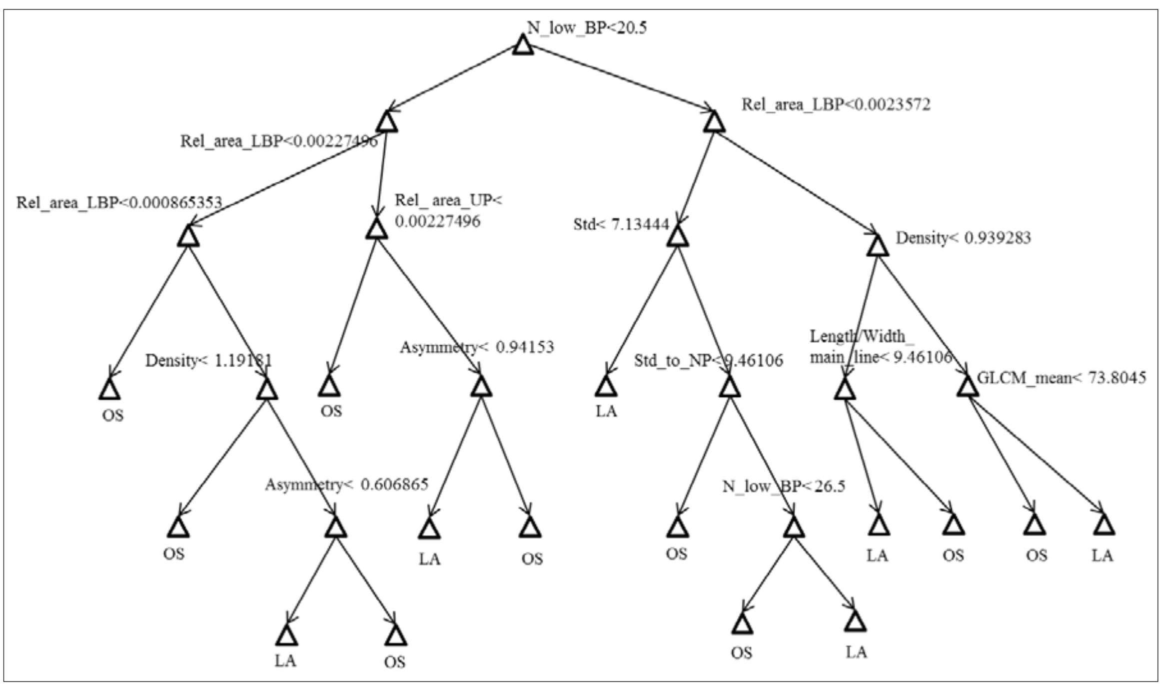

Fig 3.37: ASAR selected classification tree.

The results of the selected tree on the entire set of look-alikes and oil spills training samples leads to a False Alarm Rate (*FAR)* = 0.011 and Correct Classification Rate (*CCR)* = 0.8742.

RADARSAT

From the classification tree analysis of the dark and bright object extracted from RADARSAT-1 and -2 ScanSARNarrow mode images, the minimum error (see Figure 3.38) is represented by a tree with 28 terminal nodes. In order to reduce the complexity, a 22-node tree is selected, representing a reasonable trade-off between classifier complexity and misclassification cost.

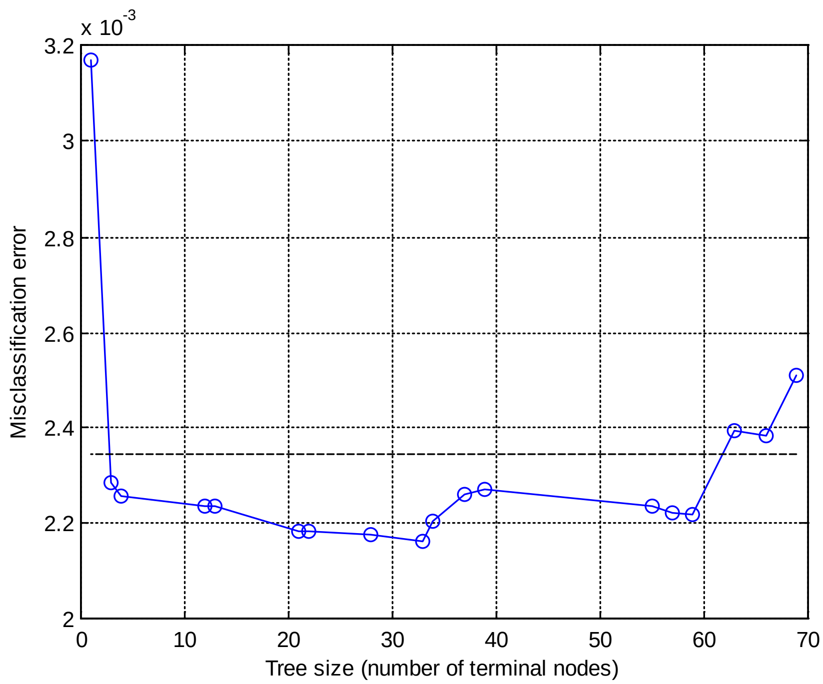

Fig 3.38: RADARSAT misclassification error associated to tree size and one standard error above the minimum error tree (dashed).

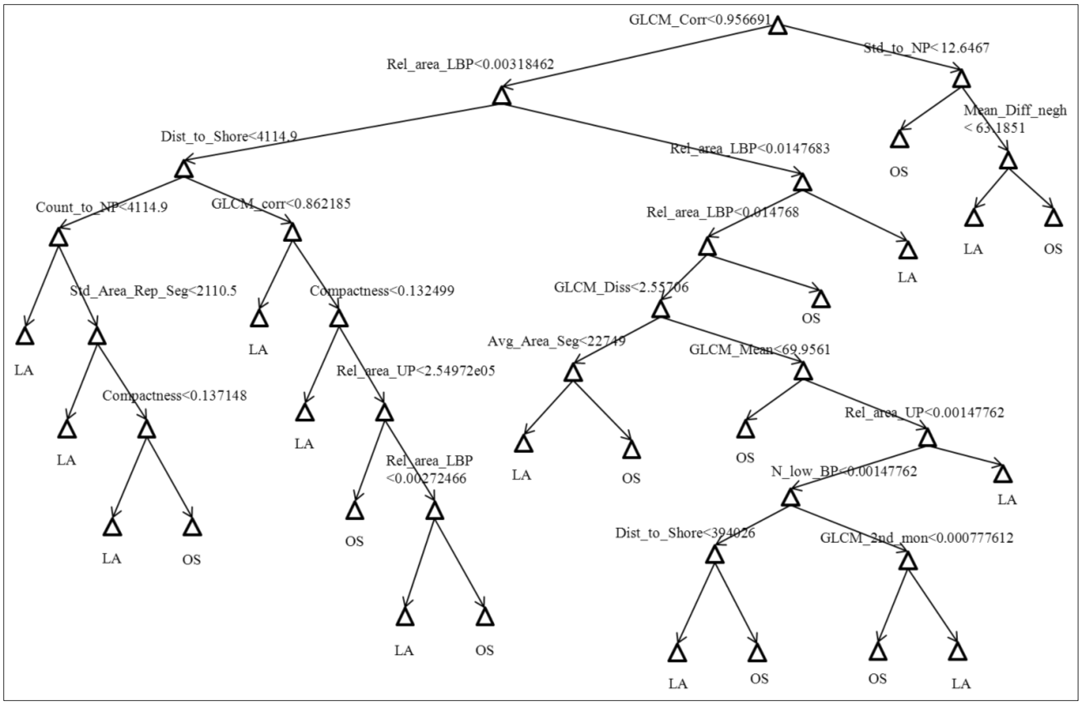

Fig 3.39: RADARSAT-1 and -2 selected classification tree.

The tree implemented follows the structure reported in Figure 3.39. The classification results of the classification tree obtained by this analysis yields the following performance *FAR*= 0.084 and *CCR* =0.756.

As expected the classification trees for both instruments, in the higher level nodes, somehow reflect the feature ranking tables (see Section 2.4).

Fuzzy Logic Analysis

The cost is related to classifying a dark patch as look-alike if the true class is an oil spill and vice versa. In this work we favor the misclassification of look-alikes as oil spills over missed detections. For this reason, the potential detected oil spill candidates are further analyzed through an additional discrimination stage in order to reduce the number of false alarms. The second classification stage employs membership functions derived from the probability densities of false alarms produced by the previous classification stage for some features described in Section 2.4 (Figure 3.35). It was observed that many of the look-alikes misclassified by the first stage are characterised by the combination of significant brightness and a large size. Others present high brightness associated with an edge contrast that is lower than typical oil spills, or a smaller difference between inner and outer object boundaries. Some of these composite conditions only apply in low homogeneity areas: a large pixel standard deviation suggests non-uniform wind conditions that often lead to look-alikes. These rules have been implemented as fuzzy logic categories membership functions. The results using this proposed methodology is presented in the next chapter.

3.7 ANN Classification and Validation

In order to compare the results from rule based classifier, previously implemented ANN classification method has been adopted and trained for full spectrum of feature parameters. A total of 970 feature vectors were generated, among which 700 were used for ANN training purpose and 270 were used for ANN performance validation after training. An additional 108 feature vectors were used for network performance testing. All training, validation and testing dataset are mutually exclusive and include sufficient number of oil spill and look alike examples. Details of training and testing of the neural network is described below.

Various neural network architectures were tested in order to achieve optimum accuracy keeping in mind the near real time performance of the entire processing chain. Framework of determining optimum neural network architecture is described in section 3.3. After network performance evaluation a neural network with 41 input neuron and 90 hidden neuron (41:90:1) has been selected for its optimal performance.

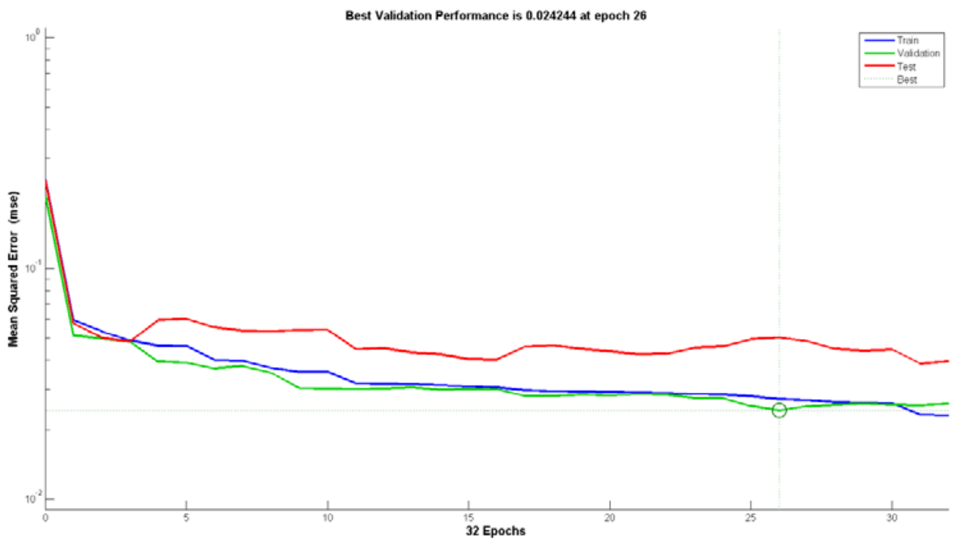

Fig 3.40: Network performance estimation for full spectrum of feature extraction parameters.

During the validation of the neural network, optimum performance was achieved within 25 to 35 iterations with approximately 98% classification accuracy. The neural network performance curve for all training, validation and testing stage is presented in Fig 3.40.

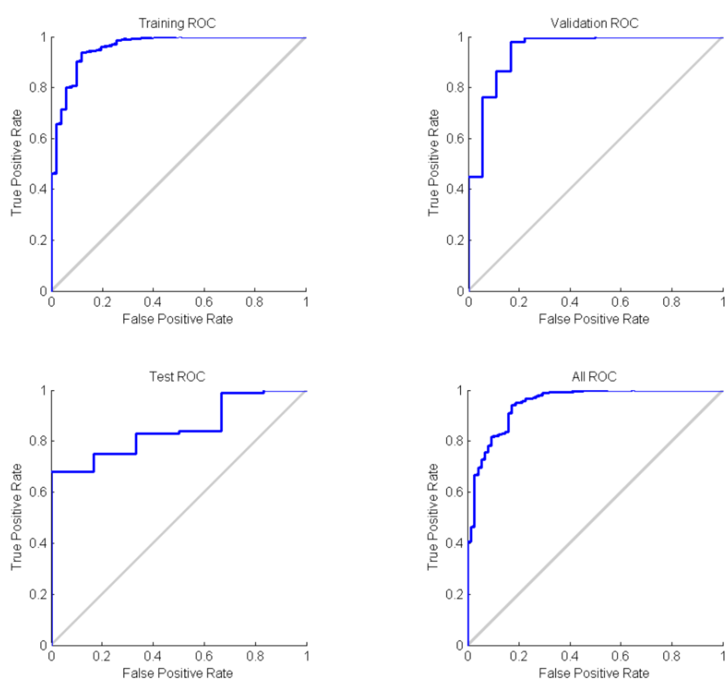

Fig 3.41: ROC curves for training, testing and validation of neural network.

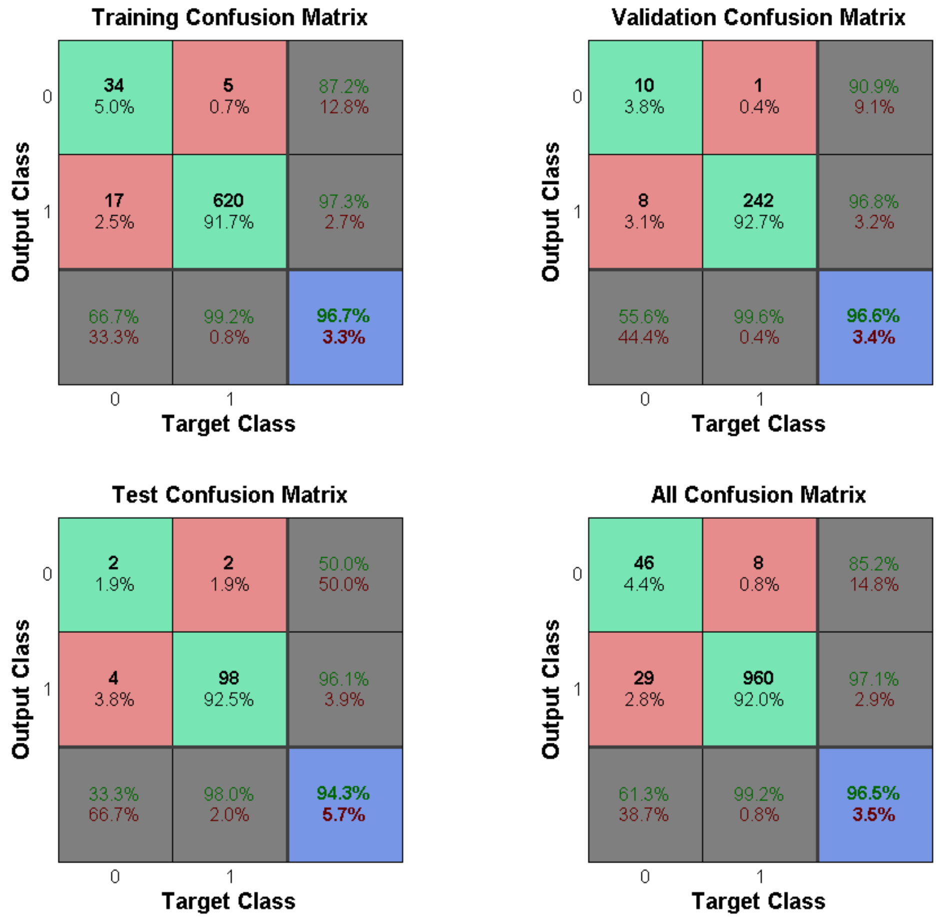

Fig 3.42: Confusion matrix for training, validation and testing dataset.

Fig. 3.41 shows the ROC curve for all stage of the neural network development along with confusion matrix in Fig 3.42. Classification accuracy of 96.6% and 94.3 % were achieved for validation and test dataset respectively. A detailed evaluation and results of the proposed neural network is presented in the next chapter.

The work presented in this chapter was supported in part by the European Maritime Safety Agency–European Commission-Joint Research Centre collaboration for the development and support of satellite monitoring techniques for oil spill detection. The views, opinions, and findings contained in this chapter are those of the author and should not be construed as an official EMSA, JRC or European Commission position, policy, or decision. The

development of preprocessing tool for SAR oceanographic application and methodologies are reported and published in *Marine Pollution Bulletin, IEEE Journal of Selected Topics in Applied Earth Observations and Remote Sensing* and in different conference proceedings. Some of the figures and findings are directly adopted from journal articles listed below.

Journal article: ***S. Singha,*** *M. Vespe and O. Trieschmann, "Automatic SAR based Oil Spill Detection and Performance Estimation via Semi-Automatic Operational Service Benchmark",* ***Marine Pollution Bulletin****, Volume 73, Issue 1, Pages 199–209, 15 August 2013.*

Journal article : ***S. Singha,*** *T. Bellerby and O. Trieschmann, "Satellite oil spill detection using artificial neural networks",* ***IEEE Journal of Selected Topics in Applied Earth Observations and Remote Sensing****, Volume 6, Issue 6, Pages 2355–2363, December 2013.*

Journal article: **S Singha,** D Velotto and S Lehner, "Near Real Time Monitoring of Platform Sourced Pollution using TerrraSAR-X over the North Sea" *Marine Pollution Bulletin, Volume 86, Issue 1-2, Pages 379‑390,* 15 July 2014.

Conference Paper: ***S. Singha****, T. J Bellerby and O. Trieschmann, "Detection and classification of oil spill and look-alike spots from SAR imagery using an artificial neural network", In Proc.* ***IEEE International Geoscience and Remote Sensing Symposium*** *2012, Munich, Germany, pp.4403-4406.*

Conference Paper: ***S. Singha****, K. Topouzelis, M. Vespe and O. Trieschmann, "Radiometric Normalization on SAR Images for Oil Spill Detection", In Proc.* ***ESA Living Planet Symposium*** *2013, Edinburgh, United Kingdom.*

CHAPTER 4
RESULTS AND DISCUSSIONS

4.1 INTRODUCTION

In the previous chapter, the concept and the implementation of the techniques used were introduced. This chapter discusses the results of experiments carried out in this study for oil spill detection involving three parts of the methodology, i.e. dark spot segmentation, feature extraction and finally classification on two separate training and a common validation dataset.

4.2 DARK SPOT SEGMENTATION TECHNIQUES

In order to investigate the efficiency of different dark spot detection techniques, image segmentation based on edge detection adaptive thresholding and neural network have been implemented on the ERS-2, ENVISAT and RADARSAT-2 SAR images. Results for all the techniques have been presented in this section.

The new ANN based segmentation technique was implemented using the 97-image training and calibration dataset described in the previous chapter. To evaluate the initial, image segmentation stage of the algorithm, two alternative segmentation techniques (edge detection and adaptive thresholding) were also applied to the calibration dataset. Figure 4.1(b) shows an example output from the neural network image-segmentation stage for a dark spot. Figure 4.1 (c) shows the same output for adaptive thesholding and Figure 4.1 (d) for edge detection. The neural network approach, while not generating a perfect classification, does appear to be relatively robust against noise.

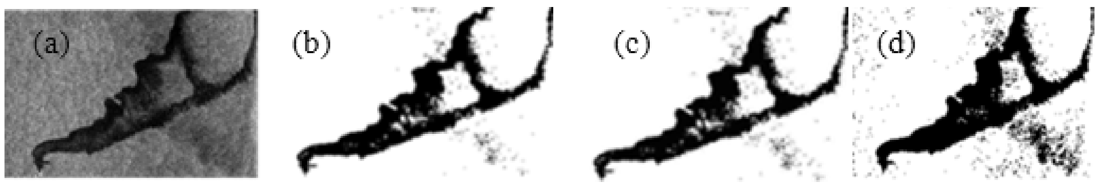

Fig 4.1: Segmentation of an example SAR image (ENVISAT ASAR Wide Swath image acquisition date: 17 November 2002) (a) SAR image containing dark spot. (b) Segmentation using ANN. (c) Segmentation using Adaptive Thresholding. (d) Segmentation using Edge Detection.

In order to assess the image segmentation stage, a manual image classification was performed on each image. Contrast Split Segmentation was not considered as it generates more than two classes and implementation was based on a separate dataset. Figure 4.2 compares the overall segmentation accuracies using edge detection, adaptive thresholding and neural network, validated against manually segmented imagery for a subset of training and calibration dataset. The average accuracy (accuracy assessment was carried out using confusion matrix for each image) obtained using edge detection was 59.27% and for Adaptive Thresholding was 74.13%, whereas the average overall accuracy achieved using the neural network was 96.57%.

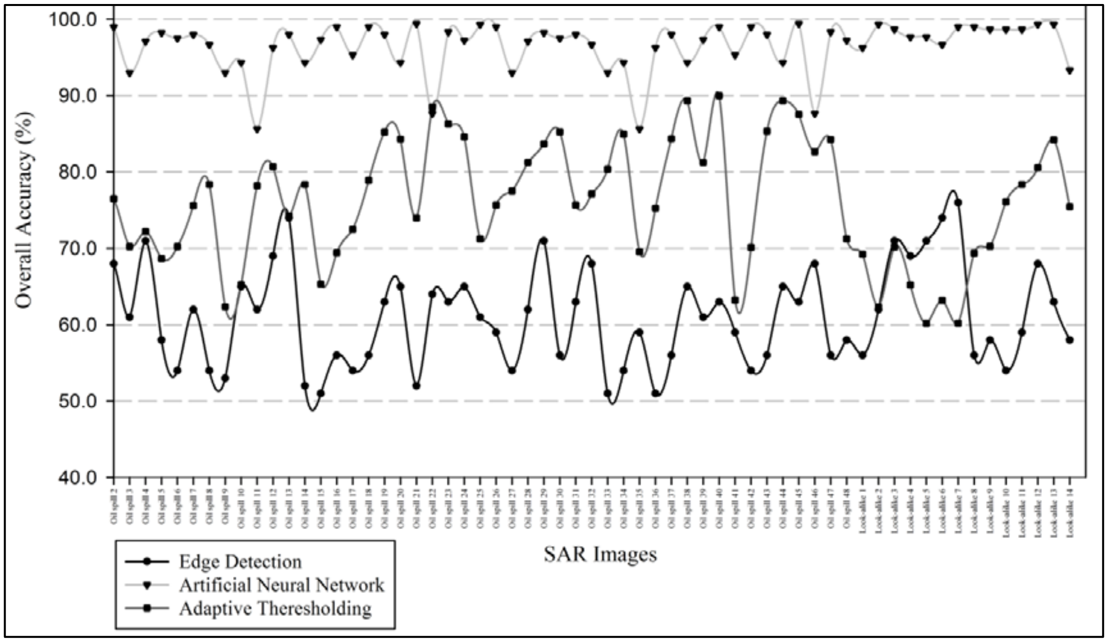

Fig 4.2: Comparison of the segmentation accuracy obtained using Edge Detection, Adaptive Thresholding technique and the proposed ANN.

Contrast Split Segmentation

Contrast Split Segmentation (eCognition Developer, 2010) is applied after pre-processing as discussed in the previous chapter. Clusters of pixels are thus formed depending on a threshold adaptively computed for each sub-image maximizing the contrast between bright and dark object. Clusters of bright and dark pixels belonging to adjacent sub-images are then collated together. This is followed by a preliminary discrimination stage based on size of the dark patch detection and its distance to the shoreline. Contrast split segmentation applied on a pre-processed RADARSAT-2 SAR image shown the Figure 4.3.

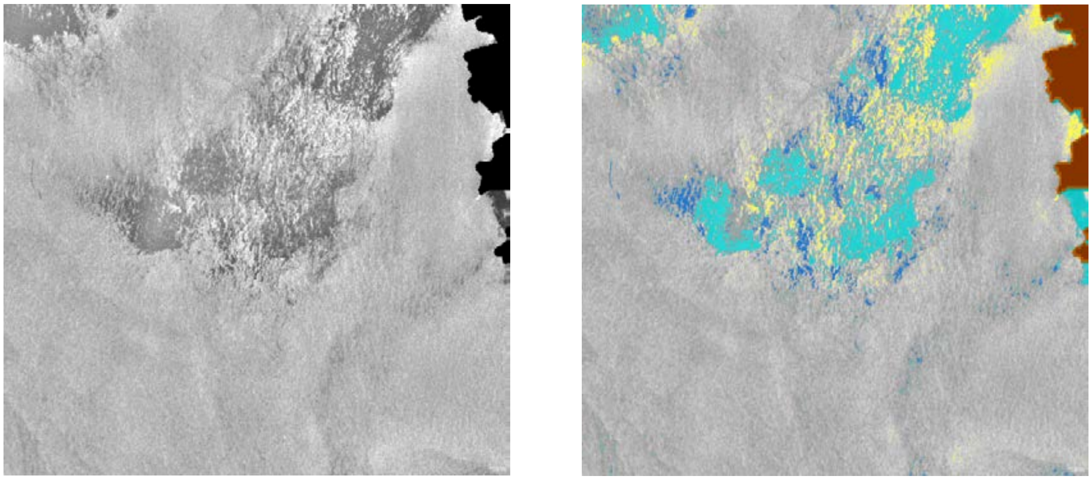

Fig 4.3: Radiometric normalized input image (left) and contrast based segmentation (right). Bright objects are highlighted in yellow, while darker objects (dark blue) are selected between the low backscattering patches (blue) on the basis of their area and distance from land (brown).

4.3 FEATURE EXTRACTION

Feature Set 1:

A set of features has been calculated for 903 dark objects, in which 183 are oil spills, and 720 are look-alikes. As the data were collected for European Maritime Safety Agency's (EMSA) CleanSeaNet service, the ground truth was known for most of the cases. In Table 4.1, some statistical parameters of the features extracted from these datasets are reported. The table shows that oil spills have less complex, while in case of the look-alikes, the values of the backscattering either in the object or in the surroundings are more dispersed. Also, oil spills show mean value of the gradient along the border higher than look-alikes. Look-alikes are generally much larger than oil spills. Dark spots power to mean ratio for oil spill is significantly lower than the look alike. It can also be observed from Table 4.1 that 'Gradient

Min' did not perform well compared to other parameters in terms of segregating two types of spots.

Fig. 4.4 illustrates the response of Sobel operator on a SAR image containing oil spill spot**.** The operation of Sobel operator creates the image presented in Fig 4.4 where the texture of the background class and the dark spot becomes almost similar to each other, although the boundary between background class and dark spot turns to be much brighter than the background texture. The magnified view of a portion of the boundary region has been shown aside.

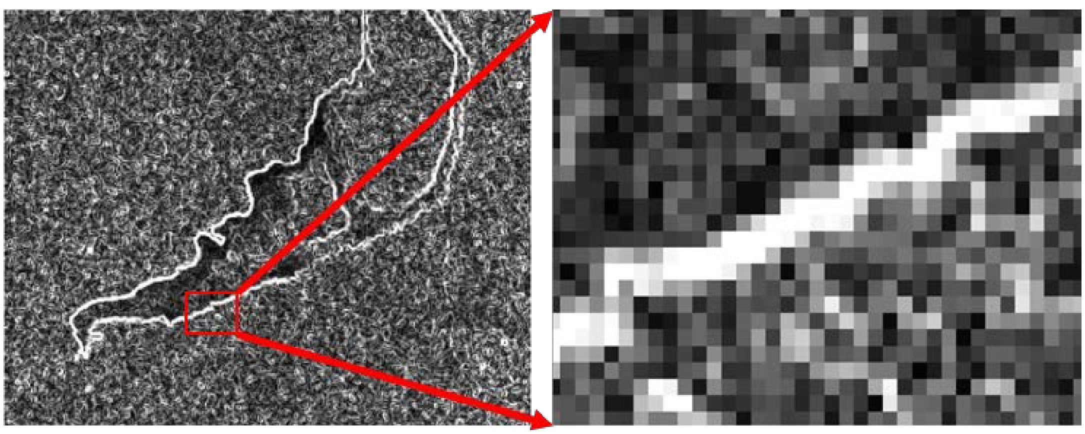

Fig 4.4: Implementation of SOBEL operator on a SAR image

Table 4.1: Extracted feature parameters for ANN based Methodology (Data Set 1)

Feature Parameters	**Oil Spill Spot**		**Look-Alike Spot**	
	Mean	**Standard Deviation**	**Mean**	**Standard Deviation**
AREA	145.705	447.963	58613.997	118732.399

PERIMETER	129.974	307.935	13712.673	29226.876
COMPLEXITY	6.445	4.246	11.857	12.108
DARK SPOT MEAN	25.456	8.931	5.913	5.923
DARKSPOT S.DEV	20.105	5.116	13.170	11.072
DSPMR	0.820	0.118	2.793	0.874
BACKGROUND MEAN	124.892	23.254	157.518	21.295
BACKGROUND S.DEV	22.692	9.648	21.018	5.489
BPMR	0.183	0.080	0.135	0.038
GRADIENT MEAN	114.375	42.068	93.517	21.698
GRADIENT S.DEV	84.672	21.951	68.625	17.326
GRADIENT MAX	854.579	145.781	930.531	207.372
GRADIENT MIN	1.439	0.120	1.384	0.110
GRDPMR	0.766	0.117	0.745	0.129

DSPMR – Dark Spot Power to Mean Ratio, BPMR – Background Spot Power to Mean Ratio, GRDPMR – Gradient Power to Mean Ratio.

Feature Set 2:

A total of 41 features presented in previous III, (Table 3.3) were extracted from 237 oil spill and several look-alike features. Extracted features were analysed by deriving Patrick-Fisher distance between the two classes, separately for the two instruments, ENVISAT ASAR and RADARSAT-1/2 SAR. The relevant ranking is reported in Table 4.2 (Based on Patrick-Fisher feature ranking). As previously anticipated, the ranking analysis shows how some features densities are quite dissimilar between the ASAR and RADARSAT instruments, leading to the conclusion that two different classification processes have to be designed accordingly and seperately. It is also worth underlining that spatial relationship features are characterised by significant discrimination potential. In particular, the number and the relative area of low backscattering patches identify the most discriminating features. Fig 4.5 and 4.6 shows the distribution of each feature parameters for ENVISAT ASAR and RADARSAT-2 separately.

Table 4.2: Patrick-Fisher feature ranking, ASAR (left) and RADARSAT (right) data (Data Set 2).

	Feature (ASAR)	*Score*
1	Rel. area of Low Backscattering Patches (50)	1.1825
2	Std Dev of Area represented by Segments	1.0534
3	GLCM Correlation (all dir.)	1.0190
4	Width (only Main Line)	0.9475
5	Average Area Represented by Segments	0.9325
6	GLCM Mean (all dir.)	0.8895
7	Normalised Amplitude	0.8815
8	Standard Deviation	0.8667
9	Length	0.8532
10	Number of Low Backscattering Patches (100)	0.8430
11	GLCM StdDev (all dir.)	0.8360
12	Length of Main Line (no Cycles)	0.8151
13	GLCM Entropy (all dir.)	0.7728
14	Average Branch Length	0.7672
15	Width	0.7656
16	Contrast to Neighbour Pixels	0.7607
17	Curvature over Length	0.7607
18	Standard Deviation to Neighbors Pixels	0.6942
19	GLCM Ang. 2nd moment (all dir.)	0.6892
20	Length of Longest Edge (Polygon)	0.6649
21	Number of Segments	0.6580
22	Perimeter (Polygon)	0.6503
23	Number of Edges (Polygon)	0.6280
24	Mean Difference to Neighbors Objs	0.5916
25	Distance to Shore Line	0.5586

26	Length/Width	0.5457
27	Border Length	0.5168
28	Area	0.4727
29	Asymmetry	0.4535
30	Length/Width (only Main Line)	0.4044
31	Density	0.3341
32	Shape Index	0.3083
33	GLCM Contrast (all dir.)	0.2909
34	Curvature Standard Deviation (only Main Line)	0.2811
35	Degree of Skeleton Branching	0.2620
36	Rel. area of Unstable | Coastal Patches (50)	0.2607
37	Compactness (Polygon)	0.2320
38	GLCM Dissimilarity (all dir.)	0.2263
39	GLCM Homogeneity (all dir.)	0.1584
40	Number of Unstable | Coastal Patches (20)	0.1022
41	Number of Inner Objs	0.0930

	Feature (RADARSAT)	*Score*
1	Number of Low Backscattering Patches (100)	1.0304
2	Normalised Amplitude	0.9038
3	GLCM StdDev (all dir.)	0.8978
4	GLCM Entropy (all dir.)	0.8958
5	Contrast to Neighbour Pixels	0.8949
6	GLCM Mean (all dir.)	0.8875
7	GLCM Ang. 2nd moment (all dir.)	0.8816
8	Length	0.8663
9	Standard Deviation	0.8630
10	Length of Longest Edge (Polygon)	0.8116
11	Curvature over Length	0.8098
12	Length/Width	0.8093
13	Stad Dev of Area represented by Segments	0.8007
14	Standard Deviation to Neighbors Pixels	0.7473
15	Length of Main Line (no Cycles)	0.7461
16	Mean Difference to Neighbors Objs	0.7298
17	Rel. area of Low Backscattering Patches (50)	0.7217
18	Average Area Represented by Segments	0.7190
19	Width	0.7102
20	Asymmetry	0.6872
21	Average Branch Length	0.6616
22	GLCM Contrast (all dir.)	0.6233
23	Width (only Main Line)	0.6116
24	GLCM Dissimilarity (all dir.)	0.6004
25	Perimeter (Polygon)	0.5969

26	Density	0.5825
27	Area	0.5730
28	GLCM Homogeneity (all dir.)	0.5080
29	Distance to Shore Line	0.5047
30	Border Length	0.5030
31	GLCM Correlation (all dir.)	0.4627
32	Length/Width (only Main Line)	0.4288
33	Degree of Skeleton Branching	0.3933
34	Shape Index	0.3741
35	Number of Segments	0.3734
36	Curvature Standard Deviation (only Main Line)	0.3580
37	Compactness (Polygon)	0.3508
38	Number of Edges (Polygon)	0.2869
39	Rel. area of Unstable | Coastal Patches (50)	0.1870
40	Number of Unstable | Coastal Patches (20)	0.1325
41	Number of Inner Objs	0.0748

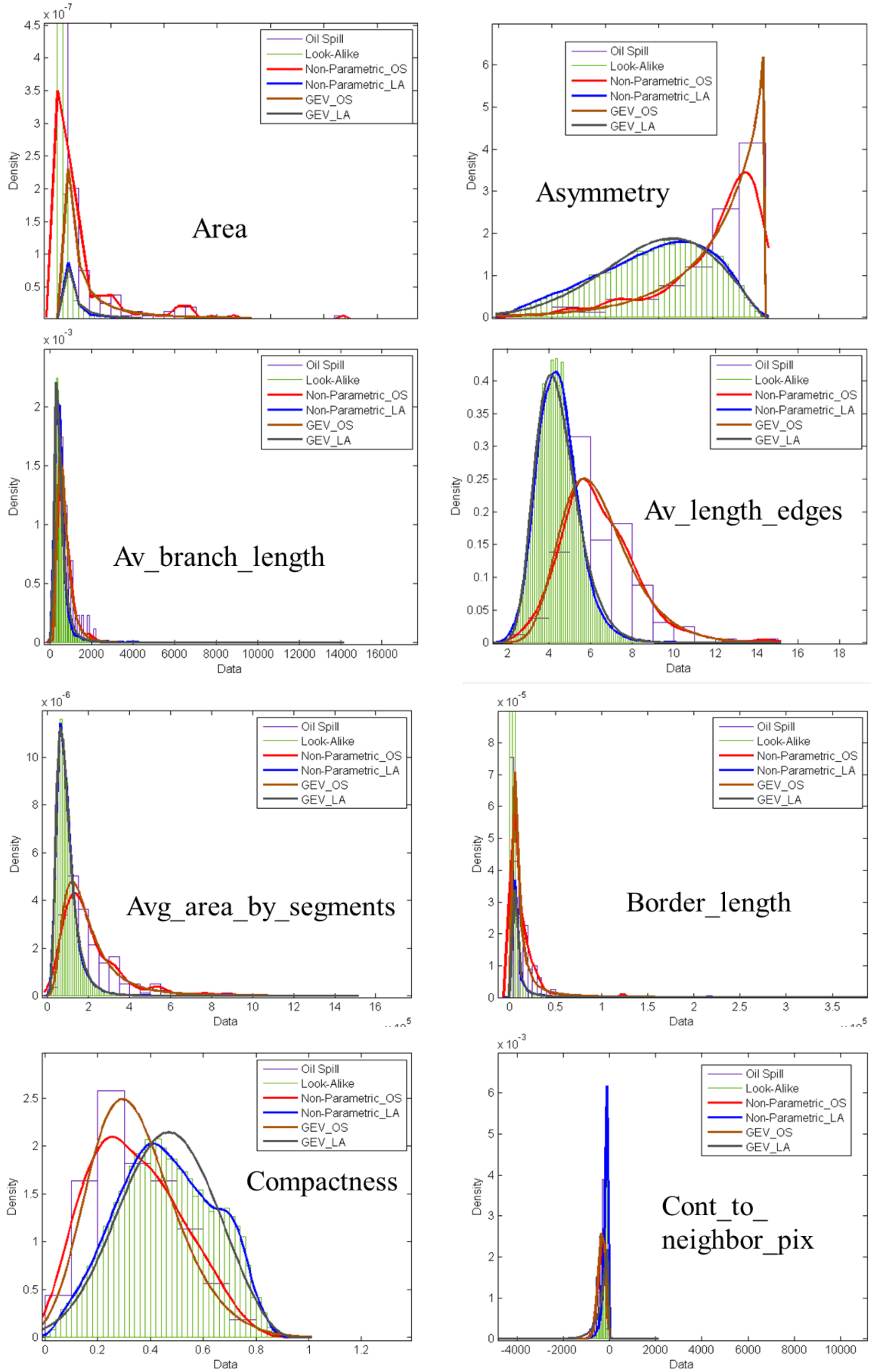
Area
Asymmetry
Av_branch_length
Av_length_edges
Avg_area_by_segments
Border_length
Compactness
Cont_to_
neighbor_pix
Oil Spill
Look-Alike
Non-Parametric_OS
Non-Parametric_LA
GEV_OS
GEV_LA
Density
Data

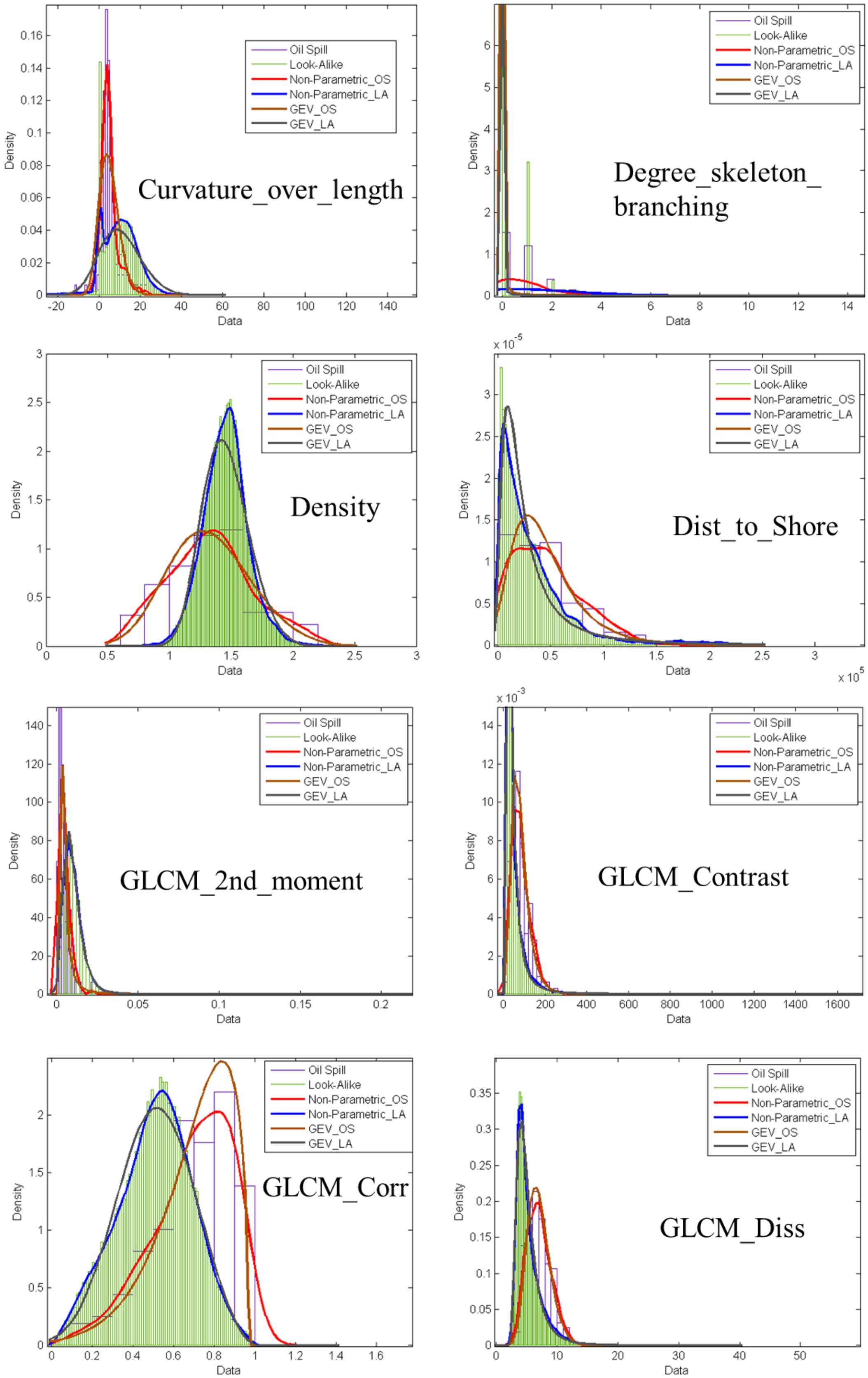
Curvature_over_length
Degree_skeleton_
branching
Density
Dist_to_Shore
GLCM_2nd_moment
GLCM_Contrast
GLCM_Corr
GLCM_Diss
Oil Spill
Look-Alike
Non-Parametric_OS
Non-Parametric_LA
GEV_OS
GEV_LA
Density
Data
x 10^-5
x 10^5
x 10^-3

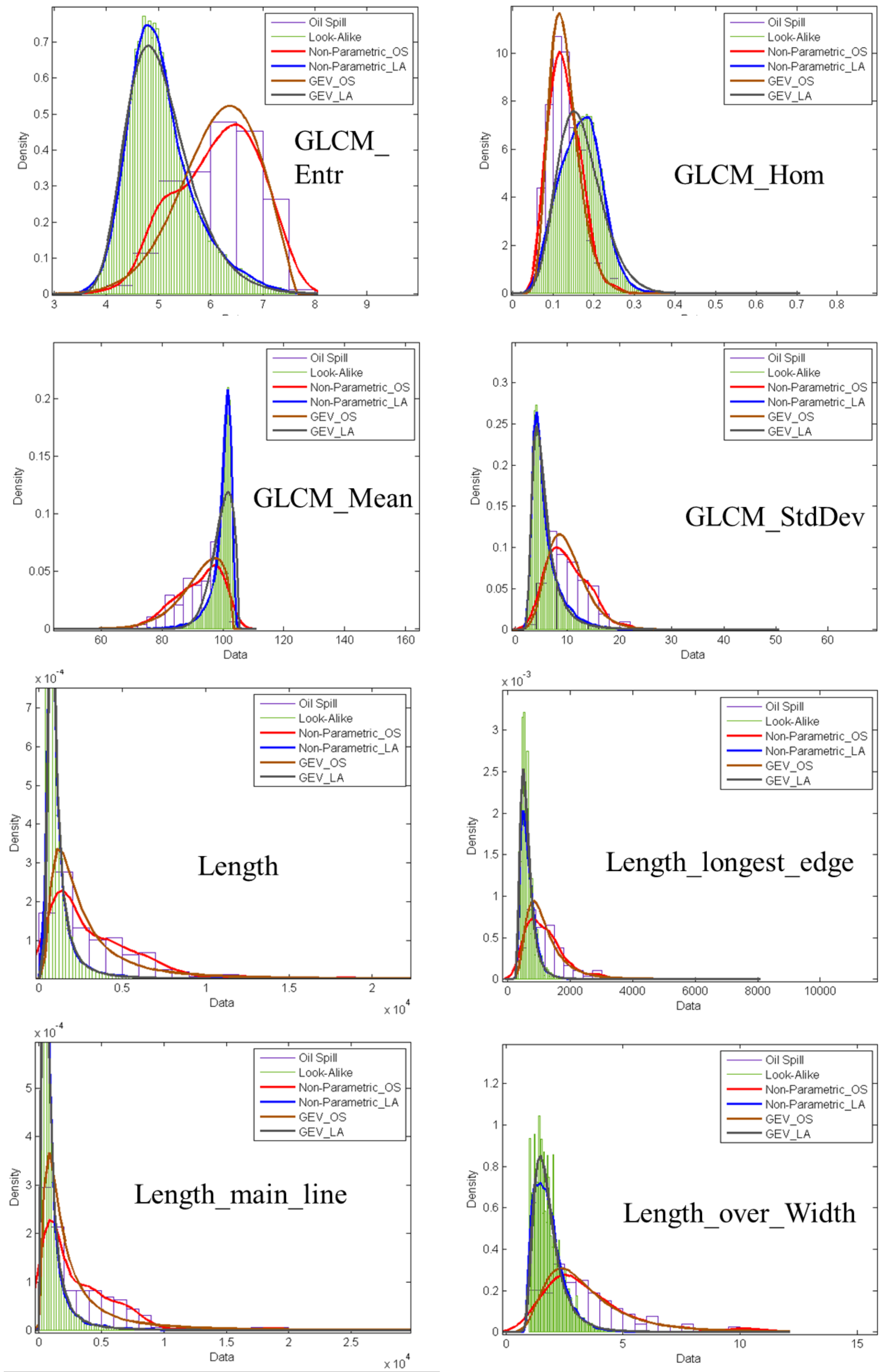
GLCM_Entr
GLCM_Hom
GLCM_Mean
GLCM_StdDev
Length
Length_longest_edge
Length_main_line
Length_over_Width
Oil Spill
Look-Alike
Non-Parametric_OS
Non-Parametric_LA
GEV_OS
GEV_LA
Density
Data

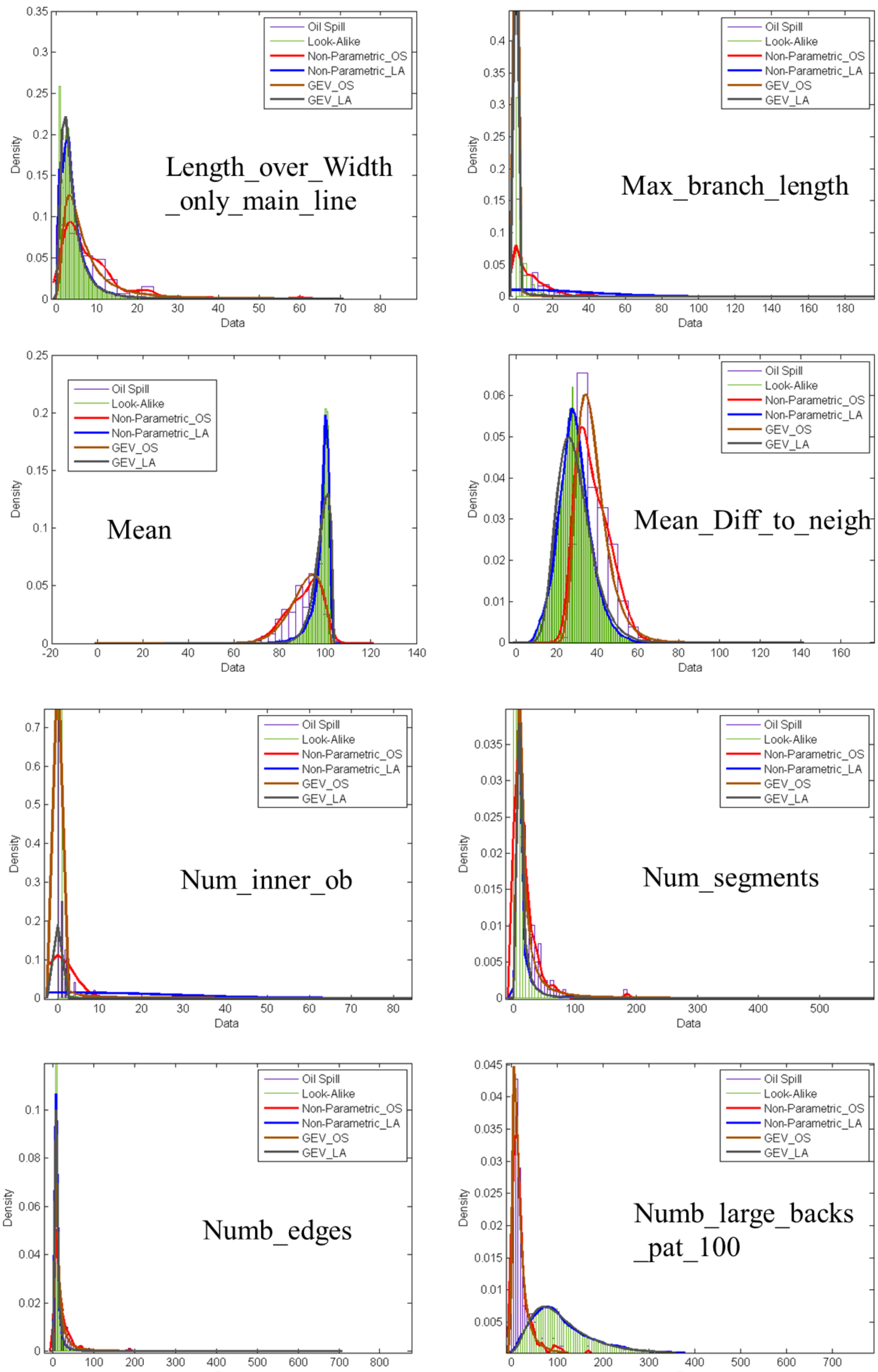
Length_over_Width
_only_main_line
Max_branch_length
Mean
Mean_Diff_to_neigh
Num_inner_ob
Num_segments
Numb_edges
Numb_large_backs
_pat_100
Oil Spill
Look-Alike
Non-Parametric_OS
Non-Parametric_LA
GEV_OS
GEV_LA
Density
Data

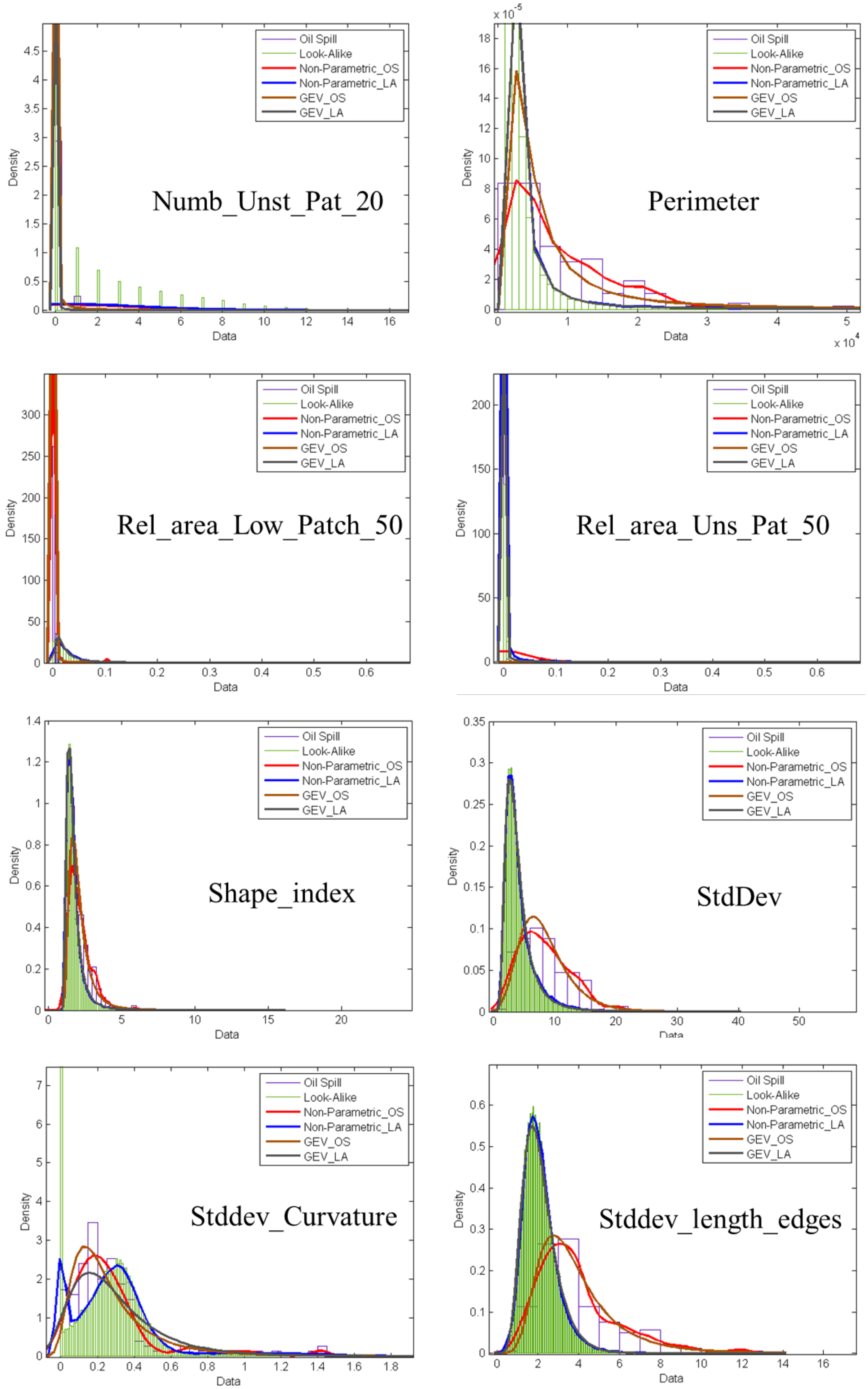
Numb_Unst_Pat_20
Perimeter
Rel_area_Low_Patch_50
Rel_area_Uns_Pat_50
Shape_index
StdDev
Stddev_Curvature
Stddev_length_edges
Oil Spill
Look-Alike
Non-Parametric_OS
Non-Parametric_LA
GEV_OS
GEV_LA
Density
Data

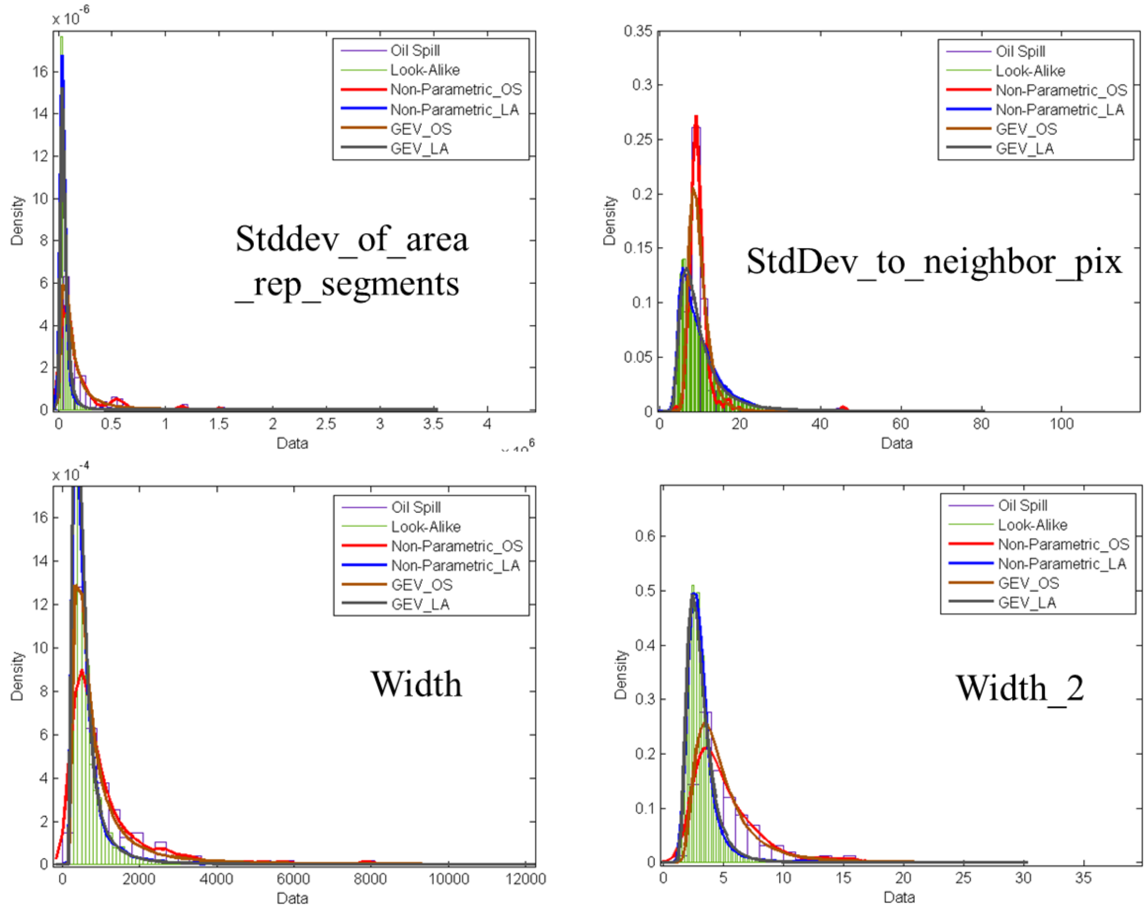

Figure 4.5: Histogram (oil spills –purple; look-alike - green), estimated Generalized Extreme Value (GEV) distribution for the dark spots (oil spills – brown; look-alike – dark gray) and estimated Non-Parametric distribution for the dark spots (oil spills –red; look-alike – blue) for ENVISAT ASAR dataset.

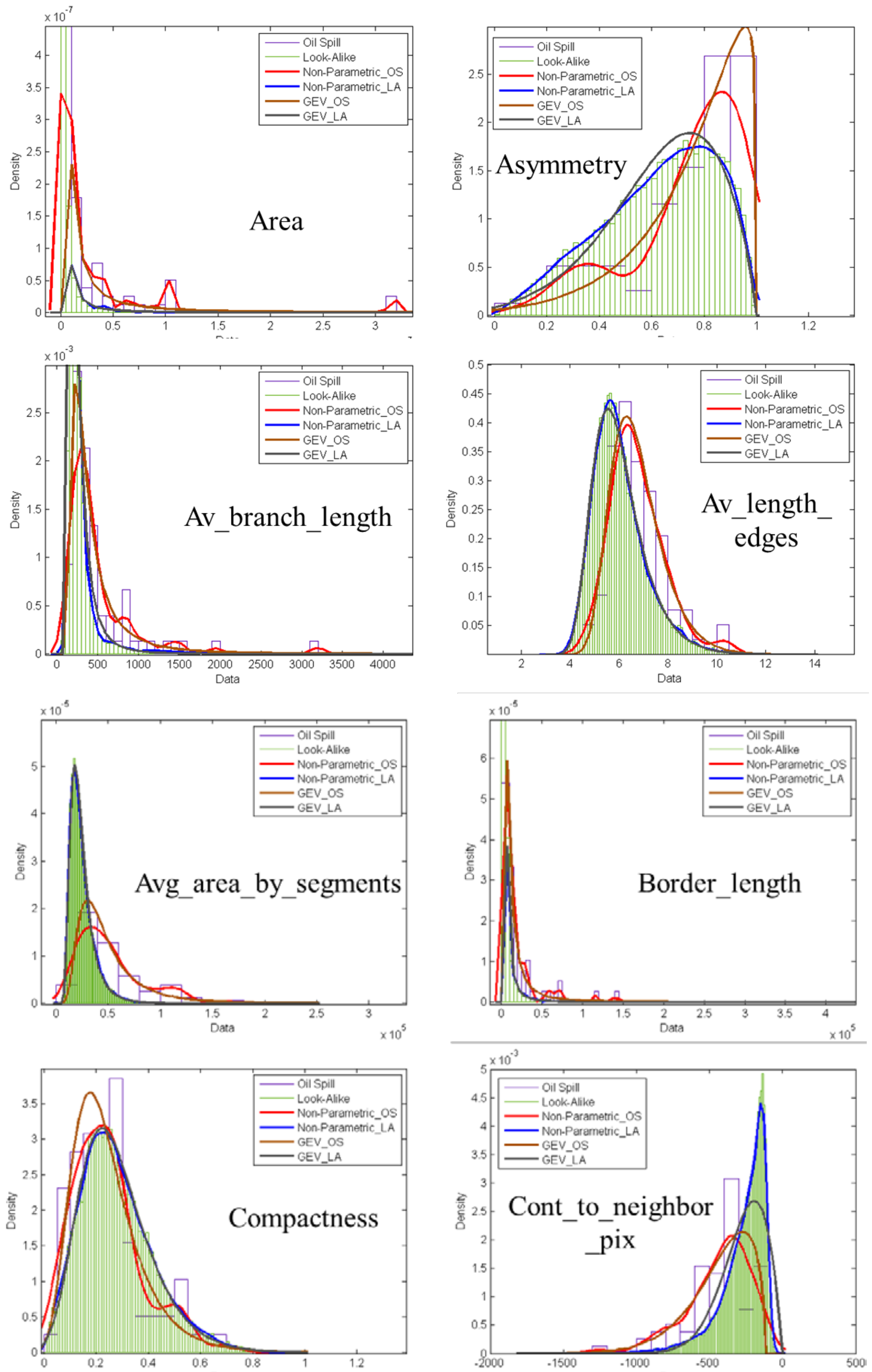
Area
Asymmetry
Av_branch_length
Av_length_
edges
Avg_area_by_segments
Border_length
Compactness
Cont_to_neighbor
_pix
Oil Spill
Look-Alike
Non-Parametric_OS
Non-Parametric_LA
GEV_OS
GEV_LA
Density
Data

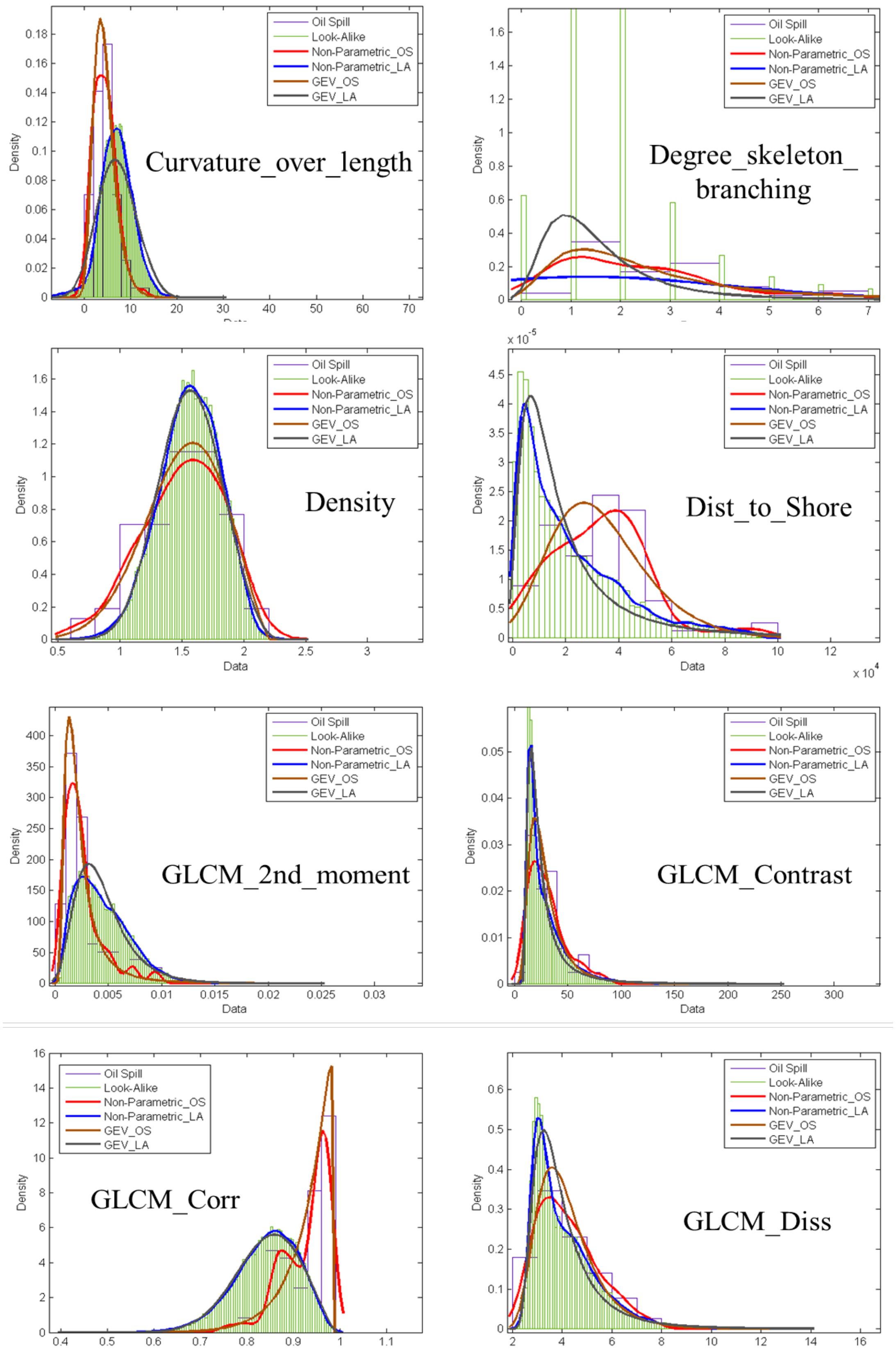
Curvature_over_length
Degree_skeleton_branching
Density
Dist_to_Shore
GLCM_2nd_moment
GLCM_Contrast
GLCM_Corr
GLCM_Diss
Oil Spill
Look-Alike
Non-Parametric_OS
Non-Parametric_LA
GEV_OS
GEV_LA
Density
Data

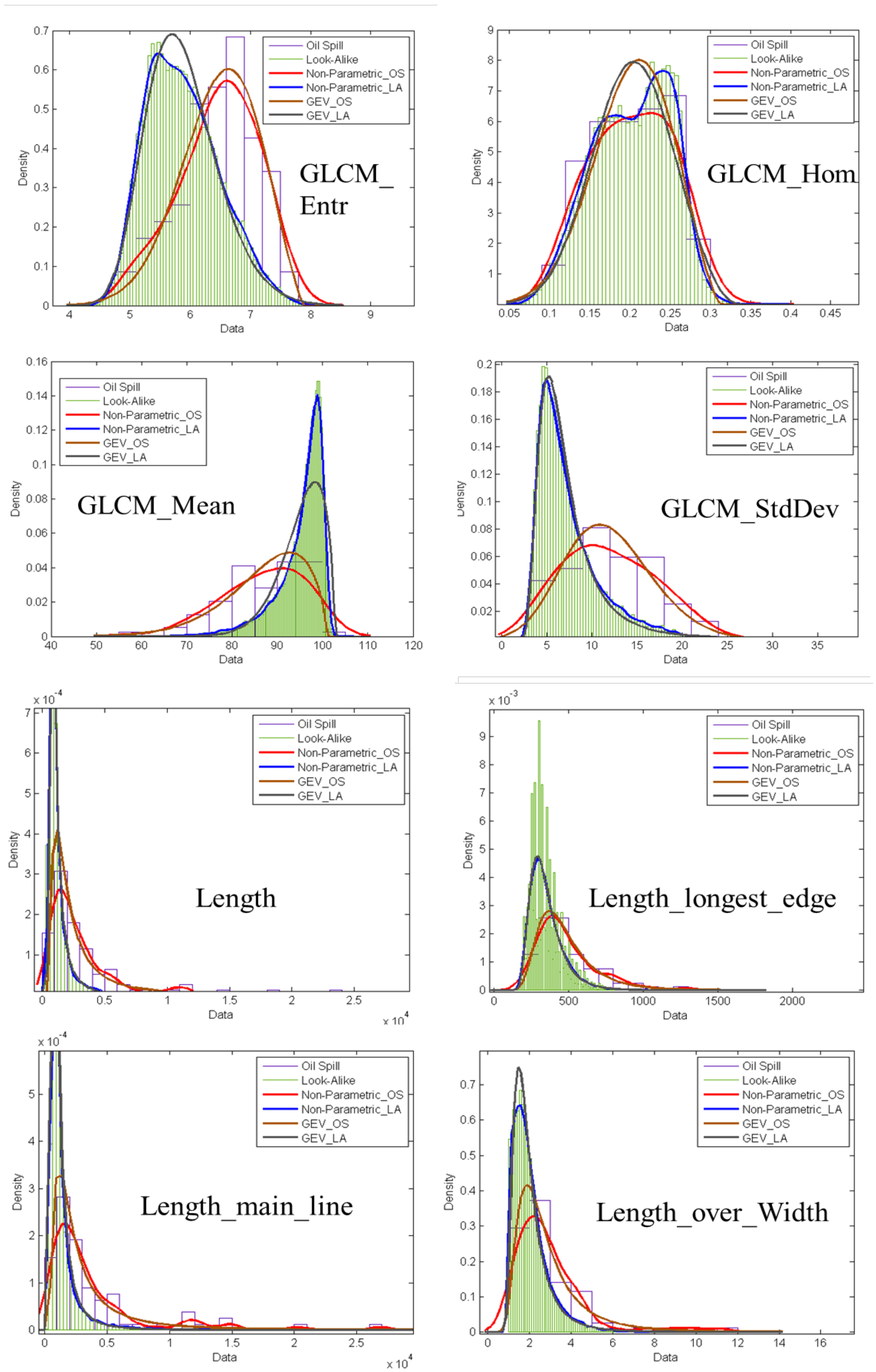
GLCM_ Entr
GLCM_Hom
GLCM_Mean
GLCM_StdDev
Length
Length_longest_edge
Length_main_line
Length_over_Width
Oil Spill
Look-Alike
Non-Parametric_OS
Non-Parametric_LA
GEV_OS
GEV_LA
Density
Data
x 10^-4
x 10^4
x 10^-3

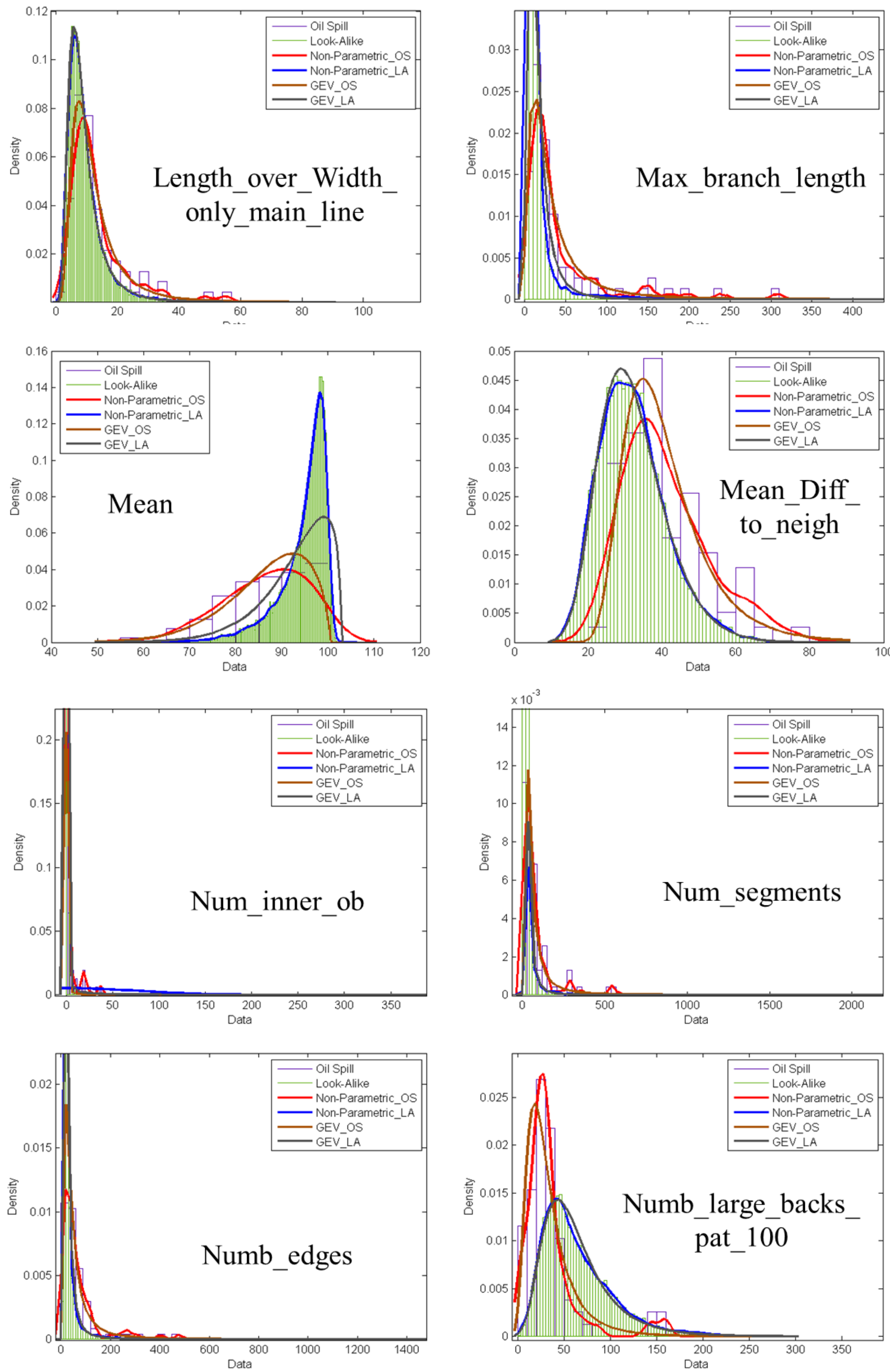
Length_over_Width_
only_main_line
Max_branch_length
Mean
Mean_Diff_
to_neigh
Num_inner_ob
Num_segments
Numb_edges
Numb_large_backs_
pat_100
Oil Spill
Look-Alike
Non-Parametric_OS
Non-Parametric_LA
GEV_OS
GEV_LA
Density
Data
x 10^-3

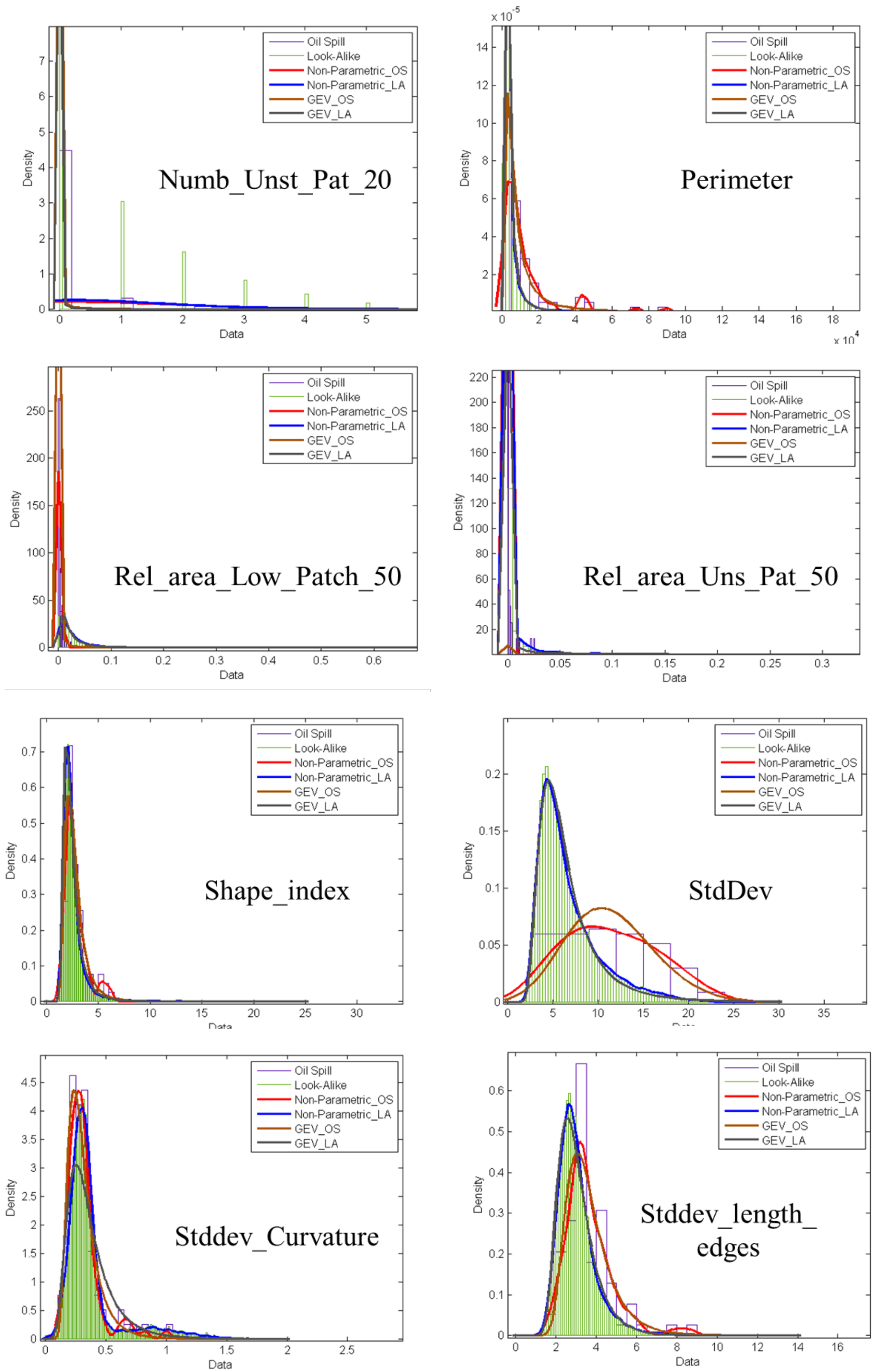
Numb_Unst_Pat_20
Perimeter
Rel_area_Low_Patch_50
Rel_area_Uns_Pat_50
Shape_index
StdDev
Stddev_Curvature
Stddev_length_
edges
Oil Spill
Look-Alike
Non-Parametric_OS
Non-Parametric_LA
GEV_OS
GEV_LA
Density
Data
x 10^-5
x 10^4

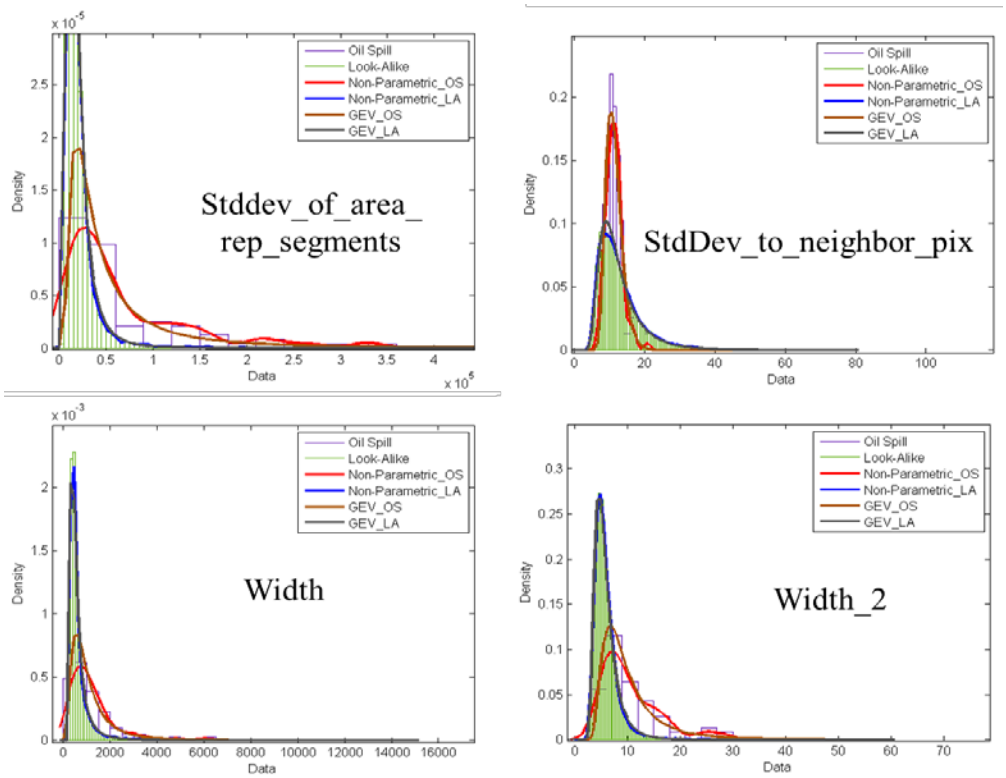

Figure 4.6: Histogram (oil spills –purple; look-alike - green), estimated Generalized Extreme Value (GEV) distribution for the dark spots (oil spills – brown; look-alike – dark gray) and estimated Non-Parametric distribution for the dark spots (oil spills –red; look-alike – blue) for RADARSAT SAR dataset.

4.4 ANN BASED CLASSIFIER

Feature vectors were divided into training and calibration sets. The training set contained 100 oil spills and 400 look-alike features, ensuring a balanced representation of object types as occurrence of look-alikes in an image is significantly higher than that of oil spills. The training set was constructed to represent a range of oil spill morphologies (e.g. linear, diffused) and types of look-alike spot (e.g. low wind, algae etc.). The validation dataset was used to evaluate the generalization capability of the network. Validation dataset contained 83 and 320 feature vector for oil spill and look-alike respectively. Training and calibration set were mutually exclusive (Foody and Arora, 1997). In addition, the classification was tested by using different combinations of feature parameters to form the feature vectors. Table 4.3 and Figure 4.7 compare the classification accuracies of different feature vector compositions, as determined using their respective calibration sets. As discussed below, these dependent accuracy values are higher than those obtained for the full-swath validation dataset, which is understandable since the latter contains a greater variety of artifacts and features.

Table 4.3: Classification accuracy of neural network classifier using different feature sets

Feature Set	Accuracy
All	**92.16%**
Reduced Feature Set which does not include the area, perimeter, or the gradient min	**89.70%**
Reduced Feature Set but Shape complexity excluded	**93.54%**
Reduced Feature Set but Backscatter Features excluded	**70.96%**
Reduced Feature Set but Gradient Features excluded	**67.74%**

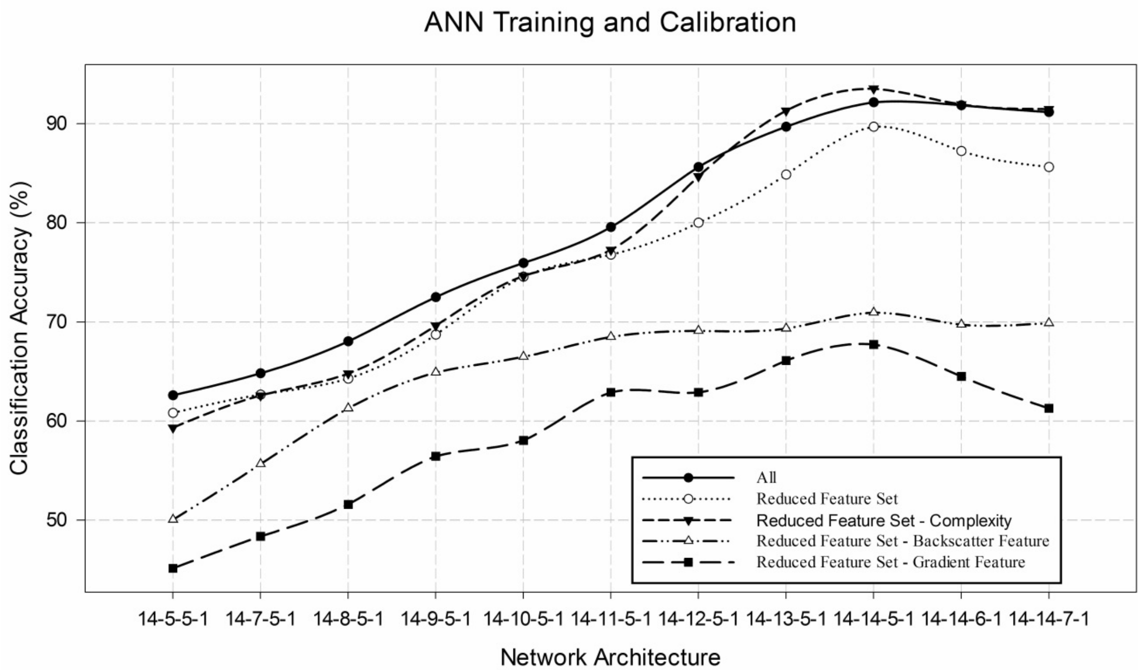

Fig 4.7: Classification accuracy of the neural network classifier using different combinations of feature parameters

Given that values for area and perimeter varied considerably between the available example oil spill and look-alike spots, it was assumed that those features may be unduly influencing the output for neural network classifier. It was also observed that one of the gradient feature, G_{min}, was statistically very similar for both types of spots. Therefore these three features were discarded from the training feature set and then similar training and classification stage were carried out using this reduced feature data set. In order to assess the relative contributions of various classes of feature, three further reduced data sets were employed for network training and validation, respectively excluding shape complexity, backscatter and gradient feature sets. Exclusion of complexity features actually improves the accuracy of the classification for all AAN configurations The gradient and backscatter features clearly make a strong contribution to the overall classification accuracy, indicating that these inputs are worthy of further study. In all cases the 14-14-5-1 network architecture proved optimal among the architectures studied and the reduced feature set with shape complexity excluded shows the best stability when varying the ANN architecture (see Fig 4.7).

The complete new methodology, including segmentation, feature extraction and classification stages, was validated using the full swath validation dataset. The basis of reported oil spills in the validation dataset is manual interpretation and a brief review of this technique can be found in (Topouzelis, 2008). Figure 4.8 shows one example of ENVISAT ASAR WideSwath image and 7 reported oil spill by EMSA via manual classification (Figure 4.8 right hand side image excerpts). Similar kinds of comparison were carried out in some previous studies (Garcia-Pineda et al., 2009).

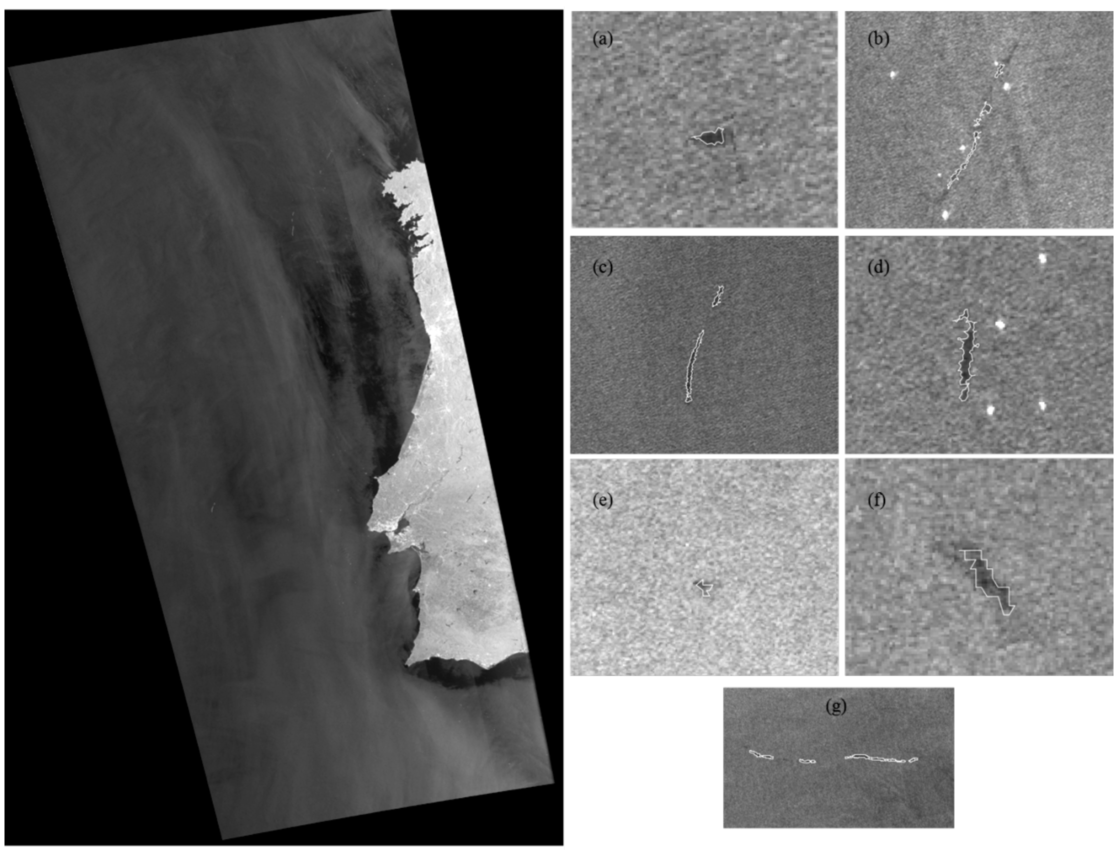

Fig 4.8: Example of dark spots detected on single ENVISAT ASAR WideSwath image acquired on 12th June 2012 at 17:31:51 over Atlantic Ocean near the west coast of Portugal. Image windows (a-g) on the right hand side inset showing potential oil spills in white outline reported by EMSA. (CleanSeaNet Image ID: 5793, ENVISAT image © ESA/EMSA 2012; Presented in Singha et al., 2013a).

As these test images includes land areas, those were removed in a pre-processing stage that included land masking, radiometric normalization and filtering. The pre-processed images were then segmented followed by feature extraction using the reduced feature set (see Table 2). After obtaining feature vectors for each spot, the second-stage ANN was used to classify detected dark spots. Altogether 207 out of 226 reported spills in the validation dataset were correctly identified by the new algorithm, a small percentage of reported oil spills were missed. The potential oil spills shown in Fig 4.8(a) and Fig 4.8(e) was missed due to its very low contrast, although the sizes of those spills were significantly smaller compared to other linear spills present in the image. Some of the look-alike spots were identified as oil spills (false positive) and main reason was identified for this type of misclassification, presence of Algae bloom (with linear feature mimicking oil spill spots).

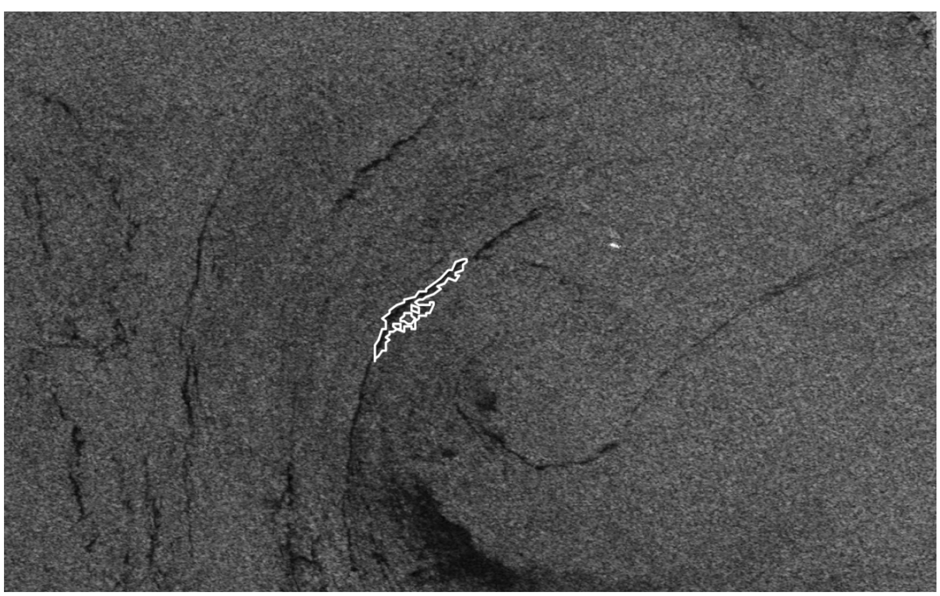

Fig 4.9: Example of a look-alike identified as an oil spill (shown in bright white outline, Presented in Singha et al., 2013a).

The presence of Algae is a very common phenomenon in the Mediterranean and Baltic seas from May to September and some of the images in validation set are from mentioned time frame. Fig 4.9 shows an example of false positive where part of a linear feature due to algae bloom identified as oil spill. The error matrix shown in Table 4.4 evaluates the performance level of the proposed methodology.

Table 4.4: Error matrix used for quantitative assessment of the proposed algorithm (see Table 4.6 for detailed description)

	Algorithm Oil Spill	Algorithm Look-Alike
Reported Oil Spill	**207**	**19**
Reported Look-Alike	**79**	**4591**

There are 19 cases where the proposed algorithm disagrees with the verified detection (false negative) and 79 cases where dark spots were identified as oil spill which are not confirmed by EMSA (potential false positive). It can be observed from Table 4.4 that the proposed algorithm is successfully able to identify most of the oil spills (91.6 %) and look-alikes (98.3 %) present in the large validation dataset, this indicates the robustness of the proposed algorithm.

While it is challenging to compare different methodologies without using exactly the same data set, a non-exhaustive comparison with previous work is given to provide context. The neural network classification proposed in (Del Frate et al., 2000) yielded accuracies of 82% for oil spills and 90% as look-alikes while (Topouzelis et al., 2007) yielded 91% for oil spill and 87% of look-alike. The probabilistic method of Fiscella et al., 2000) gave an overall accuracy close to 80% while the Probabilistic method (statistical modelling with a rule based approach) of Solberg et al., 2007 achieved 78% for oil spill and 99% for lookalikes. The final classification accuracy achieved by the proposed methodology is thus higher than some previous related studies particularly for oil spills Moreover the proposed methodology has the capability to address operational/commercial NRT requirements and has been validated against a robust and proven operational method (manual classification).

4.5 RULE BASED CLASSIFICATION TECHNIQUE

The performance evaluation of the rule based classifier is reported in the following, both for ENVISAT ASAR and RADARSAT products. A detailed description for the test dataset and approach for the quantitative assessment and benchmarking of proposed methodology is presented below.

Validation Dataset

In order to test the reliability and efficiency of the proposed approach, a test dataset from the oil-spill and look-alike target database of CleanSeaNet service was used. In CleanSeaNet, human analysts at service provider (SP) stations detect high potential dark spots, which could be oil spills (with two types of probability, high and low), through manual interpretation of SAR images. The images used for oil-spill monitoring within 'CleanSeaNet' are ENVISAT ASAR WideSwath (discontinued due to satellite communication failure in April 2012), RADARSAT-2 ScanSAR intensity data, with HH or VV polarization. As discussed in Chapter III, the validation dataset contains 35 ENVISAT ASAR images with pixel spacing of 75m and 83 RADARSAT-2 SAR images with pixel spacing of 25m. This 118 image dataset contains all potential anomalies detected under a variety of sea conditions between 2009 and 2012. The test dataset is highly complex as each image contains multiple look-alikes and in most of the cases multiple oil spill spots. These 118 images, containing 361 identified oil spills by service provider and 5728 potential look-alike spot identified by visual interpretation technique forms the reference dataset. Most of the previously developed algorithms nether have neither the capability of being completely automated nor being tested extensively using large dataset representing different complex situation. More often small image window containing single dark-spot representing oil spill on a uniform background, therefore those test dataset are incapable of showing the actual capability of the algorithm. The capability of the proposed algorithm was tested on whole images rather than small image windows mainly used by previous study. Table 4.5 shows the distribution of the testing dataset. Some test images obtained through CleanSeaNet service are shown in Figure 4.10 to 4.16.

Table 4.5: Distribution of the validation dataset (Potential look-alike was identified by visual interpretation technique)

Sensor	Number of images	No. of oil spill Spot	No. of Look-alike spot
ENVISAT-ASAR	35	135	805
RADARSAT 2 SAR	83	226	4923
TOTAL	118	361	5728

After processing all the test images with the proposed algorithm, a detailed comparison with reference dataset was carried out on spot by spot basis using visual interpretation technique. Well known confusion matrix was used for quantitative assessment of the proposed algorithm. Separate confusion matrix was constructed for each image, the framework of the confusion matrix shown below.

Table 4.6: Framework of confusion matrix used for quantitative assessment of the proposed algorithm (ALGO: Proposed algorithm; REF: Reference dataset)

	Oil Spill ALGO	**Look-Alike ALGO**
Oil Spill REF	**A**	**B**
Look-Alike REF	**C**	**D**

Explanation of the above matrix (OS: Oil spill; LA: Look-alike)

- **A- OS(REF): OS(ALGO) - Number of co-located detections both by SP and proposed Algorithm.**

- **B- OS(REF) : LA(ALGO) - Dark spots classified as oil spills by SP but not by ALGO.**

- **C- LA(REF) : OS(ALGO) - Dark spots classified as oil spill by ALGO but not by SP.**

- **D- LA(REF): LA(ALGO) - Dark areas visually detected that could lead to false positives (Look-alike). Reported neither by SP nor ALGO, indication of degree of complexity present in particular image.**

Although ‘B’ and ‘C’ are the misclassified spots by proposed algorithm, ‘B’ is considered to be more serious misclassification compared to ‘C’. Table below provide different accuracy ratio which indicate the degree of agreement between human analyst and proposed algorithm.

Table 4.7: Framework of confusion matrix used for quantitative assessment of the proposed algorithm

Overall Classification Accuracy	(A+D)/(A+B+C+D)
Classification Accuracy for oil spill	A/(A+B)
Classification Accuracy for look-alike	D/(C+D)

Figure 4.10 and 4.11 shows detection on one ENVISAT and one RADARSAT-2 image by human analyst and proposed algorithm.

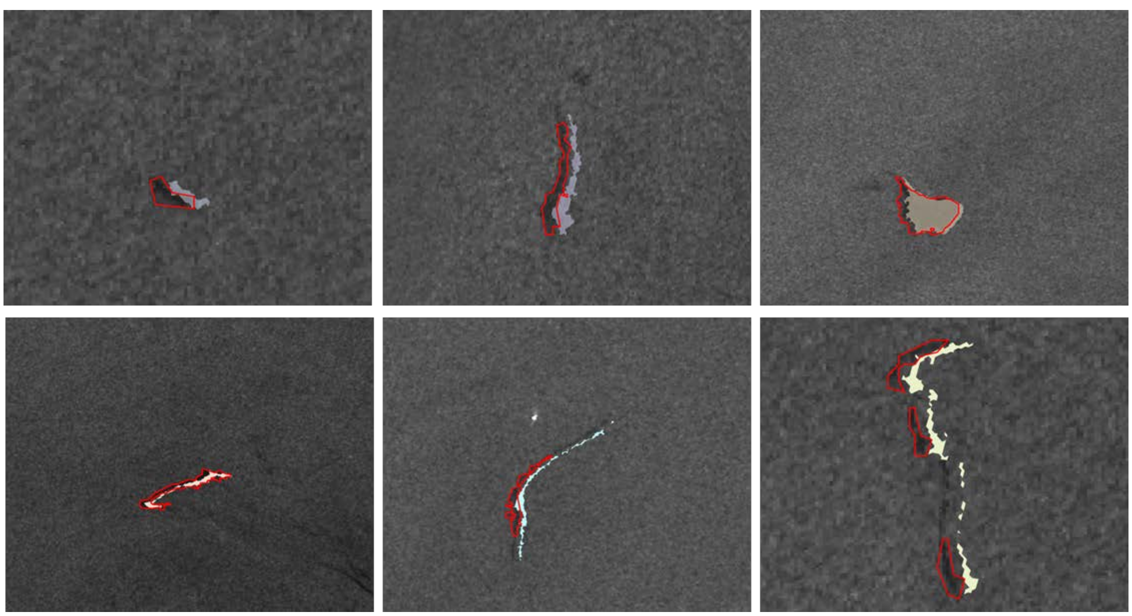

Fig 4.10: Example of dark spots detected on single ENVISAT ASAR WideSwath image. Patches with bright red out line shows detection by proposed algorithm and solid color patches shows detection by human operator. CleanSeaNet Image ID: 5889 (ENVISAT ASAR image © ESA/EMSA, Presented in Singha et al., 2013b).

Figure 4.10 shows some of the oil spill detected on an ENVISAT ASAR Wide Swath, VV polarized image, Descending orbit acquired on 14th March 2011 at 08:17:27 am over black sea near Romanian and Bulgarian coast. It has been observed that there is a high correlation between detection by proposed algorithm (Red outlined polygon) and detection from human operator (solid colored polygon)

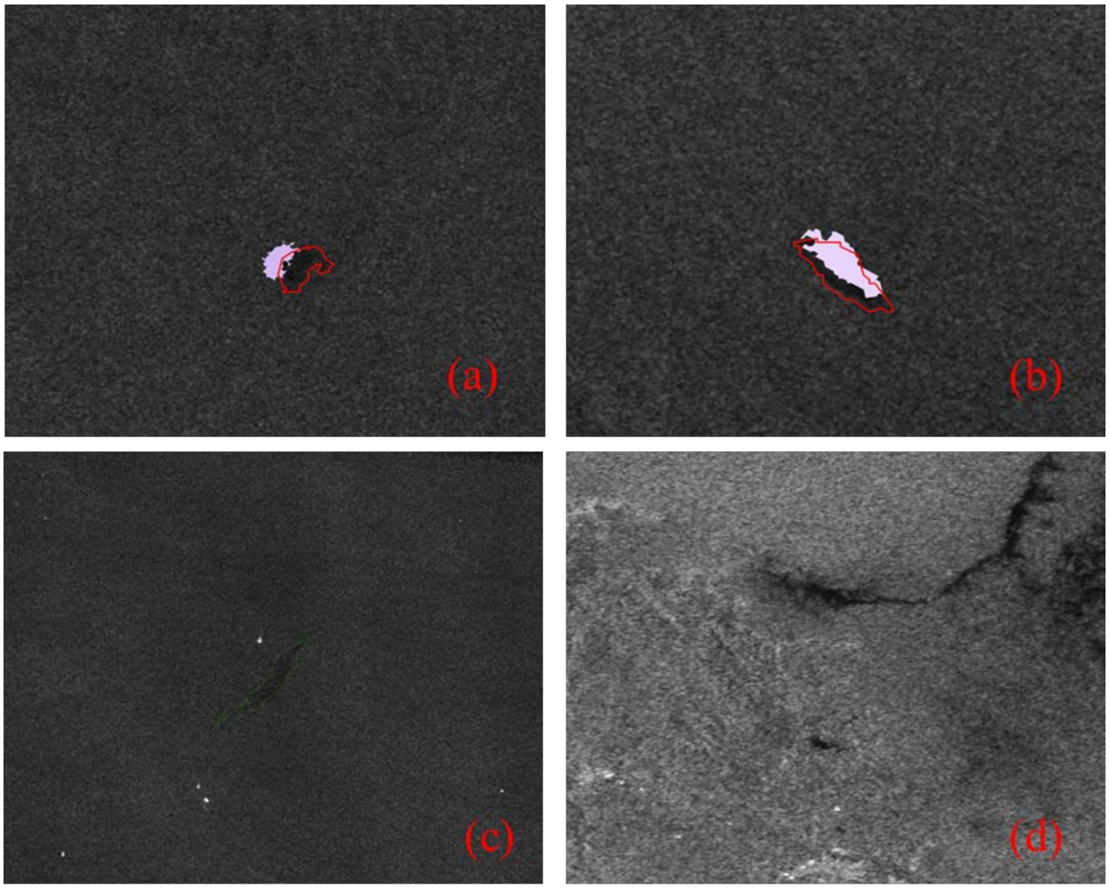

Fig 4.11: Example of dark spots detected on single RADARSAT-2 ScanSARWide image acquired on 12th June 2012 at 17:31:51 over Mediterranean Sea (Costal State : Spain, France and Italy). In Fig (a) and (b) patches with bright red out line shows detection by proposed algorithm and solid color patches shows detection by human operator. Fig (c) shows example of look-alike misclassified as oil spill by proposed algorithm. Fig (d) shows example of look-alike. CleanSeaNet Image ID: 22576 (RADARSAT-2 image ©CSA/MDA/EMSA, Presented in Singha et al., 2013b).

Figure 4.11 shows some of the oil spills and look-alikes detected on an RADARSAT-2 ScanSARWide image acquired on 12th June 2012 at 17:31:51 over Mediterranean Sea near Spanish, French and Italian coast. Similar to the ENVISAT ASAR image, there is a high correlation between detection by proposed algorithm (Red outlined polygon) and detection from human operator (solid colored polygon). In this particular image one dark spot (shown in green outlined polygon) was misclassified as oil spill by algorithm. This type of false alarm considered to be less serious in terms of operational activity, although this kind of error makes a significant contribution toward accuracy assessment figures. There are also few cases where oil spill reported by human operator, missed by algorithm. This instance was observed mainly for RADARSAT data where the image complexity (number of dark spots) is significantly higher than ENVISAT data. The main reason for this type of misclassification was identified of being the presence of Algae bloom (with linear feature). The presence of Algae is a very common phenomenon in the Mediterranean and Baltic seas from May to September. Figures 4.12 show examples of misclassification due to presence of linear algae features.

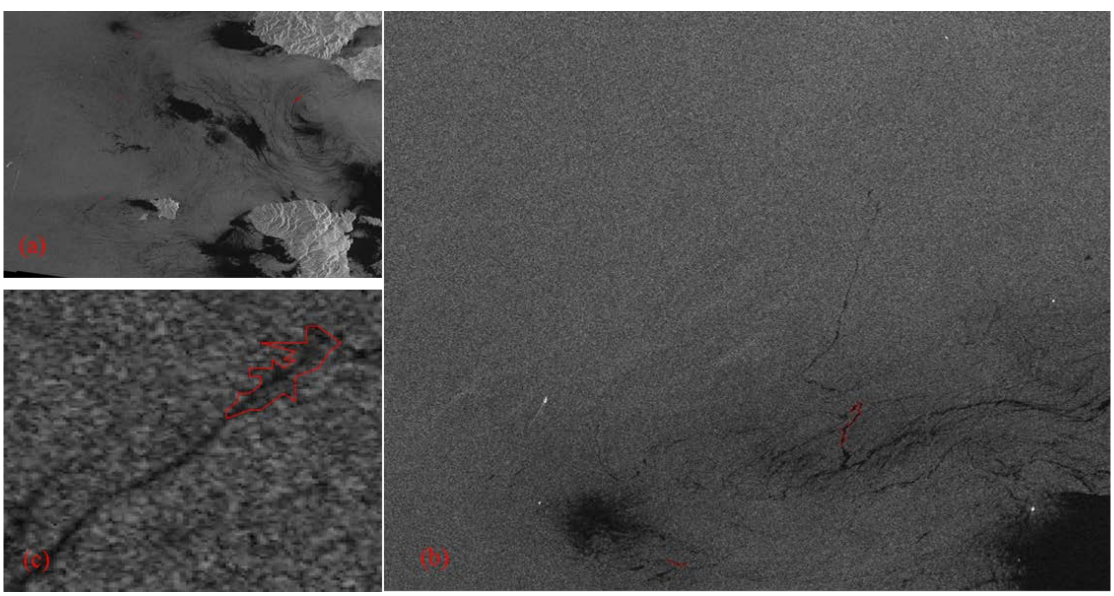

Fig 4.12: Example of misclassification due to presence of algae. (a) RADARSAT-2 ScanSARNarrow VV polarized image acquired on 26th May 2012 at 08:20:51 (CleanSeaNet Image ID 22224, Costal State: Greece and Turkey). (b) Presence of algae and misclassified dark spots (in red outlined polygon). (c) Detail view of linear algae feature and misclassification (Presented in Singha et al., 2013b).

The RADARSAT 2 SAR image presented in Figure 4.12(a) was acquired during early summer over the Mediterranean Sea, near the Greek and Turkish coast Look-alike spots due to algae bloom are a well-known phenomenon especially in Mediterranean and Baltic Sea. This particular RADARSAT-2 SAR image (Fig 4.12) in test dataset was highly affected by algae and deliberately included in test dataset in order to assess the operation capability of the algorithm. Fig 4.12(c) shows a linear algae feature, which highly resembles oil spill spot and was misclassified by the proposed methodology.

Fig 4.14 shows a snapshot of an oil spill detected by both a human analyst and the proposed algorithm in a RADARSAT-2 SAR image (ScanSARNarrow, HH polarized) acquired on 19th February 2011 at 05:40:03 near north coast of Germany and Denmark. It can be observed form this image that proposed algorithm detect the whole extent of the dark spot compared to partial detection by human analyst.

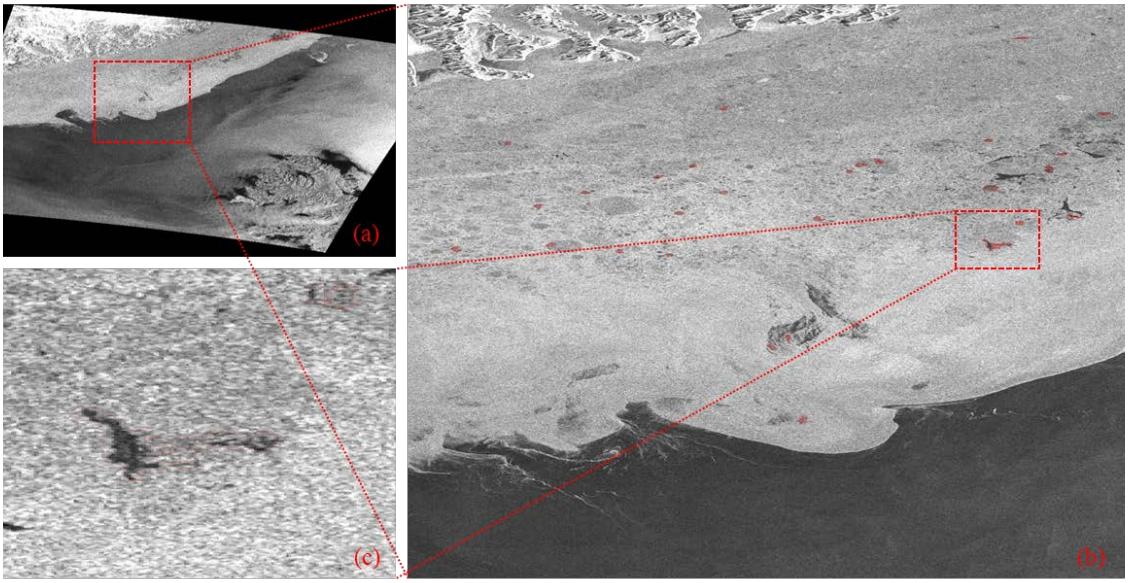

Fig 4.13: Example of misclassification due to presence of sea ice. (a) RADARSAT-2 ScanSARWide HH polarized image acquired on 24th March 2012 at 08:20:51 (CleanSeaNet Image ID 19899, Costal State: Greenland and Iceland). (b) Presence of sea ice and misclassified dark spots (in red outlined polygon). (c) Example of dark spot present in sea ice.

The RADARSAT 2 SAR image presented in Figure 4.13(a) acquired during late winter time over North Atlantic Sea (near east coast of Greenland and west coast of Iceland). Presence of sea ice can clearly observed in Figure 4.13(b, c) (indicated in red dotted rectangle, although ground truth data was not available). The continuum ice sheets scattered with cracks and ridges which produces surface with calm water hence lower backscatter (Fig 4.13 (b)). Figure 4.13 (c) shows this kind of dark patches which resemble dark spot occurred on SAR images due to presence of oil spill. The automatic methodology was trained with a set of images that did not include sea ice, thus leading to poor classification capabilities over this “look-alike”.

Although there are some minor limitations involved in proposed methodology and subjected to further development and calibration, in majority of cases the proposed algorithm performed similar or some time better than a human operator in respect to the accuracy of generated polygon around the detected oil spill. The latter is, of course, always subject to individual knowledge and expertise. Figure 4.14 shows one of the cases where result from proposed algorithm found to be superior and accurate than the human analysis.

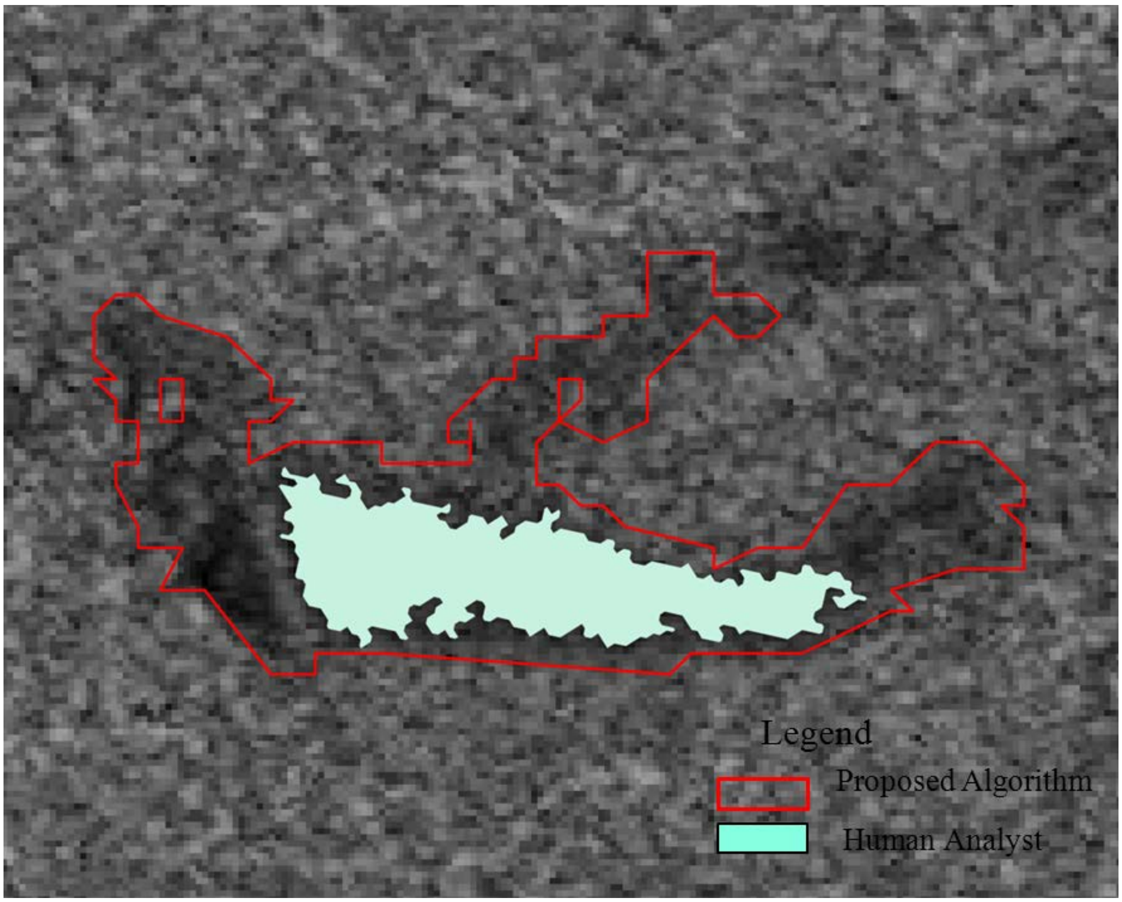

Fig 4.14: Comparison between results obtained from proposed algorithm and human analyst (Presented in Singha et al., 2013b).

Figure 4.15 (a) shows a RADARSAT-2 SAR ScanSARNarrow Beam image acquired on 22nd of April 2011 at 05:30:57 near coast of Germany and Denmark over Baltic Sea. This SAR image is excessively affected by linear biogenic films along with prominent presence of two oil spill, probably from different source (Fig 4.15 b). Both of the oil spill spot were reported by EMSA and successfully detected by the proposed algorithm in spite of the presence of linear look-alike features nearby. This example demonstrates the robustness of the proposed algorithm and its ability to segregate linear oil spill spot from linear look-alike features.

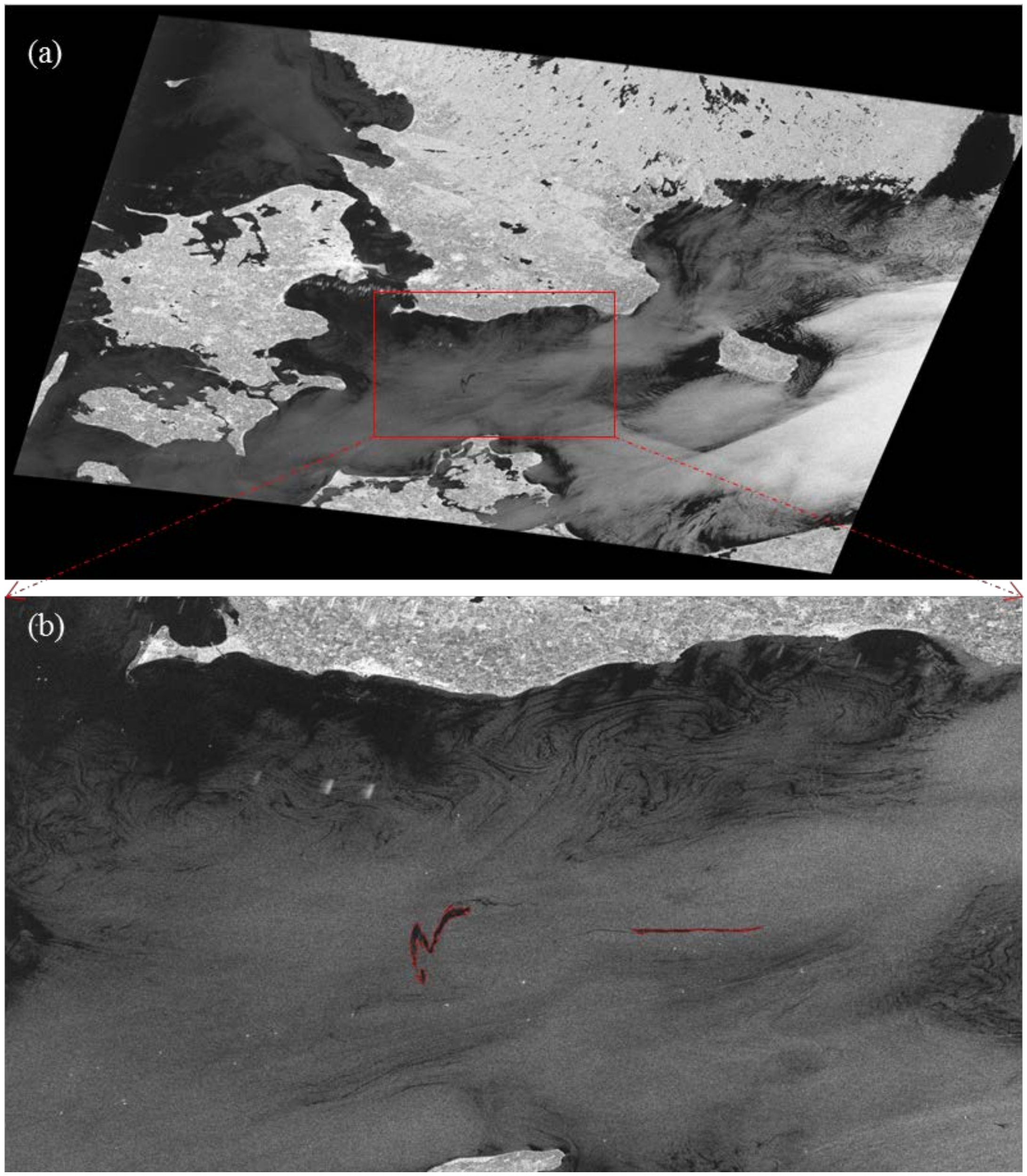

Figure 4.15: Example of oil spill on a RADARSAT-2 SAR ScanSARNarrow Beam image acquired on 22nd of April 2011 near northern coast of Germany over Baltic Sea. Patches indicated in bright red out line shows detection by proposed algorithm. CleanSeaNet Image ID: 5914 (RADARSAT-2 image © CSA/MDA/EMSA 2012).

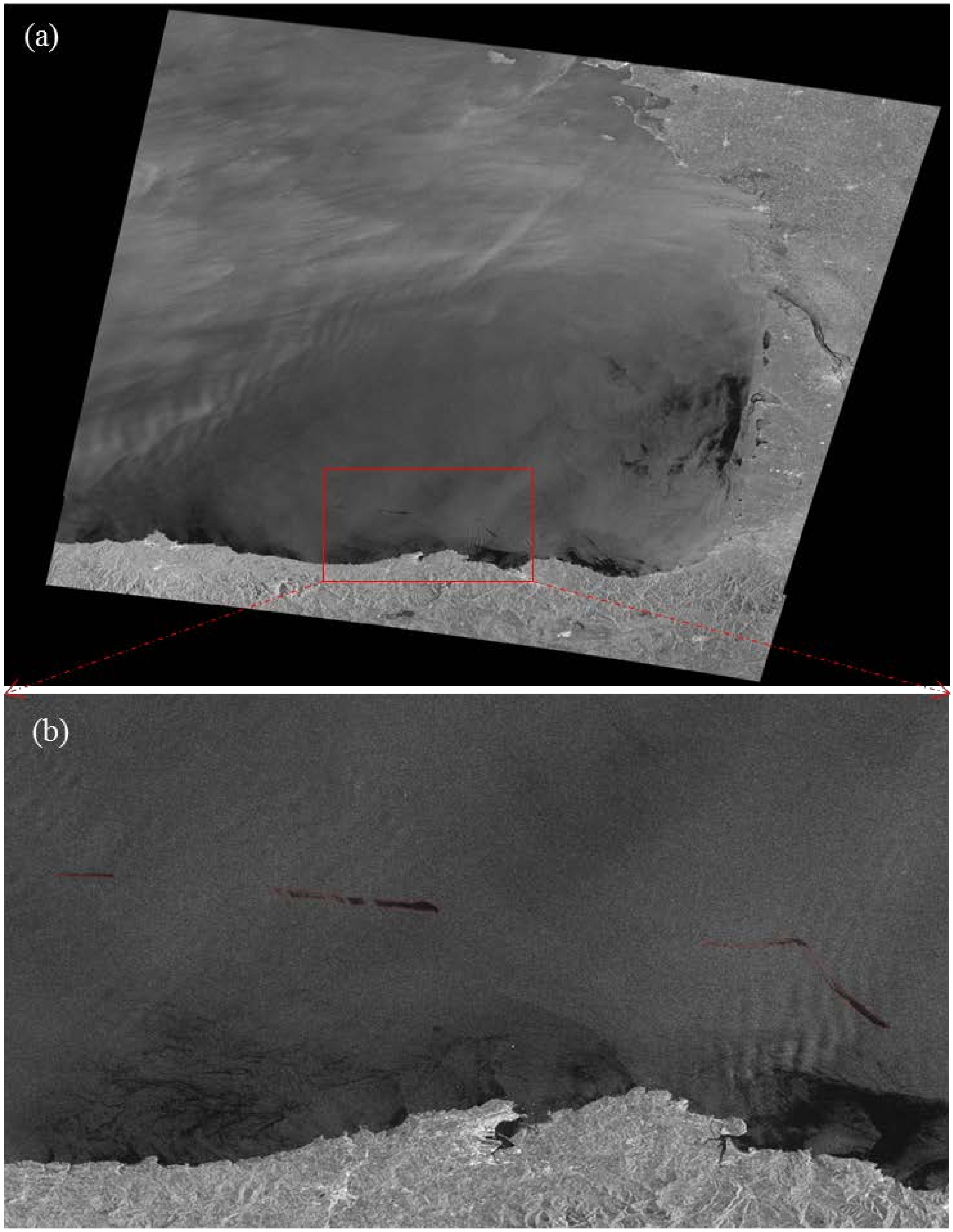

Fig 4.16: Example of oil spill on a RADARSAT-2 SAR ScanSARNarrow Beam image acquired on 15th of June 2012 at 06:24:44 near northern coast of Spain (a). Patches indicated in bright red out line shows detection by proposed algorithm near coastline (b). CleanSeaNet Image ID: 22718 (RADARSAT-2 image © CSA/MDA/EMSA 2012).

The RADARSAT-2 SAR ScanSARNarrow image presented in Figure 4.16(a) was acquired on 15th of June 2012 at 06:24:44 near northern coast of Spain over Bay of Biscay. A linear, discontinued ship sourced oil spill spot was reported by EMSA and also identified as oil spill by the proposed algorithm. Due its proximity to the shore line, these kinds of spill are real threat to costal environment and calls for a rapid response. This oil spill spot was detected by the proposed algorithm within 14 minute after level 1B image ingestion, showing the algorithm's near real time capability.

Table 4.8: Accuracy assessment of the proposed classification tree based oil spill detection methodology.

Assessment Term / Sensor	Overall Classification Accuracy	Classification Accuracy for oil spill	Classification Accuracy for look-alike
ENVISAT ASAR	85.43 %	61.48 %	89.44 %
RADARSAT SAR	93.08 %	54.43 %	94.86 %

Table 4.8 shows overall classification accuracy and as well as individual accuracy assessment for oil spills and look-alike spots. Although the test dataset is highly complex and contains multiple look-alikes and oil spills, agreement between proposed algorithm and human analysts was found to be satisfactory. As detailed above, a number of limitations were found in the proposed algorithm. These are the subject of current research and development activity.

The proposed oil spill detection chain has the unique capability to produce oil spill polygons directly from level 1B data and has been adopted for operational use on near real time basis. Feature analysis using the Patrick-Fisher distance between the relevant probability densities has led to the selection of non-parametric classification approaches. A two-stage classification tree followed by a set of membership rules has been implemented for ENVISAT ASAR and RADARSAT-2 ScanSAR multi-look detected products.

Some false alarms are still present mainly due to presence of algae and ship wakes, and some missed spills are also experienced. Some missed dark spots, which could be potential candidates for oil spills, are in proximity to the shoreline or display very low contrast due the age of the spill and low or very high wind conditions. Other missed oil spills are either small in size or characterised by EMSA with low degree of confidence. In some other cases the developed ruleset detects dark patches not classified as oil spills by the EMSA reports, and that do not seem to be false alarms from accurate detailed analysis. A few images in the dataset experience large residual scalloping and geolocation errors. This leads to incorrect land masking and a distorted statistical analysis of the scene backscatter (Vespe and Greidanus, 2012), ultimately reducing the detection capabilities of the ruleset. Techniques to reduce false alarms due algae are still in development and will reduce the false alarm rate drastically when implemented. Nevertheless, the results of the classifier show the robustness of the methodology. The procedure shown in this section also gives guidelines for future and new instrument ingestion into operational services, like CosmoSkyMed, TerraSAR-X and constellation.

4.6 ANN AND RULE BASED CLASSIFIER COMPARISON

In order to analyze the performance of the rule based classifier, a new neural network was trained, calibrated and tested using the full spectrum of feature vector. Each feature vector containing 41 feature extracted represent one darkspot. Training, validation and testing results for the neural network have been shown in the previous chapter. In addition to validation and testing (during neural network development phase) the proposed neural network also tested with additional 1078 feature vector in order to establish its reliability for near real time application. Among 1078 feature vector 78 represent oil spill spot and other 1000 represent look-alike spots. The number of feature vector representing look-alike feature were intentionally kept high as its occurrence is much higher in SAR images.

As discussed in the previous chapter the neural network is designed such a way that it gives output as 0 if the spot classified as definite oil spill and 1 for definite look-alike. However majority of the output provide a value between 0 and 1. A basic threshold is implemented in order to get a definite result from the classifier. The threshold was set to 0.85, if the out pout is greater than that value the output from the neural network labeled as lookalike otherwise oil spill.

Table 4.9: Framework of confusion matrix used for quantitative assessment of the proposed algorithm (ALGO: Proposed algorithm (ANN); REF: Reference dataset)

	Oil Spill	**Look-Alike**
Oil Spill REF	**68**	**10**
Look-Alike REF	**103**	**897**

There are 10 cases where the proposed ANN based algorithm disagree with the verified detection (false negative) and 103 cases where dark spots were identified as oil spill which are not confirmed by EMSA (potential false positive). It can be observed from table 3 that the proposed algorithm is successfully able to identify most of the oil spills (87.17 %) and look-alikes (89.7%) present in the large validation dataset, compared to 54.43 % (oil spill) and 94.68% (Look alike) using the rule based classifier.

Table 4.10: Final comparison of ANN vs rule based methodology

	ANN based Methodology	**Rule based Methodology**
Accuracy for oil spill classification	87.17 %	54.43 %
Accuracy for oil 'look-alike' classification	89.7%	94.68%

Results based on validation dataset, which was also used for the validation of the rule based methodology, shows ANN performs significantly better in terms of oil spill detection accuracy, although it suffers from higher false alarms compared to rule based methodology (Table 4.17, presented before in 4.16). Figure bellow shows an example of oil spill detection which was also identified by the rule based algorithm and reported by EMSA. Calibration of the proposed neural network using full spectrum of feature parameters is further needed in order to reduce the false alarms rate.

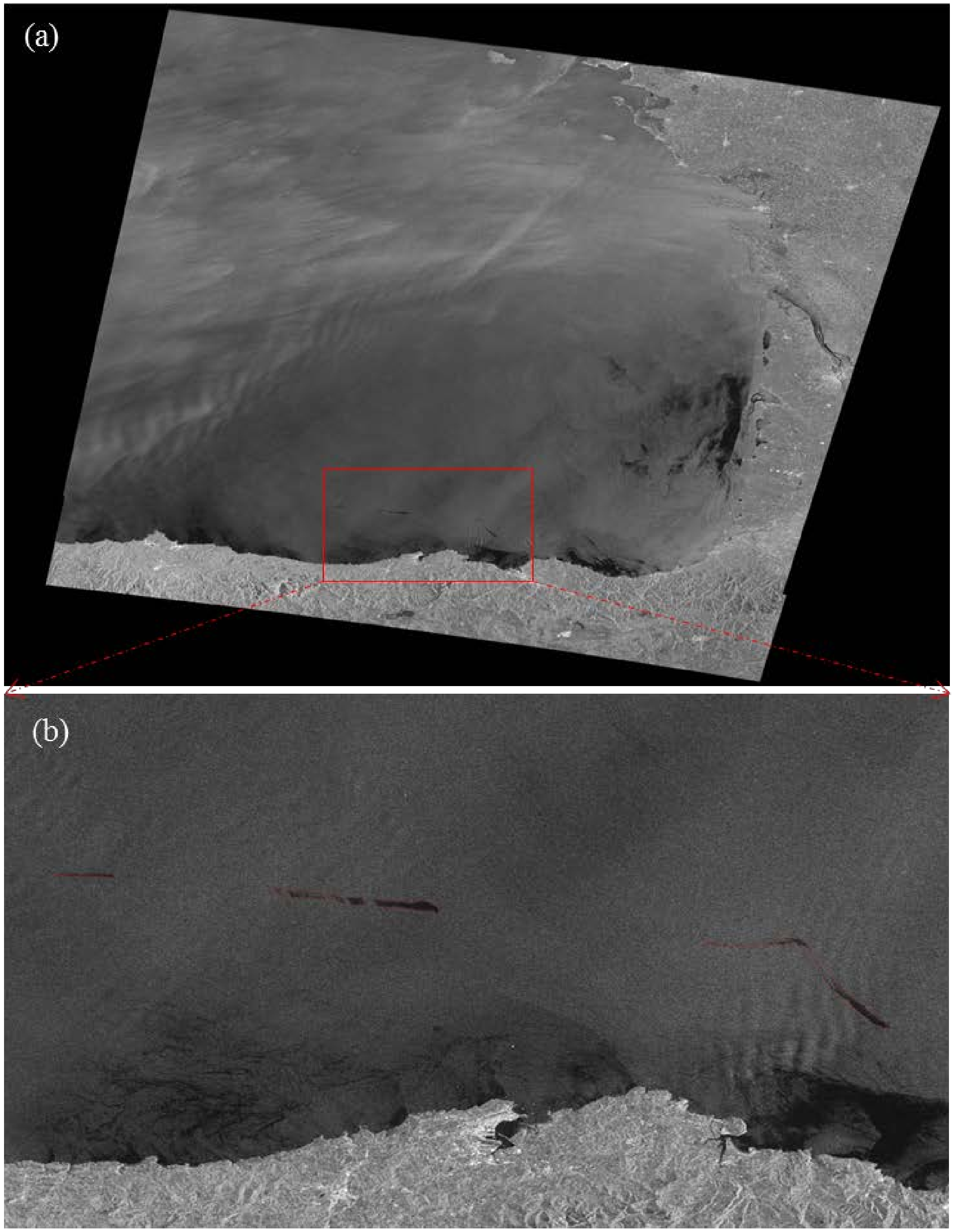

Fig 4.17: Example of oil spill on a RADARSAT-2 SAR ScanSARNarrow Beam image acquired on 15th of June 2012 at 06:24:44 near northern coast of Spain (a). Patches indicated in bright red out line shows detection by proposed ANN based algorithm using full spectrum of feature parameters near coastline (b). CleanSeaNet Image ID: 22718 (RADARSAT-2 image © CSA/MDA/EMSA 2012).

CHAPTER V

CONCLUSIONS AND FUTURE SCOPE

6.1 CONCLUSIONS

Oil spill, as already mentioned has wide environmental impact on the marine ecosystem. The largest challenge in detection of oil spills in SAR images is accurate discrimination between oil spills and look-alikes. Therefore, the main objective of this study is to detection of oil spill as dark spot and to discriminate oil spill from other oceanographic and metrological look-alike phenomenon. Space-borne SAR (ScanSAR, WideScanSAR) images are mostly used for operational oil spill detection as it covers wide areas and operates at all-weather, day and night. Although several studies successfully exploited SAR polarimetric features for oil spill detection, its operation potential is limited in current situation mainly due to reduced coverage and revisit capability in polarimetric mode. In this study, different operational methodologies based on several steps of detecting oil spill from SAR images has been implemented and investigated.

More than 200 Synthetic Aperture Radar images have been analysed and used to evaluate the proposed feature vectors. Since the characteristics of the SAR data were known a priori, it was expedient to assess the implementation and validation of the methodology for oil spill detection.

The oil spill detection methodology consists of the following steps,

i. Image pre-processing

ii. Dark spot segmentation

iii. Feature extraction

iv. Classification between oil spill and look-alike spots.

Four methods for image segmentation has been evaluated (edge detection, adaptive theresholding, artificial neural network based and contrast split segmentation). More than 40 feature extraction parameters were evaluated and used for classification stage. Two completely different classification technique (ANN and Rule based algorithms) were developed, calibrated and benchmarked with satisfactory results. Dark spots were detected (as results from segmentation stage) with an average classification accuracy of 96%

Oil spills were separated successfully from look-alikes with the classification accuracy of 91.6% for ANN based algorithm and over 85% for rule based algorithm. Significant variance was observed in the extracted parameters between oil spill and ‘look-alike’ spots. However some of the feature parameters such as, “Gradient Min” and “Number of Edges” did not perform well in terms of segregating the oil spills and ‘look-alike’ spots.

The main contributions and findings of this thesis are:

- An extensive overview of the present methodologies and technology applied in the field of oil spill remote sensing is given (Chapter I and Chapter II).

- An improved segmentation algorithm based on Artificial Neural Network for better segmentation accuracy is developed (Paper I and Chapter III).

- The classification power of various feature parameters was investigated using statistical analysis and new features are introduced. In particular some shape related features, GLCM features and a surroundings related features are found to be better description of the dark spots. All of the feature parameters were investigated found to follow ‘Generalized Extreme Value’ (GEV) distribution. (Paper II and Chapter III).

- Rule based classification follow by fuzzy logic selection is capable to reducing the number of false alarms while keeping a high detection rate (Paper II, Chapter III and Chapter IV).

- Based on a benchmark study where automatic, semi-automatic and manual SAR image analysis approaches are compared with “ground truth” data (EMSA feedback data from costal states), the potential of automatic algorithms for oil spill detection is documented (Paper II, Paper V and Chapter IV).

- An automated SAR image processing chain was developed and calibrated for oil spill detection. Intention of this work was to development of an in house service quality assessment tool for EMSA’s ‘CleanSeaNet’ service. Benchmarking study (rule based classification technique) found that the classification accuracy of this chain is satisfactory. The implemented processing chain works well under ‘CleanSeaNet’ near real time requirements (Paper II, Paper V and Chapter IV).

- The Performance of the neural network technique was found to better than that of edge detection technique for segmentation of the SAR image. The neural network's ability to successfully separate the linearly inseparable classes is a great advantage with respect to the commonly and previously used statistical approaches (Chapter IV).

- A set of 14 proposed feature extraction parameters were able to discriminate the oil spills from look-alike spots successfully using ANN (Paper I and Chapter III).

- The backpropagation ANN with two hidden layer was able to accurately segregate the oil spills from the look-alikes to an accuracy of 91.67% with 14 selected feature extracted parameters which has proved the superiority of ANN on previously used conventional statistical approaches and the selected feature vector.

- In rule based classification technique, a second step of the classification approach following classification with the regular 'ruleset' was introduced. In order to, let the user tune the system with respect to the trade-off between the number of true positives and false positives. This proposed algorithm found to be a useful in house tool for 'CleanSeaNet' operation during a benchmark study carried out at European Maritime Safety agency by the author of the thesis. (Paper II and Chapter III).

- ANN based algorithm using the full spectrum of the feature extracted parameters preforms slightly better for the oil spill detection, although it suffers from higher false alarm rate.

6.2 FUTURE SCOPE

Following recommendations are proposed for the future work,

a) Improvements of ‘ruleset’ for different kind of new and upcoming SAR sensors like ‘Sentinel 1’ and integrate into the implemented processing chain.

b) Improvements of ‘ANN’ based algorithm in order to reduce false alarm rate and implement it in a near real time processing chain.

c) Better understandings of the physical and biological phenomenon behind different kinds of ‘look-alike’ features are desirable.

d) Other segmentation and classification methods (e.g. Support Vector Machine, Spatial density thresholding etc.) could be attempted.

e) A standard set of feature extraction parameters have yet to be finalized. It has been observed that the variance in shape, contrast, and surroundings of oil slicks and look-alikes is so large that it is necessary to group them properly for a given problem of oil spill detection in a given geographic area.

As mentioned before, oil spill detection using multi polarimetric SAR data is also an emerging field. In recent years, a number of polarimetric measures useful for oil-spill and look-alike discrimination have been proposed. These include both quad-pol features like polarimetric entropy and anisotropy, mean scattering angle, polarimetric span, conformity coefficient, as well as the dual-pol features such as standard deviation of the co-polarized phase difference and the co-polarized correlation coefficient. By using polarimetric SAR as available on RADARSAT-2, COSMOS SkyMed, TerraSAR-X and upcoming Sentinel-1, it seems that oil spills can be distinguished from biogenic films. The difference in detection accuracy with single polarimetric versus polarimetric data is not yet documented and detailed study combining those two kinds of methodology on a large data set and its operational implementation is expected.

REFERENCES

Alpers, W. and Huhnerfuss, H., 1988, "Radar signatures of oil films floating on the sea surface and the Marangoni effect". *Journal of Geophysical Research*, 93, pp. 3642–3648.

Alpers, W., Brandt, P., Lazar, A., Dagorne, D., Sow, B., Faye, S., Hansen, M., Rubino, A., Poulain, P.M. and Brehmer, P., 2013, "A small-scale oceanic eddy off the coast of West Africa studied by multi-sensor satellite and surface drifter data", Remote Sensing of Environment, Vol. 129, pp.132–143.

Arora, M. K. and Foody, G. M., 1997, Log-linear modelling for the evaluation of the variables affecting the accuracy of probabilistic, fuzzy and neural network classifications. *International Journal of Remote Sensing,* Vol. 18, Issue 4, pp. 785 – 798.

Atkinson, P. M. and Tatnall, A.R.L., 1997, "Neural networks in remote sensing". *International Journal of Remote Sensing,* 18**,** pp. 699- 709.

Barni, M., Betti, M., & Mecocci, A., 1995, A fuzzy approach to oil spill detection on SAR images.", *In Proc. IEEE International Geoscience and Remote Sensing Symposium'1995*, Vol. 1 pp. 157– 159.

BBC News, 2010, *http://www.bbc.co.uk/,* Accessed during Gulf of Mexico (BP) oil spill incident (May – August 2010).

Bern, T.-I., Wahl, T., Andersson, T. and Olsen, R., 1992, Oil spill detection using satellite based SAR: experience from a field experiment. In *Proceedings of the 1st ERS-1 Symposium*, 4–6 November 1992, Cannes, France, pp. 829–834 (Paris: ESA Publication Division).

Bishop, C. M., 1995, Neural networks for pattern recognition. Oxford University Press, UK.

Bolus R.L., 1996, Airborne testing of a suite of remote sensors for oil spill detecting on water. In: *Proceedings of the Second Thematic International Airborne Remote Sensing Conference and Exhibition*, Environmental Research Institute of Michigan, Ann Arbor, Michigan pp. III 743–III 752

Brekke, C. and Solberg, A.H.S., 2005a, "Oil spill detection by satellite remote sensing". *Remote Sensing of Environment,* Vol. 95, Issue 1, pp. 1–13.

Brekke, C. and Solberg, A.H.S., 2005b, "Feature Extraction for Oil Spill Detection Based on SAR Images". SCIA 2005, *LNCS* 3540, pp. 75–84.

Brekke, C., 2007, "Automatic screening of Synthetic Aperture Radar imagery for detection of oil pollution in the marine environment" *Unpublished PhD Thesis,* Faculty of Mathematics and Natural Science, University of Oslo, 189pp.

Brekke, C., Holt, B., Jones, C. and Skrunes, C., 2014. "Discrimination of oil spills from newly formed sea ice by synthetic aperture radar", *Remote Sensing of Environment*, Vol. 145, pp. 1-14.

BONN Agreement Aerial Operations Handbook, 2009, Accessed online: April 2012 (http://www.bonnagreement.org/eng/doc/Bonn%20Agreement%20Aerial%20Operations%20Handbook.pdf)

Brown, C.E., Fruhwirth, M., Nelson, R. and Fingas, M.F., 1996, "Real-time response with a laser environmental fluorosensor: the integration of fluorescence data with down-looking video images and the prompt delivery of hard-copy maps". In: *Proceedings of the Second Thematic International Airborne Remote Sensing Conference and Exhibition*, Environmental Research Institute of Michigan, Ann Arbor, Michigan, pp. III 673–III 681.

Brown, C.; Fingas, M.; Hawkins, R., 2003, Synthetic Aperture Radar Sensors: Viable for Marine Oil Spill Response?. *In Proc. 26th Arctic and Marine Oil Spill Program (AMOP) Technology Seminar.* Victoria, Canada, June 10–12**,** 299-310.

Brown, C., Fingas, M. and Marois, R., 2004, "Oil spill remote sensing: laser fluorosensor demonstration flights off the east coast of Canada". *In Proc. 27th Arctic and Marine Oil Spill Program (AMOP) Technology Seminar,* Edmonton, Canada, June 6–8, , 317-334.

Brown,C. and Fingas, M. 2005, "A review of current global oil spill surveillance, monitoring and remote sensing capabilities". *In Proc. 28th Arctic and Marine Oil Spill Program (AMOP) Tech. Seminar* Calgary, Canada, Jun. 7–9, pp. 789-798.

Brooks, S. R. and Miller, P. F., 1979, "The influence of radiometric resolution on synthetic aperture radar design parameters," in *Proc. ESA ESASAT Workshop*, pp. 79–85, ESA SP-154.

Burger A.E., 1993, "Estimating the mortality of seabirds following oil spills: effects of spill volume". *Marine Pollution Bulletin* Vol. 26**,** pp.140–143.

Calabressi, G., Del Frate, F., Lichtenegger, J. and Petrocchi, A., 1999, "Neural networks for the oil spill detection using ERS-SAR data". *Proceedings of Geoscience and Remote Sensing Symposium, IGARSS'99*, 28 June – 2 July, Hamburg, Germany, 1, pp. 215–217.

Congalton, R. G., 1991, "A review of assessing the accuracy of classifications of remotely sensed data". *Remote Sensing of Environment*, 37, pp. 35- 46.

Curlander, J. C. and McDonough, R. N., 1991, Synthetic Aperture Radar: Systems and Signal Processing. New York: Wiley.

Del Frate, F., Petrocchi, A., Lichtenegger, J. and Calabresi, G., 2000, "Neural networks for oil spill detection using ERS-SAR data". *IEEE Transactions on Geoscience and Remote Sensing*, Vol. 38, No.5, pp. 2282–2287.

Derrode, S., Mercier, G., 2007, “Unsupervised multiscale oil slick segmentation from SAR images using a vector HMC model”, *Pattern Recognition* Vol. 40, pp.1135 – 1147.

Duda, R.O., Hart, P.E. and Stork D.G. 2001. Pattern Classification. John Wiley & Sons, New York.

eCognition Developer 8.0.1, Reference Book, Copyright © 2010 Definiens AG

EC Directive 2005/35/EC of the European Parliament and of the Council on ship-source pollution and on the introduction of penalties for infringements, 7 September 2005, http://eur-lex.europa.eu

Edwards, R., White, I., 1999. The *Sea Empress* oil spill: environmental impact and recovery. In: *Proceedings of the 1999 International Oil Spill Conference*, American Petroleum Institute, Washington, DC

Egmont-Petersen, M., De Ridder, D. And Handels, H., 2002, “Image processing with neural networks—a review”. Pattern Recognition, 35, pp. 2279–2301.

Elachi, C., 1987, “Introduction to the physics and techniques of remote sensing”, John Wiley & Sons.

ESA Portal (European Space Agency), 2010, “Envisat’s ASAR reveals extent of massive oil spill off Spanish coast”, http://envisat.esa.int/asar_oil_spill/, Last accessed on May 20, 2010.

ESA, (European Space Agency), (1998), “Oil pollution monitoring”, *ESA brochure: ERS and its applications—Marine* BR-128 p. 1.

ESA Radar Course III, accessed online 07th April 2013 (http://earth.esa.int/applications/data_util/SARDOCS/spaceborne/Radar_Courses/Radar_Course_III/bragg_scattering.htm)

Espedal, H. A., O. M. Johannessen, and J. Knulst (1996), Satellite detection of natural films on the ocean surface, *Geophysical Research Letter*., Vol. 23, No.22, pp. 3151-3154.

Espedal, H. A. and Wahl, T., 1999, “Satellite SAR oil spill detection using wind history information”. *International Journal of Remote Sensing*, Vol. 20, No. 1, pp. 49-65.

Espedal, H., Johannessen, O., Johannessen, J., Dano, E., Lyzenga, D., and Knulst, J., 1998, “COASTWATCH'95: ERS 1/2 SAR detection of natural film on the ocean surface”, *Journal of Geophysical. Research*, Vol. 103 No. C11, pp. 24969–24982.

Espedal, H. A. and Johannessen,. 2000, “Cover: Detection of oil spills near offshore installations using synthetic aperture radar (SAR)”. *International Journal of Remote Sensing*, Vol. 21, No.11, pp. 2141-2144.

European Maritime Safety Agency (EMSA), 2011. Report on CleanSeaNet First Generation 16 April 2007-31 January 2011. Accessed online July 2012. (http://emsa.europa.eu/operations/cleanseanet.html)

European Maritime Safety Agency (EMSA), 2014. Action Plan for Response to Marine Pollution from Oil and Gas Installations. Published online 28.01.2014. (http://www.emsa.europa.eu/news-a-press-centre/external-news/2-news/1961-action-plan-for-response-to-marine-pollution-from-oil-and-gas-installations.html)

European Parliament, 2007, Legislative resolution on the Council common position for adopting a directive of the European Parliament and of the Council establishing a Framework for Community Action in the field of Marine Environmental Policy (Marine Strategy Framework Directive) (9388/2/2007 – C6-0261/2007 – 2005/0211(COD), 11 December 2007, Accessed online: August 2011. http://www.europarl.europa.eu/sides/getDoc.do?type=TA&language=EN&reference=P6-TA-2007-0595#BKMD-19

Fast, O., 1986, Remote sensing of oil on water-air and Space-borne systems, In *Proceedings of the DOSS seminar*, SINTEF, Trondheim, Norway.

Ferraro, G., Baschek, B., Montpellier, G., Njoten, O., Perkovic, M., Vespe, M., 2010, On the SAR derived alert in the detection of oil spills according to the analysis of the EGEMP, *Marine Pollution Bulletin*, Vol. 60, Issue 1, pp. 91-102.

Feng, M. and Jun, H., 2007 “The critical techniques for ScanSAR radiometric correction,” in *Proc. 1st APSAR*, Huangshan, Nov. 2007, pp. 10–13.

Fingas, M.F., Brown, C.E. and Fruhwirth, M., 1996, An assessment of sensors for oil spill applications. In: *Proceedings of the Second Thematic International Airborne Remote Sensing Conference and Exhibition*, Environmental Research Institute of Michigan, Ann Arbor, Michigan, pp.689 - 698.

Fingas M. F. and Brown C. E., 1997a, “Review of Oil Spill Remote Sensing”. *Spill Science & Technology Bulletin*, Vol. 4, No. 4, pp. 199-208.

Fingas, M.F. and Brown, C.E., 1997b, Airborne oil spill remote sensors — do they have a future?. In: *Proceedings of the Third International Airborne Remote Sensing Conference and Exhibition*, Environmental Research Institute of Michigan, Ann Arbor, Michigan , pp. I715–I722.

Fingas, M.F. and Brown, C.E., 2002, Review of oil spill remote sensing, Presented at the Seventh International Conference on Remote Sensing for Marine and Coastal Environments, Miami, Florida, May 20-22.

Fingas, M. and Brown, C., 2005, An update on oil spill remote sensors. *In Proc. 28th Arctic and Marine Oil Spill Program (AMOP) Tech. Seminar* Calgary, Canada, Jun. 7–9, pp. 825-860.

Fiscella, B., Giancaspro, A., Nirchio, F., Pavese, P. and Trivero, P. 2000, “Oil spill detection using marine SAR images”. *International Journal of Remote Sensing*, Vol. 21, No. 18, pp. 3561-3566.

Foody, G. M., 1995, “Land cover classification by an artificial neural network with ancillary information”. *International Journal of Geographical Information Systems*, Vol. 9, pp. 527-542.

Foody, G. M., and Arora, M. K., 1997, “An evaluation of some factors affecting the accuracy of classification by an artificial neural network”. *International Journal of Remote Sensing*, Vol. 18, Issue 4, pp. 799- 810.

Gade, M. and Alpers, W., 1999 Using ERS-2 SAR images for routine observation of marine pollution in European coastal waters, *The Science of the Total Environment*, *237*/238, pp. 441-448.

Gade, M., Scholz, J. and Viebahn, C., 2000, “On the delectability of marine oil pollution in European marginal waters by means of ERS SAR imagery”. *International Geoscience and Remote Sensing Symposium, 2000*, VI, pp. 2510–2512.

Garcia-Pineda, O., Zimmer, B., Howard, M., Pichel, W., Li, X. and MacDonald, I. R., 2009, “Using SAR images to delineate ocean oil slicks with a texture-classifying neural network algorithm (TCNNA),” *Canadian Journal of Remote Sensing.*, Vol. 35, No. 5, pp. 411–421,.

Garrett J., 1994. Where and why artificial neural networks are applicable in civil engineering. *Journal of Computing in Civil Engineering*, Vol. 8, pp. 129-130.

GESAMP, 2007, Joint Group of Experts on the Scientific Aspects of Marine Environmental Protection (GESAMP) 2007 – Report n° 75 Estimates of Oil Entering the Marine Environment from Sea-Based Activities – Page 61, www.imo.org

GSHHS, 2013a Global Self-consistent, Hierarchical, High-resolution Shoreline Database, http://www.ngdc.noaa.gov/mgg/shorelines/gshhs.html

GSHHS, 2013b Global Self-consistent, Hierarchical, High-resolution Shoreline data sets structure, ftp://ftp.soest.hawaii.edu/pwessel/gshhs/README.gshhs

Goodman, R., 1994, “Overview and future trends in oil spill remote sensing”. *Spill Science and Technology Bulletin*, Vol. 1, pp. 11–21.

Hanjsek, I., Pottier, E. and Cloude, S. R., 2003, ”Inversion of surface parameters frompolarimetric SAR”, IEEE Transaction of Geoscience and Remote Sensing, Vol. 41, No. 4, pt. 1, pp. 727–744.

Heijmans H., Mathematical Morphology: Basic Principles, http://citeseerx.ist.psu.edu/viewdoc/download?doi=10.1.1.50.7758&rep=rep1&type=pdf

Hühnerfuss, H., Alpers, W. and Richter, K., 1986, "Discrimination between crude-oil spills and monomolecular sea slicks by airborne radar and infrared radiometer—possibilities and limitations", *International Journal of Remote Sensing*, Vol. 7, Issue. 8, pp. 1001 – 1013.

Hühnerfuss, H., Walter, W., Lange, P. A., and Alpers, W., 1987, "Attenuation of Wind Waves by Monomolecular Sea Slicks and the Marangoni Effect", *Journal of Geophysical. Research.*, Vol. 92 No. C4, pp. 3961–3963.

Hühnerfuss, H. and Gericke, A., 1994, "Classification of sea slicks by multifrequency radar techniques: New chemical insights and their geophysical implications", *Journal of Geophysical Research*, Vol. 99, No. C5, pp. 9835-9845.

Huang, B., Li, H. and Huang, X. 2005 "A level set method for oil slick segmentation in SAR images". *International Journal of Remote Sensing*, Vol. 26, No. 6, pp. 1145–1156.

Indregard, M., Solberg, A. and Clayton, P., 2004. "D2-report on benchmarking oil spill recognition approaches and best practice". Tech. rep., Oceanides project, European Commission, Archive No. 04-10225-A-Doc, Contract No: EVK2-CT-2003-00177.

ITOPF, 2010**,** (The International Tankers Owners Pollution Federation Limited), http://www.itopf.com/, Accessed 5th July, 2010.

Ivanov, A. Yu. and Zatyagalova, V. V., 2008, "A GIS approach to mapping oil spills in a marine environment". *International Journal of Remote Sensing*, Vol 29, No 21, pp. 6297-6313.

IMO, 1973, International Convention for the Prevention of Pollution from Ships, as modified by the Protocol of 1978 relating thereto (MARPOL) http://www.imo.org/

Jha M. N., Levy J. and Gao Y., 2008**, "** Advances in Remote Sensing for Oil Spill Disaster Management: State-of-the-Art Sensors Technology for Oil Spill Surveillance". *Sensors*, Vol. 8, Issue 1, pp. 236-255.

Kanellopoulo, I., and Wilkinson, G. G., 1997, Strategies and best practice for neural network image classification. *International Journal of Remote Sensing*, Vol. 18, pp. 711–725.

Karantzalos K. and Argialas D., 2008, Automatic Detection and Tracking of Oil Spills with Level Set Segmentation from SAR Imagery, *International Journal of Remote Sensing***,** Vol. 29, Issue 21, pp. 6281-6296.

Karathanassi, V., Topouzelis, K., Pavlakis, P. And Rokos, D., 2006, "An object-oriented methodology to detect oil spills". *International Journal of Remote Sensing*, Vol. 27, pp. 5235–5251.

Kavzoglu, T. and Mather, P., 2003, "The use of backpropagation artificial neural network in land cover classification". *International Journal of Remote Sensing*, Vol. 24, Issue 23, pp. 4907–4938.

Keramitsoglou, I., Cartalis, C.and Kassomenos,P., 2003, "Decision support system for managing oil spill events", *Environmental Management* Vol. 32, No. 2, pp. 290–298

Keramitsoglou, I., Cartalis, C. and Kiranoudis, C. T., 2005, "Automatic identification of oil spills on satellite images", *Environmental Modelling & Software* Vol. 21 pp. 640–652

Kingston, P. F., 2002, "Long-term Environmental Impact of Oil Spills", *Spill Science & Technology Bulletin*, Vol. 7, No. 1–2, pp. 53–61,

Kontoes, C. C., Sykioti, O., Paronis, D. and Harisi, A., 2005, "Evaluating the performance of the space-borne SAR sensor systems for oil spill detection and sea monitoring over the south-eastern Mediterranean Sea". *International Journal of Remote Sensing,* Vol. 26, Issue 18, pp. 4029-4044.

Kubat, M., Holte, R. and Stan, M., 1998, Machine learning for the detection of oil spills in satellite radar images, *Machine Learning*, Vol. 30, pp. 195–215.

Li, Y. and Li, J., 2010, Oil spill detection from SAR intensity imagery using a marked point process, *Remote Sensing of Environment*, Vol.114, Issue 7, pp. 1590-1601.

Li H & Boufadel M. C., 2010, "Long-term persistence of oil from the *Exxon Valdez* spill in two-layer beaches" *Nature Geoscience,* (Published online: 17 January 2010).

Lillesand, T. M., Kiefer, R. W. and Chipman, J. W., 2004, Remote Sensing and Image Interpretation, Wiley.

Litovchenko, K., Ivanov, A. and Ermakov, S., 1999, Detection of oil slicks parameters from ALMAZ-1 and ERS-1 SAR imagery, In *Proc.* ", *In Proc. IEEE International Geoscience and Remote Sensing Symposium 1999* Vol. 3**,** pp. 1484–1486.

Lee, J.-S., Krogager, E., Ainsworth, T. L., and Boerner, W.-M., 2006. "Polarimetric analysis of radar signature of a manmade structure," *IEEE Geoscience. Remote Sens. Letter*, Vol. 3, No. 4, pp. 555–559.

Lu, J., Lim, H., Liew, S., Bao, M. and Knowoh, L., 1999, "Ocean oil pollution mapping with ERS synthetic aperture radar imagery". *International Geoscience and Remote Sensing Symposium (IGARSS'99)*, pp. 212–214.

Mastin, G.A., Mason, J.J., Bradley, J.D., Axline, R.M. and Hover, G.L., 1994, "A comparative evaluation of SAR and SLAR. In: *Proceedings of the Second Thematic Conference on Remote Sensing for Marine and Coastal Environments:*

Needs, Solutions and Applications, ERIM Conferences, Ann Arbor, Michigan, pp. I-7–I-17

Marghany, M., 2004, **"**RADARSAT, for oil spill trajectory model". *Environmental Modelling Software*, Vol. 19, pp. 473- 483.

MARPOL 73/78, www.imo.org, Accessed January 2013, (http://www.imo.org/About/Conventions/listofconventions/pages/international-convention-for-the-prevention-of-pollution-from-ships-(marpol).aspx)

Mera, D., Cotos, J. M., Varela-Pet, J. and Garcia-Pineda, O., 2012, "Adaptive thresholding algorithm based on SAR images and wind data to segment oil spills along the northwest coast of the Iberian Peninsula". *Marine Pollution Bulletin*, Vol. 64, Issue. 10, pp. 2090–2096.

Mercier, G. and Girard-Ardhuin, F., 2006, Partially Supervised Oil-Slick Detection by SAR Imagery Using Kernel Expansion, *IEEE Transactions on Geocience and Remote Sensing*, Vol. 44, Issue. 10, pp. 746–755.

Migliaccio, M., Gambardella, A., Tranfaglia, M., 2007. SAR polarimetry to observe oil spills. *IEEE Transaction on Geoscience and Remote Sensing* Vol. 45, Issue 2, pp. 506–511.

Migliaccio, M., Nunziata, F., Gambardella, A., 2009a. "On the copolarised phase difference for oil spill observation". *International Journal of Remote Sensing*, Vol. 30, Issue 6, pp.1587–1602.

Migliaccio, M., Gambardella, A., Nunziata, F., Shimada, M., Isoguchi, O., 2009b. The PALSAR polarimetric mode for sea oil slick observation. IEEE Transaction on Geoscience and Remote Sensing 47 (12), 4032–4041.

Migliaccio, M., Nunziata, F., Montuori, A., Li, X., Pichel, W., 2011a. A multi-frequency polarimetric SAR processing chain to observe oil fields in the Gulf of Mexico. *IEEE Transaction on Geoscience and Remote Sensing,* Vol. 49, Issue 12, pp. 4729–4737.

Migliaccio, M., Nunziata, F., Montuori, A., Brown, C.E., 2011b. Marine added-value products by RADARSAT-2 fine quad-polarization mode. *Canadian Journal of Remote Sensing* Vol. 37, Issue 5, pp. 441–450.

Miranda, F.P., Marmol, A.M.Q., Pedroso, E.C., Beisl, C.H., Welgan, P. and Morales, L.M., 2004, "Analysis of Radarsat-1 data for offshore monitoring activities in the Cantarella Complex, Gulf of Mexico using the unsupervised semivariogram textural classifier (USTC)". *Canadian Journal of Remote Sensing,* Vol. 30, pp. 424–436.

Moreira, A., Prats-Iraola, P., Younis, M., Krieger, G., Hajnsek, I. and Papathanassiou, K.P., 2013, "A tutorial on synthetic aperture radar", *IEEE Geoscience and Remote Sensing Magazine*, vol.1, no.1, pp.6-43.

Mussetto, M.S., Yujiri, L., Dixon, D.P., Hauss, B.I. and Eberhard, C.D., 1994, “Passive millimeter wave radiometric sensing of oil spills”. In: *Proceedings of the Second Thematic Conference on Remote Sensing for Marine and Coastal Environments: Needs, Solutions and Applications*, ERIM Conferences, Ann Arbor, Michigan, pp. I-35–I-46

Nirchio, F., Sorgente, M., Giancaspro, A., Biamino, W., Parisato, E., Ravera, R. and Trivero, P., (2005). Automatic detection of oil spills from SAR images. *International Journal of Remote Sensing*, Vol. 26, Issue 6, pp. 1157–1174.

NOAA, USA website, 2010, (National Oceanic and Atmospheric Administration). http://response.restoration.noaa.gov/. See Topic: Emergency Response, Responding to Oil Spills. Last accessed on May 20, 2010.

Nunziata, F., Gambardella, A., Migliaccio, M., 2008. On the Mueller scattering matrix for SAR sea oil slick observation. *IEEE Geoscience and Remote Sensing Letters* Vol. 5 Issue 4, pp. 691–695.

Nunziata, F., Migliaccio, M., Gambardella, A., 2011. Pedestal height for oil spill observation. *IET Radar Sonar and Navigation,* Vol. 5, Issue 2, pp. 103–110.

Nunziata, F., Gambardella, A., Migliaccio, M., 2012. A unitary Mueller-based view of polarimetric SAR oil slick observation. *International Journal of Remote Sensing* Vol. 33, Issue 20, pp. 6403–6425.

Nunziata, F., Gambardella, A., Migliaccio, M., 2013. On the degree of polarization for SAR sea oil slick observation. *ISPRS Journal of Photogrammetry and Remote Sensing*, Vol. 78, pp. 41–49.

O'Neil R.A., Neville R.A. and Thompson V., 1983, “The Arctic Marine Oil spill Program (AMOP) remote sensing study”. *Environment Canada Report EPS 4-EC-83-3* Ottawa, Ontario

OSPAR, 2003, Strategies, http://www.ospar.org/eng/html/welcome.html

Plaza, J.; Pérez, R.; Plaza, A.; Martínez, P.; Valencia, D., 2001, “Mapping oil spills on sea water using spectral mixture analysis of hyperspectral image data”. *Proc. of SPIE, 5995 599509-1.*

Pathegama, M. and Göl, Ö., 2004, “Edge-end pixel extraction for edge-based image segmentation”, Transactions on Engineering, Computing and Technology, Vol. 2, pp. 213-216,

Richards, J.A. and Jia, X., 1999, “Remote sensing digital image analysis, an introduction”, *3rd, revised and enlarged edition*, Springer-Verlag, Berlin, Germany.

Salem F. and Kafatos P.M., 2001, Hyperspectral image analysis for oil spill mitigation, *Proc. ACRS 2001—22nd Asian Conference on Remote Sensing, 5–9 November 2001, Singapore,* Vol. 1, pp. 748–753

Salisbury, J., D'aria, D. and Sabins, F., 1993**, "**Thermal Infrared Remote Sensing of Crude Oil Slicks". *Remote Sensing of Environment*, Vol. 45, Issue 2, pp. 225-231.

Serra, J., 1982, Image Analysis and Mathematical Morphology, *Academic Press London,*

Sheng Y. W., Xia Z. G., A. 1996, Comprehensive evaluation of filters for radar speckle suppression. In proc. *IEEE Geoscience and Remote Sensing Symposium,* Lincoln, USA, IGARSS'96, Vol. 3 pp. 1559 – 1561.

Shi, L., Ivanov, A. YU., He, M. and Zhao, C., 2008, Oil spill mapping in the western part of the East China Sea using synthetic aperture radar imagery, *International Journal of Remote Sensing,* Vol. 29, No. 21, pp. 6315 - 6329.

Shu, Y., Li, J., Yousif, H. and Gomes, G., 2010a, Dark-spot detection from SAR intensity imagery with spatial density thresholding for oil-spill monitoring, *Remote Sensing of Environment,* Vol.114, Issue 9, pp. 2026-2035.

Shu, Y., 2010b**, "**Dark spot detection from SAR intensity imagery with spatial density thresholding for oil spill monitoring", *Unpublished M.Sc Thesis*, Department of Geography, University of Waterloo.

Skolnik, M. I., 2008, *Radar Handbook*, 3rd ed. New York:McGraw-Hill, 2008.

Singh, K. P., Gray, A. L., Hawkins, R. K., and O'Neil, R. A., 1986, "The influence of surface oil and C- and Ku-band ocean backscatter". *IEEE Transactions on Geoscience and Remote Sensing*, 24, pp. 738–744.

Singha, S., Bellerby, T. and Trieschmann, O., 2012, "Detection and classification of oil spill and look-alike spots from SAR imagery using an artificial neural network", *In Proc. IEEE International Geoscience and Remote Sensing Symposium,* IGARSS'12, Munich, Germany, pp.4403-4406.

Singha, S., Bellerby, T. and Trieschmann, O., 2013a, "Satellite oil spill detection using artificial neural networks*", IEEE Journal of Selected Topics in Applied Earth Observations and Remote Sensing,* Vol. 6, Issue 6, pp. 2355–2363.

Singha, S., Vespe, M. and Trieschmann, O., 2013b, "Automatic SAR based Oil Spill Detection and Performance Estimation via Semi-Automatic Operational Service Benchmark", *Marine Pollution Bulletin,* Vol. 73, Issue 1, pp. 199–209.

Singha, S., Topouzelis, K., Vespe, M. and Trieschmann, O., 2013c, "Radiometric Normalization on SAR Images for Oil Spill Detection", *In Proc. ESA Living Planet Symposium 2013,* Edinburgh, United Kingdom, (ESA-SP -772).

Skøelv, A., Wahl, T., 1993, Oil spill detection using satellite based SAR, Phase 1B competition report. Technical report, Norwegian Defence Research Establishment.

Skou, N., Sorensen, B.M. and Poulson, A., 1994, A new airborne dual frequency microwave radiometer for mapping and quantifying mineral oil on the sea surface, In

Proc. Second thematic conference on remote sensing for marine and costal environment, Erim Conference, Ann Arbor, Michigan, pp. II-559-565.

Skrunes, S., Brekke, C. and T. Eltoft., 2014, "Characterization of Marine Surface Slicks by Radarsat-2 Multipolarization Features," *IEEE Transactions on Geocience and Remote Sensing*, vol.52, no.9, pp.5302-5319, Sept.

Solberg, A.H.S. and Volden E., 1997, "Incorporation of prior knowledge in automatic classification of oil spills in ERS SAR images", *In Proc. IEEE International Geoscience and Remote Sensing Symposium IGARSS'97,* Vol. 1, pp. 157–159

Solberg, A., Storvik, G., Solberg, R. and Volden, E., 1999, "Automatic Detection of Oil Spills in ERS SAR Images". *IEEE Transactions on Geocience and Remote Sensing*, 37(4), pp. 1916–1924.

Solberg, A. H. S., Brekke, C. and Husøy, P. O., 2007, Oil spill detection in Radarsat and ENVISAT SAR images. *IEEE Transactions on Geocience and Remote Sensing*, 45(3), 746–755.

Solberg, A.H.S. 2012, "Remote sensing of ocean oil-spill pollution". *Proceedings of the IEEE*, Vol. 100, No.10, pp. 2931–2945

Sorensen, B. M., 1992, The European operational airborne oil pollution scenario, In *Proceedings of first thematic conference on remote sensing for marine and costal environment*, Erim Conference, Ann Arbor, Michigan, pp. 989-1003.

Stathakis, D., Topouzelis, K. and Karathanassi, V., 2006, Large-scale feature selection using evolved neural networks In *Proceedings of SPIE, Image and Signal Processing for Remote Sensing XII*, L. Bruzzone (Ed.), 13–14 September 2006, Stockholm, Sweden, 6365, pp. 636513.1–636513.9.

Taylor, S. 1992, *0.45 to 1.1 μm Spectra of Prudhoe Crude Oil and of Beach Materials in Prince William Sound, Alaska*, CRREL Special Report No. 92-5, Cold Regions Research and Engineering Laboratory, Hanover, New Hampshire, 14 p., 1992.

Topouzelis, K., Karathanassi, V., Pavlakis, P. and Rokos, D., 2002, "Oil spill detection: SAR multi-scale segmentation & object features evaluation". *9th International Symposium on Remote Sensing (SPIE)*, pp. 77–87.

Topouzelis K., Karathanassi V., Pavlakis P. and Rokos D.. 2007, "Detection and discrimination between oil spills and look-alike phenomena through neural networks". *ISPRS Journal of Photogrammetry & Remote Sensing* 62, pp. 264–270.

Topouzelis, K., Karathanassi, V., Pavlakis, P. and Rokos, D., 2008a, "Dark formation detection using neural networks". *International Journal of Remote Sensing*, Vol. 29, No. 16, pp. 4705- 4720.

Topouzelis, K., 2008b, Oil Spill Detection by SAR Images: Dark Formation Detection, Feature Extraction and Classification Algorithms. *Sensors,* Vol. 8, pp.6642-6659.

Topouzelis, K., Stathakis, D. and Karathanassi, V., 2009, Investigation of genetic algorithms contribution to feature selection for oil spill detection, *International Journal of Remote Sensing,* Vol. 30 Issue. 3, pp. 611-625

Trieschmann O., Hunsänger T., Tufte L. and Barjenbruch U., 2003, "Data assimilation of an airborne multiple remote sensor system and of satellite images for the North- and Baltic sea", *Proceedings of the SPIE 10th int. symposium on remote sensing, conference "remote sensing of the ocean and sea ice 2003"*, pp. 51–60

Trieschmann, O., Reichenbach, D., 2012.The integrated european satellite-based and aerial oil spill surveillance and vessel detection services. Interspill, London, United Kingdom.

Trivero, P., Fiscella, B., Gomez, F. and Pavese, P., 1998, "SAR detection and characterisation of sea surface slicks". *International Journal of Remote Sensing,* 19, pp. 543–548.

Ulaby, F.T., Moore, R.K. and A.K. Fung, 1986, "Microwave remote sensing: Active and passive". Vol. 3: From Theory to Applications, Artech house

Vespe, M. and Greidanus, H., 2012. SAR Image Quality Assessment and Indicators for Vessel and Oil Spill Detection, *IEEE Transaction on Geoscience and Remote Sensing* 50(11), 4726 – 4734.

Vespe, M., Ferraro, G., Posada, M., Greidanus, H. and Perkovic, M., 2011. Oil spill detection using COSMO-SkyMed over the adriatic sea: The operational potential. . *In Proc. IEEE International Geoscience and Remote Sensing Symposium, Vancouver, Canada*, IGARSS'11, Vol.1, pp. 4403-4406.

Vespe, M., Posada, M., Ferraro, G. and Greidanus, H., 2010. Perspectives on Oil Spill Detection using Synthetic Aperture Radar", Oceanography from Space – Revisited, Eds: Barale, V., Gower, J.F.R. and Alberotanza, L., Springer.

Wahl, T., Anderssen, T., Skøelv, Å., 1994a. Oil spill detection using satellite based SAR, Pilot Operation Phase, final report. Technical report, Norwegian Defence Research Establishment.

Wahl, T., Skøelv, Å. and Andersen, J.H.S., 1994b, "Practical use of ERS-1 SAR images in pollution monitoring", *In Proc. IEEE International Geoscience and Remote Sensing Symposium IGARSS'94,* vol. 4 , pp. 1954–1956.

Wahl, T., Skøelv, Å. Pedersen, J.P., Seljelv, L.-G., Andersen, J.H. and Follum, O.A et. al., 1996, "Radar satellites: A new tool for pollution monitoring in coastal waters", *Coastal Management* Vol. 24, pp. 61–7

Ziemke T., 1996 “Radar image segmentation using recurrent artificial neural networks”. *Pattern Recognition Letters* 17, pp. 319-334.

Zhifu, S., Kai Z., Baojiang, L. and Futao L., 2002, “Oil-spill monitoring using microwave radiometer”, *In Proc. IEEE International Geoscience and Remote Sensing Symposium, IGARSS'02* , Vol. 5, pp. 2980–2982.